



Electromagnetic security for information systems : statistical assessment of couplings in reverberant environments

Valentin Houchouas

► To cite this version:

Valentin Houchouas. Electromagnetic security for information systems : statistical assessment of couplings in reverberant environments. Electromagnetism. Sorbonne Université, 2020. English. NNT : 2020SORUS327 . tel-03411950

HAL Id: tel-03411950

<https://theses.hal.science/tel-03411950>

Submitted on 2 Nov 2021

HAL is a multi-disciplinary open access archive for the deposit and dissemination of scientific research documents, whether they are published or not. The documents may come from teaching and research institutions in France or abroad, or from public or private research centers.

L'archive ouverte pluridisciplinaire **HAL**, est destinée au dépôt et à la diffusion de documents scientifiques de niveau recherche, publiés ou non, émanant des établissements d'enseignement et de recherche français ou étrangers, des laboratoires publics ou privés.



Agence Nationale de la Sécurité des Systèmes d'Information

Laboratoire de la Sécurité des Technologies Sans Fil (LSF)

Sorbonne Université
Laboratoire Génie électrique et électronique de Paris (GeePs)

École doctorale:

Sciences mécaniques, acoustique, électronique et robotique de Paris

Présentée par

Valentin HOUCHOUAS

Sujet de la thèse :

Electromagnetic security for information systems Statistical assessment of couplings in reverberant environments

Thèse dirigée par M. Marc HÉLIER

Soutenue le mardi 30 juin 2020 devant le jury composé de :

Mme Françoise PALADIAN, <i>Professeur à l'Université de Clermont Auvergne</i>	Rapporteur
M. Alain REINEIX, <i>Directeur de recherche CNRS à l'Institut de recherche XLIM</i>	Rapporteur
M. Philippe BESNIER, <i>Directeur de recherche CNRS à l'IETR</i>	Examineur
M. Lionel PICHON, <i>Directeur de recherche CNRS au GeePs</i>	Examineur
Mme Hélène ROUSSEL, <i>Professeur à Sorbonne Université</i>	Examinatrice
M. Emmanuel COTTAIS, <i>Inspecteur de l'ANSSI</i>	Examineur
M. José LOPES ESTEVES, <i>Inspecteur de l'ANSSI</i>	Examineur
M. Marc HÉLIER, <i>Professeur à Sorbonne Université</i>	Directeur de thèse
Mme Muriel DARCES, <i>Maître de Conférences à Sorbonne Université</i>	Invitée
M. Emmanuel DUPONCHELLE, <i>Inspecteur de l'ANSSI</i>	Invité

Remerciements

Ce travail de recherche a été financé par l'Agence Nationale de la Sécurité des Systèmes d'information (ANSSI). Il s'est déroulé au sein du laboratoire de la sécurité des technologies sans fil (LSF) de l'ANSSI ainsi qu'au Laboratoire d'Électronique et Électromagnétisme (L2E), avant que ce dernier ne fusionne le 1^{er} janvier 2020 avec le laboratoire de Génie électrique et électronique de Paris (GeePs). Je remercie l'ANSSI de m'avoir permis d'entreprendre cette thèse, et ce, avec le soutien de ma hiérarchie, et plus particulièrement de Emmanuel DUPONCHELLE, de José ARAUJO, de Renaud LABELLE et de Vincent STRUBEL. Je remercie également Aziz BENLARBI-DELAÏ de m'avoir accueilli au sein L2E.

Je suis très reconnaissant envers Marc HÉLIER et Muriel DARCES d'avoir accepté d'encadrer mon travail. Je les remercie pour leur aide et les conseils apportés tout au long de cette thèse, ainsi que pour leur disponibilité et leur bienveillance. Enfin, merci pour toutes les discussions, scientifiques ou non, que vous avons eues.

Je remercie Emmanuel COTTAIS et José LOPES ESTEVES pour le suivi apporté à mon travail, pour leurs nombreux conseils donnés tout au long de ces trois années, ainsi que pour les questions qui m'ont permis de préciser et de mieux organiser mon propos.

Je remercie Madame Françoise PALADIAN et Monsieur Alain REINEIX d'avoir accepté d'évaluer mon travail de recherche en tant que rapporteurs.

Je remercie Monsieur Lionel PICHON d'avoir accepté de participer au comité de suivi de ma thèse dès la première année, ainsi qu'au jury. Je tiens à remercier Madame Hélène ROUSSEL et Monsieur Philippe BESNIER d'avoir bien voulu de faire partie de mon jury de thèse.

Je tiens également à remercier très chaleureusement Yves CHATELON qui a fabriqué en quasi intégralité la maquette de châssis d'ordinateur utilisée tout au long de ce travail de recherche, et pour tous ses précieux conseils pratiques. Je remercie également Chloé HAMEL-DELLENBACH pour son aide dans mes démarches administratives et pour sa disponibilité.

La majeure partie des mesures réalisées pendant cette thèse ont été faites sur la plateforme d'ingénierie expérimentale du campus de Saint-Cyr-l'École de Sorbonne Université. Je remercie Philippe GUIBERT, Frédéric SEGRÉTAÏN, Anne MARCHAL et Jérôme PÉQUIN pour leur accueil et leur disponibilité, et pour avoir permis que les séances d'expérimentations se déroulent dans les meilleures conditions possibles. Merci de m'avoir dépanné à de nombreuses reprises pour divers problèmes pratiques.

Un très grand merci à Philippe VALEMBOIS, Tristan CLAVERIE, Loïc MAZET et Éric DA SILVA pour avoir scrupuleusement relu, voire disséqué, mon manuscrit, et pour leurs remarques et commentaires. Vous m'avez permis d'améliorer la qualité de ce manuscrit.

Je remercie Nicolas BOUREY pour m'avoir apporté son aide lors de la réalisation des mesures avec la sonde de champ proche. Merci également à Quentin HERBETTE pour ses nombreux coups de main en tout genre.

Je remercie Chaouki KASMI grâce à qui j'ai pu intégrer l'ANSSI, et qui a en partie initié ce travail de thèse.

Je remercie mes collègues de l'ANSSI, Christophe, Pierre-Michel, Thomas, David, Guillaume, Louisa, Karim et Adrian pour leur bonne humeur, pour les bonnes blagues et surtout les moins bonnes.

Merci aux membres du L2E avec qui j'ai partagé de nombreux repas à la cafétéria et pour ne s'être pas trop moqué de mon régime alimentaire, Aurélie, David, Guido, Guillaume, Gérard, Hakeim et Julien.

Je remercie les doctorants et post doctorants du L2E anciens et présents : Kévin, Joanna, Oussama, Matthieu, Benjamin, Sidney, Tianyu, Michael, Laurent, Qiang, Rudy et Mandiaye pour les échanges en tout genre et pour leur ouverture sur le monde, pour les pauses aussi.

De nombreuses personnes ont façonné mon intérêt et ma curiosité pour les sciences jusqu'à aujourd'hui. Je tiens à les en remercier ici. Tout d'abord, je remercie l'ensemble des membres de l'association M53 Mayenne astronomie et en particulier F. HUBERT et L. HERRIAU avec qui j'ai pu découvrir et photographier le ciel étoilé dès mon plus jeune âge. Un peu plus tard, au collège j'ai eu la chance de croiser M. THÉARD et son atelier scientifique lors duquel j'ai pu pratiquer les sciences à la pause de midi. Je remercie P. MICHEL, qui nous a permis, à trois comparses et à moi même, de participer entre autres aux Olympiades de Physique et à une exposcience Europe à Moscou, autour d'un projet qui concernait déjà l'électromagnétisme. Je remercie les bénévoles du collectif Exposcience 53 qui permettent à de nombreux jeunes (dont moi il y a quelques années) de pratiquer les sciences et de les partager avec le plus grand nombre. Je remercie également B. DUCHENNE pour le partage de ses connaissances naturalistes. Enfin, un grand merci à ma mère pour avoir encouragé ma curiosité et accompagné mon intérêt pour les sciences.

Je termine en remerciant mes parents, ma soeur et mon frère, merci à vous d'avoir été présents au printemps 2018. Merci à T. et M. mes neveux pour être là, et à ma grand-mère qui sait s'émerveiller de tout.

Contents

Introduction	12
I State of the art	14
I.1 ElectroMagnetic SECurity (EMSEC)	15
I.1.1 Introduction	15
I.1.2 EMSEC at component level	16
I.1.3 EMSEC at system level	18
I.1.4 EMSEC at building level	26
I.1.5 Conclusion	28
I.1.6 Need to study reverberant environments	28
I.2 Couplings to and inside reverberant environment	30
I.2.1 Introduction	30
I.2.2 Electromagnetic couplings through apertures	31
I.2.3 Electromagnetic couplings within a cavity	46
I.2.4 Electromagnetic field to conductors couplings	49
I.2.5 Cavity regimes	50
I.2.6 Conclusion	51
I.2.7 Selection of approaches for the study of couplings inside cavities from an electromagnetic security (EMSEC) perspective.	51
II Design and assessment of computer chassis models	54
II.1 Design of computer chassis models	55
II.1.1 Introduction	55
II.1.2 The simulation model	56
II.1.3 Design and production of a computer chassis mock-up	57
II.1.4 Design and production of devices to measure couplings	67
II.1.5 Conclusion	71
II.2 Comparison between the two models for two configurations	72

II.2.1	Introduction	72
II.2.2	Electric field amplitude and couplings assessment with the two models	72
II.2.3	Applicability of the simulation model to determine statistics	81
II.2.4	Conclusion	86

III Application of the Random coupling model 88

III.1	Application of the Random Matrix Theory to determine couplings inside microwave cavities	89
III.1.1	Introduction	89
III.1.2	The Random Matrix Theory (RMT)	90
III.1.3	The random coupling model (RCM)	96
III.1.4	Set up of the random coupling model (RCM) for the two configurations of interest	99
III.2	Determination of the impedance/admittance of an aperture	102
III.2.1	Introduction	102
III.2.2	First estimation	102
III.2.3	Second estimation	104
III.2.4	Impedance of an aperture between two regions	109
III.2.5	Mapping of the aperture impedance to the RCM	112
III.3	Numerical computation of the aperture admittance	118
III.3.1	Introduction	118
III.3.2	Numerical error estimation	118
III.3.3	Integration of G_{mn}^{rad} over k_x	119
III.3.4	Integration of $B_{mn}^{\text{rad},ms}$ over k_x and k_y	119
III.3.5	Computation of B_{mn}^{rad} by means of the HILBERT transform	122
III.3.6	Impedance and admittance	123
III.4	Monte-Carlo simulations	126
III.4.1	Introduction	126
III.4.2	Elements statistics of the normalized impedance matrix $\underline{\xi}$	127
III.4.3	RCM implementation	131
III.4.4	Statistics of the elements of the normalized impedance matrix $\underline{\Xi}$	134
III.4.5	Relation between the variance of Ξ_{ii} , Ξ_{ij} and α	135
III.4.6	Chaoticity of the random normalized impedance matrix $\underline{\Xi}$	136
III.4.7	Statistical quantity of interest for EMSEC	137
III.4.8	First RCM application	141
III.4.9	Conclusion	147
III.5	Measurements	148
III.5.1	Introduction	148
III.5.2	Use of a small stirrer to generate a chaotic environment	149
III.5.3	Methods to determine the parameters of the RCM	149
III.5.4	First comparison: monopoles	150
III.5.5	Second comparison: printed circuit boards	151
III.5.6	Effects of absorbers on the magnitude of induced currents	158

III.5.7	Coupling between the aperture and the internal ports	159
III.5.8	Conclusion	161
Conclusion		162
IV Appendix		179
A	Tables of the mock-up deformations	180
B	Admittance of an aperture	183
C	Derivation of the Random coupling model	189
C.1	Introduction	189
C.2	Derivation of the RCM in two dimensions	189
C.3	Statistical representation	191
C.4	Radiation impedance as a deterministic quantity	193
C.5	Generalisation to the multiple port case	195
D	Determination of the antenna factor from experimental data, and of the electric field from the antenna factor	197
D.1	Determination of the electric field strength at a distance D from an antenna using its antenna factor AF	197
D.2	Determination of the antenna factor with two identical antennas	199
E	Résumé des travaux	200
E.1	Introduction	200
E.2	La sécurité électromagnétique (SECEM)	201
E.3	Méthodes d'étude des couplages dans les cavités	203
E.4	Établissement et évaluation de deux modèles de châssis d'ordinateur	205
E.5	Le modèle de couplages aléatoires	207
E.6	Conclusion	214
E.7	Travaux futurs	215

Acronyms

ACS absorption cross sections. [39–44](#)

ANSSI Agence nationale de la sécurité des systèmes d’information. [201](#)

ASIC application specific integrated circuit. [16](#), [17](#)

BCa bias-corrected and accelerated. [140](#), [142](#), [144](#)

BLT BAUM-LIU-TESCHE. [27](#), [30](#), [40](#), [41](#), [44](#), [49](#), [51](#)

CDF cumulative density function. [85](#), [86](#), [128](#), [129](#), [139](#), [140](#), [142–144](#), [153](#), [156–158](#), [161](#)

COTS commercial off-the-shelf. [25](#), [164](#)

CPU central processing unit. [17](#), [21](#), [22](#)

CST-SS CST Studio Suite. [34](#), [35](#), [56](#), [61](#), [78](#), [205](#)

DP DisplayPort. [20](#)

DVI digital visual interface. [20](#)

EMC electromagnetic compatibility. [12](#), [15](#), [16](#), [30](#), [52](#)

EMI electromagnetic interferences. [12](#), [16–22](#), [28](#), [29](#), [52](#), [162](#)

EMP electromagnetic pulse. [24](#), [25](#)

EMSEC electromagnetic security. [4](#), [5](#), [12](#), [13](#), [15](#), [16](#), [18](#), [26–30](#), [51](#), [52](#), [98](#), [126](#), [137](#), [139](#), [147](#), [162–164](#)

EVM error vector magnitude. [26](#)

FDTD finite-difference time-domain. [31](#), [44](#), [48](#), [51](#)

FEM finite element method. [45](#), [48](#)

FIT finite integration technique. [31](#), [46](#), [51](#), [56](#), [205](#)

FPGA field programmable gate array. [16](#), [17](#)

GOE gaussian orthogonal ensemble. [91–96](#), [98](#), [128](#), [129](#), [131](#)

GPD generalized PARETO distribution. [141–144](#), [146](#)

GSL GNU Scientific Library. [118](#), [133](#)

GUE gaussian unitary ensemble. [91](#)

HDMI high-definition multimedia interface. [20](#)

IEMI intentional electromagnetic interference. [15](#), [16](#), [18](#), [24–29](#), [52](#), [87](#), [162](#), [164](#)

INFOSEC information system security. [12](#), [13](#), [15](#), [16](#), [18](#), [28](#), [29](#), [72](#), [162](#)

IS information system. [12](#), [25](#), [26](#), [28](#)

KDE kernel density estimation. [132](#)

L2E Laboratoire d’Électronique et Électromagnétisme. [201](#), [206](#)

LNA low noise amplifier. [26](#)

MFMM multilevel fast multipole method. [45](#)

MKL Math Kernel Library. [133](#)

MoM method of moments. [31](#), [44–48](#), [51](#), [110](#), [112](#)

MSC mode-stirred chamber. [42](#), [44](#), [85](#), [91](#)

NRZI non-return to zero inverted. [22](#)

PCB printed circuit board. [13](#), [30](#), [41–43](#), [45](#), [48](#), [51](#), [55](#), [56](#), [67](#), [69](#), [71](#), [77–83](#), [86](#), [87](#), [99–101](#), [113](#), [136](#), [148](#), [149](#), [152](#), [155](#), [160–163](#)

PDF probability density function. [52](#), [80](#), [86](#), [92–95](#), [98](#), [128](#), [132](#), [134](#), [135](#), [137](#), [138](#), [149](#), [151](#), [154](#), [163](#)

PEC perfect electric conductor. [32](#)

PLL phase locked loop. [26](#)

PWB power balance. [27](#), [39–44](#), [46](#), [52](#)

RAM random access memory. [48](#), [77](#)

RCM random coupling model. [5](#), [6](#), [13](#), [45](#), [46](#), [51](#), [53](#), [87](#), [89](#), [96–100](#), [102](#), [112](#), [113](#), [126](#), [127](#), [131](#), [133](#), [136](#), [137](#), [140–142](#), [147–155](#), [158](#), [159](#), [161–164](#), [189](#)

RMT random matrix theory. [13](#), [44](#), [89–93](#), [95–97](#), [128](#), [162](#), [163](#)

SDR software defined radio. [20](#), [22](#), [23](#)

SIMD single instruction multiple data. [21](#)

SNR signal to noise ratio. [22](#), [25](#)

TRNG true random number generator. [18](#)

VCO voltage-controlled oscillator. [23](#), [26](#)

VGA video graphics array. [20](#)

VNA vector network analyzer. [48](#), [64](#), [78](#), [79](#), [100](#), [142](#), [149](#), [150](#), [159](#), [160](#)

Nomenclature

ω	Angular frequency ($\omega = 2\pi f$ rad s ⁻¹).
$\text{Ci}(x)$	Cosine integral $C_i(x) = \gamma + \ln x + \int_0^x \frac{\cos(t)-1}{t} dt$
$*$	Complex conjugate.
\wedge	Cross product.
ϵ	Dielectric permittivity (F m ⁻¹).
\cdot	Dot (or scalar) product.
γ	EULER's constant, $\gamma = 0.5772156649 \dots$
σ	Electric conductivity (S m ⁻¹).
J_α	First kind BESSEL function of order α .
f	Frequency (Hz).
$\mathcal{H}(g)$	HILBERT transform of g .
$\underline{\underline{I}}$	Identity matrix.
j	Imaginary number ($j^2 = -1$).
$\Im[\cdot]$	Imaginary part of a complex number.
$\mathbf{1}_A(x)$	Indicator function $\mathbf{1}_A(x) = \begin{cases} 1 & \text{if } x \in A, \\ 0 & \text{if } x \notin A. \end{cases}$
μ	Magnetic permeability (H m ⁻¹).
$\underline{\underline{M}}$	Matrix.
$\mathcal{N}(\mu, \sigma)$	Normal distribution with mean μ and standard deviation σ .
\otimes	Outer product.
\hbar	PLANCK's constant $\hbar = \frac{h}{2\pi}$, with $h = 6.626\,070\,15 \times 10^{-34}$ J s.
$\mathbb{P}[A]$	Probability of an event A .
Q	Quality factor (unitless).
$\Re[\cdot]$	Real part of a complex number.

$\text{Si}(x)$	Sine integral $S_i(x) = \int_0^x \frac{\sin(t)}{t} dt$
\mathbf{H}_α	STRUVE function of order α .
c	The speed of light in vacuum: $299\,792\,458\,\text{m s}^{-1}$.
\vec{e}_i	Unit vector in a cartesian coordinate system Oi .
η_0	Vacuum impedance, $\eta_0 = \sqrt{\frac{\mu_0}{\epsilon_0}}\,(\Omega)$.
μ_0	Vacuum permeability $\mu_0 = 4\pi \times 10^{-7}\,\text{H m}^{-1}$.
ϵ_0	Vacuum permittivity, $\epsilon_0 = 8.854\,187\,812\,8\,\text{F m}^{-1}$.
η	Wave impedance, $\eta = \sqrt{\frac{\mu}{\epsilon}}\,\Omega$.
λ	Wavelength of a monochromatic electromagnetic field (m).
k	Wavenumber $k = \frac{2\pi}{\lambda}\,\text{m}^{-1}$.

Introduction

The three major principles of [information system security \(INFOSEC\)](#) are: confidentiality, integrity and availability of information. Confidentiality consists in protecting resources from unauthorized access. Integrity assures protection of data against unauthorized changes to guarantee its reliability and accuracy. Availability guarantees authorized users to have access to the resources when they need.

Information is overwhelmingly handled by [information system \(IS\)](#). These systems may offer information security vulnerabilities. The aim of the [INFOSEC](#) is to reduce threats by mitigating these vulnerabilities. Among the large variety of threats, one can identify the [electromagnetic interferences \(EMI\)](#).

Indeed, the susceptibility and the emissivity of electronic devices can be a threat for the information security. This field of interest is a prominent research area, and exists since the 1940s. These threats are nowadays well considered at the earliest stage of the design of a critical infrastructure, and throughout its operation.

It is common to embed electronic devices into casings as they limit the susceptibility to the environment and their emissivity towards the environment. The casing creates reverberant conditions for the electromagnetic field. However, it seems that no study has yet investigated the issue of reverberant environments from an [INFOSEC](#) viewpoint.

The Wireless Security Laboratory of the National Cybersecurity Agency of France (ANSSI) is committed to the study of threats related to [EMI](#). Moreover, it provides advices to enhance the information security in critical infrastructures. To reinforce its level of expertise, it has been decided to engage a research work to study electromagnetic couplings within reverberant environments, with the collaboration of the Group of electrical engineering of Paris at Sorbonne University.

The research work that will be exposed in this thesis manuscript is a first attempt to analyze such environments and to put forward a methodology that can be used during a risk assessment process from the [electromagnetic security \(EMSEC\)](#) point of view. Furthermore, the large diversity and the lack of knowledge regarding the content (printed circuit boards, cables, fans, etc.) of equipment make deterministic approaches, like circuit models, inappropriate. It thus seems pertinent to favour the use of probabilistic approaches in order to characterize such equipment by assessing occurrence probabilities for quantities of interest, voltages or currents typically.

This report is organized as follows: the first part is dedicated to define the goals concerning this PhD work. An overview of the threats posed by [EMI](#) towards [INFOSEC](#) will be exposed in chapter [I.1](#). A domain of research, the [EMSEC](#), will be defined as the interweaving of the [electromagnetic compatibility \(EMC\)](#) and the [INFOSEC](#). Multiple risks related to [INFOSEC](#) at different scales (components, devices, systems, buildings, etc.) will be listed. We will show that the effects of the casing of electronic

equipment to the [INFOSEC](#) is a little explored field and that it warrants attention. Specifically, the electromagnetic couplings (energy transfer by means of electromagnetic waves) in equipment casings can be accentuated by the reverberant behavior of such environments. This research work will tackle this problem: how to study electromagnetic couplings within equipment casings, from the [INFOSEC](#) viewpoint.

The following chapter [I.2](#) is devoted to the selection of mathematical and physical tools used to study electromagnetic couplings within reverberant environments. We will highlight that statistic tools are the most relevant approaches.

In the second part, a case study will be exposed. It consists of a common equipment casing: a desktop computer chassis. In chapter [II.1](#), two models will be set to describe it, a simulation model and an experimental one in the form of a mock-up. The design steps of that mock-up, and its manufacturing validation will be presented. Especially, its quality factor will be measured and some slight defects in the manufacturing process will be characterized. Devices will then be added inside the case study, from which couplings will be determined. It consists of four simple [printed circuit boards \(PCBs\)](#).

In chapter [II.2](#), both simulation and experimental models will be compared with each other. The aim will be to assess the ability of the simulation model to determine couplings within a desktop computer chassis. At first, the electric field within the empty mock-up will be measured, and then compared to simulated data. Afterwards, the coupling of a plane-wave to [PCBs](#) through an aperture will be studied.

The third part is dedicated to the [random coupling model \(RCM\)](#). This circuit model seems to be well-suited to determine, from a statistical viewpoint, couplings in chaotic reverberant environments. The [RCM](#) relies on the [random matrix theory \(RMT\)](#) that can describe chaotic microwave cavities. The [RMT](#) and the [RCM](#) will be detailed in the first chapter [III.1](#), and some key properties will be exposed. The next two chapters [III.2](#) and [III.3](#) are dedicated to the integration of apertures into the [RCM](#), and to some numerical computations. Chapter [III.4](#) explains how the [RCM](#) can be implemented in a practical and efficient way. Several statistical quantities of interest for [EMSEC](#) will be stated, and their implementation will be exposed. Finally, in chapter [III.5](#), a comparison between experimental data and [RCM](#) simulations will be presented.

The last appendix [E](#) of this manuscript is an extensive French-language summary of the thesis work.

Part I

State of the art

Chapter I.1

ElectroMagnetic SECurity (EMSEC)

Contents

I.1.1	Introduction	15
I.1.2	EMSEC at component level	16
I.1.2.1	Side-Channel Analysis	16
I.1.2.2	Fault attacks	17
I.1.3	EMSEC at system level	18
I.1.3.1	Electromagnetic eavesdropping	18
I.1.3.2	Intentional electromagnetic interference (IEMI) ...	24
I.1.3.3	Covert channel	26
I.1.4	EMSEC at building level	26
I.1.4.1	Radiated emissions	27
I.1.4.2	Conducted emissions	27
I.1.5	Conclusion	28
I.1.6	Need to study reverberant environments	28

I.1.1 Introduction

Electromagnetic security (EMSEC) may be considered as the fusion of [electromagnetic compatibility \(EMC\)](#) with [information system security \(INFOSEC\)](#). Fig. [I.1.1](#) depicts the links between EMC and INFOSEC. The EMSEC study of an electronic item leads to consider electromagnetic couplings between systems or between the elements of a system [[Guri et al., 2015](#), [Camurati et al., 2018](#), [Cottais et al., 2018](#)]. The occurrence of electromagnetic couplings means that an energy transfer occurs between voltages/currents and electromagnetic radiations. If a signal carrying sensitive information couples with another system, the risk of uncontrolled signal leakage exists (loss of the confidentiality of information). Such a risk defines the TEMPEST threat. Another risk would involve an attacker handling a malicious equipment in order to interfere with its victim's equipment nominal operation, leading to the loss of the availability and integrity of the information. This type of aggression is called [intentional electromagnetic interference \(IEMI\)](#).

The analysis of the electromagnetic emanations radiated from electronic devices to recover information was firstly outlined in [[Van Eck, 1985](#)]. From then, numerous talks and papers have highlighted that threat. In [[Hayashi et al., 2014](#), [Kuhn, 2013](#)] the electromagnetic emanations from computer screens, cables and connectors of digital video signals are processed to recover the displayed information. In [[Vuagnoux and Pasini, 2009](#)], keyboards signals are analyzed and the keystroke information is

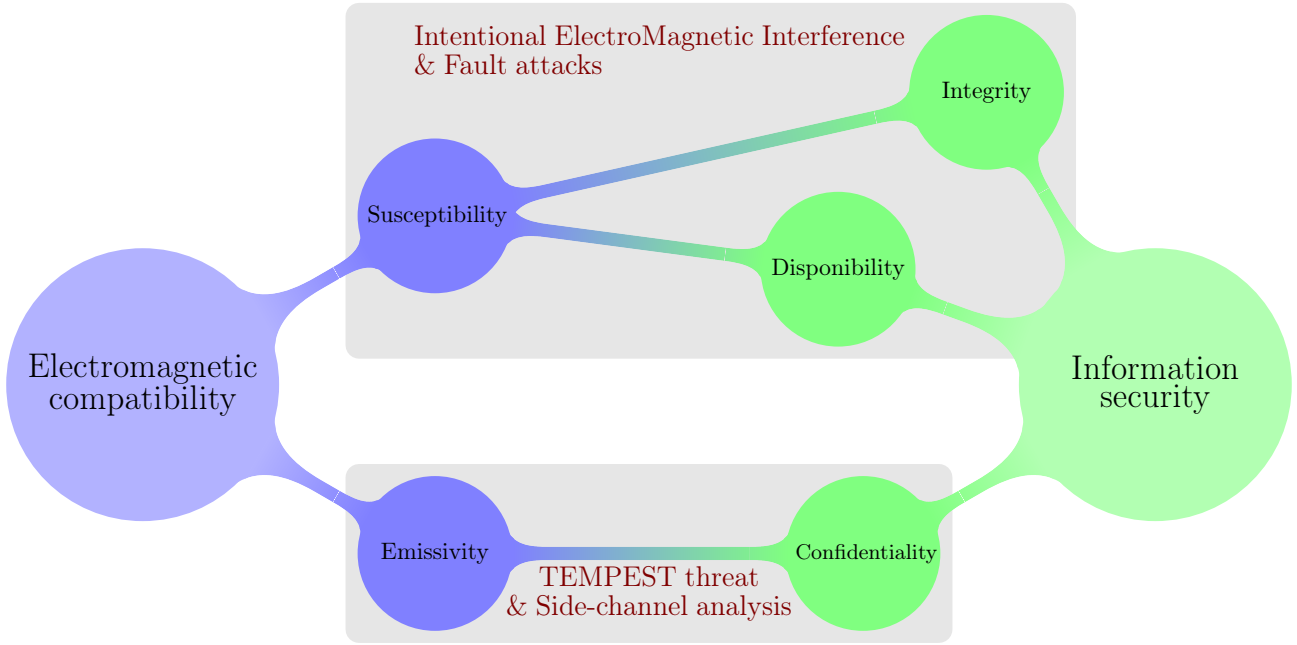


Fig. I.1.1 – Relations between [electromagnetic compatibility \(EMC\)](#) and [information system security \(INFOSEC\)](#).

recovered. Researches on the effects of [IEMI](#) were also carried out like in [[Kune et al., 2013](#), [Backstrom and Lovstrand, 2004](#), [Kasmi et al., 2014b](#)] where desktop computers were stressed with [IEMI](#).

An [EMSEC](#) overview at different scales will be given in this chapter. First, the component level will be considered, through fault attacks and side-channel analysis. Then, threats at the equipment scale will be addressed, and especially [TEMPEST](#) and [IEMI](#) threats. Finally, a focus on building level will be given where conducted and radiated phenomena will be examined from the [EMSEC](#) standpoint.

I.1.2 [EMSEC](#) at component level

At component level ([application specific integrated circuits \(ASICs\)](#), [field programmable gate arrays \(FPGAs\)](#), etc.), two different applications of [electromagnetic interferences \(EMI\)](#) may be encountered. The first one is the side-channel analysis, where the [EMI](#) generated from components are studied from an [INFOSEC](#) viewpoint. The second one is related to fault attacks where components are stressed.

I.1.2.1 Side-Channel Analysis

In the general case, the goal of side-channel analysis is to recover information from unintentional leakage of information. It thus concerns the confidentiality of information. The vector of this leakage of information may be acoustic waves, currents, electromagnetic fields, etc. An attacker will try to recover this information by means of a signal processing analysis.

An important field of study, related to side-channel analysis, deals with components, where the aim is to recover a secret parameter from an algorithm. For a cryptographic algorithm, it often means recovering a secret key. For that specific case, running a side-channel analysis requires:

- to fully understand the implementation of the targeted algorithm;
- to measure a physical quantity (such as: voltages/currents, power consumption, electromagnetic fields, etc.), while executing an algorithm implementation.

From these data, one might retrieve values of internal variables processed by an algorithm implementation by means of statistical analysis [Thillard, 2016].

In [Kocher et al., 1999], it was shown that the power consumption of an integrated circuit can leak information regarding processed secret values. Later, it was highlighted that EMI radiated by components may also leak sensitive information [Quisquater and Samyde, 2001]. When the electromagnetic field is the vector of the leaked quantity, its magnitude is low and near-field probes are required [Genkin et al., 2016].

However, in some situations, the leaked quantity may be propagated at long ranges. Some recent integrated circuits integrate central processing unit (CPU) cores and radio front ends. Therefore, both digital and analog signals flow on the same chip. Depending on its design quality, crosstalk between the noisy digital part of the chip and the analog circuit through their common substrate may occur. This phenomenon is referred to as substrate noise coupling [Bronckers et al., 2007]. It has been demonstrated in [Camurati et al., 2018] that digital signals generated by cryptographic computations may be mixed up with baseband signals of a radio front end, located on the same chip. Then, while transmitting, microwave signals are generated, radiated and propagated at long range as well as the leakage signal from the cryptographic computations. By means of statistical tools, it has been possible in [Camurati et al., 2018] to recover AES¹ keys at 10 meters in an anechoic chamber, and at 1 meter inside an office environment.

I.1.2.2 Fault attacks

Fault attacks consist in stressing an electronic component in order to generate internal errors that can somehow lead to a security failure. Several means are available for that purpose. The time constraint violation of clock signals beyond permissible limits is a widely-used fault injection technique that creates a clock glitch. One can also underpower the component. Some other methods require to inject a given amount of energy \mathcal{E} towards the component during a short time interval Δt . Several types of energy sources may be employed [Timmers et al., 2016]:

- a voltage $v(t)$ and a current $i(t)$: $\mathcal{E} = \int_0^{\Delta t} i(t)v(t)dt$. A voltage source is superposed to the circuit trace of interest (power fault attacks, [Bozzato et al., 2019]);
- an electromagnetic field: $\mathcal{E} = \iint_S \left[\int_0^{\Delta t} \vec{E}(\vec{r}, t) \wedge \vec{H}(\vec{r}, t) dt \right] d\vec{S}$, where $\vec{E}(\vec{r}, t)$ and $\vec{H}(\vec{r}, t)$ are respectively the electric and magnetic field at location \vec{r} . The term between the square brackets is the total surface energy density. The use of a near-field probe allows to focus the energy towards a small area (electromagnetic fault attacks, [Moro et al., 2013]);
- a light pulse of N photons with an angular frequency ω : $\mathcal{E} = N\hbar\omega$. The aim is to provide enough energy to ionize a specific semiconductor region which results in a change of the integrated circuit behavior. Usually, lasers are used to focus the energy to a very precise location of the component die where a depackaging operation is sometimes required (optical fault attacks, [Skorobogatov and Anderson, 2002]).
- an amount of thermal energy \mathcal{E} (temperature heating fault attacks, [Hutter and Schmidt, 2013]).

The common procedure to generate an electromagnetic field to trigger faults is to inject a pulse, with an amplitude of several hundred volts and tens of nanosecond duration into a near-field probe. Fig. I.1.2 depicts the set-up used for an electromagnetic fault injection. For processors, which execute a program as a sequence of instructions, it may lead to an instruction skipping, replay or corruption. Faults may be exploited to bypass authentication mechanisms, by skipping (or forcing) a branch instruction for example. ASICs and FPGAs are also exposed to fault attacks, and numerous works are

¹AES: Advanced Encryption Standard is an encryption algorithm.

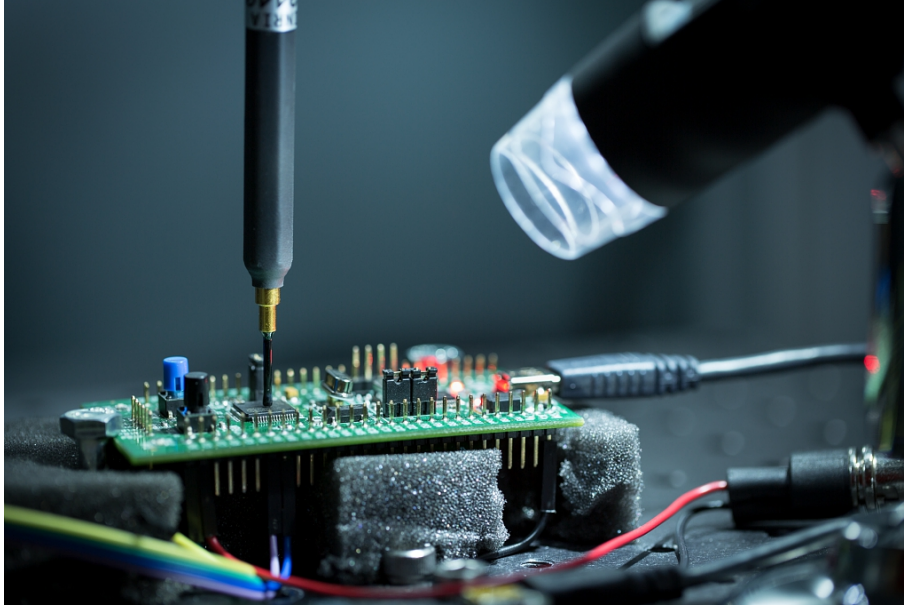


Fig. I.1.2 – Set-up for fault injections in order to obtain a fault model. Credits: Ronan LASHERMES (High Security Laboratory of the INRIA Rennes).

dedicated to fault cryptographic implementations, such as [true random number generators \(TRNGs\)](#) that are used to generate random values [[Haddad et al., 2016](#), [Maistri et al., 2014](#)].

I.1.3 EMSEC at system level

A system is a set of components that executes tasks by processing electric signals (like a computer hardware, a screen, a robot, etc.). Its emissivity and susceptibility towards [EMI](#) will be evaluated from the [INFOSEC](#) perspective. First, threats related to the loss of confidentiality due to radiated [EMI](#) will be investigated. Then, the susceptibility of systems to electromagnetic aggressions will be addressed through the [IEMI](#) threat and through the covert channel threat.

I.1.3.1 Electromagnetic eavesdropping

Electromagnetic eavesdropping refers to the interception and processing of uncontrolled parasitic [EMI](#) in order to recover confidential information. If [EMI](#) are generated by the nominal behavior of the system, it is named TEMPEST, and if [EMI](#) are forced in a software-based way, it is designated as soft-TEMPEST. Both unintentional and intentional electromagnetic emissions will now be put in relation with eavesdropping threats.

I.1.3.1.1 Radiated [EMI](#) from digital communications

While operating, electronic circuits generate time-varying currents which can generate electromagnetic fields. The relation between the radiated electric \vec{E} and magnetic \vec{H} fields and the current density \vec{j} is given by the MAXWELL–AMPÈRE equation:

$$\text{rot} \vec{H} = \vec{j} + \epsilon \frac{\partial \vec{E}}{\partial t} \quad (\text{I.1.1})$$

If \vec{j} conveys information, then information linked to it is carried by \vec{E} and \vec{H} .

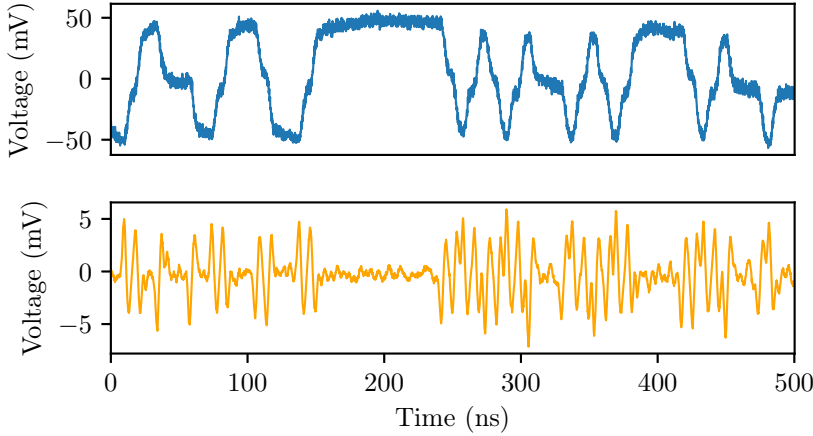


Fig. I.1.3 – Ethernet frame measured by direct voltage probing (top), and through a near-field probe (bottom). The orange curve is an image of the near magnetic field (a loop probe was employed) by the antenna factor ($AF = \frac{|\vec{H}|}{V}$) of the probe (magnetic field to output voltage ratio). The antenna factor of the probe is frequency-dependent, however it is almost constant for the bandwidth of interest. (Measurement ANSSI - 2020.)

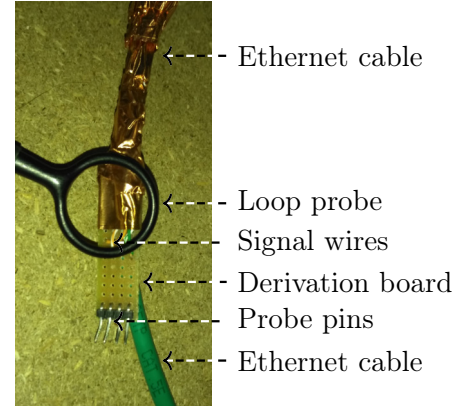


Fig. I.1.4 – Derivation board to probe Ethernet signals and the loop antenna. The derivation allows to probe Ethernet signal while guaranteeing the electrical continuity of the cable. Remark that the shielding was removed at the probing location.

As an example of radiated EMI, Fig. I.1.3 depicts a section of an Ethernet frame of throughput 100 Mbit s^{-1} . Fig. I.1.4 shows the measurement setup. The upper plot shows the probed voltage on an Ethernet cable. The lower plot shows an image of the radiated magnetic field \vec{H} measured with a near field loop antenna. One notices that the edges (raising and falling) are responsible for the maximum generated field. Therefore, by observing the radiated magnetic field, an attacker could be able to recover the original data.

I.1.3.1.2 TEMPEST

TEMPEST is a codename and refers to analysis of radiated and conducted compromising EMI. Compromising EMI are defined from the [Committee on National Security Systems, 1995] as: *"unintentional signals that, if intercepted and analyzed, would disclose the information transmitted, received, handled, or otherwise processed by telecommunications or automated information systems equipment."*

Some practical entailments of compromising EMI will now be exposed.

Video streams The first published work about the emanations of electromagnetic signals from computer screens is [Van Eck, 1985]. Van Eck proved that it is possible to recover the image displayed on a computer monitor that includes a cathode ray tube (CRT). Indeed, in CRT screens video, signals are amplified by a transistor-transistor logic unit to several hundred volts to drive the cathode ray tube. Radiated emissions from the computer monitor will then be dominated by a signal that is correlated to the signal containing the displayed information. Moreover, the tools needed to set up this eavesdropping are really cheap. It only requires a TV, an antenna and a circuit made of a variable oscillator and a frequency divider for synchronisation purposes. From then on, numerous researchers have continued to try to recover the displayed information. In [Radu et al., 2003], radiation mitigating techniques were proposed to reduce the level of compromising signals from CRT screens by adding ferrites to the video cables.

The next generation of screens (flat-panel displays) did not lower the eavesdropping risks. Readers



Fig. I.1.5 – Displayed image (left) and recovered image (right) from a [DVI](#) video stream (from [[Ricordel and Duponchelle, 2018](#)]).

may refer to the works of [[Kuhn, 2005](#)] and [[Lee et al., 2016](#)] for details. [EMI](#) emissions from a digital signal depend on its amplitude and on its time derivative. The higher the amplitude is, the higher the amplitude of the compromising signal is, and the higher the time derivative of a signal is, the wider its spectral occupancy is. Despite that in modern systems voltage amplitudes are low, the increase of the throughput requires very short rising, and falling edges, which generate high frequency emissions with numerous harmonics that can propagate at long range. Nowadays, several protocols are used to carry video streams, some are analog like the [video graphics array \(VGA\)](#), and most are digital like [digital visual interface \(DVI\)](#), [high-definition multimedia interface \(HDMI\)](#) and [DisplayPort \(DP\)](#). Note that for all the protocols, the pixels are transmitted row by row. For analog protocols, the color intensity information is coded into the amplitude, thus [EMI](#) are highly correlated to intensity variations of consecutive pixels over a row. In other words, the more the image contains variation of intensity (therefore of amplitude), the more the streamed signal generates [EMI](#).

For digital protocols the image to display is coded by several bits and serially transmitted. Thus, for the same piece of information (a pixel for example), several falling and rising edges occur (up to 10 for the [DVI](#)) and more [EMI](#) are generated.

It is worth noting that the radiation source often comes from the video cable that carries the stream and especially from its connectors because of poor grounding continuity. [Fig. I.1.5](#) presents the recovered image from [EMI](#) radiated by a cable carrying a [DVI](#) encoded video stream. The tool used to recover the displayed image from [EMI](#) is open source [[Marinov, 2016](#)] and uses a [software defined radio \(SDR\)](#).

Screen tablet may also be the source of [EMI](#) when a virtual keyboard is displayed [[Hayashi et al., 2014](#)]. This virtual keyboard is required when a user wants to enter a password for example. When the user types a letter by touching the touch screen, the color of the corresponding key on the virtual keyboard changes. This proof of concept highlights that one can recover the password of a user by analyzing [EMI](#) from tablet screens even if the password is hidden behind stars and never shown on the screen.

Keyboards Two different [EMI](#) signals from keyboards may be processed to recover the keystroke information [[Vuagnoux and Pasini, 2009](#)]. [EMI](#) generated by the PS/2 communication signals (that flow between the wired keyboard and the computer) may be processed to determine the keystroke at several meters. The second one comes from the keyboard internal signals. Inside a keyboard, the 104/105 key switches are connected by a grid of circuit traces. The keystroke is determined by the keyboard controller through a scanning process. Signals generated for this scanning generate [EMI](#) that contain information about the keystroke. Both wired and wireless keyboard generate these [EMI](#).

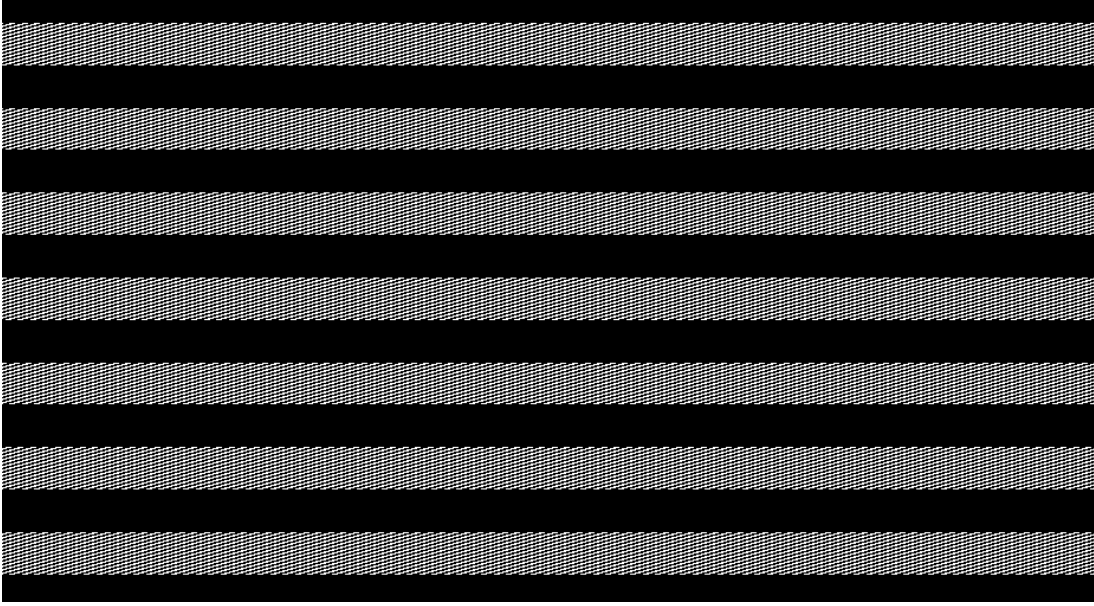


Fig. I.1.6 – Screenshot of the displayed image that generates an amplitude modulated signal of “Für Elise” from BEETHOVEN.

I.1.3.1.3 Soft-TEMPEST

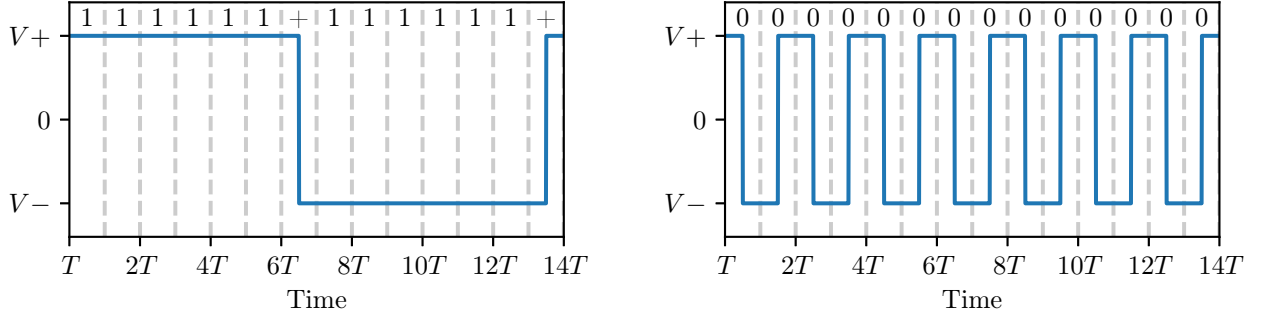
Classical TEMPEST is relative to the radiation of compromising signals by a device with a typical use. However, one can control the device radiations without hardware modifications in a way that a covert channel is created by diverting electronic elements to create a communication channel. It requires that a malicious process is running on the target device with the ability to manipulate hardware resources in a way that EMI are somehow controlled and much more easy to recover for an attacker.

Video streams A proof of concept is given in [Kuhn and Anderson, 1998], where a software is tuned to control an amplitude modulated EMI. The timings of digital video streams are characterized by the pixel clock frequency $f_p = \frac{1}{t_p}$, where t_p is the period needed to code a pixel, by the horizontal frequencies $f_h = \frac{1}{t_h}$ where t_h is the time needed to code an entire line, and by the frame refreshing frequency f_f . Thus, the pixel at position (x, y) on the n -th frame of the video stream signal will be displayed on the screen at time $t(x, y, n) = \frac{x}{f_p} + \frac{y}{f_h} + \frac{n}{f_f}$.

Moreover, if $A \cos(2\pi f_c t)$ is a carrier signal, and $m(t)$ a modulation waveform, then an amplitude modulation signal may be written as: $s(t) = A \cos(2\pi f_c t)[1 + km(t)]$, with k the modulation index. The authors have implemented a software that displays an image where every pixel is coded as an 8 bit grey scale value like $\lfloor \frac{255}{2} + s(t(x, y, n)) \rfloor$, with $A = \frac{255}{4}$ and $m = 1$. By choosing f_c as a frequency that can be received and demodulated by a radio receiver, information carried by $m(t)$ may be decoded by a commercial AM receiver. If $m(t)$ is an audio signal, that audio information may be listened to by a radio receiver.

An open source software that generates an amplitude modulated EMI to broadcast music is [Thiele, 2001]. Fig. I.1.6 is a screenshot captured while executing this software.

Communication bus In [Guri et al., 2015], a software has been developed to generate EMI within the GSM frequency bandwidth by forcing communications between the CPU and the memory on a desktop computer. The authors highlight that, by using specific single instruction multiple data (SIMD) instructions, it is possible to produce EMI from the parallel memory bus. For DDR3 memory



(a) Sequence of 12 bits '1' (the '+' indicates that a bit 0 was added).

(b) Sequence of 14 bits '0'.

Fig. I.1.7 – Chronograms of two USB sequences.

working at a clock frequency of 1600 MHz, the emitted [EMI](#) are within the 600 MHz to 1100 MHz frequency range.

Therefore, the authors managed to code information into a binary amplitude shift keying modulation (B-ASK). Three workstations have been tested by the authors and the [signal to noise ratio \(SNR\)](#) for several configurations (workstation/measurement point/RAM frequency clock) was computed. It was possible to achieve a [SNR](#) of 0.5 dB at a distance of 5 m for a measurement point in the sight of view of the front panel of the chassis.

As a receiver, the authors used a mobile phone with a modified firmware of the baseband processor based on OsmocomBB (an open source GSM baseband implementation [[Welte, 2010](#)]). It does not implement a real receiver, but a routine that measures the power on a given absolute radio-frequency channel number (ARFCN). This implementation lead to a throughput of 1 bit s^{-1} . Another implementation, using a [SDR](#), is able to handle a throughput of 1 kbit s^{-1} . The 1000 factor between the two methods is likely due to the fact that it is much easier to control the processing of the high frequency signal with a [SDR](#).

More information is given in [[Callan et al., 2014](#)] about the changes on radiated emissions of a [CPU](#) for different processor instructions.

The same research team managed to implement another soft-TEMPEST proof of concept in [[Guri et al., 2016](#)]. In that case, the electromagnetic emissions were controlled by a USB communication between an unmodified USB flash drive and a computer. Specifically chosen USB signals are transmitted onto a twisted pair using differential signaling. Thus, the two lines, namely D^+ and D^- , have an opposite voltage. The low level voltage is indicated as V^- and the high level as V^+ where $V^- = -V^+$.

USB uses a [non-return to zero inverted \(NRZI\)](#) encoding scheme. Thus, the bit '0' is coded as a change of voltage (from V^+ to V^- or from V^- to V^+) and the bit '1' as an unmodified voltage. The two devices that communicate with each other use the signal edges to keep the clock synchronized between them. If a long sequence of bits '1' is transmitted, no edge is present in the signal, and synchronisation may be lost. That is why, as soon as a sequence of 6 bits '1' appears in the data to transmit, an additional bit '0' is added. Fig. [I.1.7](#) shows two chronograms of a sequence of 14 bits '0' and 12 bits '1', both sequences have same transmission duration.

Thus, by controlling the sequence of bits to transmit over USB, it is possible to modify the spectrum of the USB signal. The fundamental frequency f_0 of the electric signal lies between $f_{0,\min} = \frac{1}{7T}$ and $f_{0,\max} = \frac{1}{T}$, where T is the clock period. As any time-varying electric signal may generate an electromagnetic radiation whose spectrum is correlated to the spectrum of the electric signal, it is possible to shift the spectrum of the electromagnetic radiation of a USB communication by controlling the transmitted bits over the link.

The authors have coded the data to leak into a binary frequency shift keying modulation (B-FSK),

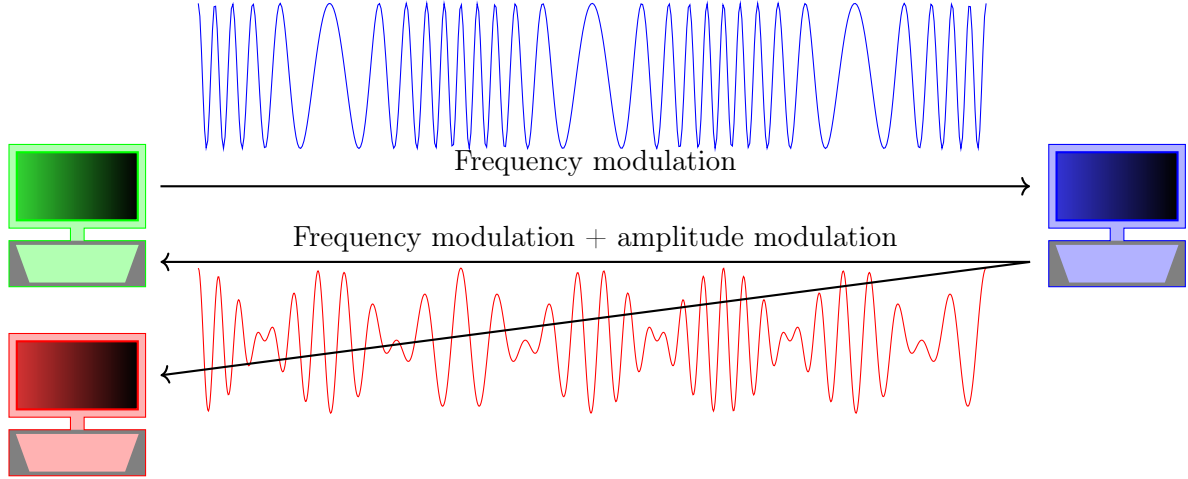


Fig. I.1.8 – Communication scheme by means of polyglot signals. Legit communication between the blue and green computers . Covert communication between the blue and red computers.

which means that the symbol “0” is coded by a frequency f_1 and the symbol “1” by a frequency f_2 . Each symbol is associated to a sequence of bits. When the sequence of bits is sent over a USB link an electromagnetic radiation is generated at frequency f_1 or f_2 . The authors have created a file containing a succession of sequences of bits associated to both symbols. Electromagnetic radiations are generated when the file is copied from the computer to the USB flash drive.

The leaked information is demodulated by a computer equipped with a [SDR](#). This proof of concept allows to send data at a throughput of 640 bits s^{-1} . We can guess that the radiation source is the USB cable. No information about the distance between the receiver and USB cable has been provided by the authors.

I.1.3.1.4 Second order soft TEMPEST and radio front ends

In [\[Cottais et al., 2018\]](#) and [\[Lopes Esteves et al., 2017\]](#) radio front ends are perturbed in such a way that polyglot signals are created. Polyglot signals consist in a superposition of two modulation schemes. Consider a communication device that sends two different pieces of information towards two receivers within the same electromagnetic signal. One receiver uses a modulation of kind A and a second one uses a modulation of kind B . Thus, the transmitted signal must be modulated twice. For example, it is possible to modulate a signal in frequency and amplitude at the same time. By doing so, both receivers will be able to demodulate the information without processing the other modulation. If the second receiver belongs to an attacker, it will be able to demodulate the information while the first receiver continues to have a nominal behavior (see Fig. I.1.8). Thus, the work of an attacker is to create this dual modulated signal by modifying the behavior of the transmitter device. This concept was first introduced in [\[Goodspeed and Bratus, 2015\]](#).

In [\[Lopes Esteves et al., 2017\]](#) a proof of concept is proposed where an amplitude modulated signal is added on top of a quadrature phase shift keying (Q-PSK), by creating an IQ imbalance. Moreover in [\[Cottais et al., 2018\]](#), a B-PSK modulation is superposed on top of a Q-PSK modulation by adding a phase offset $\Delta\theta$ on the local oscillator. Several approaches are given to control this IQ imbalance such as a software controlled crosstalk onto the power lines or on the configuration lines of a [voltage-controlled oscillator \(VCO\)](#). The reader may refer to section I.1.3.2.3 for an immunity assessment of a [VCO](#). This procedure is referred as second order soft-TEMPEST, as it is a two-step soft-TEMPEST attack. The attacker, through a malicious software, does not directly control the process that generates the electromagnetic emissions towards the receiver, but the controlled radiations

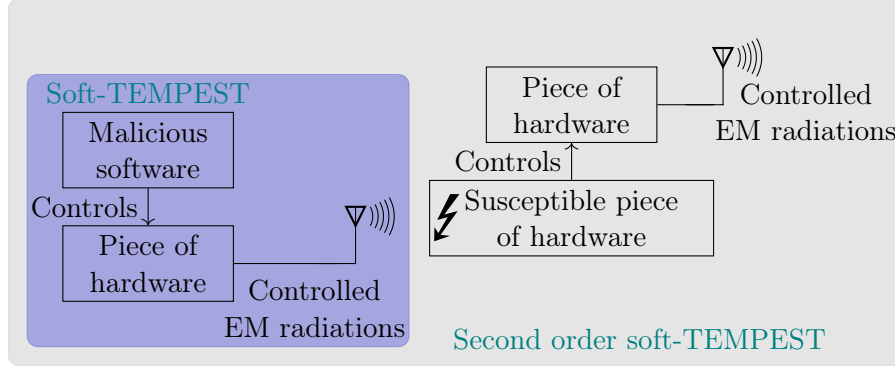


Fig. I.1.9 – Principle diagram of a Soft-TEMPEST (blue background) and second order Soft-TEMPEST (grey background) attacks.

Level	Effect	Description
U	unknown	Unable to determine due to effects on another component or not observed.
N	no effect	No effect occurs or the system can fulfill his mission without disturbances.
I	interference	The appearing disturbance does not influence the main mission.
II	degradation	The appearing disturbance reduces the efficiency and capability of the system.
III	loss of main function (mission kill)	The appearing disturbance prevents that the system is able to fulfill its main function or mission.

Table I.1.1 – Classification of EM effects by their criticality (from [Sabath, 2010]).

compromise a subsystem (a component for example) that will propagate the data towards the receiver as a knock-on effect. Fig. I.1.9 shows a schematic diagram of principle of both soft-TEMPEST and second order soft-TEMPEST attacks.

I.1.3.2 Intentional electromagnetic interference (IEMI) ...

Intentional electromagnetic interference (IEMI) defines electromagnetic aggressions that are directed towards a target in order to alter its nominal behavior. The most prominent example of **IEMI** is when a device is destroyed by a high-power aggression, leading to a loss of the availability of the information it processes [Backstrom and Lovstrand, 2004]. The integrity of the information can also be altered by **IEMI**. Indeed, an **IEMI** may couple onto electric conductors resulting into an additional parasitic signal. If these conductors are used to carry information, as when dealing with serial or parallel communications and depending on the level of coupling, the information may be incorrectly decoded by the receiver. In such a case a loss of integrity occurs. In [Sabath, 2010] a classification of **IEMI** is proposed and is reproduced in Table. I.1.1. An **IEMI** may also be triggered to exploit the susceptibility of an electronic system or component in order to create a covert channel [Houchouas et al., 2016].

Multiple types of aggressions may be considered. Some are transient, like **electromagnetic pulses (EMP)** where the peak electric and magnetic fields can be intense. The time duration of the aggression is from 1 μ s to 1 ms. However, transient aggressions are more suitable to generate perturbations on a wide frequency bandwidth [Backstrom and Lovstrand, 2004]. The shorter the aggression rise-time is, the wider the bandwidth of the aggression will be. Others are continuous, when the desired effect on the target is not generated by transient effects. Pure sine signals, amplitude modulated signals or frequency modulated signals belong to continuous aggressions.

The magnitude of the aggression may vary from a dozen of V m^{-1} to tens of thousands of V m^{-1} . EMP generated by the explosion of a nuclear bomb can generate electric fields greater than 1 kV m^{-1} .

As critical infrastructures are more and more composed of electronic devices, it is necessary to assess the immunity of these infrastructures. The European Union has funded several projects related to IEMIs [PF7, 2012c,a,b]. They are related to the resilience of critical infrastructures against IEMIs, to the high-power microwave threat, and to the security of railways against IEMIs respectively. In what follows, an overview of IEMI effects is given for systems (independent equipment), subsystems (actuators, etc.) and radio front ends, and, more generally, subsystems as a whole.

I.1.3.2.1 ... Towards systems

In [Hoad and Sutherland, 2007], the effects of IEMIs onto a commercial off-the-shelf (COTS) desktop computer are assessed. The effects are listed and classified by their severity, from no effect to functional damage (a short loss of availability), and up to physical damage (a permanent loss of availability). An indication of the field strength needed to trigger a severe upset is given in [Hoad et al., 2004]. A severe upset occurs when a manual intervention is needed to recover a nominal behavior. The computer was exposed to a continuous wave during a time interval of $30 \mu\text{s}$ every 1 ms . The frequency of the continuous wave was between 400 MHz and 8 GHz .

A critical aspect in mitigating the risks of IEMIs onto an information system (IS) is to be able to detect the aggression itself or to detect the effects of the aggression. In [Kasmi et al., 2014] a software method is used. The software analyzes the event logs of the operating system, and under exposure one can observe:

- integrity issues on PS/2, USB or Ethernet links;
- integrity issues on a USB link (it appears that disconnection occurs during the aggression);
- major change of the temperature sensor reading value;
- rise of the noise floor on sound cards while recording;
- SNR reduction of wireless communications (Wi-Fi, Bluetooth, etc.).

By combining these information an IEMI detection agent has been developed allowing a realtime detection of aggressions.

Another detection approach is described in [Hoad and Sutherland, 2007] where an electromagnetic disruption detection system is designed and tested. It is based on an IEMI detection agent like in [Kasmi et al., 2014], and is combined with an electromagnetic sensor. These two information sources are correlated to detect an IEMI. In recently published work [Zhang and Rasmussen, 2020], a novel method to detect the effects of IEMI onto active and passive sensors is proposed, allowing the sensor to work properly during an IEMI. Medical devices are also studied in [Kune et al., 2013]. The authors highlight that a pacemaker can be disturbed by an IEMI (at close range). A detection mechanism, that avoids wrong behaviors based on heartbeat properties, is implemented.

I.1.3.2.2 ... Towards subsystems

Responses of actuators to IEMIs have been investigated in the literature. The reliability of these devices is mandatory for many applications. Erratic behaviors of servomotors have been highlighted in [Houchouas et al., 2017] and in [Selvaraj, 2018] when exposed to IEMI. A functional safety analysis needs to cover this issue in order to prevent personal injuries and damages on the device environment.

I.1.3.2.3 ... Towards radio front ends

Radio front ends are dedicated to process communications. As a consequence, a malfunction in radio front ends may lead to data integrity issues or to a loss of availability. An investigation into the effects of an **IEMI** towards a **voltage-controlled oscillator (VCO)** was given in [Dubois et al., 2014]. Two configurations were considered: the **VCO** alone, and the **VCO** used in a **phase locked loop (PLL)**. The **IEMI** consists of a continuous wave and is generated by a custom-made near-field probe. When the **VCO** is integrated in a **PLL** to generate a frequency f_0 , it appears that spurious frequencies are generated when exposed to a continuous wave of frequency f_p . The generated spurious frequencies are $f_0 \pm \frac{n}{2}|f_0 - f_p|$ where n is an integer. The quality of a communication (in terms of throughput or bit error rate) may suffer from this exposure if an **IEMI** reaches the **VCO**. This can happen when f_p is close to f_0 (the carrier frequency of the communication), as the **IEMIs** will not be filtered or blocked by a circulator. Finally, the **error vector magnitude (EVM)** is measured for **IEMI** of different powers and frequencies f_p . From these **EVMs**, it is possible for an attacker to select the frequency f_p and the power of an **IEMI** in order to degrade the communication. Moreover, it was highlighted that a field of 3.8 V m^{-1} is enough to degrade the communication.

Another approach is given in [van de Beek et al., 2015] where the saturation of the receiver is sought. It results in the blocking of the receiver. Two types of components may be targeted, namely the **low noise amplifier (LNA)** and mixers. This blocking is achieved by placing these components at an operating point that saturates them (above the 1 dB compression point). Therefore, the output of the **LNA** or the mixer is not anymore linearly linked to its input. It results in the loss of the availability of the receiver. Finally, the power $P_{-1\text{dB}}$ related to the 1 dB compression point is determined when a continuous wave is injected into a given radio front end (evaluation kit). Thus, if an **IEMI** signal of power greater than $P_{-1\text{dB}}$ reaches the front end input, the receiver is likely to be blocked. Moreover, it was highlighted that $P_{-1\text{dB}}$ is frequency-dependent and that $P_{-1\text{dB}}$ varies within tens of dBm. Thus, an attacker may select a frequency that blocks the receiver while minimizing the **IEMI** power.

I.1.3.3 Covert channel

The exploitation of the induced effects of an **IEMI** to create a covert channel is also achievable. Indeed, by taking advantage of the susceptibility of a component, it is possible to create simplex communication channels. In [Houchouas et al., 2016], the susceptibility of a temperature sensor located on a given computer motherboard, is evaluated. When a computer is aggressed by an **IEMI**, the reading temperature (accessible from the operating system) returned by the sensor is erroneous. It appears that the returned value depends on the surface power density at the location of the sensor (see Fig. I.1.10a). The aggression signals considered here are amplitude modulated with a carrier frequency of 1.1 GHz. As the surface power density at the sensor location depends on the amplitude of the aggression signal, it is possible to code data by modulating the amplitude of the **IEMI**. Fig. I.1.10b depicts a chronogram of a transmission using this procedure. Four amplitude levels are considered so 2 bits of information are coded on each symbol. A malicious process running on the computer may monitor the evolution of the reading temperature in order to demodulate and to process the transmitted data. A throughput of 10 bits s^{-1} can be reached with that method.

I.1.4 EMSEC at building level

At building level, **EMSEC** studies investigate interactions or couplings between the building and **ISs**. Two interaction modes are considered whether for a leaked information or an aggression. The first one is relative to the propagation of electromagnetic waves within the structure (radiated signal). It depends on the constitutive materials of the building and on its structure. The second one focuses on the propagation along metallic conductors (conducted signal). Several conductors may be considered

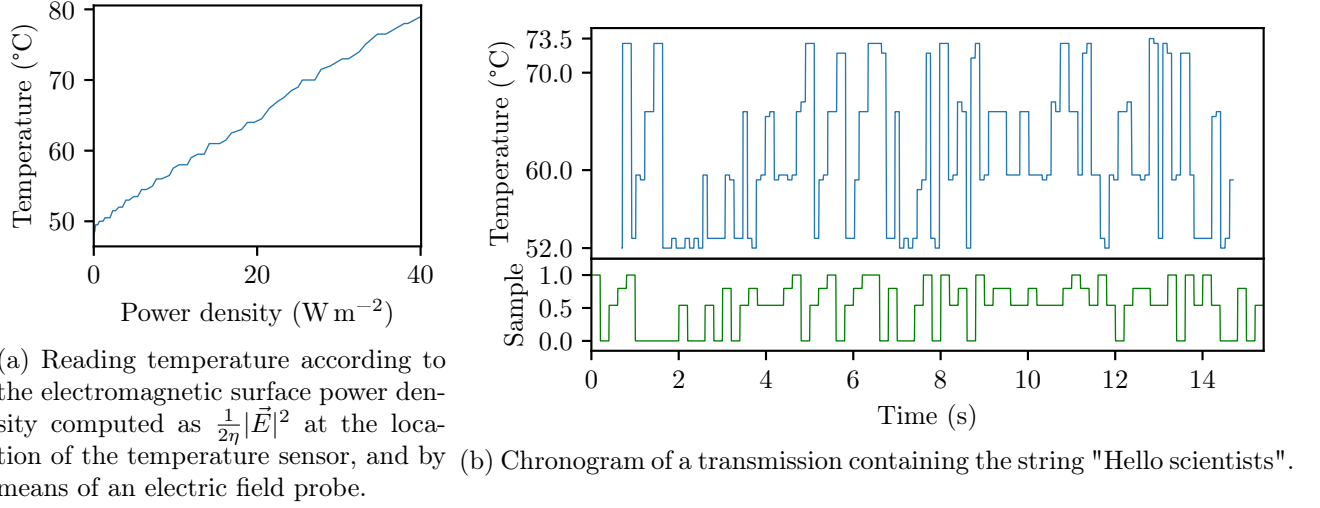


Fig. I.1.10 – Use of the susceptibility of a temperature sensor to create a covert channel.

like metallic water pipes, electric cables, reinforced concrete, etc. Conducted perturbations are generated when an electromagnetic perturbation couples onto a conductor, or when an equipment injects perturbations through the electric power network.

I.1.4.1 Radiated emissions

The propagation of electromagnetic waves into complex structures such as a building was studied in [Junqua et al., 2014b]. Building structures are modeled by a topological network using the **BAUM-LIU-TESCHE (BLT)** technique. Nodes account for dissipative mechanisms, and branches for transfer of energy paths. The interaction processes are described by the **power balance (PWB)** approach (see section I.2.2.3.1 for further information). This approach shall apply to both TEMPEST and IEMI issues.

Remark that for the TEMPEST domain the legislation on classified information requires to enforce rules about how to arrange equipment in order to ensure that compromising emissions outside a restricted area are small enough to prevent their analysis and interpretation.

I.1.4.2 Conducted emissions

IEMI threats Effects of electric pulse injections into power network cables inside civilian facilities are studied in [Mansson et al., 2007] from an **IEMI** viewpoint. A time-domain approach is considered where the injected pulses rising time are less than 1 ns with a maximum amplitude of 450 V. Both common and differential propagation/injection modes are studied. It was highlighted that: the injected power can propagate at large distance, losses are mainly due to impedance mismatch, cable bends may be neglected (no impact on the propagation) and threats mainly come from differential mode propagation.

A proof of concept of conducted emissions related to **EMSEC** was proposed in [Kasmi and Lopes Esteves, 2016]. It was demonstrated that it is possible to inject voice commands to smartphones connected to a power network. First, an amplitude modulated signal was injected on the power network. A part of this signal reaches the smartphone power charger. It was highlighted that somehow, the signal bypasses the power charger, reaches the smartphone, and interferes with the microphone in such a way that it is demodulated and interpreted as a legitimate voice command. To be practicable, the virtual assistant must be activated.

TEMPEST threats There are still very few literature related to the TEMPEST threat for conducted emissions. However, in [Kasmi et al., 2014a] the problem of the propagation of sensitive information on low voltage power network was addressed. Consider a sensitive **IS** plugged on the power network. The risk exists that signals correlated to sensitive information processed by the **IS**, propagate on the power network. If an attacker can somehow access that network, he will be able to intercept and analyze these signals and then recover information. In order to mitigate that risk, one can add filters between the power network and the electronic device power socket. In [Kasmi et al., 2014a], the impact of the use of counter-TEMPEST filters was analyzed. Both common and differential modes were considered by means of two attenuation factors, and both loaded and unloaded power networks were studied.

I.1.5 Conclusion

An overview of **INFOSEC** threats related to **EMI** have been outlined in this chapter for devices of different scales. The TEMPEST threat is related to the interception and to the analysis of parasitic **EMI** in order to recover confidential information. Several sources of **EMI** can be considered such as video stream signals or keyboard signals. These **EMI** sources have been well investigated. However, more broadly, all **EMI** radiated by sensitive **IS** can be considered as a TEMPEST threat. It is also sometimes possible to control somehow **EMI** of electronic devices by means of softwares. This defines the soft-TEMPEST domain, and **EMIs** are a vector to propagate information that an attacker want to leak.

The susceptibility of electronic devices can also be a threat in regards with **IEMI**. Different impacts on an **IS** can be desired by an attacker. From one hand, **IEMI** may be employed to destroy an **IS** or to prevent an **IS** from functioning normally. On the other hand, **IEMI** can create a mean of communication by using the susceptibility of a piece of electronics. Therefore a covert channel is created.

Two different paths may be considered for the **EMI**. Firstly, the radiated one when **EMIs** propagate in the free space medium, and secondly the conducted one when **EMIs** propagate on conductors (typically on the low voltage power network).

A wide range of scenarios has been listed, and it underlines the importance for examining electromagnetic phenomenon from an **INFOSEC** viewpoint. We highlight that some threats may be mitigated by controlling the environment of a sensitive **IS**. By environment we mean:

- the others **ISs** (maybe out of control) close to the sensitive **IS**;
- the power network that may be physically accessible by an attacker and where other uncontrolled electronics equipment may be plugged;
- the physical area around the sensitive **IS** where **EMI** may propagate at long range.

I.1.6 Need to study reverberant environments

From this literature review, one can notice that there are few (if any) published work related to the implications of equipment casing from an **EMSEC** viewpoint. And yet, it is common to embed electronic devices into casings as they limit the susceptibility to the environment and their emissivity towards the environment. A downside of placing equipment in casings, is that it creates reverberant conditions for the electromagnetic field. The electromagnetic modeling of such environment is complex.

Two behaviors can be considered. For some pairs (frequency of interest, cavity shape), the electromagnetic field is evanescent: it does not propagate inside the structure. For other pairs, standing waves will appear as superposed propagating electromagnetic waves. The latter behavior occurs especially

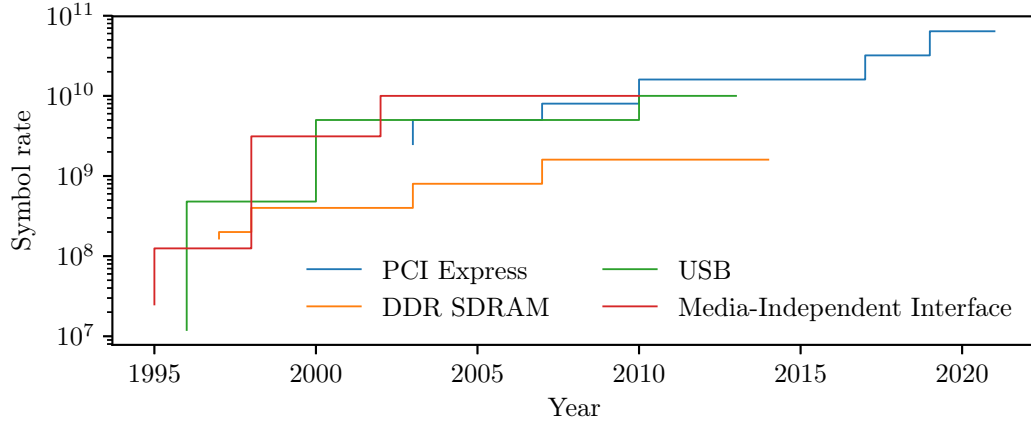


Fig. I.1.11 – Symbol rate of four protocols. The PCI Express communication bus is the common interface to connect daughterboards to the motherboard. Media-Independent Interface refers to communication buses that are present on ethernet controllers.

as the frequency of interest increases. It is also for this latter behavior that the risk for the [INFOSEC](#) is higher as it dramatically increases the coupling risk. Therefore, it is relevant to study casing of equipment from the [EMSEC](#) viewpoint. Two coupling paths will be considered.

Couplings inside a cavity between two (or several) inner elements The risk on the confidentiality of information is caused by the couplings between elements that should remain electrically isolated. Consider encryption devices which are dedicated to encrypt sensitive data. In such devices, the signal that carries the plaintext information penetrates the device from a cable, then the information is encrypted and this generated signal exits the equipment through another cable. It is thus mandatory to prevent couplings of the signal containing the plaintext (that may radiate inside the equipment chassis) to the conductor that carries the encrypted data. Indeed the information confidentiality is not guaranteed anymore if a parasitic signal, correlated to the plaintext, will be superposed on the outgoing signal.

Couplings between an outer electromagnetic field and elements inside a cavity In that case, the risk on the confidentiality of the information is high (TEMPEST threat), as [EMI](#) generated by the device may be radiated outside the casing. Moreover, in that case, [IEMI](#) may be responsible for the loss of the integrity and availability of information, when a powerful electromagnetic field is pointed towards the equipment.

Both configurations need to be studied. Moreover, from the LORENTZ reciprocity theorem [[Balanis, 2016](#), chap 3.8], studying the coupling between an item A and item B is equivalent to study the coupling between the item B and the item A. Remark that this reciprocity does not hold from the [EMSEC](#) viewpoint. The risk assessment is different for each coupling “direction”.

The next section will expose tools that may be employed to study reverberant environments. It will be highlighted that the choice of the technique to apply strongly depends on the minimum and maximum frequency of interest. To determine these frequencies, symbol rates for several common communication protocols have been listed. Fig. I.1.11 gives symbol rates for four communication protocols. These symbol rates cover a wide frequency bandwidth, up to several tens of GHz. Methods that will be selected to address the issue of couplings inside reverberant environments should be applicable up to these frequencies.

Chapter I.2

Couplings to and inside reverberant environment

Contents

I.2.1	Introduction	30
I.2.2	Electromagnetic couplings through apertures	31
I.2.2.1	Analytical methods: the diffraction theory	31
I.2.2.2	Intermediate level circuit models (ILCM).	36
I.2.2.3	Topological formalism associated to the power balance approach	39
I.2.2.4	Power balance approach combined with the random matrix theory	44
I.2.2.5	Full BLT application	44
I.2.2.6	Methods based on full-wave simulations	45
I.2.2.7	Statistical methods	45
I.2.2.8	Conclusion	46
I.2.3	Electromagnetic couplings within a cavity	46
I.2.3.1	Analytical methods by use of the GREEN's functions	46
I.2.3.2	Statistical methods	47
I.2.3.3	Hybrid circuit methods	48
I.2.4	Electromagnetic field to conductors couplings	49
I.2.5	Cavity regimes	50
I.2.6	Conclusion	51
I.2.7	Selection of approaches for the study of couplings inside cavities from an EMSEC perspective.	51

I.2.1 Introduction

Couplings within reverberant environment have been widely investigated from the [EMC](#) standpoint in order to prevent equipment dysfunctions. Two kinds of couplings may occur. The first one is the coupling of an outer electromagnetic field with an enclosure through an aperture, and the second one is the coupling between several inner elements inside a cavity (*i.e.* between a cable and a [printed circuit board \(PCB\)](#) for example).

To characterize these interactions, various approaches have been proposed in the literature. Some consider a fully determined configuration, whereas others focus on a situation where some parameters are considered as random variables. The latter refers to statistical methods. Depending on the

application, different physical quantities of interest may be looked at by means of various approaches. Some of them are useful to evaluate the electromagnetic field at any location in the studied structure. Others can help to characterize the electromagnetic environment such as through the mean values of electromagnetic energy or power. Yet others are aimed at determining currents or/and voltages onto coupled conductors. A review of these methods is exposed in this chapter, and some will be selected and then investigated in detail throughout this dissertation.

Before listing those methods, and because some rely on full-wave electromagnetic field solvers, it is necessary to briefly expose these solvers. Full-wave electromagnetic field solvers, resolve the MAXWELL's equations without any assumption. The resolution technique requires either integral equations or differential equations. Moreover, for time-domain solvers, the computed electromagnetic field is returned versus the frequency, whereas for frequency-domain solvers, the electromagnetic field is returned for only one frequency. Let us consider the most frequently employed resolution techniques.

The [finite-difference time-domain \(FDTD\)](#) is a time-domain solver where the field is computed at each cell of a grid (over the computation volume). It relies on differential equations. The [finite integration technique \(FIT\)](#), implements integral equations, and is a time-domain technique. The [method of moments \(MoM\)](#) is a frequency-domain resolution technique, based on integral equations.

I.2.2 Electromagnetic couplings through apertures

I.2.2.1 Analytical methods: the diffraction theory

Several models can describe diffraction phenomena, their choice depends on the size of the aperture. At first, general purpose principles will be exposed, then specific models suitable for small electric dimensions will be reminded.

I.2.2.1.1 Description of general apertures

The description of the electromagnetic field behind an aperture is a complex procedure [[Bouwkamp, 1954](#)]. Small apertures can be described from the BETHE's theory (which will be reminded in the next section), while large ones may be considered by means of the geometrical theory of diffraction [[Balanis, 2016](#), chap. 12.10]. For aperture dimensions close to the wavelength of interest, the two following principles apply.

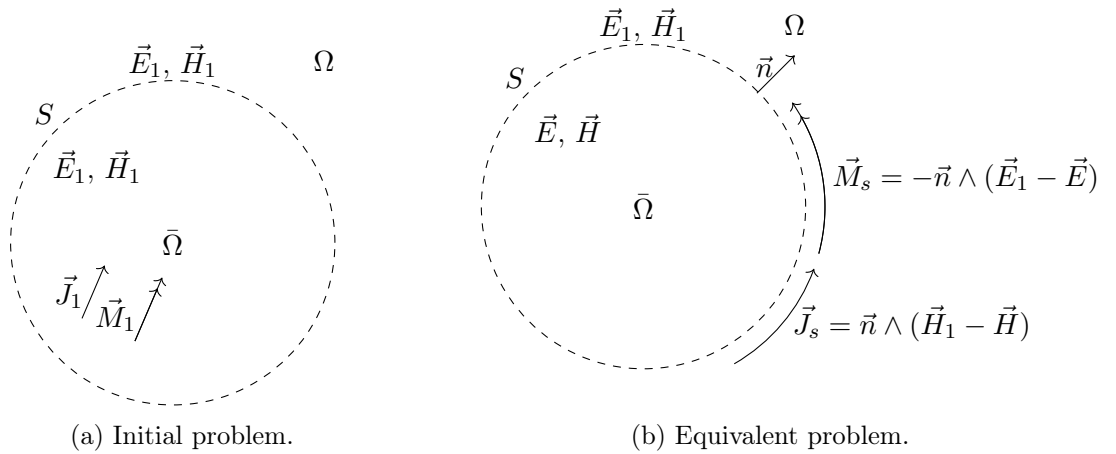


Fig. I.2.1 – Initial and equivalent models.

The HUYGENS equivalence principle [Balanis, 2016, chap. 12.1] Assume that electric \vec{J}_1 and magnetic \vec{M}_1 sources (as current densities) generate electric \vec{E}_1 and magnetic \vec{H}_1 fields everywhere. Consider the situation depicted in Fig. 1.2.1 which represents a closed volume $\bar{\Omega}$ containing the electric \vec{J}_1 and magnetic \vec{M}_1 current densities. The volume outside $\bar{\Omega}$ is referred as Ω . An equivalent configuration that generates \vec{E}_1 and \vec{H}_1 outside $\bar{\Omega}$ consists in removing the \vec{J}_1 and \vec{M}_1 sources from $\bar{\Omega}$, and to impress magnetic \vec{M} and electric \vec{J} current densities at the boundary S between the two volumes. The new fields inside $\bar{\Omega}$ are \vec{E} and \vec{H} . \vec{M} and \vec{J} are expressed from the tangential fields to $\bar{\Omega}$ as:

$$\vec{J} = \vec{n} \wedge (\vec{H}_1 - \vec{H}) \quad (\text{I.2.1})$$

$$\vec{M} = -\vec{n} \wedge (\vec{E}_1 - \vec{E}) \quad (\text{I.2.2})$$

where \vec{n} is an outwards unit normal vector.

As the fields of interest are outside $\bar{\Omega}$, \vec{E} and \vec{H} can take any value. Especially, one can define sources \vec{J}_s and \vec{M}_s such that the radiated fields inside $\bar{\Omega}$ are null ($\vec{E} = \vec{0}$ and $\vec{H} = \vec{0}$). These sources are expressed as:

$$\vec{J}_s = \vec{n} \wedge \vec{H}_1 \quad (\text{I.2.3})$$

$$\vec{M}_s = -\vec{n} \wedge \vec{E}_1 \quad (\text{I.2.4})$$

This result is used in [Harrington and Mautz, 1976] where the problem of two regions separated by a **perfect electric conductor (PEC)** screen containing an aperture is addressed. Further information about its application will be given in section III.2.4.

The BABINET's principle [Balanis, 2016, chap. 12.8] states that for complementary screens, the sum of the electric field \vec{E}_e diffracted through a screen with a given aperture, and the electric field \vec{E}_m diffracted by its complementary shape, is equal to the electric field \vec{E}_0 radiated if no screens were present. The same statement holds for the magnetic field, thus:

$$\vec{E}_0 = \vec{E}_e + \vec{E}_m \quad (\text{I.2.5})$$

$$\vec{H}_0 = \vec{H}_e + \vec{H}_m \quad (\text{I.2.6})$$

Fig. 1.2.2 depicts an infinite screen with an aperture and its complementary shape. Another formulation of the BABINET's principle involves impedances. It states that if both an aperture and its complementary screen can be described by two input impedances (Z_s and Z_c respectively), then the following equality holds:

$$Z_s Z_c = \frac{\eta^2}{4} \quad (\text{I.2.7})$$

Aperture problems may be solved from this result when used jointly with the planar antenna theory (see III.2.2).

I.2.2.1.2 Equivalent electric and magnetic dipoles for small apertures

Some simple geometry apertures, may be modeled by electric and magnetic dipoles. This method was introduced in [Bethe, 1944] but is limited to apertures with small electrical dimensions: the condition is that the maximum transversal dimension d_{\max} of the aperture should be smaller than $\frac{\lambda_{\min}}{2\pi}$, with λ_{\min} the shortest wavelength of interest. If so, the aperture may be replaced by an elementary electric dipole of moment \vec{P}_e and an elementary magnetic dipole of moment \vec{P}_m while shorting the aperture with a metallic wall. The expressions of these elementary moments are:

$$\vec{P}_e = \epsilon \alpha_e \vec{E}_{sc} \quad (\text{I.2.8})$$

$$\vec{P}_m = -\underline{\underline{\alpha}}_m \vec{H}_{sc} \quad (\text{I.2.9})$$

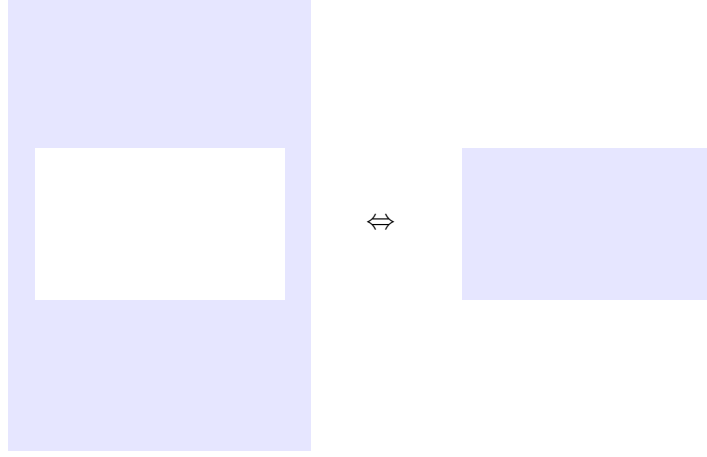


Fig. I.2.2 – BABINET's principle for a planar rectangular aperture.

where \vec{E}_{sc} and \vec{H}_{sc} are respectively the short circuit electric and magnetic field at the location of the aperture, and are expressed from the incident field \vec{E}_i as:

$$\vec{E}_{sc} = 2(\vec{n} \cdot \vec{E}_i) \cdot \vec{n} \quad (\text{I.2.10})$$

$$\vec{H}_{sc} = 2(\vec{n} \wedge \vec{E}_i) \wedge \vec{n} \quad (\text{I.2.11})$$

with \vec{n} the unitary vector normal to the aperture. The scalar α_e and the matrix $\underline{\underline{\alpha}}_m$ are the polarizabilities associated to the aperture. These quantities depend on the size and on the geometry of the aperture. Values of α_e and $\underline{\underline{\alpha}}_m$ are available in the literature for canonical aperture shapes (such as circles, ellipses, etc.). Formulations of polarizabilities may be found in [Butler et al., 1978, Collin, 1991] with the constraint that the aperture is smaller than the wavelength. For example, for a circle, α_e and matrix $\underline{\underline{\alpha}}_m$ are expressed as:

$$\alpha_e = \frac{2}{3} R^3 \quad (\text{I.2.12})$$

$$\underline{\underline{\alpha}}_m = \begin{pmatrix} \frac{4}{3} R^3 & 0 & 0 \\ 0 & \frac{4}{3} R^3 & 0 \\ 0 & 0 & 0 \end{pmatrix} \quad (\text{I.2.13})$$

where R is the aperture radius. Then, the total electric field \vec{E}_{total} diffracted at the position \vec{r} and in the direction \vec{u} created by the coupling of an incident field \vec{E}_i to the aperture is given by [Jackson, 1999]:

$$\begin{aligned} \vec{E}_{\text{electric dipole}} &= -\omega_0^2 \mu_0 G(\vec{r}) \\ &\quad \left[\left(-1 + \frac{3j}{|\vec{k}||\vec{r}|} + \frac{3}{|\vec{k}|^2 |\vec{r}|^2} \right) ((\vec{P}_e \wedge \vec{u}) \wedge \vec{u}) + \left(\frac{2j}{|\vec{k}||\vec{r}|} + \frac{2}{|\vec{k}|^2 |\vec{r}|^2} \right) \vec{P}_e \right] \end{aligned} \quad (\text{I.2.14})$$

$$\vec{E}_{\text{magnetic dipole}} = |\vec{k}| \omega_0 G(\vec{r}) \left[\left(1 - \frac{j}{|\vec{k}||\vec{r}|} \right) \vec{P}_m \wedge \vec{u} \right] \quad (\text{I.2.15})$$

$$\vec{E}_{\text{total}} = \vec{E}_{\text{magnetic dipole}} + \vec{E}_{\text{electric dipole}} \quad (\text{I.2.16})$$

where $G(\vec{r})$ is the free-space GREEN's function, expressed as:

$$G(\vec{r}) = -\frac{e^{-j|\vec{k}||\vec{r}|}}{4\pi|\vec{r}|} \quad (\text{I.2.17})$$

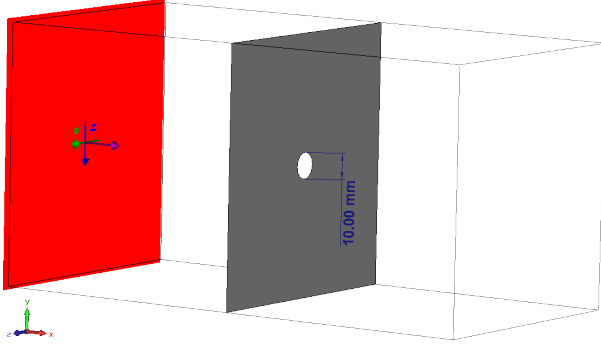


Fig. I.2.3 – Model in a full-wave simulation software [CST Studio Suite \(CST-SS\)](#), the incident plane wave is in red and the aperture has a diameter of $d_0 = 1$ cm.

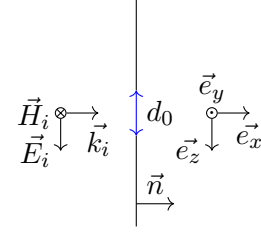


Fig. I.2.4 – Axes conventions for the comparison between the full-wave simulation software and the BETHE's theory.

The total magnetic field \vec{H}_{total} is given by:

$$\vec{H}_{\text{magnetic dipole}} = -\omega_0^2 \epsilon_0 \mu_0 G(\vec{r}) \left[\left(-1 + \frac{3j}{|\vec{k}||\vec{r}|} + \frac{3}{|\vec{k}|^2 |\vec{r}|^2} \right) ((\vec{P}_m \wedge \vec{u}) \wedge \vec{u}) + \left(\frac{2j}{|\vec{k}||\vec{r}|} + \frac{2}{|\vec{k}|^2 |\vec{r}|^2} \right) \vec{P}_m \wedge \vec{u} \right] \quad (\text{I.2.18})$$

$$\vec{H}_{\text{electric dipole}} = -|\vec{k}| \omega_0 G(\vec{r}) \left[\left(1 - \frac{j}{|\vec{k}||\vec{r}|} \right) \vec{P}_e \wedge \vec{u} \right] \quad (\text{I.2.19})$$

$$\vec{H}_{\text{total}} = \vec{H}_{\text{magnetic dipole}} + \vec{H}_{\text{electric dipole}} \quad (\text{I.2.20})$$

A simulation has been launched to compare the electric field obtained by means of this method to the electric field computed with a full-wave simulation software. The simulated geometry, depicted on Fig. I.2.3, is a panel with a circle aperture of diameter $d_0 = 10$ mm which is illuminated by a horizontally polarized plane wave of amplitude 1 V m^{-1} . Fig. I.2.5 shows the electric field, given by equation (I.2.16), on the plane xOy containing the center of the aperture, at frequencies 1 GHz, 5 GHz and 10 GHz. The axes conventions are shown in Fig. I.2.4 and the aperture is located at $x = 0$. Moreover, a comparison between simulations and the analytical formulation is given for the mean electric field on a vertical line ($x = 10$ mm and $z = 0$ mm with y within the -50 mm to 50 mm range). The mean electric field over a period T is computed as in [CST-SS](#) like:

$$\begin{aligned} \langle |\vec{E}| \rangle &= \frac{1}{T} \int_0^T |\vec{E}| dt \\ &= \frac{1}{T} \int_0^T \sqrt{\Re(E_x e^{-j\omega t})^2 + \Re(E_y e^{-j\omega t})^2 + \Re(E_z e^{-j\omega t})^2} dt \end{aligned} \quad (\text{I.2.21})$$

The simulations agree well for a frequency associated to a wavelength close to the dimension d_0 of the aperture, *i.e.* 3 GHz. When the wavelength is much shorter than d_0 , see Fig. I.2.5a, the BETHE's theory does not agree with the simulation. For wavelength greater than d_0 , the simulation fits the theory but only apart the axis of the aperture (where $y = 0$).

I.2.2.1.3 Equivalent dipoles and couplings in cavities

An application of the BETHE's diffraction theory for small apertures is proposed in [\[Seidel, 1978\]](#), where the coupling between an outer electric field and a wire located inside a cavity needs to be determined by computing the current density on that wire. The configuration is depicted in Fig. I.2.6. The aperture

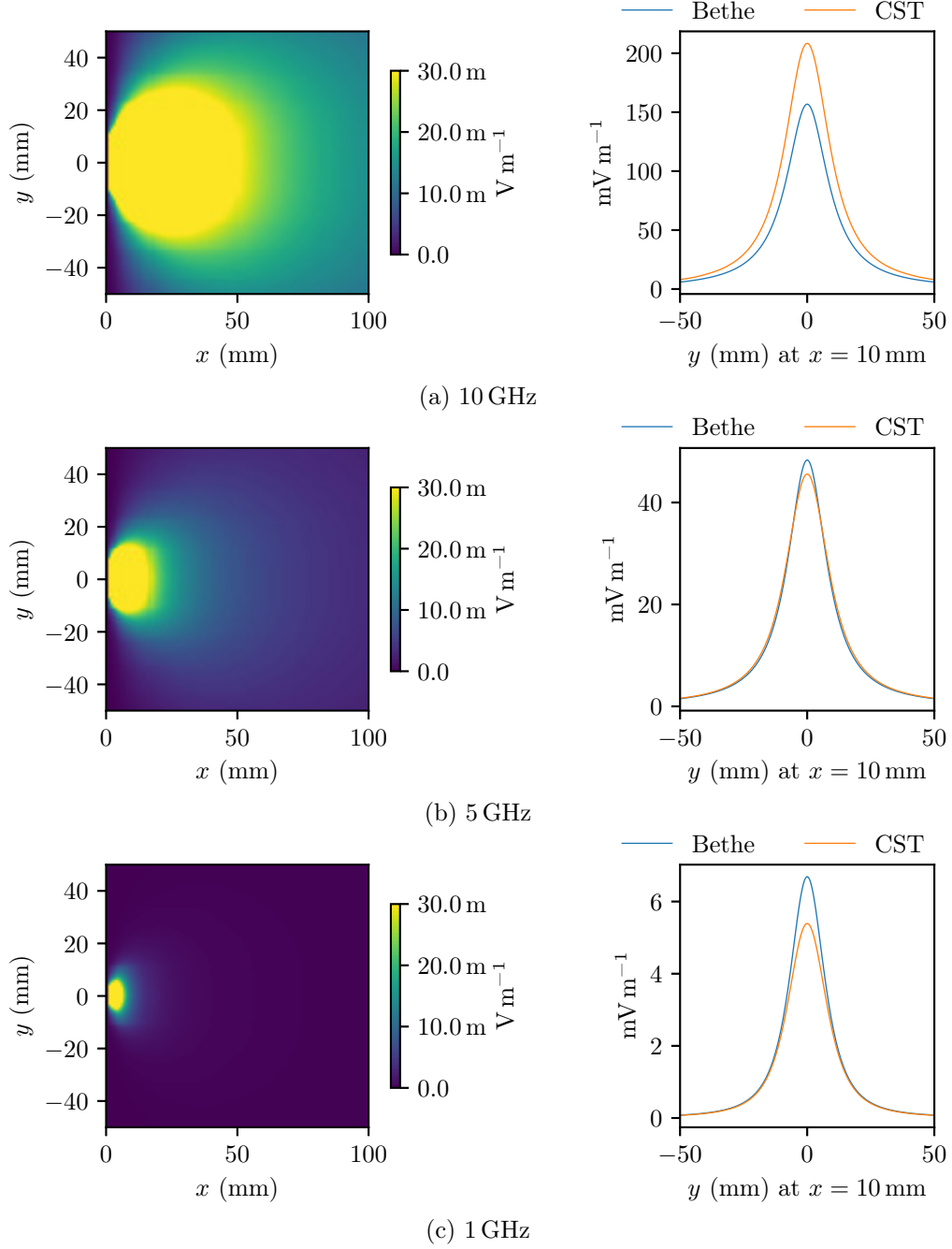


Fig. I.2.5 – Mean value of the electric field in the plane xOy containing the center of the aperture calculated from (I.2.16), and comparison with full-wave simulation results (CST-SS).

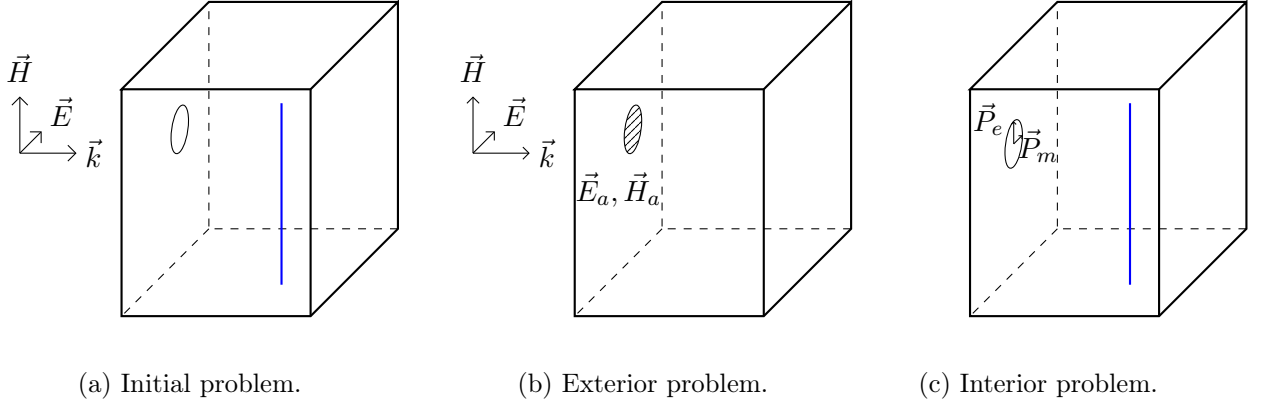


Fig. I.2.6 – Scheme of the configuration studied in [Seidel, 1978, Lecoïnte et al., 1992]. The wire is in blue.

is modeled by an electric dipole and a magnetic dipole of respective moments \vec{P}_e and \vec{P}_m . From \vec{P}_e , \vec{P}_m , and the GREEN's function of the cavity, two integral equations are set and solved by the method of moments. The dimensions of the studied cavity are 40 cm \times 30 cm \times 130 cm (see Fig. I.2.6). Two equations are solved, where \vec{r}' refers to the source location (the dipole at the aperture), and \vec{r} to the observation point location. The POCKLINGTON's equation, allows to determine the current density \vec{J}_s on a wire of radius a and length l from its nearby electric field. Assuming that the wire is oriented along the Oz axis, then $I(z) = 2\pi a \vec{e}_z \cdot \vec{J}_s(z)$ can be calculated by solving:

$$\int_{-\frac{l}{2}}^{\frac{l}{2}} 2\pi r \vec{e}_z \cdot \vec{J}_s(z') \left[\left(\frac{\partial^2}{\partial z'^2} + k^2 \right) K(\vec{r}, \vec{r}') \right] dz' + j\omega \epsilon \vec{e}_z \cdot \vec{E}(\rho = a) = 0 \quad (\text{I.2.22})$$

with:

$$K(\vec{r}, \vec{r}') = \frac{1}{2\pi} \int_{-\pi}^{\pi} \underline{\underline{\mathbf{G}}}_{A_{zz}}(\vec{r}, \vec{r}') d\phi' \quad (\text{I.2.23})$$

where $\underline{\underline{\mathbf{G}}}_A(\vec{r}, \vec{r}')$ is the dyadic GREEN's function for the potential due to electric current source. From a second equation, the electric field \vec{E} inside the cavity is computed from \vec{P}_e and \vec{P}_m as:

$$\vec{E}(\vec{r}) = \frac{1}{\epsilon} \underline{\underline{\mathbf{G}}}_e(\vec{r}, \vec{r}') \vec{P}_e + j\eta k \underline{\underline{\mathbf{g}}}_e(\vec{r}, \vec{r}') \vec{P}_m \quad (\text{I.2.24})$$

where $\underline{\underline{\mathbf{G}}}_e(\vec{r}, \vec{r}')$ and $\underline{\underline{\mathbf{g}}}_e(\vec{r}, \vec{r}')$ are the GREEN's dyads for the electric field due to the electric and magnetic sources respectively. This method is strongly bound to the geometry of the cavity as the GREEN's function of the cavity is required.

The study exposed in [Lecoïnte et al., 1992, Lecoïnte, 1995] addresses the same problem as in [Seidel, 1978], but provides a comparison with measurements up to 3 GHz. Measurements data, acquired from a chassis mock-up, are compared to two different models. The first one does not take into account the reactions of the cavity and the cable with the aperture, and the second one takes these reactions into consideration. The author concludes that considering the reactions of the wire on the aperture improves the results.

I.2.2.2 Intermediate level circuit models (ILCM).

Intermediate level circuit models refer to analytical formulations based on a circuit approach that intends to compute the shielding effectiveness of cuboid enclosures with apertures. The seminal papers

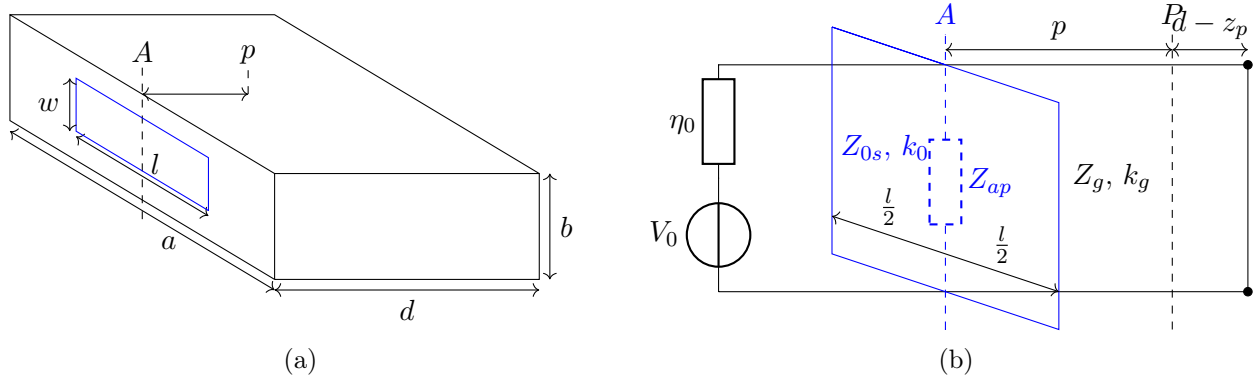


Fig. I.2.7 – Schematic I.2.7a and equivalent circuit I.2.7b of the problem exposed in [Robinson et al., 1998].

related to this method are [Robinson et al., 1996, 1998]. A brief review of this method is now proposed, as well as the improvements that were since exposed in the recent literature.

In that type of model, the enclosure is represented by a short-circuited waveguide of characteristic impedance Z_g and of propagation constant $k_g = j\beta_{10}$ (only the TE_{10} mode is considered in the initial formulation). Then, the aperture, of length l and of width w , is modeled by a coplanar stripline short-circuited at both ends with a characteristic impedance Z_{0s} . The width of the coplanar stripline is equal to the height b of the enclosure, and the gap length between the two conductors corresponds to the aperture width w . The expression of Z_{0s} can be found in [Gupta, 1996, chap. 7]. The radiating incident source is modeled by a waveguide with a characteristic impedance η and an electromotive force V_0 (see Fig. I.2.7). As the coplanar stripline is short-circuited, the aperture impedance at its center is given by [Balanis, 2012, chap. 8]:

$$Z_{ap} = j \frac{Z_{0s}}{2} \frac{l}{a} \tan \left(\frac{k_0 l}{2} \right) \quad (I.2.25)$$

By employing all these analogies together, and using the THÉVENIN's model, the voltage $V_{eq}^{TE_{10}}$ at a distance $d - z_p$ from the back of the enclosure is:

$$V_{eq}^{TE_{10}} = \frac{V_1 \sin(\beta_{10}(d - z_p))}{\sin(\beta_{10}d) - j \frac{Z_1}{Z_g^{TE_{10}}} \cos(\beta_{10}d)} \quad (I.2.26)$$

with $Z_1 = \frac{\eta Z_{ap}}{\eta + Z_{ap}}$, $V_1 = \frac{V_0 Z_{ap}}{\eta + Z_{ap}}$. Finally, the shielding effectiveness is computed as:

$$SE = -20 \log \frac{2|V_{eq}^{TE_{10}}|}{|V_0|} \quad (I.2.27)$$

This analytical model was tested against measurements on a copper made enclosure whose dimensions are $30 \text{ cm} \times 30 \text{ cm} \times 12 \text{ cm}$, for several rectangular apertures. Comparisons are proposed in [Robinson et al., 1998] for three enclosure sizes, and for frequencies up to 1 GHz. Measurement and simulation data agree well with each other. However only the transmission line TE_{10} mode is considered, thus this method is limited to electrically small enclosures.

This model was improved in [Azaro et al., 2001] to take into account any direction of incidence and any polarization of the incident plane wave. Elementary sources were added to the coplanar stripline (that models the aperture) and a voltage $V_x(x)$ was determined across the aperture. Then

the voltage $V_g(z)$ along the z -axis (on the short circuited waveguide) was expressed in terms of forward and backward waves as $V_g(z) = V_{\text{forw}}e^{-jk_g z} + V_{\text{back}}e^{jk_g z}$. $V_g(z)$ is fully determined by applying the boundary conditions $V_g(0) = V_x(\frac{l}{2})$ and $V_g(d) = 0$. Finally, a parametric study over the angles of incidence of the plane wave and over the aperture sizes is given.

The ability to evaluate the shielding effectiveness everywhere in the cavity was added to that model in [Azaro et al., 2002]. Considering only the TE₁₀ mode at the aperture, the y component of the electric field is expressed as:

$$E_y^{\text{ap}}(x) = V_x(x) \sqrt{\frac{2}{wl}} \frac{Z_s}{Z_s + Z_{\text{ap}}} \quad (\text{I.2.28})$$

where Z_s is the impedance of the waveguide at $d - z_p$, *i.e.* $Z_s = jZ_g \tan(k_g(d - z_p))$. Then, by use of a modal expansion over m , the electric field in the cavity is given by:

$$\vec{E} = \sum_m \left[\frac{\int_S (\nabla \times \vec{E}^{\text{ap}}) \cdot \nabla \times \vec{e}_m ds}{(k_m^2 - k_0^2) \int_V |\vec{e}_m|^2 ds} \right] \vec{e}_m \quad (\text{I.2.29})$$

where S is the surface of the aperture, V is the cavity volume and \vec{e}_m are the divergenceless electric eigenvectors of the cavity. Finally, the shielding effectiveness is computed from (I.2.29). This formulation is not restrictive about the cavity modes considered (contrarily to the previous models). However, the aperture center should still be located at the center of the front face of the cavity. A method to take TE₀₀ and TM_{1n} modes into account is presented in [Belokour and LoVetri, 2002].

The possibility to locate the aperture anywhere on the front face was proposed in [Konefal et al., 2005]. Additionally, a radiation impedance for the aperture was added to this model to represent its re-radiation. It is determined by using the BABINET's principle and a full-wave simulation. Further details about this principle will be given in section III.2.2. Unfortunately, this formulation only allows to consider slot apertures (*i.e.* aperture whose height is a small fraction of its length).

More recently, several improvements to the ROBINSON's method have been proposed:

- [Shim et al., 2010]: the shielding effectiveness calculation is extended to apertures located on different faces of the cavity;
- [Yin and Du, 2016]: a new definition of Z_{ap} (substituted to (I.2.25)) is proposed. It allows to consider N_a apertures of center position (x_i, y_i) and of length l_i , for the m, n aperture mode:

$$Z_{\text{ap}} = j \frac{Z_{0S}}{2} \sum_{i=1}^{N_a} \frac{l_i}{a} \tan\left(\frac{k_0 l_i}{a}\right) \sin\left(\frac{m\pi}{a} x_i\right) \cos\left(\frac{n\pi}{b} y_i\right) \quad (\text{I.2.30})$$

- [Rabat et al., 2017]: the TAYLOR model is employed to determine the current on a wire that is placed in a cavity. This current results from coupling of the eigenmodes onto the wire. It consists in the addition of sources localised onto transmission lines to include electromagnetic field couplings;
- [Rabat et al., 2018]: the losses on cavity walls are integrated in the model by substituting the wavenumber k_g of the waveguide by $k_g = \alpha_{mn} + j\beta_{mn}$. The comparison of full-wave simulations for cavities having different wall materials (thus with different conductivities) with this method gives good agreement.

All the applications of that model were restricted to undermoded (low mode density) cuboid enclosures. To overcome this issue, one can use an eigenmode solver to precompute the eigenmodes and to inject them into the circuit formulation (by use of (I.2.29) for example) with the drawback that the computation time will grow. Moreover, the wider the frequency bandwidth is, the longer the computation time will be.

I.2.2.3 Topological formalism associated to the power balance approach

I.2.2.3.1 The power balance approach

The **power balance (PWB)** approach was set by HILL (see [Hill, 2009, chap. 8.2]) with the intent to qualify energy transfers inside reverberant environments at a macroscopic scale. Thus, instead of determining electric/magnetic fields or voltage/current values, electromagnetic environments are identified by means of average power values. It models transfer of energy into cavities from a macroscopic viewpoint. To be valid, the model requires that the environment is overmoded such that the field inside the reverberant environment is uniformly distributed in polarization and in phase. It is thus mandatory that the size of the cavity is large compared to the longest studied wavelength.

Applying this method involves to solve an equilibrium equation that describes energy transfers inside a cavity. The **PWB** states that the sum of the energy losses and energy transfers in a cavity must be equal to the injected power P_t :

$$P_t = \sum_i P_{d_i} \quad (\text{I.2.31})$$

Each loss is linked to a given elementary mechanism (subscript i), and all these elementary mechanisms are assumed to be independent. P_{d_i} is the power dissipated by the i^{th} mechanism. A quality factor Q_i may be defined for each one as:

$$Q_i = \omega \frac{U_s}{P_{d_i}} \quad (\text{I.2.32})$$

where $U_s = WV$ is the stored energy in the cavity (with V the volume of the cavity and W its volume energy density). Then, the power density S_c in the cavity is:

$$S_c = \frac{\langle |\vec{E}|^2 \rangle}{2\eta_0} = cW \quad (\text{I.2.33})$$

where \vec{E} is the total field within the cavity. Moreover, the power P_{d_i} may be written like:

$$P_{d_i} = S_c \sigma_i \quad (\text{I.2.34})$$

where S_c is the surface power density of the cavity in W m^{-2} and σ_i is an **absorption cross sections (ACS)** (in m^2).

By combining the equations (I.2.32) to (I.2.34), we obtain:

$$S_c = cW = c \frac{U_s}{V} = c \frac{Q_i P_{d_i}}{V \omega} = \lambda f \frac{Q_i P_{d_i}}{2\pi f V} = \frac{\lambda Q_i P_{d_i}}{2\pi V} \quad (\text{I.2.35})$$

which leads to an equilibrium equation between the power transmitted to the cavity P_t and the losses and energy transfers modeled by its **ACS** σ_i .

$$P_t = P_d = S_c \sum_i \sigma_i \quad (\text{I.2.36})$$

The loss mechanism may be split into four types:

- power loss through apertures;
- power absorbed by the cavity walls;
- power absorbed by antennas;
- power absorbed by the loads present into the cavity.

Cross section expressions for each of these mechanisms may be found in [Hill, 2009, chap. 8.2]. In what follows, it will be highlighted that the **PWB** approach can be integrated into topological descriptions of systems to describe the interactions between different reverberant environments (such as cavities).

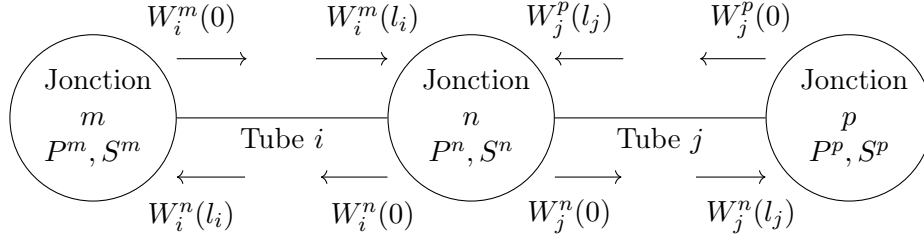


Fig. I.2.8 – Example of BLT network with three nodes and two tubes. Figure inspired from [Junqua, 2010].

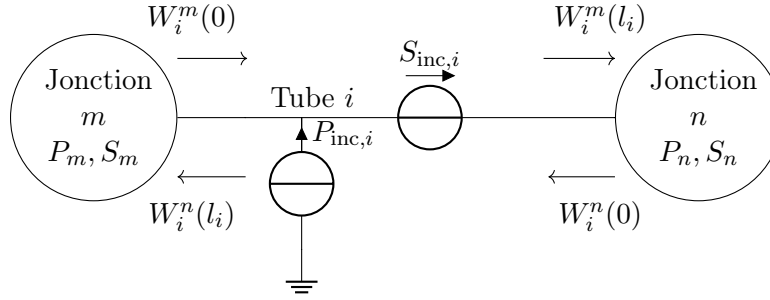


Fig. I.2.9 – Example of BLT network with two nodes and one tube, with sources. Figure inspired from [Junqua, 2010].

I.2.2.3.2 The BLT formalism

The BAUM-LIU-TESCHE (BLT) formalism models a complex system by a topological network where the interactions between travelling waves W are determined. It was set by BAUM, LIU and TESCHE in [Baum et al., 1978]. Its purpose is to provide a convenient method to solve problems with multiconductor transmission lines. Topological networks are composed of tubes (or branches) for the propagation, and of junctions for the scattering.

This model was updated and specified to integrate the PWB approach [Junqua et al., 2005]. The quantities of interest became ACS, power densities and mean powers. Thus the propagation phenomena are not relevant anymore and were removed from the initial formulation of the BLT formalism. In [Junqua et al., 2005], it has been stated that applying the PWB method may be reduced to the analysis of an electrical circuit. Indeed the following equivalences are set between PWB and electric quantities:

$$\text{the average dissipated power } P \leftrightarrow \text{the current } I \quad (\text{I.2.37})$$

$$\text{the average power density } S \leftrightarrow \text{the voltage } V \quad (\text{I.2.38})$$

$$\text{the average cross section (ACS) } \langle \sigma \rangle \leftrightarrow \text{the admittance } Y. \quad (\text{I.2.39})$$

which leads to an equivalent Ohm's law $P = \langle \sigma \rangle S \leftrightarrow I = YV$.

In the network, the tubes model the propagation of travelling waves and the nodes characterize the scattering of the travelling waves as well as the dissipative phenomena. The terms "propagation" and "travelling waves" come from the BLT formalism and will be used even if they are not relevant when integrating the PWB, as no propagation phenomena are considered.

Nodes may refer to metallic walls, apertures, wires, antennas, etc. Fig. I.2.8 illustrates the case of a topological network with three nodes and two tubes. Each node k is associated to an average dissipated power P^k (in W) and an average power density S^k (in W m^{-2}). The travelling waves on

the tube i of length $l_i = l$ between the nodes m and n are defined by their values at each node by the following formulas:

$$W^n(0) = \langle \sigma \rangle S^n - P^n \quad (\text{I.2.40})$$

$$W^m(0) = \langle \sigma \rangle S^m - P^m \quad (\text{I.2.41})$$

$$W^n(l) = \langle \sigma \rangle S^m + P^m \quad (\text{I.2.42})$$

$$W^m(l) = \langle \sigma \rangle S^n + P^n \quad (\text{I.2.43})$$

Moreover, on each tube, power sources may be added (see Fig. I.2.9). In the tube i it leads to:

$$W_{s,i}^m = -\langle \sigma \rangle S_{\text{inc},i} + P_{\text{inc},i} \quad (\text{I.2.44})$$

$$W_{s,i}^n = \langle \sigma \rangle S_{\text{inc},i} + P_{\text{inc},i} \quad (\text{I.2.45})$$

where $S_{\text{inc},i}$ is an incident density power and $P_{\text{inc},i}$ is an incident transmitted power on the tube i . P_{inc} may represent the power injected by an antenna. All these sources are contained in the super vector $\underline{[W_s]}$. Finally, a super matrix $\underline{[\Gamma]}$ models the propagation and a second one $\underline{[S]}$ the scattering. They are related by:

$$\underline{[W(l)]} = \underline{[\Gamma]} \underline{[W(0)]} + \underline{[W_s]} \quad \text{Propagation equation} \quad (\text{I.2.46})$$

$$\underline{[W(0)]} = \underline{[S]} \underline{[W(l)]} \quad \text{Scattering equation} \quad (\text{I.2.47})$$

$$(\underline{[I]} - \underline{[S]} \underline{[\Gamma]}) = \underline{[S]} \underline{[W_s]} \quad \text{BLT equation} \quad (\text{I.2.48})$$

I.2.2.3.3 Applications of the PWB approach associated to the BLT formalism

This method was successfully employed in [Junqua et al., 2005] and [Junqua, 2010] to determine the mean power in several environments, such as building rooms, cavities in missiles, or avionic equipment casings. In every scenario, the mean power inside the N cavities of the system was determined with a good agreement up to 12 GHz. The resolution of this multi-cavity problem consists in solving a system of N linear equations and provides the mean power density in each cavity. It is possible to solve this problem by taking advantage of the software CRIPTE (developed at the ONERA)¹, which is a general purpose tool dedicated to solve topological problems. More recently, an open-source tool developed by the York university² was published to solve topological problems but it is specific to the PWB approach (it is not a general purpose tool).

A similar approach was proposed more recently by [Tait et al., 2011] where transmission ACS are determined for two configurations: nested reverberation chambers with aperture coupling and weapons bays in a fighter aircraft.

I.2.2.3.4 Experimental determination of absorption cross sections (ACS)

In a recent work [Flintoft et al., 2016], a method has been proposed to assess the shielding effectiveness of enclosures. As the shielding performances rely on how much the inner elements of enclosures absorb energy, it is valuable to assess the ACS of these elements, and especially for PCB or PCB stackings. Two electromagnetic environments have been identified. The internal environment consists in an enclosure with PCB, which is itself placed into a mode-stirred chamber which represents the external environment.

¹<https://www.onera.fr/fr/valorisation/moyens> CRIPTE: Calcul sur Réseaux des Interactions Perturbatrices en Topologie Electromagnétique.

²<https://bitbucket.org/uoyaeg/aegpwb/src> AEGPWB: An open-source electromagnetic power balance toolbox and solver.

To assess the average power densities S_i and S_e for both environments, one needs to quantify the **ACS** of all the loss mechanisms in the system. The equivalent circuit based on the **PWB** method is shown in Fig. I.2.10b. **ACS** are defined to describe each loss mechanism, and are listed as:

- $\langle \sigma_{e;w}^a \rangle$ are the average losses in the internal walls of the enclosure;
- $\langle \sigma_{i;w}^a \rangle$ are the average losses in the interior walls of the cavity;
- $\langle \sigma_{\text{PCB}}^a \rangle$ are the losses in the **PCB**;
- $\langle \sigma_{e;\text{Tx}}^a \rangle$, $\langle \sigma_{i;\text{Tx}}^a \rangle$, $\langle \sigma_{e;\text{Rx}}^a \rangle$ and $\langle \sigma_{i;\text{Rx}}^a \rangle$ are the average losses of the antennas in the two regions when they are receiving or emitting power;
- $\langle \sigma^t \rangle$ is the total **ACS** that represents the apertures on the internal enclosure faces;
- $\langle \sigma_{e;\text{env}}^a \rangle$ are the losses in the **mode-stirred chamber (MSC)**.

The injected power in antennas placed in the interior and exterior environments are referred as $P_{e;\text{Tx}}^t$ and $P_{i;\text{Tx}}^t$ respectively.

Then, the electromagnetic environments are solved by applying classical electrical theorems (THÉVENIN, NORTON and MILLMAN using the equivalences (I.2.37), (I.2.38) and (I.2.39)). The average power densities inside (S_i) and outside (S_e) the enclosure are computed as:

$$\begin{pmatrix} S_e \\ S_i \end{pmatrix} = \frac{1}{\Delta} \begin{pmatrix} \langle \sigma_i^a \rangle + \langle \sigma^t \rangle & \langle \sigma^t \rangle \\ \langle \sigma^t \rangle & \langle \sigma_e^a \rangle + \langle \sigma^t \rangle \end{pmatrix} \begin{pmatrix} P_e^t \\ P_i^t \end{pmatrix} \quad (\text{I.2.49})$$

with $\Delta = (\langle \sigma_e^a \rangle + \langle \sigma^t \rangle)(\langle \sigma_i^a \rangle + \langle \sigma^t \rangle) - (\langle \sigma^t \rangle)^2$ and where $\langle \sigma_i^a \rangle = \sum_j \langle \sigma_{i;j}^a \rangle$ and $\langle \sigma_e^a \rangle = \sum_j \langle \sigma_{e;j}^a \rangle$.

To solve (I.2.49), $\langle \sigma_{\text{PCB}}^a \rangle$ has to be determined. It was decided to measure it and an experimental set-up was created. $\langle \sigma_{\text{PCB}}^a \rangle$ is obtained by a double weighing operation. First, the board was installed inside a **MSC** with two monopole antennas mounted on the panels of the chamber. The scattering matrices S^{loaded} were then measured for numerous stirrer positions. Secondly, the board was removed from the cavity and another set of matrices S^{unloaded} was acquired. The **ACS** was then computed like:

$$\langle \sigma_{\text{PCB}}^a \rangle = \frac{\lambda^2}{8\pi} \eta_1^T \eta_2^T \left(\frac{1}{\langle |S_{21}^{\text{loaded}}|^2 \rangle} - \frac{1}{\langle |S_{21}^{\text{unloaded}}|^2 \rangle} \right) \quad (\text{I.2.50})$$

where $\eta_{1,2}^T$ are the efficiency of the two monopole antennas, and $\langle \cdot \rangle$ is the average operator.

23 boards were considered in that study, sorted into the four following categories:

- the board presents a shielded surface that covers the whole **PCB**;
- the board presents a ground plane on one side;
- the board is densely filled with components;
- the board is a compound one consisting of two boards attached together by a spacer.

The authors measured the **ACS** $\langle \sigma_{\text{PCB}}^a \rangle$ for each of these categories, and they concluded that the more densely the components are on the board, the more they absorb energy, thus the higher the **ACS** are.

As a second step, a stacking of N_{PCB} **PCBs** was considered and a model to assess the global **ACS** $\langle \sigma_{\text{stack}}^a \rangle$ was proposed. Two scalar shadowing factors, $\overleftarrow{\gamma}_{\text{shad}}^i$ for the bottom side and $\overrightarrow{\gamma}_{\text{shad}}^i$ for the top

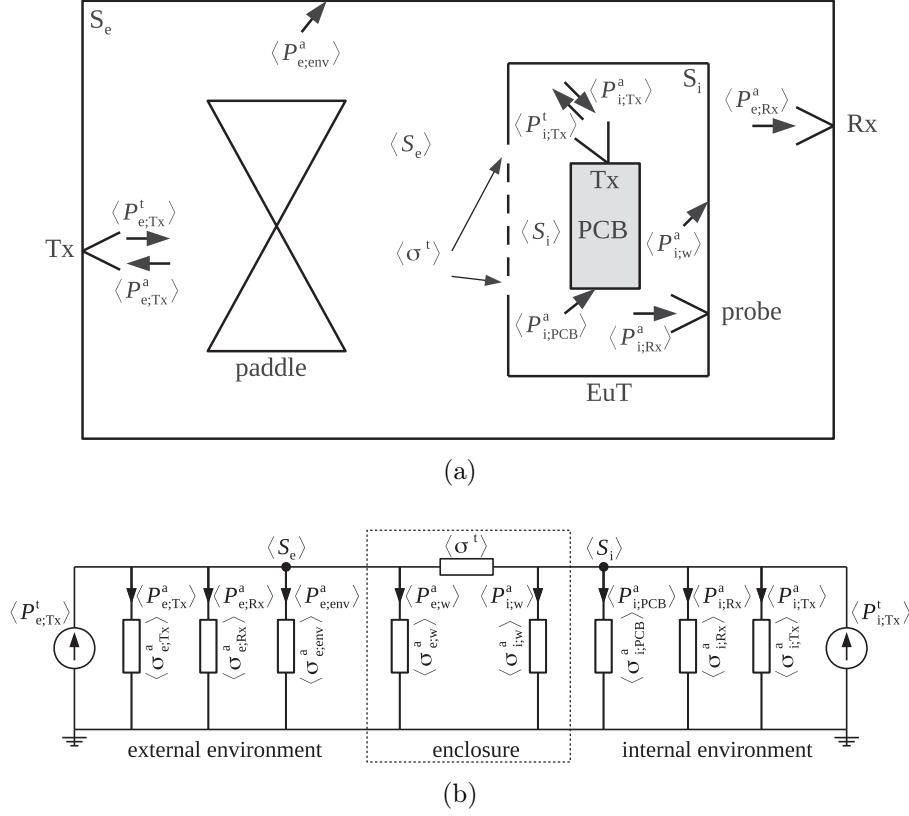


Fig. I.2.10 – The studied configuration (a) in [Flintoft et al., 2016] and its power balance (PWB) model (b), © [2016] IEEE.

side, model the shadowing effects for the i th-PCB in the stacking. These factors should stay within the 0 and 1 range. It leads to the following formula:

$$\langle \sigma_{stack}^a \rangle = \frac{1}{2} \sum_{i=1}^{N_{PCB}} (\overleftarrow{\gamma}_{shad}^i + \overrightarrow{\gamma}_{shad}^i) \langle \sigma_i^a \rangle \quad (I.2.51)$$

where $\langle \sigma_i^a \rangle$ is the ACS of the i th-board in isolation. Equation (I.2.51) reduces to $\langle \sigma_{stack}^a \rangle = \langle \sigma^a \rangle (1 + (N-1)\gamma_{shad})$ when all the stacked boards are identical. While imposing $\overleftarrow{\gamma}_{shad}^{bottom\ board} = \overrightarrow{\gamma}_{shad}^{top\ board} = 1$, *i.e.* no shadowing effects occur on the outer PCB sides of the stacking (upper face of the top board and lower face of the bottom board), it is expected that the following inequality holds:

$$\langle \sigma^a \rangle \leq \langle \sigma_{stack}^a \rangle \leq N_{PCB} \langle \sigma^a \rangle \quad (I.2.52)$$

Several measurements were conducted to determine γ_{shad} for stackings of N_{PCB} boards ($N_{PCB} \in [2, 4]$) with a high component density on each side and a low proportion of shielded surface. It was highlighted that γ_{shad} is in the $[0.6, 0.8]$ range. Thus, the absorbed energy for that configuration is between 20 % and 40 % less than N_{PCB} times the amount of energy absorbed by one board.

This work was extended in [Parker et al., 2016a] where the changes of the ACS when a PCB was placed in the vicinity of the enclosure walls were studied. A PCB with components on a single side was considered first. The authors concluded that, for a PCB placed parallel to a wall, while the components are not facing that wall, the ACS does not change much when the distance from the wall to the board varies. However, when the components face the wall, the ACS may be reduced up to 30 % compared to

the case where the boards are located at the center of the [MSC](#) working volume. One can also notice the work published in [\[Carlberg et al., 2004\]](#) where the [ACS](#) of canonical shapes were determined. These [ACS](#) were obtained from full-wave simulations (the [MoM](#) and [FDTD](#) method were used), and validated by a set of measurements.

I.2.2.4 Power balance approach combined with the random matrix theory

A [PWB](#) approach was applied in [\[Kovalevsky et al., 2014, 2016\]](#) and associated to the [random matrix theory \(RMT\)](#). The aim was to determine couplings between two cavities linked by an aperture. The output quantities were the averaged energies U_i in each i th-cavity. An equivalent equation close to [\(I.2.49\)](#) was derived. For an overmoded cavity, the modal density n_i is [\[Hill, 2009\]](#):

$$n_i = \frac{8\pi f^3 V_i}{3c^3} = \frac{V_i \omega^3}{3\pi^2 c^3} \quad (\text{I.2.53})$$

where V_i is the cavity volume. The power flow between two cavities coupled by an aperture is [\[Junqua et al., 2007\]](#):

$$\begin{pmatrix} \frac{\omega}{Q_{12}} n_1 & -\frac{\omega}{Q_{12}} n_1 \\ -\frac{\omega}{Q_{21}} n_2 & \frac{\omega}{Q_{21}} n_2 \end{pmatrix} \begin{pmatrix} \frac{U_1}{n_1} \\ \frac{U_2}{n_2} \end{pmatrix} = \begin{pmatrix} P_{12} \\ P_{21} \end{pmatrix} \quad (\text{I.2.54})$$

where, by reciprocity implications $\frac{Q_{12}}{n_1} = \frac{Q_{21}}{n_2}$.

Losses in the i th-cavity were characterized by a quality factor Q_i . The dissipated power at the angular frequency ω was expressed as in [\(I.2.32\)](#) which became for a two-cavities network as:

$$\begin{pmatrix} \frac{\omega}{Q_1} n_1 & 0 \\ 0 & \frac{\omega}{Q_2} n_2 \end{pmatrix} \begin{pmatrix} \frac{U_1}{n_1} \\ \frac{U_2}{n_2} \end{pmatrix} = \begin{pmatrix} P_{d_1} \\ P_{d_2} \end{pmatrix} \quad (\text{I.2.55})$$

From the [PWB](#) equilibrium equation [\(I.2.31\)](#) which states that the average input power of the i th-cavity $P_{i,\text{in}}$ is balanced by the power transferred from the others cavities P_{ij} and by its dissipated power P_{d_i} , thus: $P_{d_i} + P_{ij} = P_{i,\text{in}}$. For a two-cavities network, this leads to the following matricial formulas:

$$\begin{pmatrix} P_{d_1} \\ P_{d_2} \end{pmatrix} + \begin{pmatrix} P_{12} \\ P_{21} \end{pmatrix} = \begin{pmatrix} P_{1,\text{in}} \\ P_{2,\text{in}} \end{pmatrix} \quad (\text{I.2.56})$$

$$\begin{pmatrix} \frac{\omega}{Q_1} n_1 + \frac{\omega}{Q_{12}} n_1 & -\frac{\omega}{Q_{12}} n_1 \\ -\frac{\omega}{Q_{21}} n_2 & \frac{\omega}{Q_2} n_2 + \frac{\omega}{Q_{21}} n_2 \end{pmatrix} \begin{pmatrix} \frac{U_1}{n_1} \\ \frac{U_2}{n_2} \end{pmatrix} = \begin{pmatrix} P_{1,\text{in}} \\ P_{2,\text{in}} \end{pmatrix} \quad (\text{I.2.57})$$

From the [RMT](#), the average energy in cavities may be statistically described ([\[Langley and Cotoni, 2005\]](#)). Especially, the variance of $\frac{U_i}{n_i}$ can be determined from the [RMT](#) ([\[Kovalevsky et al., 2014\]](#)). Further information will be exposed later in this dissertation about the benefit of this theory to estimate couplings in cavities. Another interesting part of this work ([\[Kovalevsky et al., 2014\]](#)) is related to the determination of the quality factors Q_{ij} , expressed as $Q_{ij} = \frac{4\pi V_i}{\lambda \langle \sigma_{\text{Aperture}} \rangle}$ [\[Hill, 2009\]](#). The [ACS](#) $\langle \sigma_{\text{Aperture}} \rangle$ of the aperture was computed from an aperture impedance [\[Levine and Schwinger, 1950\]](#). Finally, Q_{ij} was determined from experimental acquisitions and for two cavity sizes (up to 7 GHz).

I.2.2.5 Full [BLT](#) application

The problem of an outer field that couples onto an aperture cavity was addressed in [\[Park et al., 2009\]](#), to determine the surface current on a wire inside the cavity by using the [BLT](#) formalism. Propagation phenomena were included in this study by applying the initial formulation of the [BLT](#). Four coupling mechanisms, bound with junctions were determined. The first (1) one was due to the

free-space propagation towards the aperture, then (2) the aperture was represented by an equivalent magnetic current distribution at its location. Two other mechanisms were set up in parallel to analyze the scattered field in the cavity. First, (3) the POCKLINGTON's equation [Balanis, 2016, Chap. 8.3.1] was used to compute the surface current on the wire from the electric field in the cavity, and secondly (4) the scattered field in the enclosure was obtained from GREEN's functions. The authors proposed a comparison with a full-wave simulation (FDTD) from 1 GHz to 6 GHz and for an enclosure size of 10 cm × 10 cm × 15 cm. As the cavity was relatively small with regard to the frequency, only a few eigenmodes were considered.

I.2.2.6 Methods based on full-wave simulations

The problem explored in [Lecointe et al., 1992] was evaluated by a full-wave based simulation method in [Carpes et al., 2002]. In [Lecointe et al., 1992], the goal was to determine the coupling between a small aperture and a wire inside a cavity using an analytical method (use of the GREEN's functions and electric and magnetic dipoles of the aperture, refer to I.2.2.1.2). Here, the finite element method (FEM) (in time and frequency domains) method was employed. The simulation results were compared to experimental results with good agreement. However, only small apertures were considered in this study.

The work presented in [Siah et al., 2003] allows to consider apertures of different sizes and shapes (rectangular, slots, circles, etc.). Its goal was to maximize the shielding effectiveness of common casings in the automotive industry, while keeping a good ventilation in the equipment. The studied cavity dimensions were 30 cm × 12 cm × 30 cm and the surface of the aperture was up to 20 cm × 3 cm. Simulation results were obtained from the multilevel fast multipole method (MFMM) combined with the MoM. That combination allowed to consider larger structures while reducing the memory and CPU usage. Several simulations were run, and some guidelines were raised for the problem.

I.2.2.7 Statistical methods

Statistical methods able to take into account apertures are all related to the random coupling model (RCM) that will be later extensively exposed (see section III.2.2). A brief abstract is now proposed. In this model, the interactions between the ports (cables, PCB, etc.) are modeled by the impedance matrix $\underline{\underline{Z}}^{\text{cav}}$ in a chaotic system. Two behaviors are combined in the RCM, defined by two impedance matrices $\underline{\underline{Z}}^{\text{rad}}$ and $\underline{\underline{\xi}}$. The first one represents the system without the boundary conditions that make it reverberant, *i.e.* in a free-space environment. The latter, included in $\underline{\underline{\xi}} = -\frac{j}{\pi} \underline{\underline{W}} [\underline{\underline{\lambda}} - j\alpha \underline{\underline{1}}]^{-1} \underline{\underline{W}}^T$, models the reverberant part of the system. The random matrix $\underline{\underline{\lambda}}$ includes the eigenmode spectrum of the system and $\underline{\underline{W}}$ models the coupling between eigenmodes and ports. Finally, the losses are included in the frequency-dependent factor α . $\underline{\underline{Z}}^{\text{cav}}$ is obtained by [Zheng et al., 2006a]:

$$\underline{\underline{Z}}^{\text{cav}} = j\Im \left\{ \underline{\underline{Z}}^{\text{rad}} \right\} + \left[\Re \left\{ \underline{\underline{Z}}^{\text{rad}} \right\} \right]^{1/2} \underline{\underline{\xi}} \left[\Re \left\{ \underline{\underline{Z}}^{\text{rad}} \right\} \right]^{1/2} \quad (\text{I.2.58})$$

MONTÉ-CARLO iterations, where random matrices $\underline{\underline{\xi}}$ are generated, allow to compute statistical quantities. Then, currents or voltages at ports can be estimated.

As the RCM is a circuit model, the aperture is modeled as an impedance. Two formulations are available in the literature, both of them for rectangular apertures. The first approach was presented in [Caudron et al., 2010] and [Caudron, 2012] where the problem of the coupling between an aperture and a monopole placed inside a computer chassis was considered. The BABINET's principle expressed for impedances was applied to determine the impedance of the aperture (see sections I.2.2.1.1 and III.2.2). Another formulation of the aperture impedance was proposed in [Antonsen et al., 2011] (see section III.2.3 for more details). The incident electric and magnetic fields were projected onto a basis of

N modes TE_{n0} . This impedance is then mapped to the cavity using the MoM as exposed in [Harrington and Mautz, 1976].

I.2.2.8 Conclusion

Several formalisms have been exposed to describe the coupling of a plane wave to an aperture. Some of them determine the electric shielding effectiveness (as methods related to the ROBINSON circuit model), others deal with the electromagnetic environment like power density in enclosure (PWB approach), while some study voltage or current (as seen in the RCM).

Methods to determine couplings from apertures are strongly related to their size (regarding the wavelength). Small ones may be considered through the BETHE's theory of diffraction. Apertures are substituted by elementary magnetic and electric dipoles expressed from their polarizabilities [Butler et al., 1978, Collin, 1991]. On the other side, electrically large apertures may be considered from a geometrical optics standpoint with good approximations [Balanis, 2012, chap. 13].

Apertures within the order of magnitude of the wavelength of interest, are much more difficult to describe. One can take advantage of full-wave simulations while accepting a high computation cost. Other solutions require the application of the HUYGENS's equivalence principle, to determine magnetic current density at the aperture location [Harrington and Mautz, 1976]. Some methods are based on the BABINET's principle [Caudron, 2012, Konefal et al., 2005].

I.2.3 Electromagnetic couplings within a cavity

I.2.3.1 Analytical methods by use of the GREEN's functions

Analytical methods have been proposed in the literature and mostly rely on the computation of the GREEN's functions of rectangular cavities. The electric field \vec{E} at location \vec{r} is given by:

$$\vec{E}(\vec{r}) = j\omega\mu \iiint_{V'} \underline{\underline{\mathbf{G}}}(\vec{r}, \vec{r}') \vec{J}_e(\vec{r}') d\vec{r}' \quad (\text{I.2.59})$$

where \vec{r}' is the source location, $\vec{J}_e(\vec{r}')$ the electric current density, and V' is the volume where the sources are set. The computation of the GREEN's function $\underline{\underline{\mathbf{G}}}$ is not an easy task. Efficient methods to compute this function are given in [Park et al., 1998], [Wu and Chang, 1988] and [Marliani and Ciccolella, 2000].

A closed-form formulation of the coupling between Hertzian dipoles and transmission lines placed in a cavity is proposed in [Spadacini et al., 2005]. In addition to the GREEN's function of the cavity, the AGRAWAL's method [Agrawal et al., 1980] was used to determine the current on the transmission line (see below, section I.2.4). The results were compared to a full-wave FIT simulation. The same problem was addressed in [Tkachenko et al., 2013], but for a symmetric geometry with regard to the transmission line placed in the cavity. In doing so, the computation of the GREEN's function is simplified. More recently, in [Boutar et al., 2015], a similar configuration was considered, and two sub-models were expressed. A small monopole was used as a source. The sub-model was relative to the cavity, and the electric field emitted inside the cavity was computed from an ad-hoc GREEN's function. Then, the transmission line was modeled in free-space as a Π -equivalent circuit. These two sub-models were linked together by adding voltage sources on the equivalent circuit, defined by the AGRAWAL's model [Agrawal et al., 1980].

For all these formulations, neither the re-radiation of the transmission line is taken into account, nor the direct coupling between the source and the transmission line. In addition, these formulations are unworkable if the shape of the cavity is too complex.

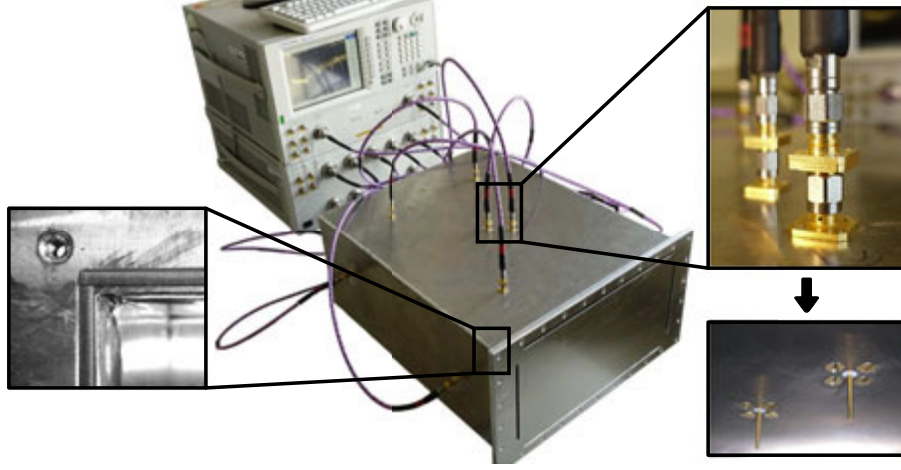


Fig. I.2.11 – Cavity used to test simulation in [Vogt et al., 2015], © [2015] IEEE.

I.2.3.2 Statistical methods

The aim of the VOGT's work ([Vogt, 2016]) was to analyze the electromagnetic interferences between several monopoles in a computer chassis mock-up. The mock-up was 20 cm wide, 61 cm deep and 40 cm high. These dimensions were comparable to those of commercial computer chassis. A set of 12 monopoles were randomly distributed on the walls of the cavity, and the interactions between them were modeled. As there was no anisotropic materials in the cavity, interaction between monopoles i and j was the same as between monopole j and i . Several models were provided, one of them was analytical and relied on source stirring, the other one was a full-wave simulation based model.

The analytical model was based on the GREEN's function of the cavity to determine the coupling. The mutual impedance between two monopoles of length l_i and l_j was given by the following formula [Gronwald, 2006, eq. 3.185]:

$$Z_{ij} = \frac{j\omega\mu l_i}{2k \sin(kl_j/2)} [G_{zz}^A(\vec{r}_j, \vec{r}_i + l_i/2\vec{e}_z) - G_{zz}^A(\vec{r}_j, \vec{r}_i - l_i/2\vec{e}_z) - 2 \cos(kl_i/2) G_{zz}^A(\vec{r}_j, \vec{r}_i)] \quad (\text{I.2.60})$$

where the GREEN's function of an empty cuboid is given by:

$$G_{zz}^A(\vec{r}, \vec{r}') = \sum_{m=1}^{\infty} \sum_{n=1}^{\infty} \sum_{p=0}^{\infty} \left[\frac{\epsilon_{0p}}{l_x l_y l_z} \frac{\sin(k_x x) \sin(k_x x') \sin(k_y y) \sin(k_y y') \cos(k_z z) \cos(k_z z')}{k_x^2 + k_y^2 + k_z^2 - k^2} \right] \quad (\text{I.2.61})$$

where $k_x = \frac{m\pi}{l_x}$, $k_y = \frac{n\pi}{l_y}$ and $k_z = \frac{p\pi}{l_z}$. ϵ_{0p} is the NEUMANN such as:

$$\epsilon_{0p} = \begin{cases} 1 & \text{if } p = 0 \\ 2 & \text{otherwise} \end{cases} \quad (\text{I.2.62})$$

(I.2.61) was not directly computed as it has a convergence issue when \vec{r} was close to \vec{r}' . The EWALD's formulation may be used [Gronwald, 2006] to overcome this problem. Moreover, to compute the scattering matrix $\underline{\underline{S}}$ from the impedance matrix $\underline{\underline{Z}}$, all the matrix elements of $\underline{\underline{Z}}$ need to be determined. As I.2.61 presents also a convergence problem when the source \vec{r} is to close the observation point \vec{r}' , an ad-hoc circuit model is provided for the on-diagonal elements of $\underline{\underline{Z}}$.

The second model was based on the MoM with the implementation of hierarchical \mathcal{H} -matrices which allowed to reduce the memory use. This particular implementation was not provided to the community.

Measurements are performed on the mock-up by using a 12 ports [vector network analyzer \(VNA\)](#). The acquired scattering matrix was compared with both the analytical model and the implementation of the [MoM](#) with \mathcal{H} -matrices. The computation time was given for the [MoM](#) method and for several frequencies. At 3 GHz, the computation time was 5.2 min and 63 min at 6 GHz on a modern computer. As the [MoM](#) is a frequency solver, one simulation needs to be run per frequency (unlike with the [FDTD](#) method for example). As a comparison, a [FEM](#) based simulation was performed and leads to a computation time of 3.5 min at 3 GHz and by a higher [random access memory \(RAM\)](#) usage cost.

Finally, a statistical analysis was performed using source stirring. The 5% and 95% percentiles were computed from the 66 interactions between the monopoles ($\frac{12 \times 11}{2}$). Three different frequency-dependant behaviors were then identified. The first behavior was corresponding to frequency bands where the eigenmodes can be clearly separated ($f < 2.5$ GHz). The second behavior concerns a frequency band ($f > 3.5$ GHz) where the couplings were considered as noise (the cavity was in an overmoded regime). The third region, between 2.5 GHz and 3.5 GHz was a transition region.

In [\[Vogt et al., 2015\]](#), the cavity was populated with simple elements that could represent parts found in computers, like [PCBs](#) or heat sinks. [PCBs](#) were modeled as simple conducting planes, and heater sinks as conducting boxes. The formulation of the [MoM](#) was updated with that new problem. Again, a comparison between the simulation and measurements allowed to validate the new model. No information was given about the computation cost of this model.

Couplings between monopoles in a real computer and in a 19-inches server were provided as measurement results but no comparison with simulations was given.

I.2.3.3 Hybrid circuit methods

A hybrid circuit method was proposed by [\[Lange and Leone, 2017\]](#). Again, coupling between two monopoles was considered inside a cavity. First, the eigenmodes of the cavity were determined thanks to an eigenmode solver. The N first eigenmodes were such that $f_{\max} < \frac{k_N c}{2\pi}$, with f_{\max} the maximal frequency to consider for the analysis, and k_N the wavenumber associated to the N^{th} cavity eigenmode. The mutual impedance between the two ports is [\[Gronwald, 2006\]](#):

$$Z_{ij} = -\frac{1}{I_j I_i^*} \langle \vec{E}_j, \vec{J}_i^* \rangle \quad (\text{I.2.63})$$

where I_i and I_j are the currents that flow into the two ports. \vec{E}_j is the electric field generated by the j^{th} -port and \vec{J}_i is the current density along port i . Ports were monopoles here. The electric field in the cavity was expanded as a sum over the eigenmodes of the cavity and was split into two terms. A solenoidal part \vec{E}_n (with zero divergence) and an irrotational part \vec{F}_n (with zero curl) from an HELMHOLTZ decomposition:

$$Z_{ij} = \frac{j\omega\mu}{I_j I_i^*} \sum_{n=0}^{\infty} \frac{\langle \vec{E}_n, \vec{J}_j \rangle \langle \vec{E}_n, \vec{J}_i^* \rangle}{(k_n^2 - k^2) \kappa_{E,n}} - \frac{j}{\omega \epsilon I_j I_i^*} \sum_{n=0}^{\infty} \frac{\langle \vec{F}_n, \vec{J}_j \rangle \langle \vec{F}_n, \vec{J}_i^* \rangle}{\kappa_{F,n}} \quad (\text{I.2.64})$$

where $\kappa_{E,n}$ and $\kappa_{F,n}$ are two constants.

Equation (I.2.64) was then modeled as a passive FOSTER-type equivalent circuit [\[Foster, 1924\]](#), and a SPICE solver was used to determine the coupling.

Two configurations were tested against full-wave simulations, both frequency (up to 1.2 GHz) and time analysis were provided. The full procedure required a computation time of ≈ 40 min for $N = 53$ eigenmodes (on a recent powerful computer).

Another hybrid formation was proposed in [\[Xiao et al., 2016\]](#) where reverberant environments were studied. Two nested cavities were considered, and a [PCB](#) with a transmission line was placed

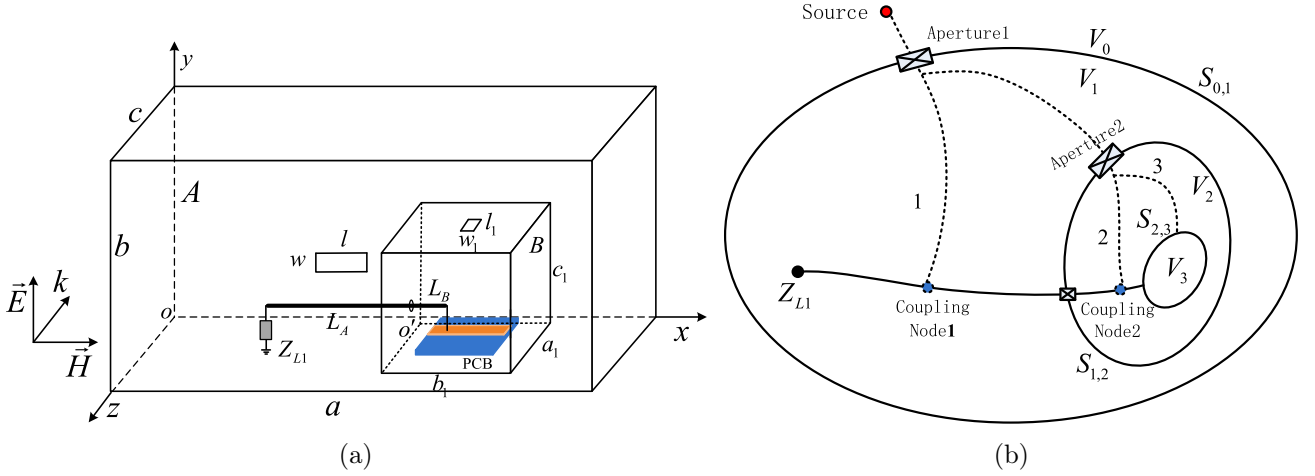


Fig. I.2.12 – Studied configuration I.2.12a and topological representation of configuration I.2.12b of the study [Xiao et al., 2016], © [2016] IEEE.

in the inner cavity. The outer cavity dimensions were $30\text{ cm} \times 12\text{ cm} \times 30\text{ cm}$, and the inner ones were $9\text{ cm} \times 6\text{ cm} \times 6\text{ cm}$. These two cavities had a common aperture. A coaxial cable connected the transmission line to a load placed inside the outer cavity through the aperture (see Fig. I.2.12a). The purpose of this work was to provide the voltage at one edge of the transmission line when the outer enclosure was illuminated by an electromagnetic field (up to 2 GHz).

At first, the problem was modeled as a topological network by use of the BLT formalism (Fig. I.2.12b) and the couplings are determined by application of the AGRAWAL's method [Agrawal et al., 1980]. Then, the field was computed by full-wave simulation (where the cable and the microstrip transmission line are removed) and was injected into the BLT set of equations. No information about the type of solver involved was provided.

The method was compared to full-wave simulations with all the details (a TLM solver was used). This comparison shows that not every resonance is considered by the hybrid method, however the order of magnitude was satisfactory. The computation time was reduced by 6.5 in comparison to the full-wave simulation with all the details.

I.2.4 Electromagnetic field to conductors couplings

Along this review, several studies have applied the TAYLOR's method to determine the voltage or the current impressed by the coupling of an electromagnetic perturbation onto a transmission line composed of a wire and a ground plane spaced by distance h .

Its formulation derives from the Telegrapher's equation where elementary sources (that are determined from the nearby electromagnetic field) are added all along the transmission line. Fig. I.2.13 depicts the transmission line circuit model with the added sources. The two integro-differential equations that need to be solved are:

$$\frac{dV(x)}{dx} + j\omega L' I(x) = -j\omega \int_0^h B_y^e(x, 0, z) dz \quad (\text{I.2.65})$$

$$\frac{dI(x)}{dx} + j\omega C' V(x) = -j\omega C' \int_0^h E_z^e(x, 0, z) dz \quad (\text{I.2.66})$$

where $V(x)$ is the voltage on the transmission line at position x , $I(x)$ is the current, C' and L' are the linear capacitance and inductance. The boundary conditions must be enforced at the ends of the

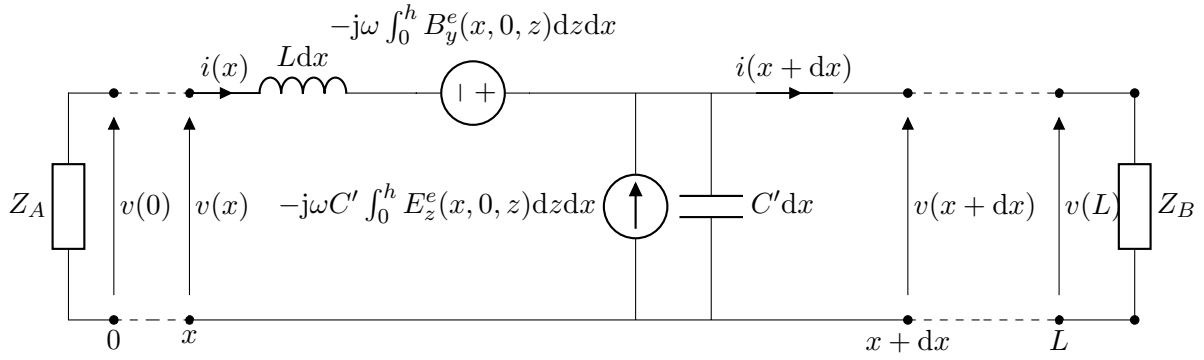


Fig. I.2.13 – [Taylor et al.](#) lossless model as presented in [\[Rachidi, 2012\]](#).

transmission line, which is terminated on impedances Z_A and Z_B , as:

$$V(0) = -Z_A I(0) \quad (\text{I.2.67})$$

$$V(L) = Z_B I(L) \quad (\text{I.2.68})$$

The electric field \vec{E}^e is the sum of the incident electric field \vec{E}^i and the ground-reflected field \vec{E}^r .

Two similar formulations were derived from the TAYLOR's one to determine $I(x)$ and $V(x)$:

- the AGRAWAL's method where only the component E_z of the field is needed [\[Agrawal et al., 1980\]](#);
- the RACHIDI's method where the components B_y and B_x are both needed [\[Rachidi, 2012\]](#).

I.2.5 Cavity regimes

Before drawing a conclusion and selecting methods that comply with the requirements, let us describe the different cavity regimes. These regimes are related to the eigenmode density within a cavity, and on its losses. The number of solutions to the HELMHOLTZ's equation increases with the frequency up to a point where, the eigenmodes overlap. Under that limit, the cavity is qualified as undermoded, and above as overmoded. The boundary between the two regimes is quite difficult to determine, and refers to the LUF (lowest usable frequency). Moreover, the higher the losses, the wider the eigenmodes are. Thus, the probability that an overlap occurs increases with the losses inside the cavity. [Fig. I.2.14](#) depicts, for a realistic cavity, a spectrum of the eigenmodes, versus the frequency, to illustrate such trends. The LUF is represented for an interval as there is no single definition for it.

For some problems, it is much easier to be confronted with an undermoded regime, and especially the one with none or just a few parameters (lengths, impedances, etc.). Whereas, for others, the overmoded regime is an asset.

Inside overmoded cavities, the field can be asymptotically described as an infinite superposition (a sum) of plane waves with random incidence and polarization, as stated by [\[Berry, 1977\]](#) and [\[Hill, 1998\]](#). This theoretical behavior may be practically obtained within a cavity by means of statistical models. The goal is to increase the number of modes having an effect at a given frequency. To do so, a possibility is to change the boundary conditions of the cavity and, thus, the set of eigenmodes. This may be accomplished by inserting an irregular metallic device, also known as stirrer. This stirrer can usually rotate and, for each position, a new set of eigenmodes is enforced. The infinite sum of plane waves representation of the fields is achieved over the ensemble average of numerous sets of eigenmodes.

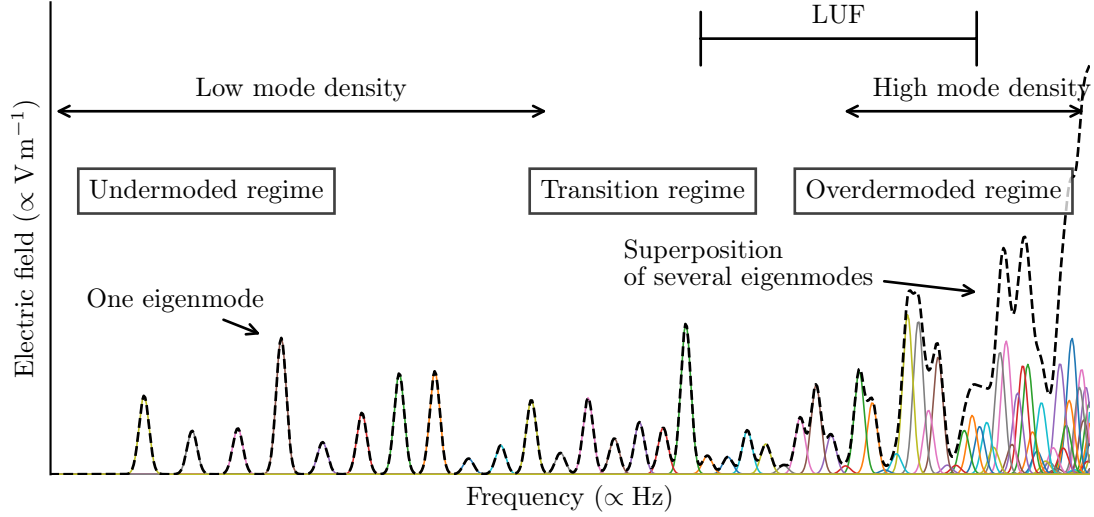


Fig. I.2.14 – Mode density within cavities versus frequency. Each curve corresponds to an excited eigenmode inside the cavity. The dashed black curve is the superposition of all the eigenmodes.

I.2.6 Conclusion

Very different approaches have been examined in this literature review. A comparison between the aforementioned methods is proposed in Table I.2.1. Analytical methods have been listed, and some of them are based on the GREEN's functions of the cavity to compute the internal field. These methods are strongly bound to the geometry of the cavity and do not allow to consider apertures [Tkachenko et al., 2013], [Boutar et al., 2015]. Some analytical circuit models allow to determine the shielding effectiveness, considering apertures of cavities with the assumption that they should remain unloaded (empty) [Robinson et al., 1998]. Another circuit model, the **random coupling model (RCM)**, is based on the theory of the random matrices [Caudron, 2012], [Antonsen et al., 2011]. By design, its goal is to determine couplings in reverberant environments with overlapping eigenmodes. The boundary conditions of the cavity are randomized, thus the output of the model are statistical quantities (probability density functions, quantiles, etc.). Full-wave simulation based models are widely adopted in the literature where mostly **MoM** solvers are implemented. The drawback of **MoM** methods is that one simulation needs to be run for each frequency of interest. Little coverage has been found regarding time-domain solvers like the **FDTD** method or the **FIT**, except in [Park et al., 2009] where the **FIT** is used as ground truth results for comparison. The advantage of time-domain solvers is that a wide frequency bandwidth is handled within a single simulation. The last class of methods combines several techniques and are named hybrid methods. Two of these can be highlighted. In [Lange and Leone, 2017], an eigenmode solver is coupled to a circuit model and, in [Xiao et al., 2016], **BLT** equations are combined with a full-wave solver.

I.2.7 Selection of approaches for the study of couplings inside cavities from an **EMSEC** perspective.

The need to determine coupling in reverberant environments is justified from an **EMSEC** point of view as explained in the previous chapter. An identified constraint is that the boundaries of the system may not be clearly characterized due to the fact that they may vary in the course of time or because the environment where the inner elements (like **PCBs**, cables, etc.) are integrated is unknown *a priori*. Such a configuration can correspond to a computer chassis inside which additional elements

are added over time, or when its internal components (cables, etc.) are not mechanically constrained nor constant over the time. One can also consider the early design stage of equipment (when its exact future casing shape is not determined yet) but the coupling between elements need to be assessed anyway. Additionally, the selected method needs to take into account an electromagnetic interference that couples to the cavity through apertures.

By determining couplings, we meant that [probability density functions \(PDFs\)](#) of coupled currents and voltages need to be determined, with randomized boundary conditions. From these values, one can determine the probability:

- that a radio front end becomes unavailable (remind section [I.1.3.2.3](#));
- to propagate information by means of polyglot signals (see section [I.1.3.1.4](#));
- that a covert channel is created by taking benefit from the susceptibility to conducted [EMI](#) of an electric component or a system (see section [I.1.3.3](#));
- that a voltage/current correlated to sensitive information reaches a threshold at which the confidentiality of information is not guaranteed anymore (TEMPEST threat, see section [I.1.3.1](#));
- that a component/system stops to work properly during an [IEMI](#) (section [I.1.3.2](#));
- etc.

To solve these problems, the plane waves superposition representation of the field inside an overmoded cavity (see section [I.2.5](#)) will be favourably used. If the boundary conditions are randomized, thus for each draw a new set of eigenmodes are enforced. By considering numerous random boundary conditions, and through an ensemble average of the field inside the cavity, the cavity of interest can be considered as overmoded. Thus, all the methods, that require that regime, apply.

Based on that analysis and from Table [I.2.1](#), several approaches may be rejected. All the methods where the cavity is empty are disqualified as there is no [EMSEC](#) applications for such cavity. It concerns all methods based on [\[Robinson et al., 1996\]](#), and all the methods that require to compute GREEN's functions of the cavity of interest such as [\[Park et al., 2009\]](#) and [\[Boutar et al., 2015\]](#).

The [PWB](#) approach is not restricted to a given cavity geometry, and is a statistical method. This method was applied already to study of the electromagnetic field attenuation between several rooms inside a building, or between the outside of a building and one room [\[Junqua et al., 2014a\]](#). Within that context, it is relevant for both [IEMI](#) and TEMPEST threats.

However, there is no straightforward mean to implement that method in order to obtain statistics of couplings, such as currents or voltages. The work of [\[Junqua, 2010\]](#) and [\[Flintoft et al., 2016\]](#) can thus be put aside regarding our issue.

One can notice that the two hybrid methods, [\[Lange and Leone, 2017\]](#) and [\[Xiao et al., 2016\]](#), rely on full-wave simulations. Thus, they are comparable, in terms of cost and resources, to full-wave simulation based methods.

Full-wave simulation based models are versatile and can be applicable to any geometry, assuming that it can be discretized. These methods seem appealing. From an [EMSEC](#) point of view (as well as from an [EMC](#) viewpoint), one does not limit the analysis to a unique frequency but a frequency bandwidth that could be large. Thus, all the methods based on frequency-domain solvers are not relevant (like [\[Vogt, 2016\]](#)).




Literature	Power balance model	Topological model	Circuit model	Statistical model	Fullwave simulation based model	Experimental model	Without geometry dependencies	Apertures taken into account	Mode density	Computation time
Robinson et al. [1996]			●				●	U		⊕
Siah et al. [2003]				●		●		U		⊕⊕
Park et al. [2009]		●				◐	◐	U		⊕⊕
Junqua [2010]	●	●		●		●	●	O		⊕
Caudron et al. [2010]			●	●		●	◐	O		⊕
Antonsen et al. [2011]			●	●		●	◐	O		⊕
Kovalevsky et al. [2014]	●			●		●	●	O		⊕
Boutar et al. [2015]			●				●	O		⊕
Vogt [2016]			●	◐	●	●		O&U		⊕⊕⊕
Xiao et al. [2016]		●			●	◐	●	U		⊕⊕⊕
Flintoft et al. [2016]	●			●		●		O		⊕
Lange and Leone [2017]			●		●			U		⊕⊕
Rabat et al. [2018]			●				◐	U		⊕
<div style="display: flex; justify-content: space-around; align-items: center;"> <div style="text-align: center;">  Types of models </div> <div style="text-align: center;">  Capabilities </div> <div style="text-align: center;">  Costs </div> </div>										

Table I.2.1 – Comparison between the reviewed methods. The models divided into six classes and three capabilities are listed. Half bullets ◐ denote limitations. U states for Undermoded environment and O for Overmoded environment. The cost column is related to the computation time.

Time-domain solvers are more suitable for wide bandwidth studies and few, if any, published work was related to the study of couplings within cavities. It thus seems interesting to investigate the applicability of time-domain solvers for our matter.

Finally, it appears that the method applied in [Caudron, 2012] and [Antonsen et al., 2011] associated to the RCM is able to model couplings within an enclosure and through apertures. Moreover, it integrates by design randomized boundary conditions. So, it was decided to investigate that method in detail as well. Notice that this method has not been applied for realistic applications for now.

Part II

Design and assessment of computer chassis models

Chapter II.1

Design of computer chassis models

Contents

II.1.1	Introduction	55
II.1.2	The simulation model	56
II.1.3	Design and production of a computer chassis mock-up	57
II.1.3.1	Spacing between screws and shielding gasket	57
II.1.3.2	Frequencies of the first modes and mode density	58
II.1.3.3	Study of the mock-up deformations	60
II.1.3.4	Shielding effectiveness determination of the mock-up	63
II.1.4	Design and production of devices to measure couplings	67
II.1.4.1	Simple printed circuit boards production	67
II.1.4.2	Determination of an accurate simulation model	69
II.1.5	Conclusion	71

II.1.1 Introduction

The state of the art related to the characterization of coupling in reverberant environments has shown that a full-wave simulation based model may be relevant to study that situation. As for any simulation model, it is necessary to set an accurate description of the given problem (3D model, software parameters, etc.). Moreover, the quality of the results obtained with the numerical model must be assessed, and that also requires a comparative model. The latter consists in a mock-up from which experimental data are acquired. As it is not possible to fulfill all the requirements that will be listed below with commercial off-the-shelf devices, it has been decided to design and to produce a mock-up.

Especially, a desktop computer chassis has been chosen, in order to model a widespread reverberant environment. Its dimensions are approximately the same as those of real ATX¹ computer chassis, *i.e.*, 170 mm large, 400 mm high and 440 mm deep, and its constitutive materials are similar as well. Furthermore, these two models, the simulation model and the mock-up, must be fitted with devices from which couplings can be obtained. Such devices should be typical of the inner elements of desktop computers, as PCBs. An acceptable solution is to replace these devices by simple transmission lines printed on circuit boards. It has been highlighted in the previous part that couplings need to be assessed for a wide frequency range up to tens of GHz. Measurement equipment available for this work allows to measure couplings up to 26.5 GHz. Both models must be valid for, at least, an

¹ATX (Advanced Technology eXtended) defines, *inter alia*, form factors for desktop computer elements (see ATX Specification Version 2.2).

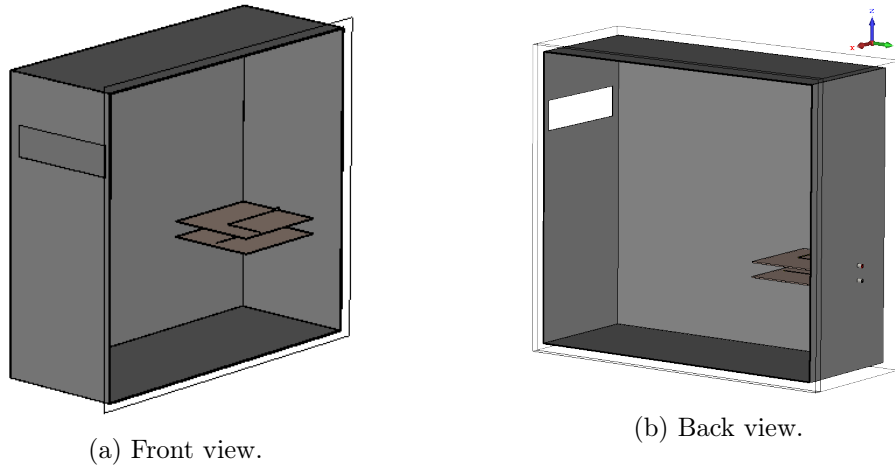


Fig. II.1.1 – 3D model of the computer chassis, with an aperture and two [PCBs](#).

electromagnetic study up to that frequency. Thus, the wavelengths that have to be considered in the making are longer than ≈ 1 cm.

As a consequence, two models have been worked out:

1. a simulation scheme that integrates a 3D model of a computer chassis and all the solver parameters;
2. a real computer chassis mock-up from which experimental data can be measured.

Several requirements have been raised for the two models. First, the simulation model needs to be easily modeled by means of a commercial simulation software. It is also required that the simulation should be run in an acceptable amount of time. Thus, the modeled structure should be described with a minimum of geometrical details and a minimum number of materials. Secondly, both models need to be versatile so that couplings for several configurations may be determined (location of apertures, inner elements, etc.). For the simulation model, this is not a constraint as the 3D model can easily be modified. For the mock-up it has multiple implications. The mock-up must have different exchangeable panels to be configured with an aperture size similar to a CD reader, (146.1 mm large and 41.3 mm high) at different heights on the front panel. On the back panel, three configurations will be available: a solid panel without any aperture, a panel with one aperture extended by a waveguide (in order to introduce a field probe) and one to offer the option to insert and hold [PCBs](#) inside the mock-up.

This chapter presents how these two models have been set up.

II.1.2 The simulation model

The commercial software [CST Studio Suite \(CST-SS\)](#), by Dassault Systèmes, offers general purpose solvers. It consists of three parts: a 3D modeler, a mesher and an electronic solver. As the study should cover a wide frequency range, a time-domain solver has been chosen. The resolution technique implemented in [CST-SS](#) for the time-domain solver is the [finite integration technique \(FIT\)](#). To speed up the computation, the thickness of the panels are set to zero. Thus the panels will not be meshed and their thickness will be set to their skin depths δ by [CST-SS](#). Fig. II.1.1 depicts the 3D model of the desktop computer chassis.

II.1.3 Design and production of a computer chassis mock-up

The computer chassis mock-up has been manufactured from 1 mm thick steel panels. The left, right, top and bottom sides have been welded together and define the main body of the mock-up. Front and back panels are attached to the main body of the chassis thanks to screws. These panels are screwed to two steel frames. Their purposes are to stiffen the mock-up, to fix the front and back panels, and to guarantee an electric continuity between the panel and the main body. Most of this mock-up was designed and prepared in the former Electronics and Electromagnetism Laboratory of Sorbonne University, but the welding had to be subcontracted. Fig. II.1.2 is a picture of the mock-up.

Positions and angles will be identified using the axis conventions given in Fig. II.1.3. The angles θ and φ define the incidence of plane waves. The origin of the axis is at the lower left corner of the mock-up. Moreover, as explained above, the mock-up allows to set several front panels that include apertures at different positions. Fig. II.1.3c identifies these positions on the front panel.

II.1.3.1 Spacing between screws and shielding gasket

The choice of the spacing between screws has an important impact on the overall shielding effectiveness of the mock-up. Indeed, between two consecutive screws a slit will appear (as shown in Fig. II.1.4), which will alter the shielding effectiveness. A very pessimistic assessment of the overall attenuation of panels attached with such assembly is given by the following expression [Mardiguian, 2014, p. 224]:

$$A_{\text{dB}} = 100 - 20 \log l - 20 \log F_{\text{MHz}} + 20 \log \left(1 + 2.3 \log \frac{l}{h} \right) + 30 \frac{d}{l} \quad (\text{II.1.1})$$

where l is the length of the slit, h its height and d its depth. The abacus shown in Fig. II.1.5 gives this attenuation for different slit lengths. As a compromise between attenuation and ease of manipulation, a spacing of 50 mm has been chosen. It leads to an lower attenuation limit of nearly 15 dB at 10 GHz.

To increase the shielding performances, an electric gasket is added. Its goal is to seal the slits between the main body of the mock-up and the two panels. The chosen gasket is made by Würth Elektronik and is specified to provide an attenuation larger than 80 dB between 100 MHz and 10 GHz. To be effective, it must be properly compressed. Fig. II.1.6 shows the gasket placement. Moreover, for reproducibility purposes, all the screws are tightened with a dynamometric screwdriver adjusted at a torque of 3 N m according to standards ¹.

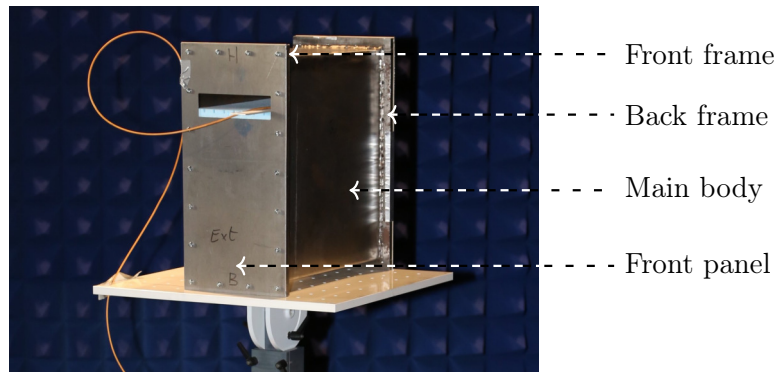


Fig. II.1.2 – Picture of the mock-up.

¹<http://www.norbar.com/Portals/0/NorbarProducts/catalogue/Pg6-10.pdf>

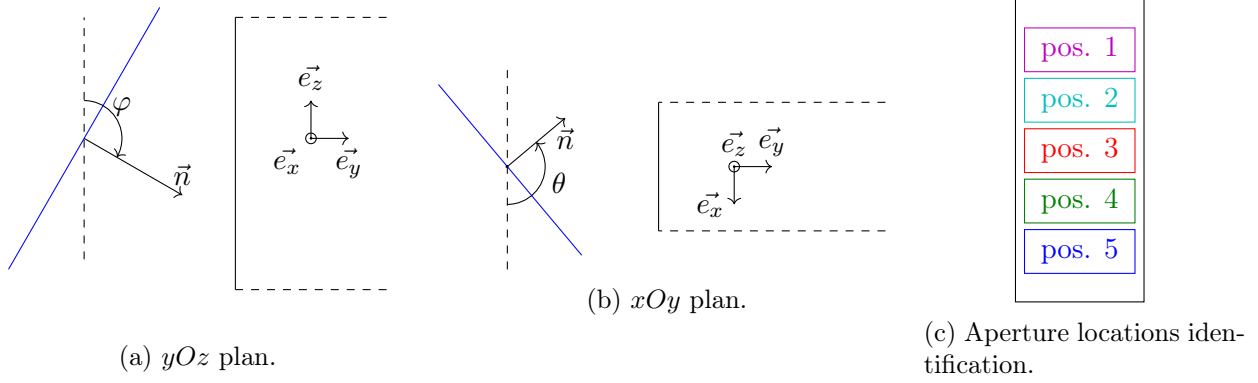


Fig. II.1.3 – Axis convention and aperture locations.

$f_{011} = 506.8 \text{ MHz}$	$f_{021} = 778.1 \text{ MHz}$	$f_{012} = 823.8 \text{ MHz}$	$f_{110} = 945.9 \text{ MHz}$
$f_{101} = 958.7 \text{ MHz}$	$f_{022} = 1.014 \text{ GHz}$	$f_{111} = 1.018 \text{ GHz}$	$f_{031} = 1.089 \text{ GHz}$
$f_{120} = 1.115 \text{ GHz}$	$f_{102} = 1.158 \text{ GHz}$	$f_{013} = 1.176 \text{ GHz}$	$f_{121} = 1.176 \text{ GHz}$
$f_{112} = 1.207 \text{ GHz}$	$f_{032} = 1.268 \text{ GHz}$	$f_{023} = 1.315 \text{ GHz}$	$f_{122} = 1.344 \text{ GHz}$
$f_{130} = 1.351 \text{ GHz}$	$f_{131} = 1.402 \text{ GHz}$	$f_{041} = 1.414 \text{ GHz}$	$f_{103} = 1.430 \text{ GHz}$

Table II.1.1 – Resonance frequencies of the first 20 cavity modes.

II.1.3.2 Frequencies of the first modes and mode density

It may be useful to determine the first modes, and the mode density in the mock-up. As it is a rectangular cuboid, its eigenfrequencies are given by [Besnier and Démoulin, 2013]:

$$f_{m,n,p} = \frac{1}{2\sqrt{\epsilon_0\mu_0}} \sqrt{\left(\frac{m}{a}\right)^2 + \left(\frac{n}{b}\right)^2 + \left(\frac{p}{d}\right)^2} \quad (\text{II.1.2})$$

where, m , n , and p are integers, ϵ_0 the vacuum permittivity and μ_0 the vacuum permeability. a is the width, b the depth and d the height of the mock-up. The 20 first eigenfrequencies are listed in table II.1.1.

The WEYL's formula [Liu et al., 1983] may be applied to determine the number of modes in the mock-up.

$$N_a(f) = \frac{8\pi V}{3} \left(\frac{f}{c}\right)^3 - (a + b + d) \left(\frac{f}{c}\right) + \frac{1}{2} \quad (\text{II.1.3})$$

where c is the speed of light in the vacuum, $V = abd$ the volume of the mock-up and f the frequency of interest. By differentiating (II.1.3), we can compute the mode density $D(f)$ in the mock-up:

$$D(f) = \frac{\partial N_a(f)}{\partial f} = 8\pi V \frac{f^2}{c^3} - \frac{a + b + d}{c} + \frac{1}{2}\delta(f) \quad (\text{II.1.4})$$

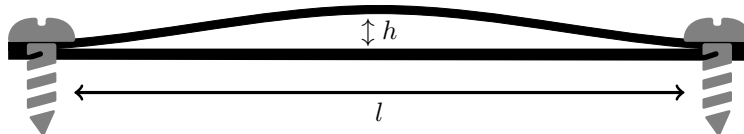


Fig. II.1.4 – Slit, of depth d , that may appear between two screws.

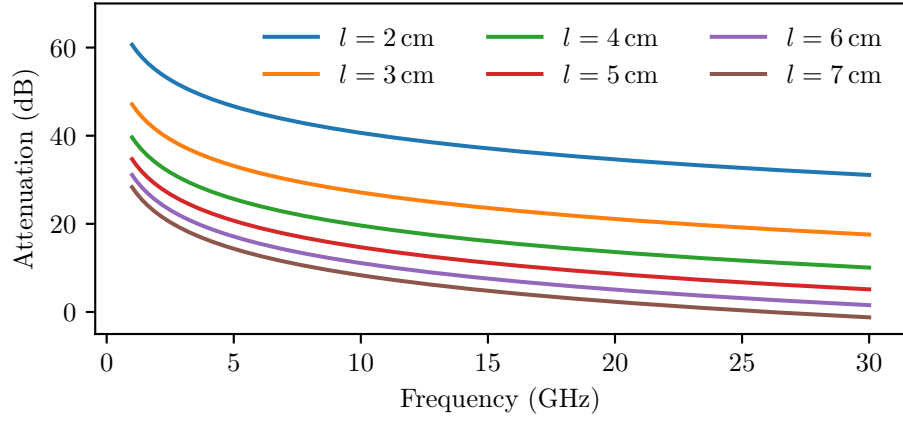
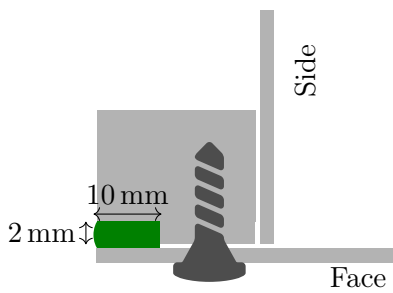


Fig. II.1.5 – Attenuation for different slit lengths from 1 GHz to 30 GHz.



(a) Schematic of the panel fixing method. The shielding gasket is in green and is compressed between the front (or back) panel and a groove in the frame.



(b) Front view of the mock-up's main body with the electric gasket along the edges of the frame and the uniformly distributed screw threads.

Fig. II.1.6 – Overview of the panel fixing method.

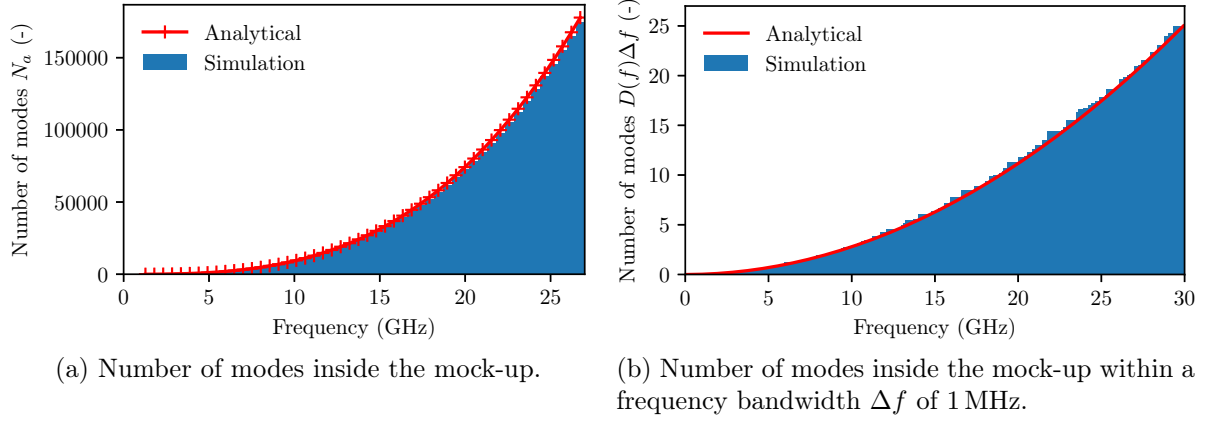


Fig. II.1.7 – Evolution, versus the frequency, of $N_a(f)$ and $D(f)\Delta f$ in the mock-up, computed from (II.1.3) and (II.1.4) and from histograms by use of (II.1.2) for numerous combinations of n, m, p .

Thus, the number of modes in a frequency bandwidth of Δf is: $D(f)\Delta f$. Fig. II.1.7 shows the number and the density (for $\Delta f = 1$ MHz) of modes in the mock-up.

A relevant quantity when dealing with reverberant environments, is the lowest frequency for which the cavity is considered overmoded. In this regime, the mode density is sufficiently high so that there are spectral overlaps between the eigenmodes. It depends on the volume V (see (II.1.3) and (II.1.4)) and on the quality factor of the cavity. In the literature, several statements allow to determine the lowest frequency f_{LUF} from which a cavity is overmoded [Bruns, 2005]. LUF means lowest usable frequency and is commonly used in the mode-stirred chambers community. These statements are:

- $f_{\text{LUF}} \in [3f_{\text{firstmode}}, 6f_{\text{firstmode}}]$: the first eigenfrequency of the mock-up is $f_{011} = 507$ MHz, thus $f_{\text{LUF}} \in [1.52 \text{ GHz}, 3.04 \text{ GHz}]$;
- at least 60 to 100 eigenmodes in the cavity: from (II.1.3) then we have $f_{\text{LUF}} \in [1.92 \text{ GHz}, 2.26 \text{ GHz}]$;
- a mode density of 1.5 modes per MHz: we solve $D(f_{\text{LUF}})1 \text{ MHz} = 1.5$, and we get $f_{\text{LUF}} = 7.34 \text{ GHz}$;

Other statements rely on measurements. However, field measurements at high frequencies require a complex and expensive measurement equipment that was not available for this work.

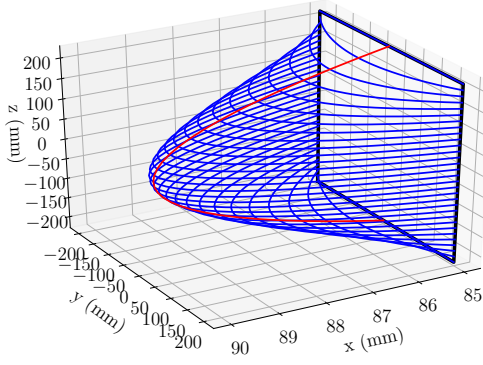
These definitions lead to a wide range of possible frequencies for the LUF:

$$f_{\text{LUF}} \in [507 \text{ MHz}, 7.34 \text{ GHz}] \quad (\text{II.1.5})$$

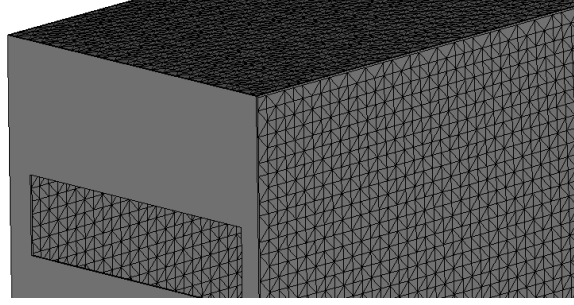
Another definition is related to the chaoticity of a cavity and relies on the comparison of the spacing between two consecutive eigenmodes of the cavity and the spacing between two consecutive eigenvalues of matrices from an appropriate ensemble. It is based on the random matrix theory, and will be discussed later (see Chapter III.1). In [Gros, 2014], this definition is used to determine the shape of a cavity such that it can be considered as chaotic. This work relied on eigenfrequencies computed by an eigenmode solver.

II.1.3.3 Study of the mock-up deformations

The welding of the side elements of the mock-up has created small deformations. We suspect that the mock-up has been warmed up too much during the welding process. A convex deformation appear on



(a) Deformation model of the mock-up's left side by arcs of ellipses. Note that the figure is not put to scale.



(b) Description of the mock-up by a set of triangles.

Fig. II.1.8 – Modeling of the deformation of the mock-up due to the welding.

the left and right sides, and a concave one on the top and bottom sides. As it was not possible to rectify these deformations, a study has been undertaken to assess their effects on the eigenfrequencies.

II.1.3.3.1 Model of the deformations

Eigenmode solvers are well suited for this issue but require a 3D model of the deformation. For the left and right sides, the maximum deformation d measured is around 3 mm and 2 mm for the top and the bottom sides. Accurately modeling the deformation is not an easy task and would require a complex procedure. Nevertheless, a first order estimate of the deformation may be the following one. It can be reasonably stated that the maximum of the deformation occurs at the center of a panel, and is symmetrical with the planes xOz and xOy for the right and left panels, and with the planes xOz and yOz for top and bottom panels. Moreover, the edges of the mock-up are not deformed. The deformation is then approximated by a set of arcs of ellipses, see Fig. II.1.8a. The red ellipse (located in the plane xOz) has a center that coincides with the mock-up center. Its semi-minor axis is $\frac{a}{2} + d$ and passes through the upper and lower edges of the panel. From this first ellipse a set of N ellipses (in blue) located within planes parallel to the plane xOy and passing through the red ellipse are determined. In commercial electromagnetic solvers (such as CST-SS) only simple geometries can be modeled. For more complex ones, it is necessary to create files that mesh the geometry as a set of triangles, and to finally import it in the commercial solver. The estimated deformation has been projected onto a $N_a \times N_b$ grid and $N_a N_b$ points have been computed. Then, by use of the library Python-STL a set of $2N_a N_b$ triangles was determined. It was chosen to set $N_a = 61$ and $N_b = 81$. It was stored into the STL format and finally imported in CST-SS (see Fig. II.1.8b).

Two meshing possibilities are available for the eigenmode: the tetrahedral mesh (triangle faces) and the hexahedral mesh (irregular orthogonal grid). As curvy shapes model the deformation, the tetrahedral mesh was chosen.

II.1.3.3.2 Simulation and results

It was chosen to take advantage of a general purpose solver: CST-SS. The eigenmode solver was configured to compute the first 20 modes of the cavity. As open boundaries are not supported by the eigenmode solver, the cavity has been sealed (*i.e.* without any aperture). For this study, the deformations are supposed to be symmetric (identical for opposite sides). The effects on left/right sides, and on top/bottom sides are studied separately. Tables A.1, A.2, A.3 and A.4 in appendix A list these 20 computed eigenfrequencies. The eigenfrequencies are associated to their mode mnp for the

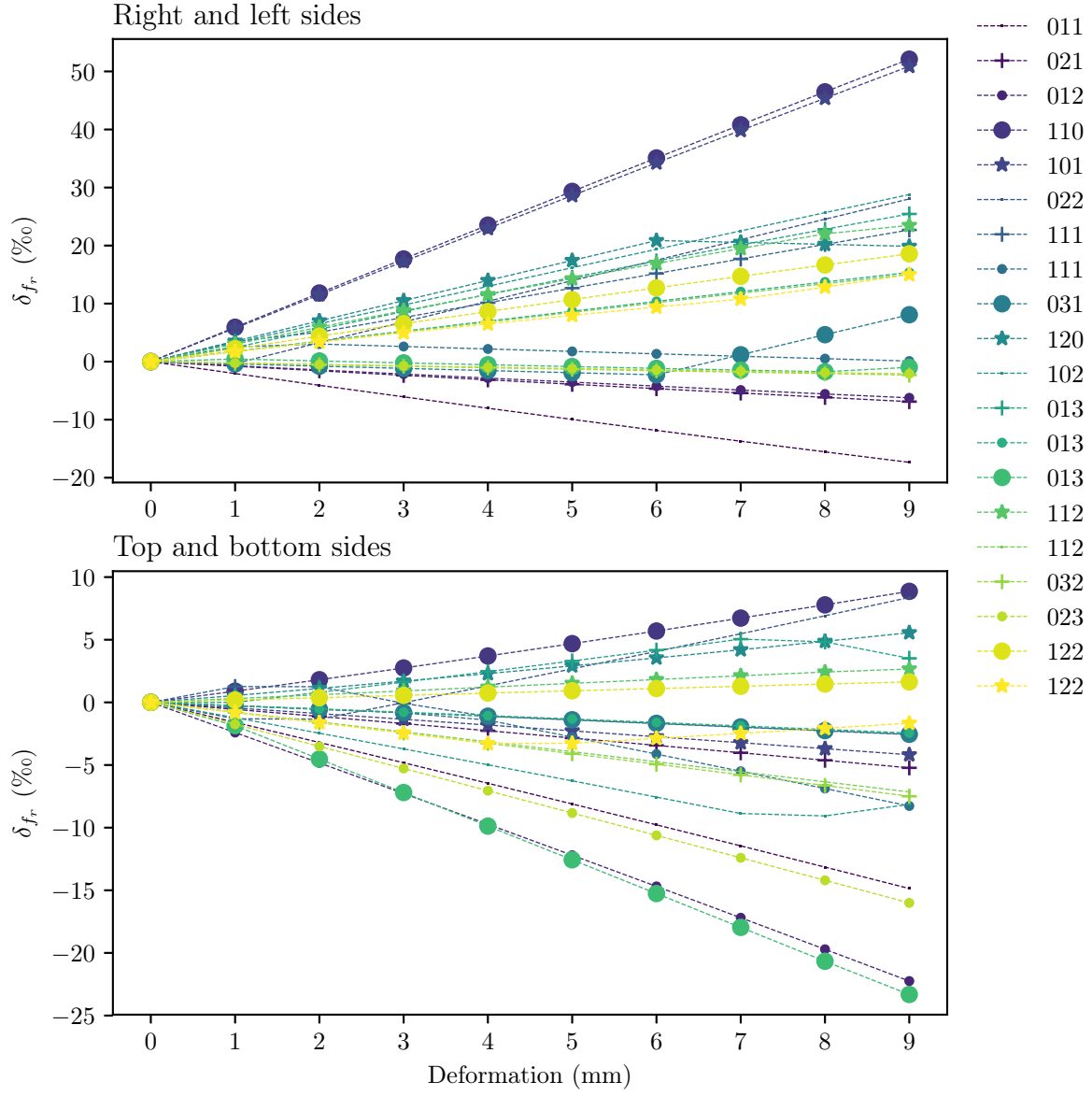


Fig. II.1.9 – Relative errors δ_{f_r} between eigenmodes of a cuboid cavity and the deformed cavity. The deformation d goes from 1 to 9 mm.

null deformation (cuboid shape) by use of equation (II.1.2). To compare the deviations between the eigenfrequencies for a perfect cavity f_0 and for the deformed one f_i , relative errors are calculated as:

$$\delta_{f_r} = \frac{f_0 - f_i}{f_0} \quad (\text{II.1.6})$$

Relative errors δ_{f_r} for deformations d from 1 to 9 mm have been analyzed. Fig. II.1.9 depicts δ_{f_r} as d increases. The maximal frequency shifts appear for the modes $mnp = 110$ and $mnp = 101$ for the left and right sides. As the estimated deformation is of approximately 3 mm, the relative error is $\delta_{f_r} \approx 17.69\%$. δ_{f_r} is mainly positive for the convex deformation. Indeed the volume of the cavity increases with d , thus the eigenmodes tend to decrease. In the same way, when the deformation reduces the volume of the cavity (concave shape) δ_{f_r} is mostly negative. Concerning the deformation of the top and bottom sides, the modes $mnp = 012$ and $mnp = 013$ are the most affected ones.

A rule of thumb to assess the upper limit for δ_{f_r} is to consider that $\lambda_{mnp,0}$ (the wavelength of the non-deformed mock-up) is increased by $2d$ where d is the deformation amplitude. The factor 2 considers both left and right, or top and bottom sides. Thus:

$$\lambda_{mnp,d} = \lambda_{mnp,0} + 2d \quad (\text{II.1.7})$$

$$\delta_{f_r \max} = 1 - \frac{\lambda_{mnp,0}}{\lambda_{mnp,0} + 2d} \quad (\text{II.1.8})$$

If we consider the mode $mnp = 110$, with $\lambda_{110,0} = \frac{c}{945.27 \text{ MHz}} = 317.15 \text{ mm}$, we obtain $\delta_{f_r \max} = 18.6\%$ which is close to the simulated value $\delta_{f_r} = 17.69\%$.

From these relative errors, we conclude that the cavity deformations due to its welding cannot be neglected when it comes to estimate the eigenmodes of the mock-up. All the simulation results presented throughout this document have been obtained considering these deformations. Comparable situations may occur when casing walls are deformed, by a heavy load for example.

II.1.3.4 Shielding effectiveness determination of the mock-up

The performances of the mock-up now need to be validated and especially the mechanism used to fix the different front and back panels. A relevant quantity is the shielding effectiveness SE of the mock-up. It will be determined from electric field measurements and is expressed as the ratio [Besnier and Démoulin, 2013]:

$$SE = \frac{|\vec{E}_i|}{|\vec{E}_e|} \quad (\text{II.1.9})$$

$$SE_{\text{dB}} = 20 \log_{10} \left(\frac{|\vec{E}_i|}{|\vec{E}_e|} \right) \quad (\text{II.1.10})$$

where \vec{E}_i is measured without the shielding (*i.e.* without the mock-up), and \vec{E}_e with the shielding. The other parameters of the system must remain unchanged (antenna position, distances, etc.).

The measurement setup is depicted in Fig. II.1.10, and is conducted within an anechoic chamber which dimensions are 8 m deep, 4 m wide and 4.3 m high. A frequency synthesizer (Anritsu MG3692B) is connected to a 25 W power amplifier (Amplifier Research 25S1G4A) and a standard gain horn antenna (A-info LB-8180) to generate an electric field \vec{E} . The electric field is measured with an active and directional vectorial probe. It is connected to an optical fiber that powers the probe and that carries information related to the amplitude and phase of the electric field projection on the orientation \vec{e}_u of the probe. This optical fiber is connected to a converter, which creates a voltage signal V as an image

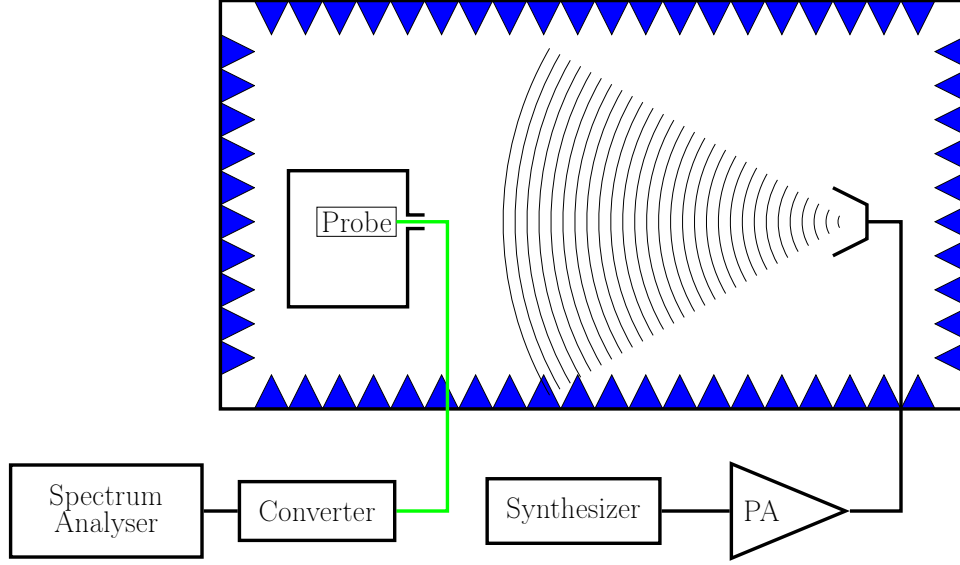


Fig. II.1.10 – Setup for shielding effectiveness measurement.

of the projected electric field $\vec{E} \cdot \vec{e}_u$ radiated by the horn antenna. The probe and the converter are constitutive of the equipment (EFS-105) manufactured by the company Enprobe. These quantities are related to the antenna factor AF of the electric probe as:

$$AF = \frac{|\vec{E} \cdot \vec{e}_u|}{V} \quad (\text{II.1.11})$$

Then, a spectrum analyzer (SignalHound BB60C) is connected to the converter to acquire the received power. Operating bandwidths of these equipment allow to measure the shielding effectiveness between 800 MHz and 3 GHz.

II.1.3.4.1 Calibration step: measurement of \vec{E}_i

The calibration step consists in the measurement of the electric reference field \vec{E}_i . The experimental conditions need to be kept after this measurement (*i.e.* position of the probe, distance to the antenna). For this first step, the shielding (thus the mock-up) is not present. An assessment of the received power on the spectrum analyzer may be determined by a power budget in order to compare it with the measured one. We write G_c the gain of the antenna, α the losses into the antenna and cables, A the gain of the amplifier, W_e the power driven by the frequency synthesizer and W_s the power driven into the antenna. The equivalent isotropic radiated power (EIRP) is expressed as:

$$\text{EIRP} = W_s G_c = \frac{W_e A}{\alpha} G_c \quad (\text{II.1.12})$$

The power density D_u at the location of the electric field probe is:

$$D_u = \frac{|\vec{E}_i \cdot \vec{e}_u|^2}{2\eta} = \frac{\text{EIRP}}{4\pi D^2} \quad (\text{II.1.13})$$

where η is the free-space impedance ($\eta = 120\pi \Omega$) and D distance between the antenna and the probe. Thus, $|\vec{E}_i \cdot \vec{e}_u| = \sqrt{D_u 2\eta}$. From equation (II.1.11), the voltage U_{\max} at the VNA port is thus:

$$U_{\max} = \frac{|\vec{E}_i \cdot \vec{e}_u|}{AF} \quad (\text{II.1.14})$$

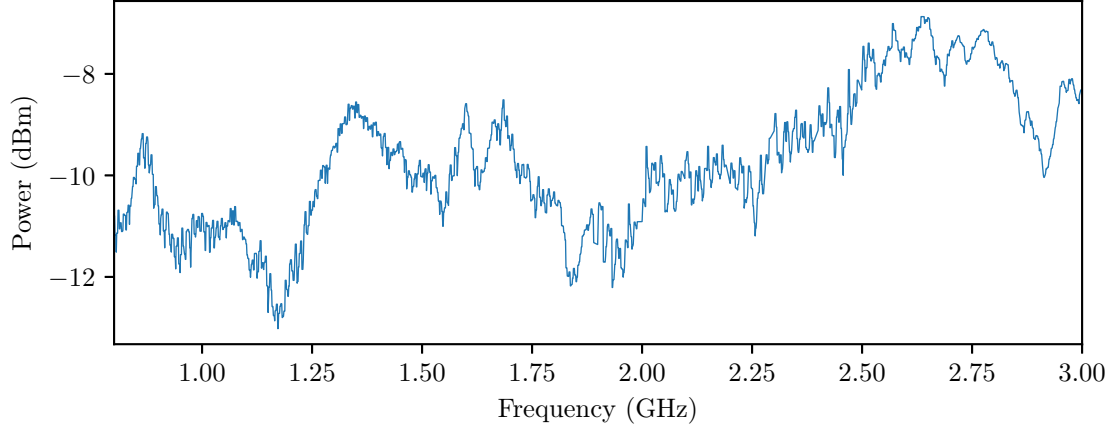


Fig. II.1.11 – Variations of the measured power on the spectrum analyzer according to the frequency for the calibration process (in free-space).

Then the measured power on a spectrum analyzer for a $50\ \Omega$ load Z_0 is:

$$P = \frac{U_{\max}^2}{2Z_0} = \frac{|\vec{E}_i \cdot \vec{e}_u|^2}{2AF^2Z_0} \quad (\text{II.1.15})$$

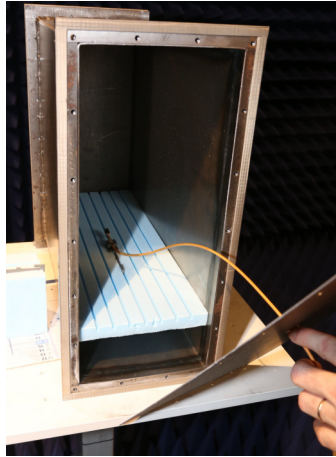
Using this method, at 2 GHz and at a distance of $D = 4.88\text{ m}$ we have $|\vec{E}_i \cdot \vec{e}_u| = 10.0\text{ V m}^{-1}$ and $P = -14.7\text{ dBm}$. Fig. II.1.11 depicts the measured power P by the spectrum analyzer, and the orders of magnitude agree with the power budget.

II.1.3.4.2 Measurement of \vec{E}_e

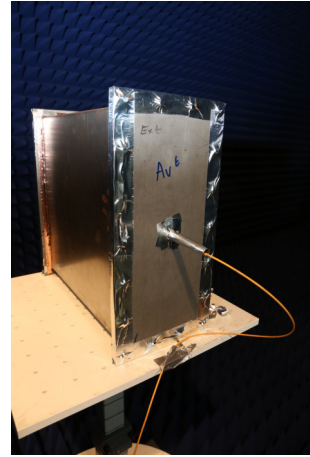
The electric field probe is then placed into the mock-up (Fig. II.1.12) on a Styrofoam stand. The mock-up is closed using a panel that has a squared aperture (sides of 1 cm) allowing to insert the probe. As the contribution of this aperture to the shielding effectiveness is not desired, it can be reduced by extending the aperture using a circular waveguide. Its diameter is 12 mm and its length is around 90 mm (as seen in Fig. II.1.12b). It acts as a high-pass filter of cut-off frequency above 10 GHz. Copper tape has also been added to seal the waveguide to the mock-up.

Fig. II.1.13 shows the shielding effectiveness of the mock-up for three different angles of incidence θ : an illumination on the side panel of the mock-up corresponds to $\theta = 0^\circ$, an illumination on the front panel (with the waveguide) corresponds to $\theta = 90^\circ$ and an illumination on the back panel corresponds to $\theta = -90^\circ$. The red dots indicate frequencies where the measured shielding effectiveness is severely reduced. These frequencies are compared to some eigenfrequencies of the mock-up in Table. II.1.2. We can state that these dips are due to the resonances inside the mock-up.

The shielding effectiveness strongly varies with the frequency, up to $\sim 50\text{ dB}$ for an illumination towards the side of the mock-up. The overall shielding effectiveness is about 55 dB for all the angles of incidence ($\theta = -90^\circ$, $\theta = 0^\circ$ and $\theta = 90^\circ$). One has to mention that the measurements have been performed for one probe position only (approximately at the center of the mock-up) and that the results may differ for other positions. However, if there were design or manufacturing errors like slits and a bad compression of the electric gasket, it would have substantially decreased the shielding performances. Thus, these measurements validate the design and the production of the mock-up.



(a) Placing of the probe in the mock-up.



(b) Closed mock-up with the waveguide and the feedthrough for the optical fiber.

Fig. II.1.12 – Shielding effectiveness measurement setup.

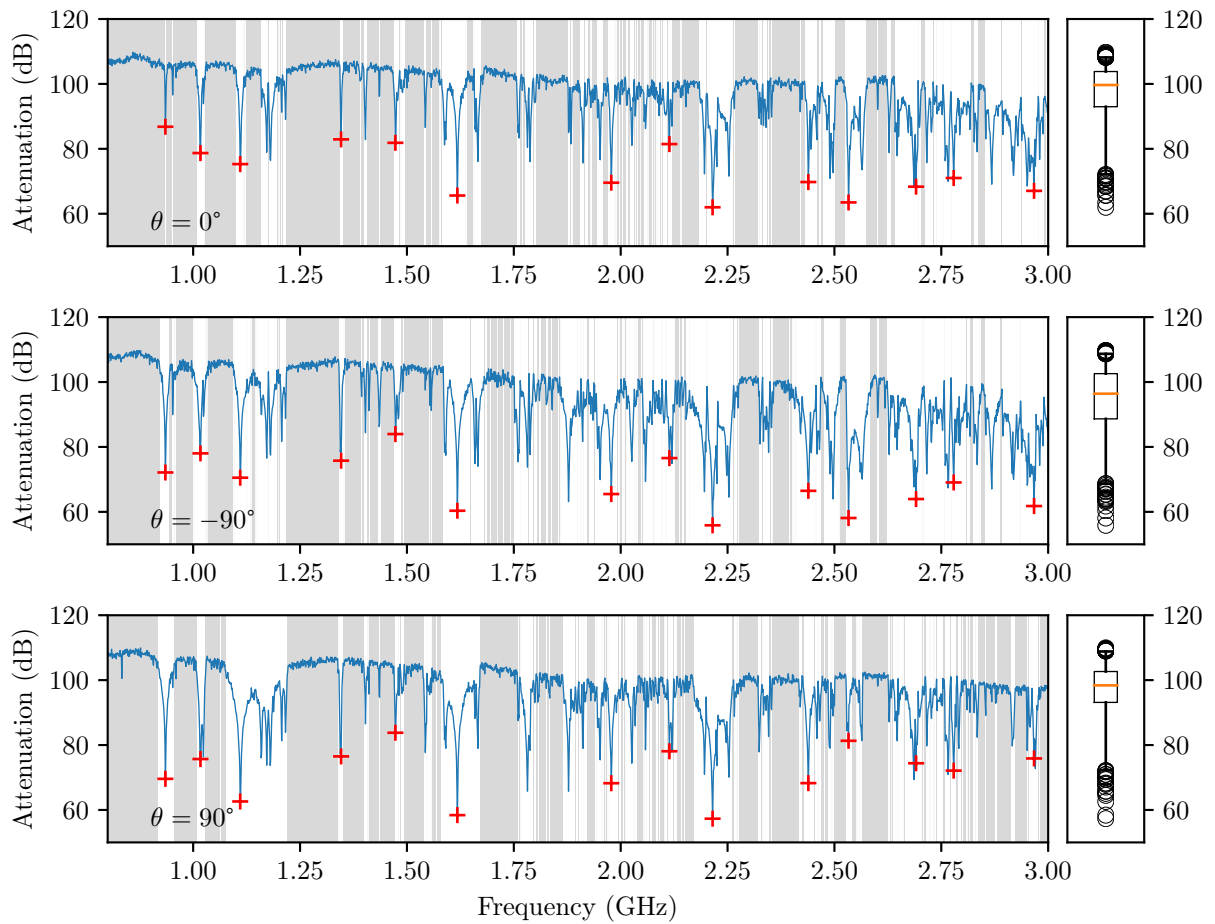


Fig. II.1.13 – Shielding effectiveness for three incidence angles θ . The regions where the background is in gray indicate that it was not possible to measure the signal (the signal did not exceed the noise floor). Thus for these frequencies the shielding effectiveness is even better.

From these measurements, another useful quantity that may be assessed is the quality factor Q of the mock-up. This quantity represents the losses in the cavity. As the mock-up dimensions are comparable to the wavelength of interest (below 3 GHz), the mode density is not high, the quality factor is thus frequency-dependent. The spectrum of mode mnp centered at frequency f_{mnp} may be expressed as:

$$|E(f)| = \frac{|E_{max}|}{\sqrt{1 + \left(2Q_{mnp} \frac{f - f_{mnp}}{f_{mnp}}\right)^2}} \quad (\text{II.1.16})$$

where $|E_{max}|$ is the magnitude of the electric field at frequency f_{mnp} . For TE modes and for a perfect cavity (without any aperture), the quality factor is ([Liu et al., 1983]):

$$Q_{mnp} = \frac{\eta_0 abdk_{xy}^2 k_{mnp}^3}{4R_s [bd(k_{xy}^4 + k_y^2 k_z^2) + ad(k_{xy}^4 + k_x^2 k_z^2) + abk_{xy}^2 k_z^2]} \quad (\text{II.1.17})$$

with

$$k_x = m \frac{\pi}{a}, k_y = n \frac{\pi}{b}, k_z = p \frac{\pi}{d}, k_{xy} = \sqrt{k_x^2 + k_y^2}, k_{mnp} = \sqrt{k_x^2 + k_y^2 + k_z^2} \quad (\text{II.1.18})$$

where $R_s = \frac{1}{\sigma \delta}$. σ is the conductivity of the steel and $\delta = \sqrt{\frac{1}{\pi f \mu \sigma}}$ its skin depth. a, b, d are respectively the width, the length and the height of the mock-up. The Q factor for several modes is given in Tab. II.1.3. For each mode, Q was estimated by a curve-fitting process using (II.1.16), and has been compared with Q_{mnp} thanks to (II.1.17). Two fittings were performed, the first one Q_{Forced} is obtained by a fitting of the equation (II.1.16) with $|E_{max}|$ and f_{mnp} fixed from measurements, and a second one Q_{Free} where $|E_{max}|$ and f_{mnp} are free. Moreover, the quality factor $Q_{-3\text{dB}}$ was also assessed from:

$$Q_{-3\text{dB}} = \frac{f}{\Delta f} \quad (\text{II.1.19})$$

where Δf is measured at $\frac{|E_{max}|}{\sqrt{2}}$ or equivalently $|E_{max}|_{\text{dBV m}^{-1}} - 3\text{dB}$. The conductivity of the steel is $\sigma \approx 6.25 \times 10^6 \text{ S m}^{-1}$ [Mitchell, 2004]. Fig. II.1.14 plots, for a given eigenmode, the fitted curves.

Moreover, we see that the order of magnitudes of Q_{Forced} , Q_{Free} and $Q_{-3\text{dB}}$ are comparable. And, the analytical expression (II.1.17) overestimates the quality factor of one order of magnitude.

II.1.4 Design and production of devices to measure couplings

In order to study couplings, one needs devices from which currents and voltages will be measured and that can radiate an electromagnetic field towards its environment. These devices should be typical of what can be found in electronic devices. We have chosen simple PCBs to ease their making, and to avoid having too many details in the 3D model used by the simulation software. Once more, two models are needed, a numerical one for the simulation of the computer chassis, and a physical one for the real computer chassis mock-up.

II.1.4.1 Simple printed circuit boards production

These PCBs will allow to measure couplings between them, or between a plane wave that couples to the cavity through an aperture and the PCBs inside the cavity. On each board, a microstrip transmission line is printed with a unique geometry that allows to efficiently propagate the induced current to a SMA connector which will be connected to a measurement equipment. These geometries will allow the different field components to couple on the transmission lines. It thus diversifies the types of couplings that may occur. The manufacturing of the boards was subcontracted to a specialized firm. Each transmission line has a characteristic impedance Z_0 of 50Ω and is terminated by a 50Ω load composed

Mode	Theoretical eigenfrequency	Measured frequency	Relative Error
f_{110}	935 MHz	945.921 MHz	1.154%
f_{111}	1017 MHz	1017.542 MHz	0.053%
f_{120}	1110 MHz	1115.089 MHz	0.456%
f_{122}	1346 MHz	1343.846 MHz	-0.160%
f_{113}	1473 MHz	1469.827 MHz	-0.216%
f_{140}	1618 MHz	1624.208 MHz	0.382%
f_{143}	1978 MHz	1975.772 MHz	-0.113%
f_{213}	2114 MHz	2120.385 MHz	0.301%
f_{144}	2215 MHz	2210.894 MHz	-0.186%
f_{116}	2439 MHz	2440.751 MHz	0.072%
f_{055}	2533 MHz	2533.989 MHz	0.039%
f_{244}	2691 MHz	2687.693 MHz	-0.123%
f_{173}	2779 MHz	2781.888 MHz	0.104%
f_{270}	2967 MHz	2967.982 MHz	0.033%

Table II.1.2 – Comparison between measured frequencies corresponding to low shielding effectiveness (with regards to other frequencies) and some eigenfrequencies (in MHz) of the mock-up.

Mode	f_{Forced}	Q_{Forced}	f_{Free}	Q_{Free}	$f_{-3\text{ dB}}$	$Q_{-3\text{ dB}}$	f_{Theory}	Q_{Theory}
110	935.00	1122.0	935.21	1345.9	935.00	1009.6	945.27	7255.4
111	1017.0	747.50	1016.5	1570.3	1017.0	318.18	1016.8	7797.5
120	1110.0	883.84	1110.5	2305.6	1110.0	451.48	1114.3	7974.0
122	1346.0	1591.5	1345.9	1721.6	1346.0	1366.5	1342.9	9209.5
113	1473.0	1102.2	1473.4	1877.2	1473.0	689.94	1468.8	10917.
140	1618.0	2654.5	1617.9	3057.3	1618.0	1944.5	1623.1	9775.1
143	1978.0	2181.1	1978.1	2274.7	1978.0	1963.8	1974.4	10894.
213	2114.0	1242.9	2113.7	1299.8	2114.0	1218.5	2118.9	11863.
144	2215.0	1788.8	2215.3	2263.2	2215.0	1721.7	2209.4	11595.
116	2439.0	2573.7	2439.1	2718.2	2439.0	2333.4	2439.1	15966.
055	2533.0	3299.4	2533.3	4902.1	2533.0	2708.7	2532.2	11942.
244	2691.0	1744.3	2690.0	335.80	2691.0	2826.3	2685.8	13024.
173	2779.0	2151.9	2778.9	2270.5	2779.0	1966.7	2780.0	12836.
270	2967.0	2026.5	2966.7	1688.6	2967.0	2826.0	2965.9	13179.

Table II.1.3 – Assessed quality factor Q for some modes, and for an illumination on the back panel $\theta = -90^\circ$. Frequencies are in MHz.

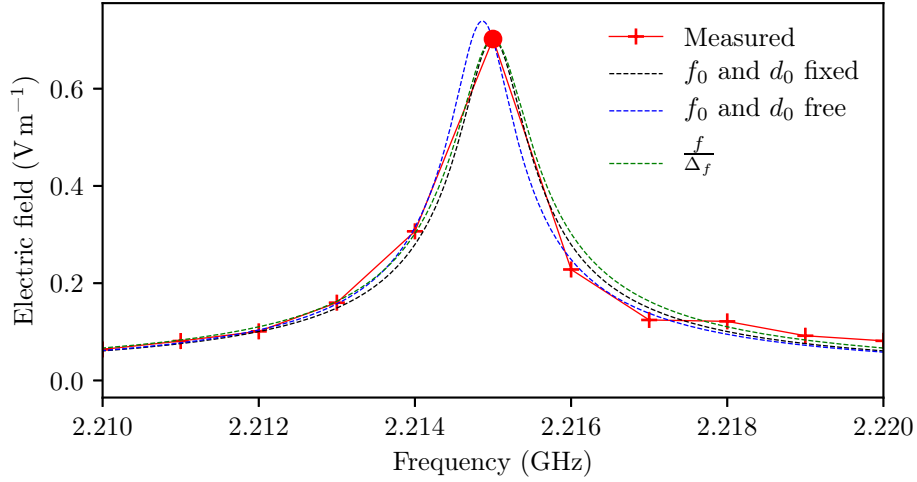


Fig. II.1.14 – Fitting example for the assessment of the quality factor for the mode 144 ($f_{144} = 2.215$ GHz). In red, the electric field measured, in black $|E(f)|$ fitted with f_0 and $|E_{\max}|$ free using (II.1.16), in blue $|E(f)|$ fitted with f_0 and $|E_{\max}|$ free and in green Q assessed from $\frac{|E_{\max}|}{\sqrt{2}}$ using (II.1.19).

of a surface mount resistor and a via. The substrate of the boards is made of FR4¹ ($\epsilon_r = 4.6$). The bottom layer of each PCB is a ground plane. Pictures of the four boards are exposed in Fig. II.1.15.

II.1.4.2 Determination of an accurate simulation model

At first, the scattering parameter S_{11} of these boards have been measured in free-space. The results are depicted in Fig. II.1.18.

Then full-wave simulations have been conducted for the four boards. The surface mount resistor at the end of the transmission line has been modeled as exposed in [CST, 2016], and the via consists in a metalized through hole. The thickness of the microstrip transmission line has been set to its skin depth.

A first simulation has been launched where energy has been driven towards the transmission line by a waveguide port directly at the edge of the board. It corresponds to a perfect impedance match and is not representative of any realistic sources (orange curves in Fig. II.1.18). We note that the computed results did not match the measured data. There is an average gap of ≈ 25 dB between the two curves.

A second model was then set to improve the results by taking the SMA connector into account (see Fig. II.1.16). The SMA connector consists in a section of a coaxial transmission line with an extended core to join the microstrip transmission line of the board. Then the energy has been driven towards the SMA connector by means of a waveguide port. Better agreement is observed (green curves in Fig. II.1.18). With this upgraded model, the order of magnitude of S_{11} agrees for the two models (the real PCBs and the simulation models). The drawback is that the computation time significantly increases (as the number of cells in the mesh increases). For the following simulations, SMA connectors will be taken into account.

¹FR4: Flame Retardant 4

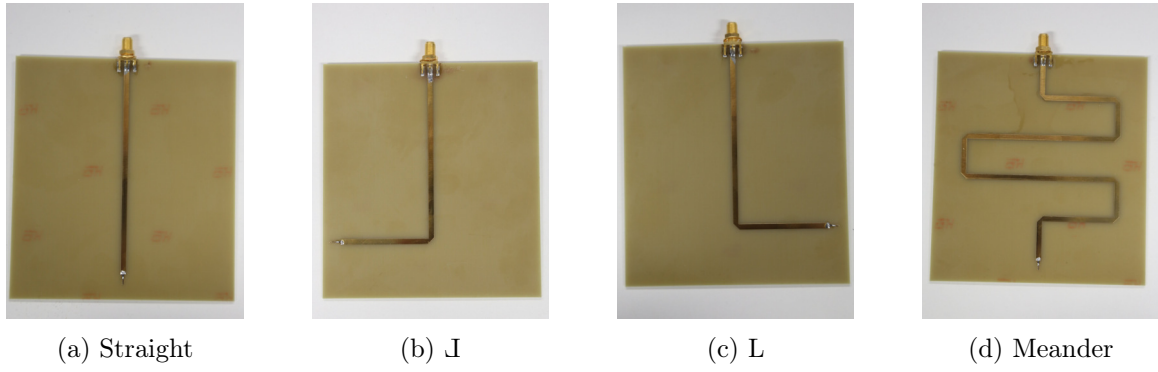


Fig. II.1.15 – Pictures of the four boards.

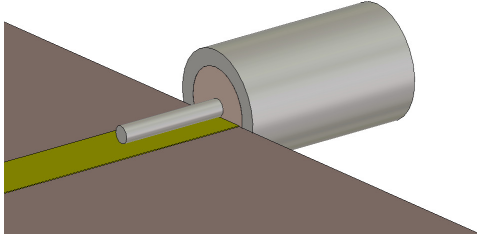


Fig. II.1.16 – Model of the SMA connector.

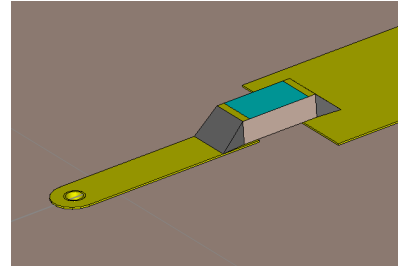


Fig. II.1.17 – Model of the 50Ω load at the end of the transmission line, as a surface mount resistor and a via.

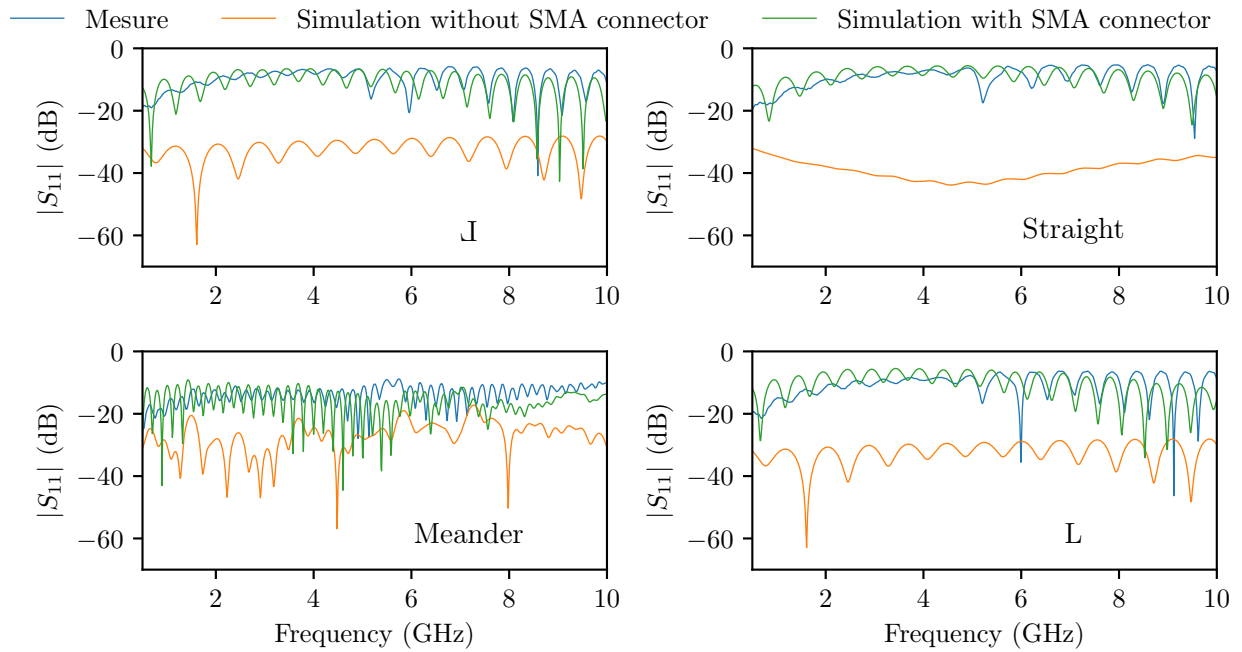


Fig. II.1.18 – S_{11} of the four boards.

II.1.5 Conclusion

The set-up of two models has been detailed in this chapter: a simulation model and a mock-up, both representative of a desktop computer chassis.

The design and the manufacturing of a computer chassis mock-up was described. That device was made to be versatile. Several steps were necessary to validate the mock-up.

During the manufacturing process, the mock-up has been deformed due to overheating during the welding of the lateral panels. Results computed by an eigenmode solver have showed that even a small deformation can lead to a noticeable shift of the eigenfrequencies. These deformations should be integrated in the 3D model when it comes to full-wave simulations. Then, the shielding effectiveness at the center of the mock-up was measured using a field probe within a frequency range from 800 MHz to 3 GHz (steps of 1 MHz). Its lowest value is 55 dB. However, the first quartile (over all the frequencies) is ≈ 70 dB. It means that for 75% of the frequencies, the shielding effectiveness is greater than 70 dB. These values indicate no design or manufacturing mistakes.

Finally, models for devices from which couplings will be obtained have been set. These take the form of simple [PCBs](#), and simulation models have been determined for each [PCB](#).

In the following chapter, electromagnetic fields and couplings between a plane wave and simple [PCBs](#) obtained by these two models will be compared.

Chapter II.2

Comparison between the two models for two configurations

Contents

II.2.1	Introduction	72
II.2.2	Electric field amplitude and couplings assessment with the two models	72
II.2.2.1	Study of the electric field in the empty desktop computer chassis . . .	72
II.2.2.2	Coupling between a plane wave and printed circuit boards	78
II.2.3	Applicability of the simulation model to determine statistics . . .	81
II.2.4	Conclusion	86

II.2.1 Introduction

In what follows, the models exposed in the previous section, *i.e.* the mock-up and the numerical model of a desktop computer chassis are compared. Two configurations will be studied. The first one will allow to acquire the electric field at several locations in the desktop computer chassis, and the second one will be devoted to measure the currents at the end of several transmission lines that are printed on simple circuit boards. These quantities may then be used to run a risk assessment related to [INFOSEC](#) for a system that can be modeled (in terms of shapes and materials).

II.2.2 Electric field amplitude and couplings assessment with the two models

II.2.2.1 Study of the electric field in the empty desktop computer chassis

The first attempt is to compare the field measured and simulated at several locations in the empty mock-up. For the simulation model, the computational volume is illuminated by a plane wave with a field strength of 1 V m^{-1} . The volume boundaries are set open. Then the electric field is computed at several locations of the mock-up model for the whole frequency range. From the simulated and

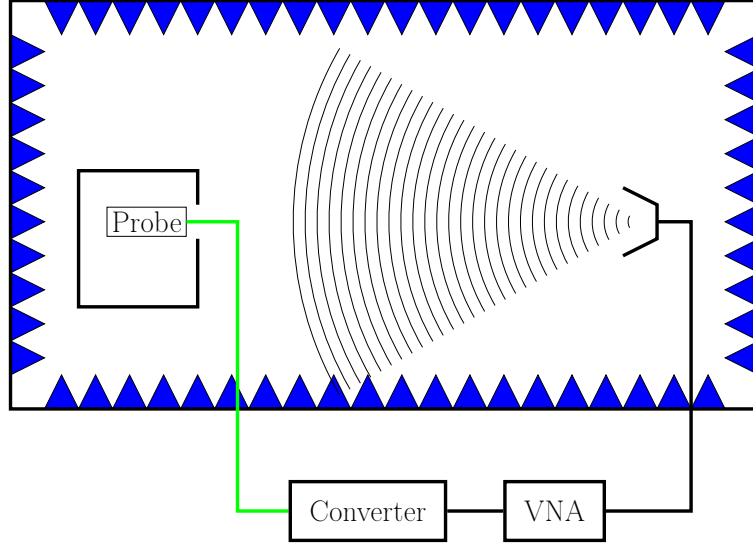


Fig. II.2.1 – Setup for the electric field measurement inside the mock-up.

measured data, the quantities $E_{\text{Measurement}}$ (dB V m⁻¹) and $E_{\text{Simulation}}$ (dB V m⁻¹) are computed as:

$$E_{\text{Measurement}} \text{ (dB V m}^{-1}\text{)} = 20 \log_{10} \left(\frac{|E_{\text{Measurement}}|}{|E_{\text{Calibration}}|} \right) \quad (\text{II.2.1})$$

$$E_{\text{Simulation}} \text{ (dB V m}^{-1}\text{)} = 20 \log_{10} \left(\frac{|E_{\text{Simulation}}|}{1 \text{ V m}^{-1}} \right) \quad (\text{II.2.2})$$

and compared. $E_{\text{Calibration}}$ accounts for the frequency response of the antenna (see next section).

II.2.2.1.1 Measurement setup

We have used the same setup and electric probe as for the shielding effectiveness measurement of the mock-up (see section II.1.3.4.1), depicted in Fig. II.2.1. Again, measurements are limited to the frequency bandwidth of the probe, thus up to 3 GHz. This probe is propped up with a 3D printed plastic support that allows the probe to be slipped along a groove in a styrofoam panel ($\epsilon_r \approx 1$ [Balanis, 2012]). This set-up allows a precise and reproducible positioning of the probe inside the mock-up. Fig. II.2.2 shows the measurement configuration. The vertical electric field component E_z was acquired for two aperture positions (see Fig. II.1.3c). To calibrate the measurement, $E_{\text{Calibration}}$ was measured in free space without the mock-up. It was measured at a distance $D = 4.88$ m from the transmitted antenna oriented in order to radiate an electric field vertically polarised (along \vec{e}_z , see Fig. II.1.3).

II.2.2.1.2 Benchmark study between the two models

Comparison between the simulated and measured electric fields was performed for several configurations: for two aperture locations (N°1 and N°3) and for several positions along the axes Ox and Oy . Fig. II.2.3 and Fig. II.2.5 are related to the field with the aperture location N°3, and Fig. II.2.4 to the position N°1. Fig. II.2.4 and Fig. II.2.3 show the field determined along the axis Oy , and Fig. II.2.5 along the axis Ox .

The box plots for the two series (of N sample values) are given. It indicates the first Q_1 , the second Q_2 (the median in orange) and third Q_3 quartiles, as well as the first ($p_{1\%}$) and last percentiles ($p_{99\%}$). The circles depict the outliers (see Fig. II.2.3, top plot for a legend). Moreover, the PEARSON correlation

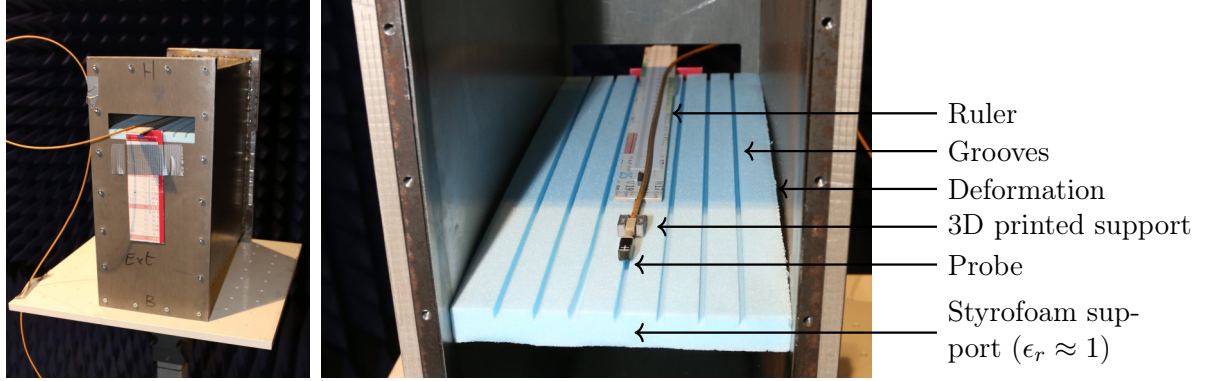


Fig. II.2.2 – Illustrations of the positioning of the electric field probe in the mock-up. In the right picture the deformation of both sides of the mock-up is noticeable. A gap between the styrofoam support (which is straight) and the side is visible.

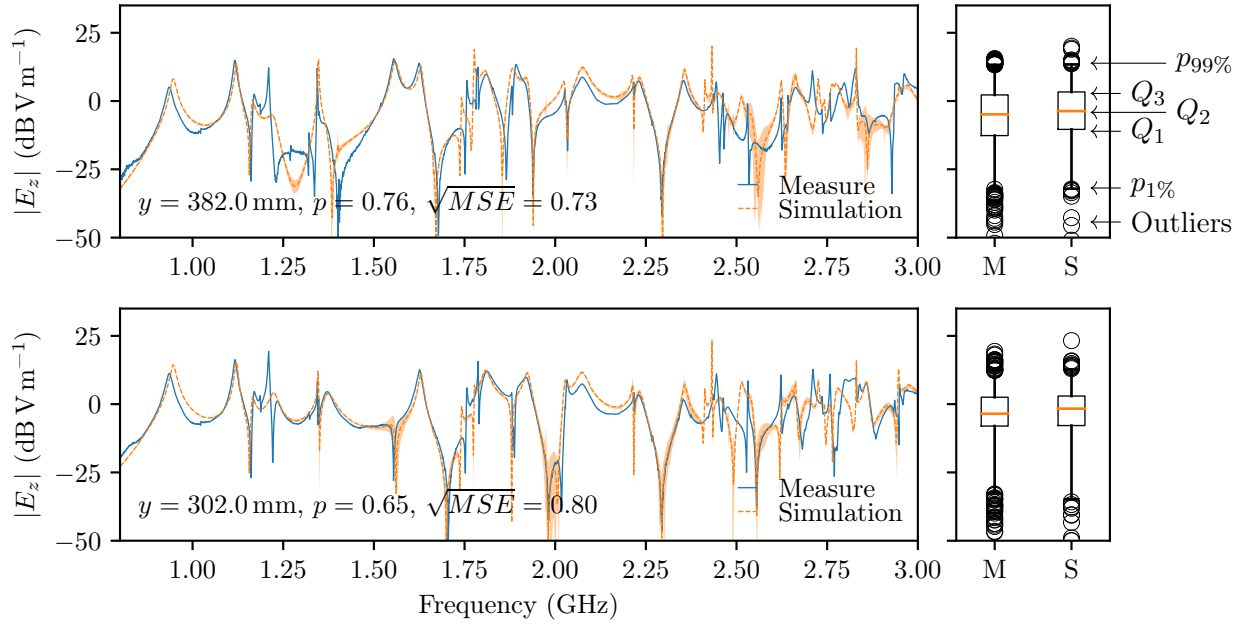


Fig. II.2.3 – $|E_z|$ in the empty mock-up for a normal incident plane wave ($\theta = 90^\circ$) and for an aperture location N°3. The measurement position is at $x = 83$ mm, $z = 198$ mm and y is indicated on the figure.

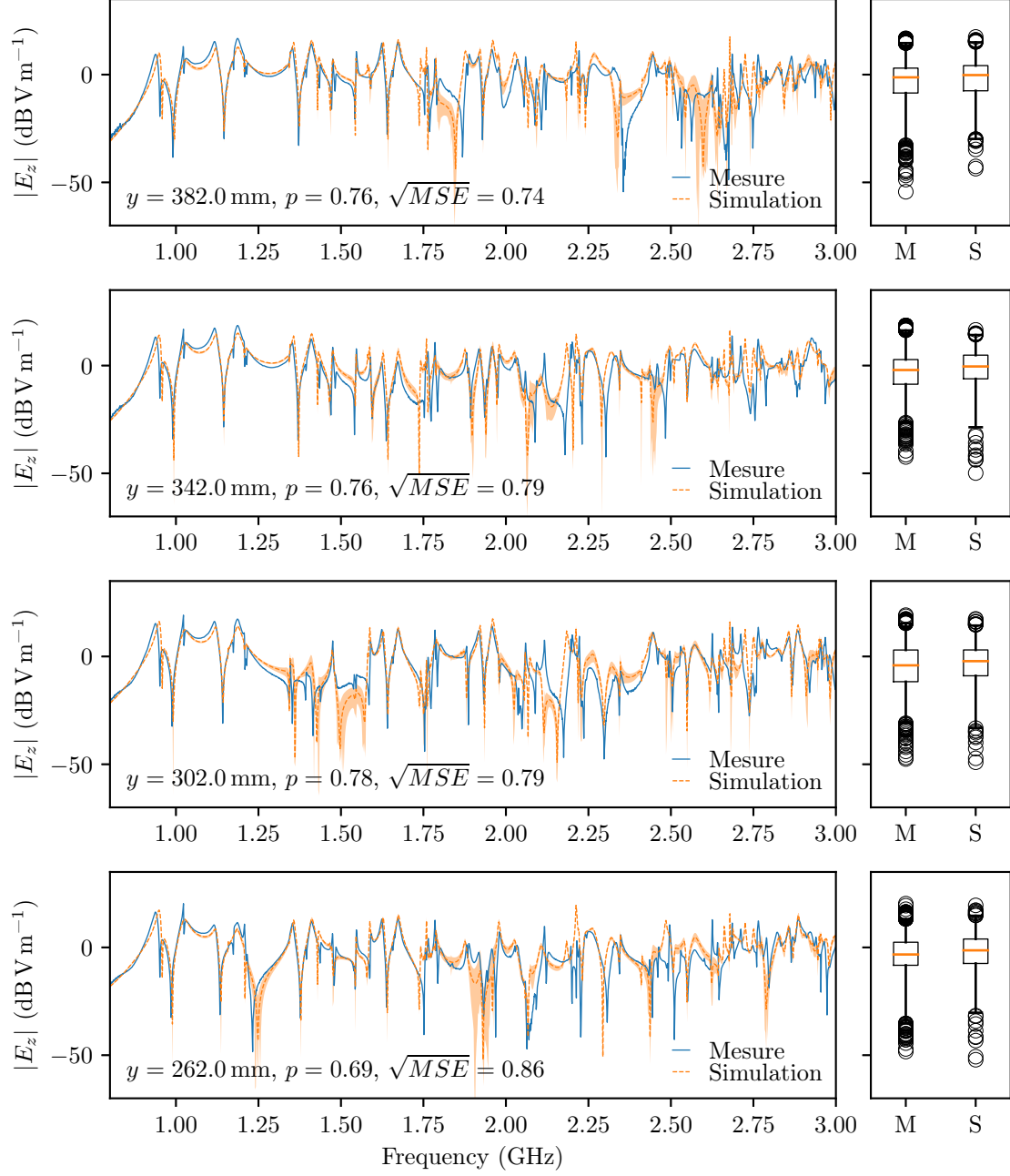


Fig. II.2.4 – $|E_z|$ in the empty mock-up for a normal incident plane wave ($\theta = 90^\circ$) and for an aperture location N°1. The measurement position is at $x = 83$ mm, $z = 308$ mm and y is indicated on the figure.

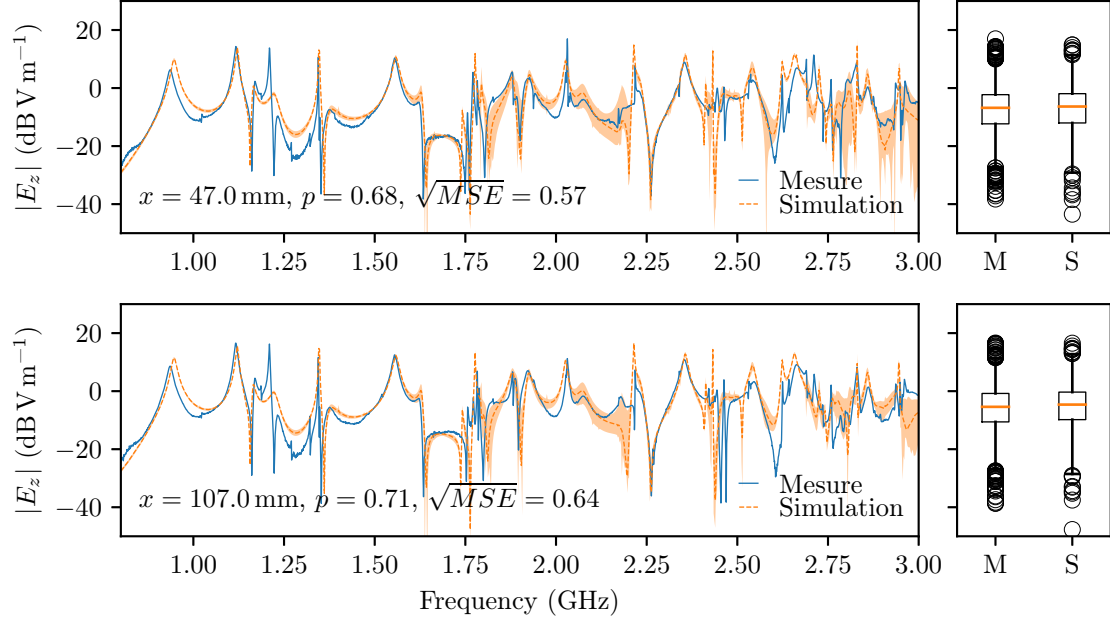


Fig. II.2.5 – $|E_z|$ in the empty mock-up for a normal incident plane wave ($\theta = 90^\circ$) and for an aperture location N°3. The measurement position is at $y = 342$ mm, $z = 198$ mm and x is indicated on the figure.

coefficient is computed as:

$$p = \frac{\sum_{i=1}^N (m_i - \langle m \rangle)(s_i - \langle s \rangle)}{\sqrt{\sum_{i=1}^N (m_i - \langle m \rangle)^2} \sqrt{\sum_{i=1}^N (s_i - \langle s \rangle)^2}} \quad (\text{II.2.3})$$

where $\{s_i\}$ is the serie related to the simulated data and $\{m_i\}$ to the measured data, and the mean square error is also given. It allows to characterize the estimator, *i.e.* the simulation here. It is computed like:

$$\text{MSE} = \frac{1}{N} \sum_{i=1}^N (m_i - s_i)^2 \quad (\text{II.2.4})$$

p and MSE are computed on the linear data (not on a logarithmic scale). Errors related to the probe positioning and to the angle of incidence of the plane wave were taken into account by running several simulations. For each position considered in the mock-up, the electric field was computed on a $3 \times 3 \times 3$ space grid with a maximum error of 5 mm. Moreover, several simulations with small deviations of the angle of incidence of the plane wave were run to take into account the incidence offset of the transmitting antenna. The maximum error is 5° for both θ and φ , and 9 simulations were run ($\theta \in [-5^\circ, 0^\circ, 5^\circ]$ and $\varphi \in [-5^\circ, 0^\circ, 5^\circ]$). The maximum and minimum errors (over $3^3 \times 3^2 = 243$ electric field values) define the orange interval between the simulation curves on figures. These errors have different significances as the frequency varies.

The results show a good match between the measurement and the simulation, for E_z and for both aperture locations and axes (Ox and Oy). The PEARSON correlation coefficient lies between 0.65 and 0.78 and $\sqrt{\text{MSE}}$ between 0.57 and 0.86 dBV m $^{-1}$. Some measurements were conducted for the E_x field component, however it was not possible to compare measurements and simulations as the field probe is not sensitive enough. The simulations show that the ratio between the mean values of the E_z and

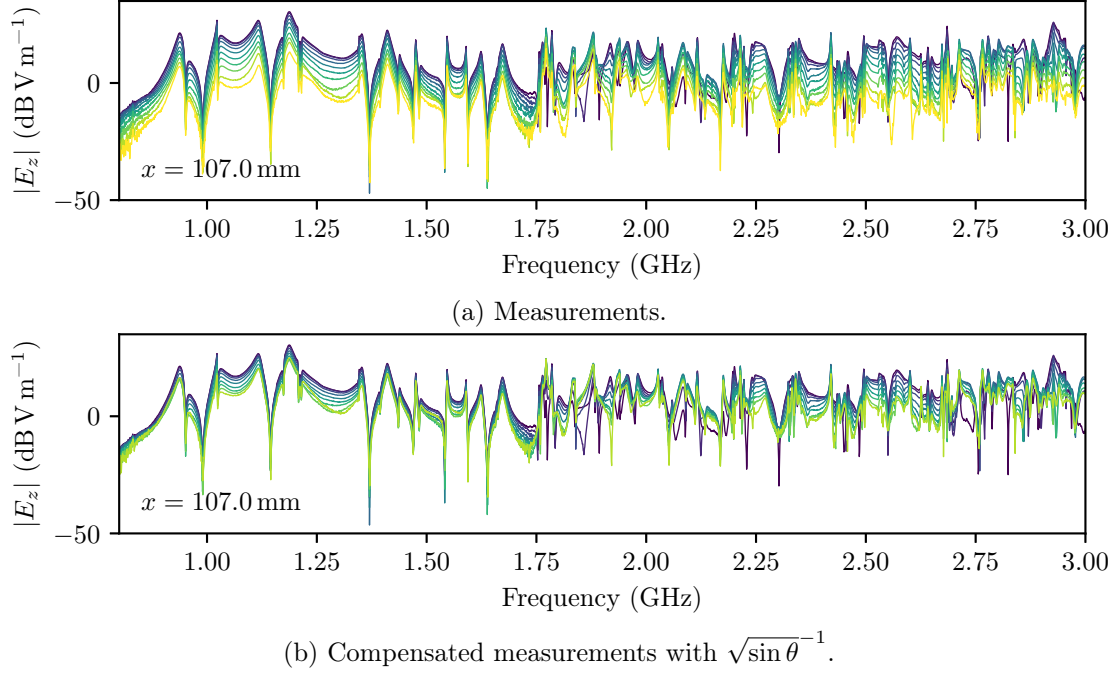


Fig. II.2.6 – $|E_z|$ in the empty mock-up for a plane wave of incidence θ between 90° (purple curve) to 180° (yellow curve) (aperture location N°1).

E_x component is $\frac{\langle |E_z| \rangle}{\langle |E_x| \rangle} \approx 45$ dB.

The effect of the incidence of the plane wave on the measured electric field was also investigated. By use of a turntable (see Fig. II.1.2), 11 angles θ were considered between 90 and 180° . We remind that $\theta = 90^\circ$ for a normal incidence (*i.e.* $\frac{\vec{k}}{|\vec{k}|} = \vec{e}_y$) and that $\theta = 180^\circ$ for a grazing incidence (*i.e.* $\frac{\vec{k}}{|\vec{k}|} = -\vec{e}_x$). Fig. II.2.6a depicts the impact of θ on the measured electric field. For a plane wave the mean value over a period of the POYNTING vector is $\langle \vec{\Pi} \rangle = \frac{1}{2\eta} |\vec{E}|^2 \frac{\vec{k}}{|\vec{k}|}$. We can calculate the flux of $\langle \vec{\Pi} \rangle$ through the aperture: $P = \iint_S \langle \vec{\Pi} \rangle \cdot d\vec{S} = \frac{1}{2\eta} |\vec{E}|^2 S \frac{\vec{k}}{|\vec{k}|} \cdot \vec{e}_y = \frac{1}{2\eta} |\vec{E}|^2 S \sin \theta$. Thus, the electric field in the mock-up should be proportional to $\sqrt{\sin \theta}$. Fig. II.2.6b shows the measurements compensated by computing $|E^{\text{Measured}}| \sqrt{\sin \theta}^{-1}$. As all the curves do not merge, we can state that the power coupled to the aperture is not strictly proportional to $\sin \theta$.

One simulation requires a computation time of ≈ 2 h and 30 min for an accuracy of -60 dB¹.

Conclusion This set of simulations has allowed to determine a configuration for the commercial software that is able to simulate reverberant environment with use of a time-domain solver (in section I.2 it was noted that these situations were mostly addressed through frequency solvers). A good agreement was found between experimental and simulation data when it comes to determine the field in an empty cavity. In what follows, a more complex problem is covered: PCBs will be added inside the mock-up.

¹All the full-wave simulations have been computed on the same desktop computer (64 GB of RAM, 2 processors with 6 cores each and with a clock frequency of 3 GHz).

II.2.2.2 Coupling between a plane wave and printed circuit boards

The mock-up is now filled with a stacking of [PCBs](#), and the aim is to quantify the coupling between a plane wave that illuminates the mock-up and a transmission line printed on a circuit board. It was found that a convenient way to compare the simulations and the measurements is to determine the couplings with two antenna factors, one for the measurement and another one for the simulation. These antenna factors will be defined in the next section.

The boards presented in section [II.1.4](#) are placed in the mock-up. The SMA connector of the transmission line on which we want to assess the coupling is connected to a [VNA](#) to measure the scattering matrix \underline{S} between the antenna and the end of the transmission lines. Two configurations were considered, both composed of two stacked [PCBs](#), vertically spaced of 20 mm: (I) and (L) for the first one and (I) and (J) for the second one. The setup is depicted in [Fig. II.2.7](#).

II.2.2.2.1 Results standardization

For the measurement, the maximum voltage amplitude $|U_{\max,M}|$ at the end of the transmission line is:

$$|U_{\max,M}| = |S_{21}| \sqrt{2P_{\text{Antenna}}Z_0} \quad (\text{II.2.5})$$

where $|S_{21}|$ is the forward scattering parameter between the horn antenna and the end of the transmission line, P_{Antenna} the power applied to the antenna and Z_0 the impedance seen from the SMA connector.

In the simulation software, the mock-up model is illuminated by a plane wave, with a constant electric field magnitude, thus the maximum voltage amplitude $|U_{\max,S}|$ is:

$$|U_{\max,S}| = |F_1| \sqrt{2P_{\text{plane wave}}Z_0} \quad (\text{II.2.6})$$

where $|F_1|$ describes the coupling between the incident plane wave and the SMA card connector. $|F_1|$ is provided by [CST-SS](#) (see [\[cst, 2020\]](#)). $P_{\text{plane wave}}$ is the power of the plane wave, and is given by:

$$P_{\text{plane wave}} = \frac{|E_{z,\text{Plane wave}}|^2}{2\eta_0} S \quad (\text{II.2.7})$$

with S the application surface of the plane wave on the simulation working volume. Thus, it is possible to compute two antenna factors, AF_M for the measurement and AF_S for the simulation, like:

$$AF_M = \frac{|E_{z,\text{Aperture},M}|}{|U_{\max,M}|} \quad (\text{II.2.8})$$

$$AF_S = \frac{|E_{z,\text{Aperture},S}|}{|U_{\max,S}|} \quad (\text{II.2.9})$$

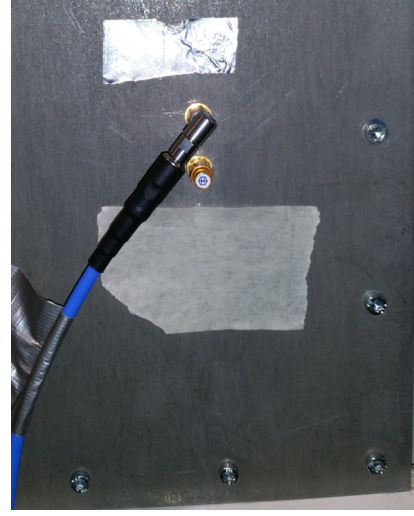
where $|E_{z,\text{Aperture},M}|$ and $|E_{z,\text{Aperture},S}|$ are the electric field magnitude at the aperture location. For the simulation, $|E_{z,\text{Aperture},S}| = |E_{z,\text{Plane wave}}|$, where $|E_{z,\text{Plane wave}}|$ is the amplitude of the incident electric field defined in [CST-SS](#). Then, $|E_{z,\text{Aperture},M}|$ was acquired during a calibration step where the electric field was measured at the aperture location, but without the mock-up. The calibration and the measurement procedures are depicted in [Fig. II.2.8](#).

II.2.2.2.2 Results for two stacked PCBs

The two antenna factors are shown in [Fig. II.2.9](#), and were computed from the voltage measured from the board at the bottom of the stacking. For each plot, p is the correlation factor between the two series computed from equation [\(II.2.3\)](#), \sqrt{MSE} is the mean squared error (equation [\(II.2.4\)](#)), and σ_M , μ_M

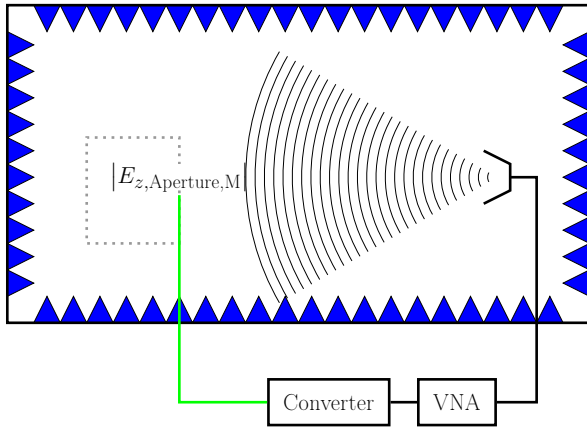


(a) (I) and (L) configuration (inside view).

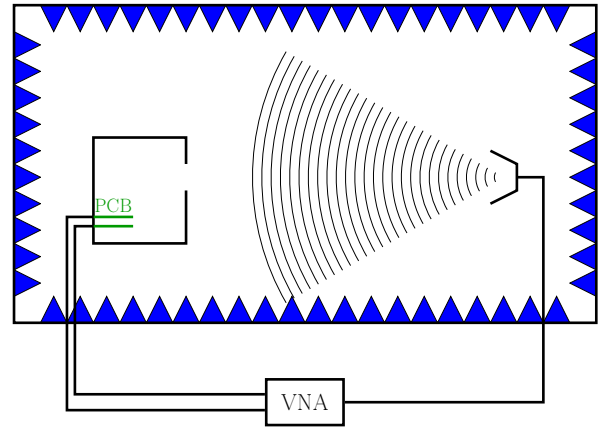


(b) SMA connectors (outside view).

Fig. II.2.7 – Pictures of the set-up.



(a) Calibration procedure by using the field probe and a [VNA](#).



(b) Measurement procedure by using a [VNA](#).

Fig. II.2.8 – Calibration (Fig. II.2.8a) and measurement (Fig. II.2.8b) setups for the couplings between [PCBs](#) and a plane wave.

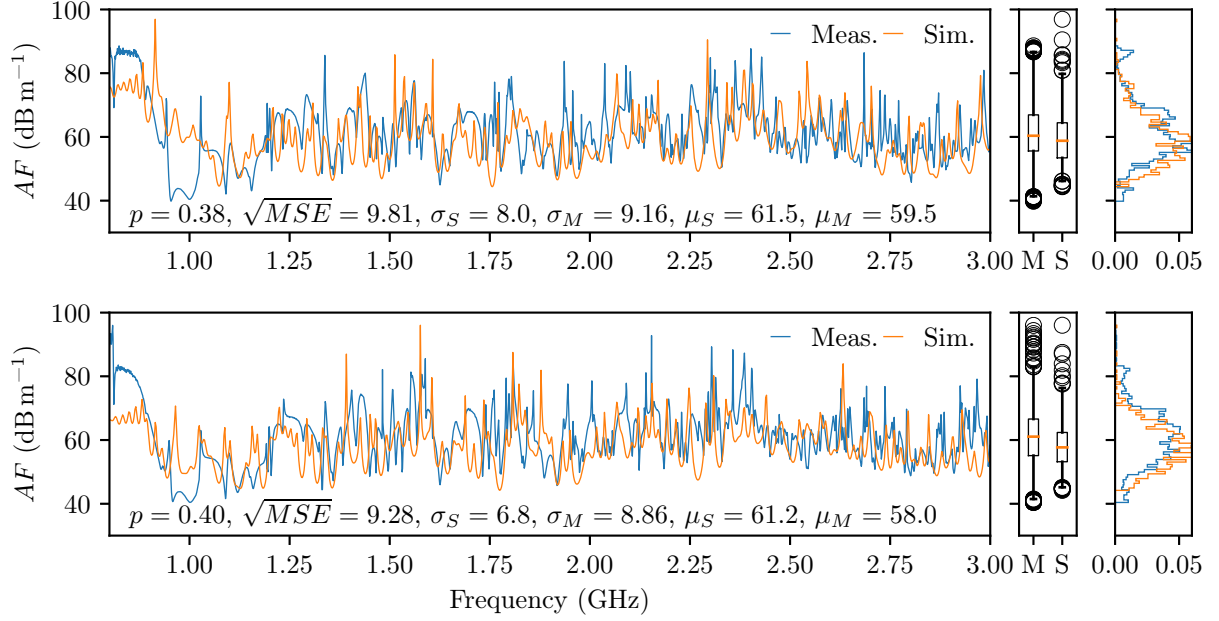


Fig. II.2.9 – Antenna factors for the two configurations (top (I) and (L), bottom (I) and (J)). The incident plane wave was vertically polarised for this measurement. The curves on the right are the PDFs of the antenna factors.

and σ_S , μ_S are respectively the standard errors and mean values for each serie. We may remind that the standard error σ and the mean value μ of a sample $\{x_i\}$ with $i \in [1, N]$ are computed like:

$$\mu = \frac{1}{N} \sum_{i=1}^N x_i \quad (\text{II.2.10})$$

$$\sigma = \sqrt{\frac{1}{N} \sum_{i=1}^N (x_i - \mu)^2} \quad (\text{II.2.11})$$

These values were calculated from the logarithmic values (not the linear one). For both configurations, the orders of magnitude are similar. Moreover, above 1 GHz, the simulation is able to take into account the overall changes. The dynamic range of the antenna factors is around 50 dB. In order to have a figure that can characterize how close the measurement and the simulation results are, the moving difference of averaged values over 40 MHz has been computed for the two configurations (see Fig. II.2.10). This allows to mitigate, in some way, the shifts of the eigenfrequencies between the simulation and the measurements. This quantity varies within a range from -10 dB to 10 dB between 1 GHz and 3 GHz. It gives a confidence interval around these measurements. The computation time needed to simulate this configuration is around 2 h, with all the details (deformation of the mock-up, SMA connectors at the PCB ends, surface mount resistor, via, etc.).

II.2.2.2.3 Results for four stacked PCB

A more complex configuration is now considered. Four boards are stacked inside the mock-up in the following order (from bottom to top): meander (P1), straight (P2), L (P3) and J (P4). Two polarizations (horizontal and vertical) are tested by rotating the standard gain horn antenna. We admit that, for the calibration procedure, the field measured at the location of the aperture is equal (in magnitude) for both polarizations (while guaranteeing that both the field probe and the standard gain

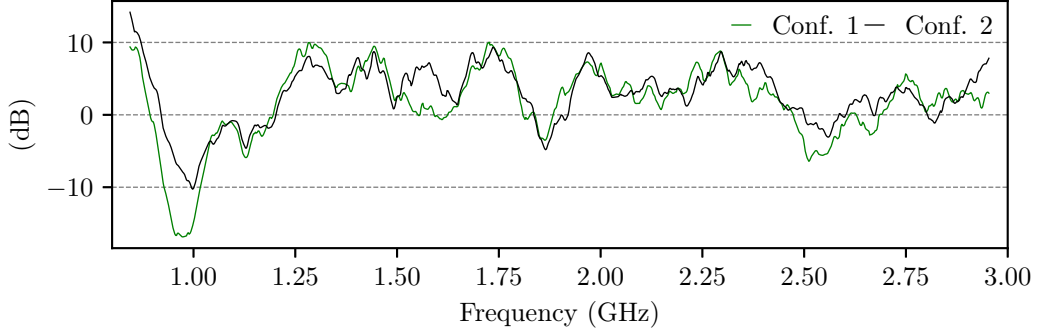


Fig. II.2.10 – Moving difference of averaged values over 40 MHz of the antenna factor for the two configurations.

horn antenna are identically polarized). Thus we have $|E_{z,\text{Aperture},M}| = |E_{x,\text{Aperture},M}|$, and antenna factors for the four boards and for both polarization are computed like:

$$AF_M = \frac{|E_{x,\text{Aperture},M}|}{|U_{\max,M}|} = \frac{|E_{z,\text{Aperture},M}|}{|U_{\max,M}|} \quad (\text{II.2.12})$$

$$AF_S = \frac{|E_{x,\text{Plane wave}}|}{|U_{\max,S}|} \quad (\text{II.2.13})$$

Fig. II.2.11 depicts the antenna factor for a horizontal polarization of the electric field, and Fig. II.2.12 for a vertical one. As for the two stacked PCB configurations, the simulations and the measurements results give a comparable order of magnitude. For both polarizations, it appears that results for the board at the top of the stacking are better than for the boards below. Indeed, we have for the horizontal polarisation $|\sigma_S - \sigma_M| = 0.04 \text{ dB m}^{-1}$ for the upper board, 4.60 dB m^{-1} for the second, 4.40 dB m^{-1} for the third and 3.3 dB m^{-1} for the lowest board (these values are given in Fig. II.2.11). For the vertical polarisation, the same behavior is noticed, $|\sigma_S - \sigma_M| = 0.26 \text{ dB m}^{-1}$ for the upper board and $|\sigma_S - \sigma_M| = 1.5 \text{ dB m}^{-1}$ for the second, 1.7 dB m^{-1} for the third, and 2.97 dB m^{-1} for the first position (see Fig. II.2.11). Likewise, the lowest mean squared error $\sqrt{\text{MSE}}$ for both configurations appears for the upper PCB, and the highest PEARSON correlation factor corresponds to the upper PCB. However, for the upper position an offset in the mean value μ is found ($|\mu_S - \mu_M| = 3.4 \text{ dB m}^{-1}$ for a vertical polarization and 4.1 dB m^{-1} for an horizontal one). These values were computed on the logarithmic values. The moving difference of averaged values over 40 MHz is given in Fig. II.2.13 for all the configurations. It appears, contrary to the previous configuration (with only two boards), that this quantity does not stay in a -10 dB to 10 dB range, but exceed $\pm 15 \text{ dB}$.

As previously, to evaluate the applicability of a full-wave simulation based model, the computation time is relevant. For four boards in the mock-up, the simulation took 4 h.

II.2.3 Applicability of the simulation model to determine statistics

First, we remind that the frequency limit of 3 GHz for all the results presented previously was due to the electric probe. For these frequencies, the cavity is not clearly overmoded (see section II.1.3.2). However, the frequency range of interest for this work extends up to several tens of gigahertz. In that frequency range, the cavity is overmoded. The aim of this section is to assess the number N of simulations to run in order to obtain statistics about couplings, while considering frequency ranges where the cavity is overmoded.

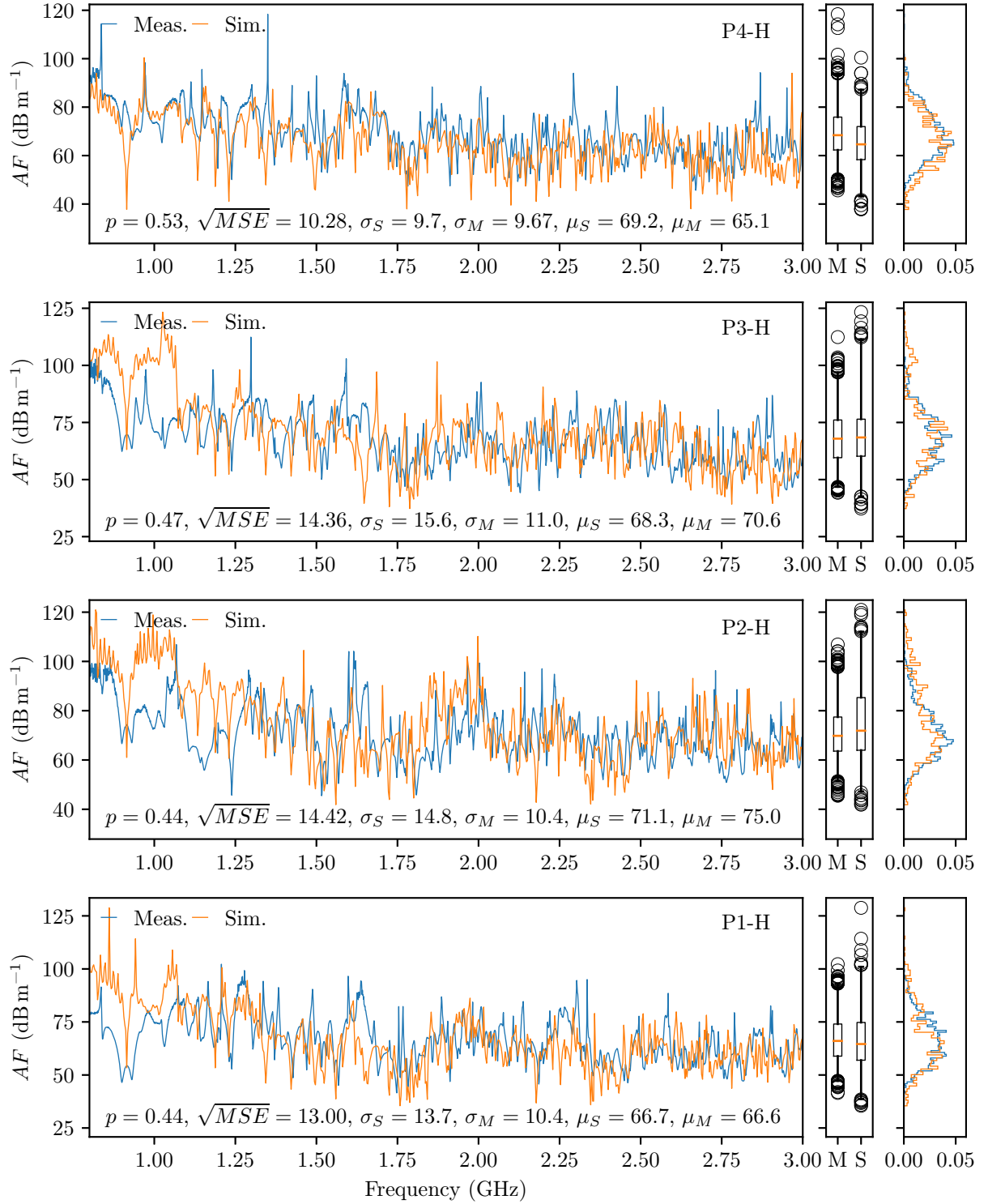


Fig. II.2.11 – Antenna factors for four **PCBs** with an electric field horizontally polarized (*i.e.* $\vec{E} = |\vec{E}|\vec{e}_x$). The **PCBs** are stacked, from the lower to the upper position in the stacking in the following order, meander (P1), straight (P2), L (P3) and I (P4).

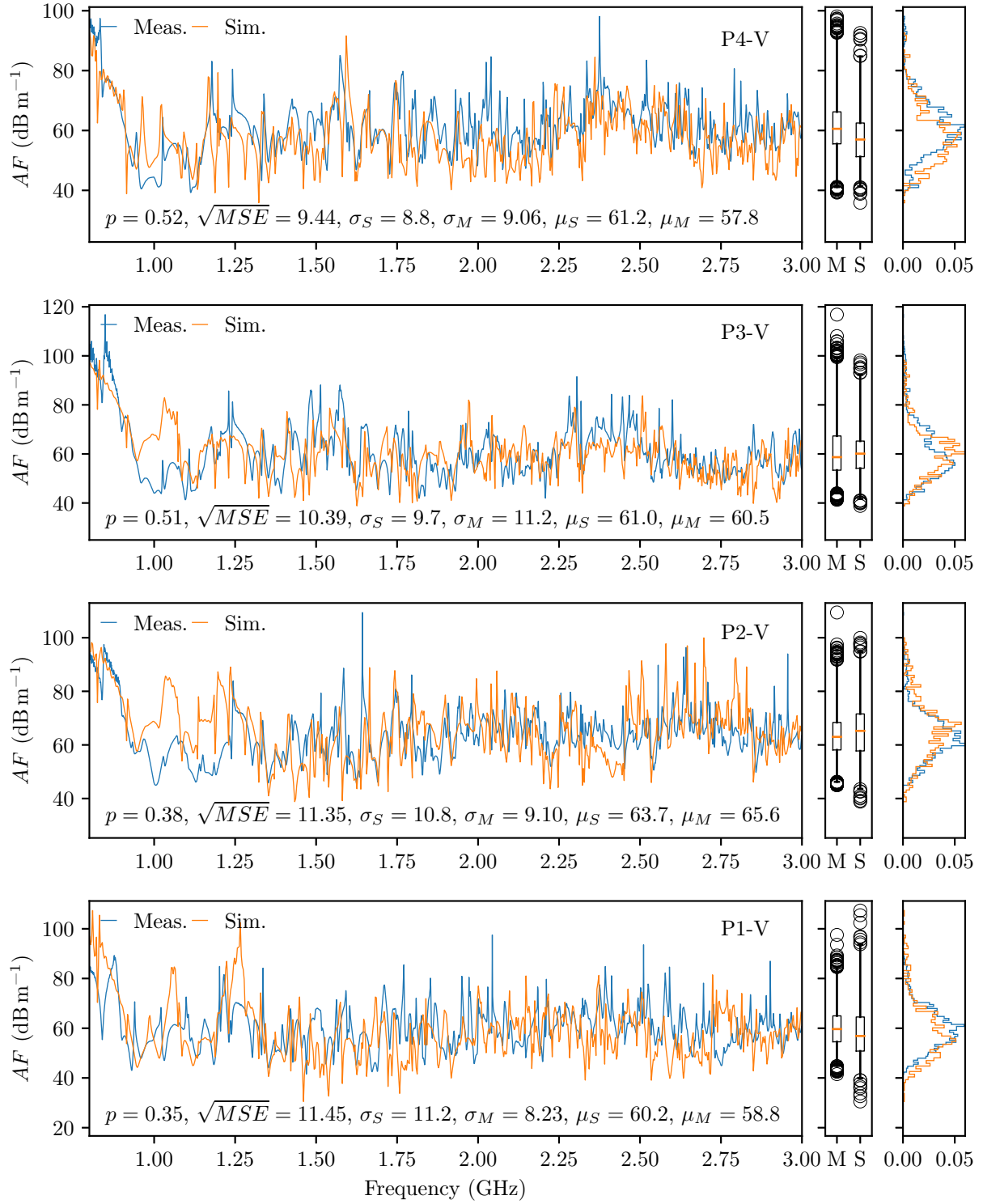


Fig. II.2.12 – Antenna factors for four PCBs with an electric field vertically polarized (*i.e.* $\vec{E} = |\vec{E}|\vec{e}_z$). The PCBs are stacked, from the lower to the upper position in the stacking in the following order, meander (P1), straight (P2), L (P3) and I (P4).

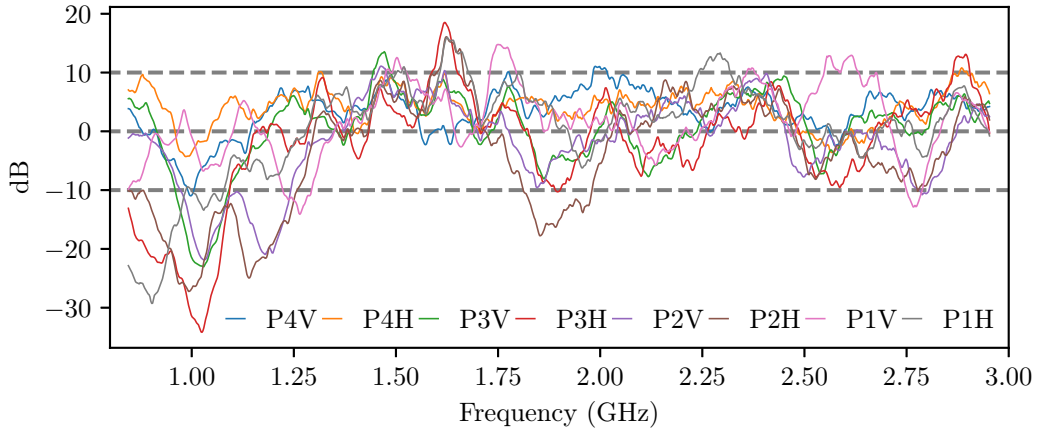


Fig. II.2.13 – Moving difference of averaged values over 40 MHz of the antenna factor AF , for the 8 configurations (two polarizations (V and H) and 4 boards (1 to 4)).

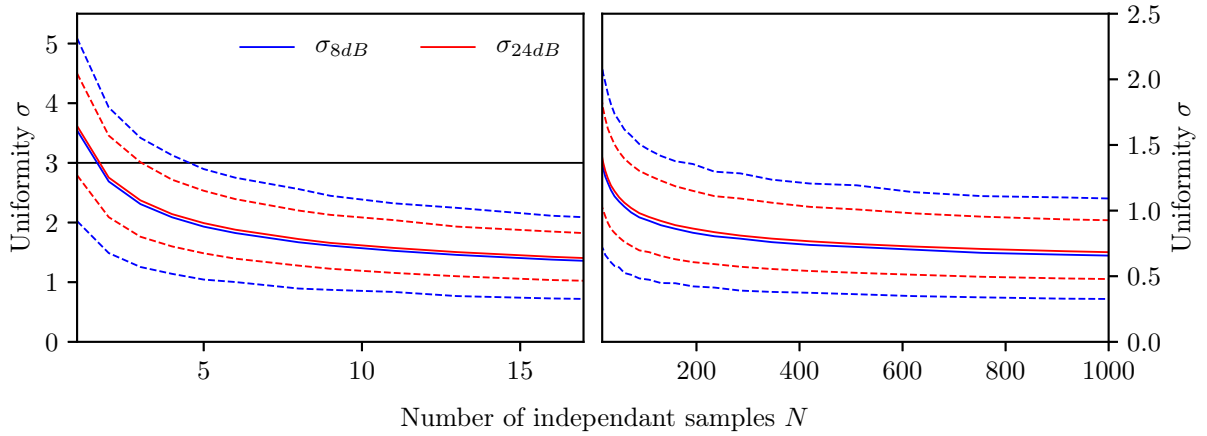


Fig. II.2.14 – Field uniformity in the working volume of a mode stirring chamber. Assessment for 8 and 24 positions. The dashed lines correspond to the percentiles, and the solid curve to the mean value.

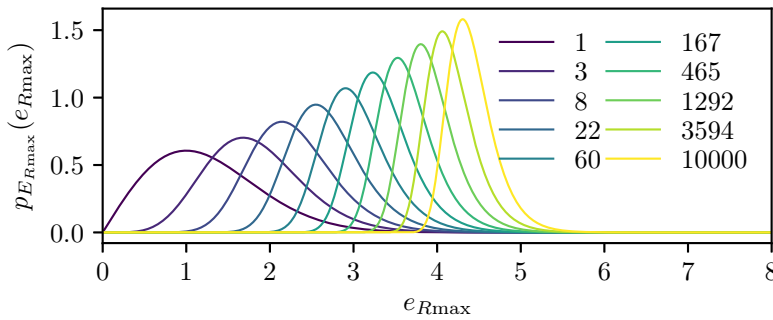


Fig. II.2.15 – Probability density functions of the maximum of the electric field from a sample of size N , for N from 1 to 10000.

e_{Rmax}	N
2.5	2
3.0	5
3.5	24
4.0	153
4.5	1281
5.0	13764

Table II.2.1 – Number N of samplings needed in order to reach $F_{Rmax}(e_{Rmax}) = 95\%$.

The HILL model As previously concluded, for some situations, the boundary conditions may be unknown. Thus, a statistical approach seems to be appropriate when the boundary conditions are randomized. We can then come back to the statistical description of the field in overmoded reverberant environments as stated by HILL. In that case, the frequency from which the cavity may be considered as overmoded is around 7 GHz (see equation (II.1.5) and section II.1.3.2).

Indeed, from [Hill, 1998], in lossless overmoded environments, the field may be expressed by a plane wave integral representation. Consequently, the field is assumed to be randomly polarized and statistically isotropic. This representation is theoretical, but may be approached by:

- increasing the losses to broaden the spectral occupancy of the modes;
- increasing the lowest frequency of the study to increase the mode density;
- changing the boundary conditions of the system N times to obtain N new sets of eigenmodes in the reverberant environment.

This representation is commonly used to describe [mode-stirred chambers \(MSCs\)](#) which are commonly cuboid cavities fitted with a stirrer that changes the boundary conditions inside the enclosure.

Here, the HILL's approach will help to describe a desktop computer chassis with random boundary conditions. To approach this statistical representation with a simulation software, one needs to run several simulations with different boundary conditions. The number N of simulations needs to be assessed by evaluating three quantities.

Field uniformity Users of [MSCs](#) have a criterion σ_{PdB} that characterizes the fluctuations of the maximum electric field amplitude sampled at several locations P of a [MSC](#). It allows to validate the statistical behavior of [MSCs](#). Theoretically, σ_{PdB} should be null. However, a reasonable threshold is given by international standards [International Electrotechnical Commission, 2010] which states that σ_{PdB} should stay below 3 dB. σ_{PdB} is computed as:

$$\sigma_{PdB} = 20 \log_{10} \left(1 + \frac{\sigma_P}{\langle |E_R|_{\max} \rangle} \right) \quad (\text{II.2.14})$$

where:

$$\langle |E_R|_{\max} \rangle = \frac{1}{N} \sum_N \max_{i \in P} (|E_R|_i) \quad (\text{II.2.15})$$

$$\sigma_P = \frac{1}{P-1} \sum_{i=1}^P (|E_R|_i - \langle |E_R|_{\max} \rangle)^2 \quad (\text{II.2.16})$$

$|E_R|_i$ is a cartesian component of the field ($|E_x|, |E_y|$ or $|E_z|$) sampled at the position i with $i \in [1, P]$, divided by the square root of the injected power in the cavity P_{in} . From Monte-Carlo iterations, we can compute σ_{PdB} as well as confidence intervals [Besnier and Démoulin, 2013, p220]. Fig. II.2.14 shows the 2.5% and 97.5% percentiles and the mean value of σ_{PdB} . It appears that if eight positions are considered, the inequality $\sigma_{8dB} < 3$ dB holds almost certainly as soon as $N \geq 6$.

Extreme field values Moreover, it is relevant to guarantee that the magnitude of the electric field can reach a given value in order to gain extreme field values (as well as extreme coupled currents). For an overmoded cavity, the cartesian component of the electric field E_R is RAYLEIGH distributed [Besnier and Démoulin, 2013, p. 198] and its [cumulative density function \(CDF\)](#) function is:

$$F_{E_R}(e_R) = 1 - e^{-\frac{e_R^2}{2\sigma^2}} \quad (\text{II.2.17})$$

and the [CDF](#) of the maximum over N independent measurements with different boundary conditions is:

$$\begin{aligned} F_{E_{R\max}}(e_{R\max}) &= \mathbb{P}[e_{R_1} < e_{R\max}; e_{R_i} < e_{R\max}; \dots; e_{R_N} < e_{R\max}] \\ &= \prod_{i=1}^N \mathbb{P}[e_{R_i} < e_{R\max}] = \prod_{i=1}^N F_{E_R}(e_{R\max}) \\ &= F_{E_R}(e_{R\max})^N \end{aligned} \quad (\text{II.2.18})$$

which [PDF](#) $p_{E_{R\max}}(e_{R\max})$ is:

$$p_{E_{R\max}}(E_{R\max}) = \frac{\partial}{\partial e_{R\max}} F_{E_R}(e_{R\max})^N = N \frac{e_{R\max}}{\sigma^2} F_{E_R}(e_{R\max})^{N-1} e^{-\frac{e_{R\max}^2}{2\sigma^2}} \quad (\text{II.2.19})$$

σ depends on the physical properties of the chamber. Fig. II.2.15 plots $p_{E_{R\max}}(e_{R\max})$ for several values of N . We observe that $p_{E_{R\max}}(e_{R\max})$ shifts to higher values when N increases. Thus fixing the probability for which $e_{R\max}$ occurs (95% for example) gives the minimal number N of independent samplings. Table II.2.1 gives the minimum sample size N required to guarantee a probability of 95% to reach a given maximal value $e_{R\max}$.

Independent samples It has to be noted that equations (II.2.14) and (II.2.19) hold when the N sample values are independent. This assertion is not always valid as, two consecutives measurements/simulations may not change enough the boundary conditions of the system such that these measurements/simulations are not statistically independent. In [Lemoine, 2008], the number of independent N_{eq} may be assessed from N and by the autocorrelation function r_N as:

$$N_{eq} \approx N \frac{1 - r_N}{1 + r_N} \quad (\text{II.2.20})$$

(II.2.20) was obtained by application of an autoregressive model of order 1. This equation holds only if N is sufficiently large and if r_N is below 0.55. For an autocorrelation value r_N of 0.1, only 82% of the samples are independent. Yet, r_N tends to decrease with the frequency.

Finally, the effective number of independent samples N_{eq} , the first order autocorrelation function r_N , the required distribution function of the maximum of cartesian component of the field and the field uniformity will determine the number N of sample values to record. This number N is likely to be of several tens, which leads to a computation time of hundreds of hours.

II.2.4 Conclusion

The ability of the full-wave simulation software to produce reliable data in a reasonable amount of time was assessed in this chapter. First, the electric field was determined at several random positions through a set of measurements and simulations. A good agreement was found between experimental and simulation data for the co-polarization case (same orientation of the electric field probe and the emitted field). This step allowed to define an accurate 3D model (in terms of details to take into account and in terms of parameterization of the simulation software) for the empty mock-up and to move forward.

As the aim of this work is to provide a model that can easily determine coupling in reverberant environments, full-wave simulations have been used to this end. Thus, four [PCBs](#) with microstrip transmission lines were installed inside the desktop computer chassis models. It was found that

the antenna factor is a convenient quantity to compare simulation and experimental data. Two configurations were tested, one with a stacking of two boards and a second one with four boards. To compare the results, moving differences of averaged values over 40 MHz were computed. This quantity is bounded between ± 10 dB for the two PCBs configurations. For the four boards configuration, this quantity varies much more around ± 17 dB.

Finally, on one hand we notice a significant uncertainty of the antenna factor for a deterministic configuration. We recall that it binds the field at the location of the aperture (an intentional electromagnetic interference (IEMI) for example) to the parasitic induced voltage at the end of the transmission lines. On the other hand, the high computation time assessed to apply the model in order to compute statistics is important. It has been assessed to be of hundreds of hours.

Therefore, it seems appropriate to investigate the other model identified in section I.2.7, *i.e.* the random coupling model (RCM), as it is statistical by design.

Part III

Application of the Random coupling model

Chapter III.1

Application of the Random Matrix Theory to determine couplings inside microwave cavities

Contents

III.1.1	Introduction	89
III.1.2	The Random Matrix Theory (RMT)	90
III.1.2.1	Introduction	90
III.1.2.2	Chaotic approach of microwave cavities	90
III.1.3	The random coupling model (RCM)	96
III.1.3.1	Introduction	96
III.1.3.2	Interest and application of the RCM	98
III.1.4	Set up of the RCM for the two configurations of interest	99
III.1.4.1	Configuration 1: plane wave coupling to a port inside a cavity	99
III.1.4.2	Configuration 2: Coupling between several ports in the cavity	101

III.1.1 Introduction

In this last part a third approach to model a desktop computer chassis will be set up. It is based on the [random matrix theory \(RMT\)](#) and is named the [random coupling model \(RCM\)](#).

This chapter intends to lay down how some properties of the [RMT](#) may be used to model overmoded cavities. Then, the [RCM](#) formulation will be introduced. Finally, the implementation of the [RCM](#) for both coupling configurations aforementioned, *i.e.* coupling between inner elements and coupling between an aperture and inner elements in the chassis, will be exposed.

The next two chapters are dedicated to the integration of apertures in the [RCM](#). As this model relies on Monte Carlo iterations, one has to determine an [RCM](#) formulation that can be easily implemented. That is the purpose of the fourth chapter, when coupled currents and voltages generated from the [RCM](#) will be compared to experimental data.

III.1.2 The Random Matrix Theory (RMT)

III.1.2.1 Introduction

Probably, the first work about random matrices was from WISHART in the 1930s [Wishart, 1928]. Then, numerous physicists and mathematicians found interest in this theory like WIGNER, MEHTA and DYSON. Especially, the theory was found to be useful for nuclear physics. In quantum physics, the energy levels of an atomic system are the eigenvalues of the Hamiltonian of the system. The Hamiltonian takes the form of a matrix, thus the resolution of such a problem leads to solve:

$$H\psi_n = E_n\psi_n \quad (\text{III.1.1})$$

which is known as an eigenvalue problem, where E_n are the eigenlevels and ψ_n the eigenfunctions.

For complex systems, the diagonalization of this operator is almost impossible. WIGNER found that the statistics of the eigenlevel spacings of the Hamiltonian of some systems are the same as those of the eigenvalue spacings of random matrices. In [Dyson, 1962], DYSON stated that:

"The statistical theory will not predict the detailed sequence of levels in anyone nucleus, but it will describe the general appearance and the degree of irregularity of the level structure that is expected to occur in any nucleus which is too complicated to be understood in detail."

Later, BOHIGAS, GIANNONI and SCHMIT awaked the attention and interest for the RMT. They stated in [Bohigas et al., 1984] that the RMT should apply to spectrum of all chaotic systems. We remind that the spectrum of a system is the set of its stationary energy levels, and that the spectrum of a matrix is the set of its eigenvalues. From then, it has become common to predict the statistical behavior of the eigenlevels of chaotic systems with the RMT. Especially, it was highlighted that the RMT allows to describe the trajectory of a moving point mass in chaotic 2D cavities, also known as billards, such as SINAÏ billards or BUMINOVICH stadiums. Then, 3D cavities were considered from the RMT perspective and especially microwave cavities (see next section). Readers who want to learn more about random matrices may refer to [Mehta, 2004] for the main mathematical results on the RMT and to [Stöckmann, 1999, Chap. 3] for an introduction to quantum chaos.

When dealing with chaotic systems, one can find the term “semi-classical limit”. It refers to the limit from which a system can be considered as chaotic. For microwave cavities, it indicates the threshold from which a cavity is overmoded (*i.e.* its eigenmode density is high).

III.1.2.2 Chaotic approach of microwave cavities

III.1.2.2.1 Brief review of RMT applications related to microwave cavities

The RMT predictions have been tested with success against microwave cavities in numerous cases. At first, only lossless superconducting 2D cavities were considered. Then losses were handled as well as 3D geometries. 2D means in reality that one dimension is small compared to the other two. Among all the studies published in the literature, one can cite in chronological order:

- [Stein et al., 1995]: one of the first comparison of RMT results against a 2D microwave billard;
- [So et al., 1995]: a 2D microwave billard with or without broken time symmetry is considered. It was the first application of the RMT for a microwave cavity with broken time symmetry.
- [Richter, 1999]: many comparisons of experimental data to the RMT for both 2D and 3D cavities, with and without super-conductivity;

- [Dembowski et al., 2002]: the spectrum of a generalized BUNIMOVICH stadium billiard is confronted against measured spectrum;
- [Kuhl et al., 2005]: absorptions (losses) are considered in a chaotic cavity from both analytical and experimental data;
- [Zheng, 2005]: the RMT is integrated into a circuit model to determine couplings in a 2D cavity. This result was generalized for 3D cavities later [Hemmady, 2006];
- [Gros et al., 2014]: application of the RMT to determine the shape of a MSC in order to obtain a chaotic behavior for the field inside the MSC.

We will see that the work of [Zheng, 2005] and [Hemmady, 2006] can be applied to determine couplings in reverberant environments.

III.1.2.2.2 Analogy between the spacing fluctuation of the spectrum, for random matrices and for (microwave) cavities

The eigenmodes of a wave system are included in its GREEN's function [Eric Akkermans, 2007]. Determining the GREEN's function requires to solve the HELMHOLTZ equation (we consider only scalar waves here):

$$(\Delta_{\vec{r}} + k^2)G(\vec{r}, \vec{r}', k) = \delta(\vec{r} - \vec{r}') \quad (\text{III.1.2})$$

In the lossless case, $G(\vec{r}, \vec{r}', k)$ may take the form:

$$G(k) = \frac{1}{k^2 - \mathcal{H}} \quad (\text{III.1.3})$$

where \mathcal{H} is the Hamiltonian of the system.

For integrable systems, \mathcal{H} may be determined analytically, while the other systems require numerical methods. However, when the mode density is high in the system, like in an overmoded cavity, numerical methods may be inapplicable as the computation time severely increases (refer to the previous part). Indeed, above a certain frequency threshold, the specific contribution of a given mode is no longer recognizable. It is then much more relevant to statistically describe the eigenlevels of the system, and the RMT can provide that statistical description.

Indeed, it exists a relation between the statistical properties of the fluctuations of the eigenlevels (the eigenfrequencies for microwave cavities) in the semi-classical limit (*i.e.* in overmoded cavities), and the statistical properties of eigenvalues of matrices taken from gaussian ensembles after an unfolding procedure [Mehta, 2004]. This procedure will be detailed later. That property is qualified as “universal” because it applies to all chaotic systems. Thus, the operator \mathcal{H} may be statistically replaced by large (theoretically of infinite size) square matrices H which are randomly drawn from different gaussian ensembles [Bohigas et al., 1984].

The choice of the ensemble depends on the system under consideration, and among these ensembles are:

- the gaussian orthogonal ensemble (GOE) which is the most common one and models time-reversal invariant systems;
- the gaussian unitary ensemble (GUE) which, contrarily to the GOE, allows to consider system without time-reversal symmetry [So et al., 1995].

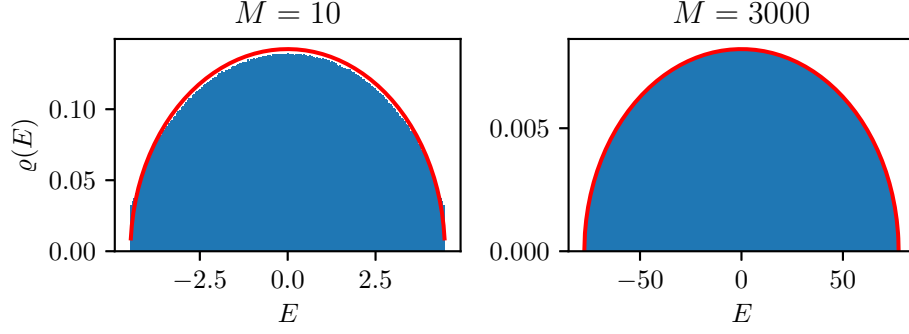


Fig. III.1.1 – Histograms (blue) of the eigenvalues of matrices from the **GOE** of $\sim 2\,000\,000$ random matrices of size M . The red curve is $\langle \varrho_{\text{GOE}}(E) \rangle$, the mean eigenvalue density around E (see equation (III.1.14)).

Issues considered in this work (couplings inside a desktop computer chassis) do not require to take into account broken time symmetry. Thus, the random matrices will be generated from the **GOE** throughout this work. To break the time reversality, one can add ferrites into the cavity as in [So et al., 1995]. The **GOE** defines real symmetric matrices whose elements are distributed according to a normal distribution with zero-mean. Diagonal elements have a variance σ^2 which is twice the one of off-diagonal elements. All the elements of the matrix are independent (while maintaining the symmetry). The choice of σ does not matter, and we set:

$$\sigma_{ii}^2 = 2\sigma_{ij}^2 \text{ for } i \neq j \quad (\text{III.1.4})$$

$$H_{ii} \sim \mathcal{N}(0, \sqrt{2}) \quad (\text{III.1.5})$$

$$H_{ij} \sim \mathcal{N}(0, 1) \text{ for } i \neq j \quad (\text{III.1.6})$$

III.1.2.2.3 Eigenvalues **PDF** of matrices from the **GOE**, unfolding procedure, nearest neighbor spacing distribution and number variance

Unfolding procedure To compare the Hamiltonian spectrum of a system (a cavity for example) with the prediction of the **RMT**, one needs to perform an unfolding procedure on both spectrums (Hamiltonian and **RMT**). The density $\varrho(E)$ of the eigenlevels close to the energy E may be split into a constant and a fluctuating part and reads

$$\varrho(E) = \bar{\varrho}(E) + \widetilde{\varrho(E)} \quad (\text{III.1.7})$$

The aim of the unfolding procedure is to remove the constant part $\bar{\varrho}(E)$ as it is specific to the system of interest, whereas the fluctuating part $\widetilde{\varrho(E)}$ is universal among all the chaotic systems. This procedure will enforce that the moving average of $\varrho(E)$ around ΔE is the same all along the spectrum. $\{E_n\}$ refers to the set of eigenlevels of a folded spectrum, and $\{\tilde{E}_n\}$ to the same set after an unfolding procedure. Comprehensive information about unfolding can be found in [Haake, 2010]. Instead of considering level densities, one can determine an accumulated level density:

$$\mathcal{N}(E) = \int_{-\infty}^E \varrho(E') dE' \quad (\text{III.1.8})$$

and, as for (III.1.7) we write:

$$\mathcal{N}(E) = \bar{\mathcal{N}}(E) + \widetilde{\mathcal{N}(E)} \quad (\text{III.1.9})$$

Let's define the eigenlevel density around the eigenlevel E by:

$$\varrho(E) = \frac{1}{N} \sum_{n=1}^N \delta(E - E_n) \quad (\text{III.1.10})$$

Beside that, the quantity $\bar{\varrho}(E)$ refers to the ensemble mean as defined in statistical physics. To determine $\bar{\varrho}(E)$, one can take advantage of a powerful property of the **RMT** which is the ergodicity of the eigenlevels [Haake, 2010]. Firstly, the ensemble mean for the first eigenlevel E_1 is written as [Haake, 2010, Eq 4.9.4]:

$$\bar{\varrho}(E) = \int \delta(E - E_1) p_{E_1, \dots, E_N}(e_1, \dots, e_N) dE^N \quad (\text{III.1.11})$$

where $p_{E_1, \dots, E_N}(e_1, \dots, e_N)$ is the joint **PDF** of the eigenlevels $\{E_n\}$. Secondly, the spectral average of the eigenlevel density $\varrho(E)$ around E and within ΔE is:

$$\langle \varrho(E) \rangle = \frac{1}{\Delta E} \int_{E-\Delta E/2}^{E+\Delta E/2} \varrho(E') dE' \quad (\text{III.1.12})$$

From the ergodicity property, one can equal (III.1.11) and (III.1.12): $\bar{\varrho}(E) = \langle \varrho(E) \rangle$ [Haake, 2010, Chap. 4.10]. Indeed, in the **RMT**, observables are computed by averaging over a set of random matrices H (quantities indicated by a bar). From the experimental point of view, the average is calculated over a part of a spectrum (the first N eigenfrequencies of a microwave cavity for example), and is designated by the operator $\langle \dots \rangle$ [Guhr et al., 1998, Section III.B.7]. The unfolding procedure must enforce:

$$\langle \varrho(E) \rangle = \frac{1}{N} \quad (\text{III.1.13})$$

For matrices from the **GOE**, an analytical formulation is available: $\langle \varrho_{\text{GOE}}(E) \rangle$ [Mehta, 2004] with

$$\langle \varrho_{\text{GOE}}(E) \rangle = \frac{1}{\Delta E} \int_{E-\Delta E/2}^{E+\Delta E/2} \varrho(E) dE' = \frac{\sqrt{2M - E^2}}{\pi M} \mathbf{1}_{[-\sqrt{2M}, \sqrt{2M}]}(E) \quad (\text{III.1.14})$$

(III.1.14) is known as the **WIGNER** semicircle distribution (M is the order of the matrices). Fig. III.1.1 shows histograms (blue) and theoretical **PDFs** (red) of the eigenlevels E for two samples of random matrices with different sizes M .

Procedures related to spectrum unfolding will be detailed in section III.4.2.2. Fig. III.1.2 depicts the histogram of the eigenvalues plotted in Fig. III.1.1 after an unfolding procedure. The obtained eigenlevel density is almost uniformly distributed as stated by equation (III.1.13). When considering microwave cavities, and to confront their spectrum to one computed by means of the **RMT**, $\bar{\mathcal{N}}(E)$ may be assessed by the **WEYL's** formula. This formula gives the number of modes in a cavity depending on its geometry [Gros et al., 2014].

Nearest neighbor spacing distribution To highlight the effect of the unfolding procedure, let's now consider the sequence of spacings of the sorted eigenlevel defined as:

$$s_n = E_{n+1} - E_n \quad (\text{III.1.15})$$

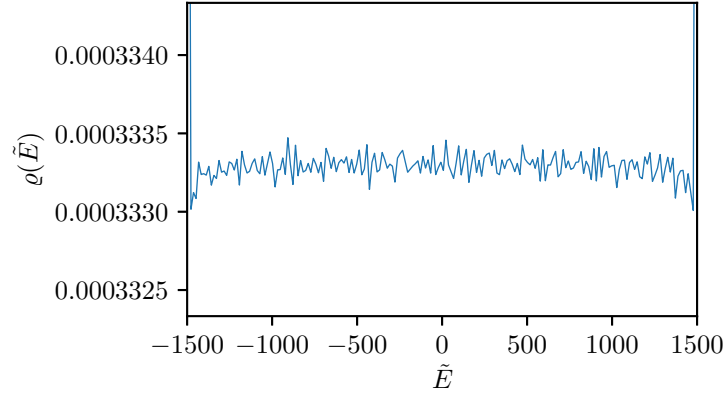


Fig. III.1.2 – Histogram of eigenvalues of random matrices of order $M = 3000$ after an unfolding procedure. The obtained empirical PDF is almost uniformly distributed.

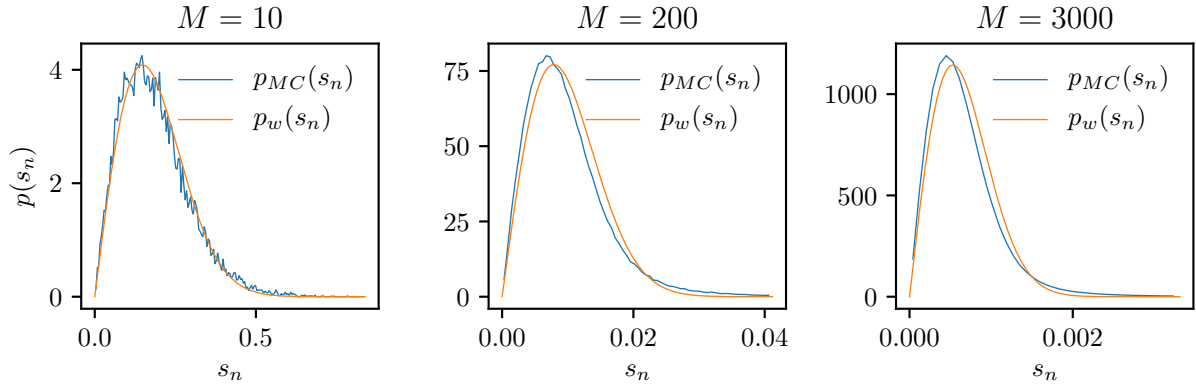


Fig. III.1.3 – Nearest neighbor spacing distribution $p(s_n)$ (with $s_n = E_{n+1} - E_n$) of the eigenvalues of random matrices from the GOE. $p_{MC}(s_n)$ is computed from Monte Carlo iterations, and $p_w(s_n)$ is computed from equation (III.1.16) (with $D = \langle E_{n+1} - E_n \rangle$, computed from the Monte Carlo iterations).

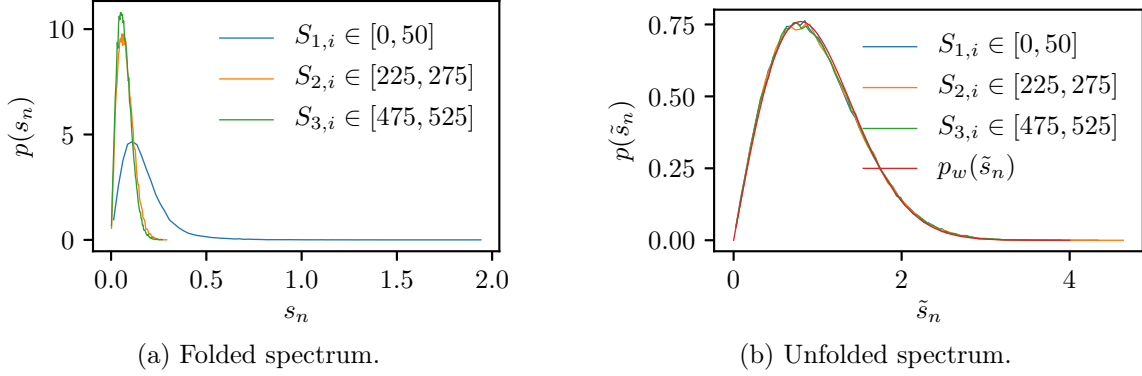


Fig. III.1.4 – Comparison between the spacing distribution at three locations (subscript j) within the folded and unfolded spectrums. The eigenvalues, of indexes $S_{j,i}$ within the ranges specified in the figures, were gathered and their spacing PDFs were computed. In Fig. III.1.4b, the theoretical PDF (with $D = 1$) has been added by using (III.1.16). We observe that all along the spectrum, the spacing distribution is similar for the unfolded spectrum. The three PDFs were from 3000 matrices of order $M = 1000$.

From the RMT the nearest neighbor spacing distribution s_n of the eigenvalues of matrices from the GOE is approximated by the WIGNER surmise and reads:

$$p_w(s_n) = \frac{\pi s_n}{2D} e^{-\frac{\pi}{4} \left(\frac{s_n}{D}\right)^2} \quad (\text{III.1.16})$$

with D the mean spacing between two consecutive eigenvalues: $D = \langle E_{n+1} - E_n \rangle$. $p_w(s_n)$ is an approximation as (III.1.16) was established for matrices of size $M = 2$, but is usually generalized. Fig. III.1.3 depicts $p_w(s_n)$ and the empirical PDF $p_{MC}(s_n)$ obtained from Monte Carlo iterations. We observe a slight difference between $p_w(s_n)$ and $p_{MC}(s_n)$.

The effect of the unfolding procedure is rendered by Fig. III.1.4. After the unfolding procedure, the new spacing distribution of the sorted eigenvalues $\tilde{s}_n = \tilde{E}_{n+1} - \tilde{E}_n$, must satisfy:

$$\int_0^\infty \tilde{s}_n p_w(\tilde{s}_n) d\tilde{s}_n = 1 \text{ and } \int_0^\infty p_w(\tilde{s}_n) d\tilde{s}_n = 1 \quad (\text{III.1.17})$$

A comparison of the nearest neighbor spacing distribution for three eigenvalue sets is given in Fig. III.1.4. These sets were extracted at three locations of the spectrum. We observe that the unfolding procedure allows to recover the same spacing distribution all along the spectrum.

Number variance The spacing distribution characterizes the eigenlevel at a short scale in the spectrum. To describe long-range correlations, the number variance $\Sigma^2(L)$ is of interest. $\Sigma^2(L)$ is related to the probability to have an eigenlevel \tilde{E}_2 when it is known that there is an eigenlevel \tilde{E}_1 in the spectrum. $\Sigma^2(L)$ is computed as the variance (the fluctuation) of the number of eigenlevels $n_{\tilde{E}}(L)$ within an interval $[\tilde{E}, \tilde{E} + L]$ of length L .

$$\Sigma^2(L) = \text{Var}(n_{\tilde{E}}(L)) \quad (\text{III.1.18})$$

For unfolded spectra, we know that $\langle n_{\tilde{E}}(L) \rangle = \bar{\mathcal{N}}(\tilde{E} + L) - \bar{\mathcal{N}}(\tilde{E}) = L$, thus $\Sigma^2(L)$ is:

$$\Sigma^2(L) = \langle (n_{\tilde{E}}(L) - L)^2 \rangle_{\tilde{E}} \quad (\text{III.1.19})$$

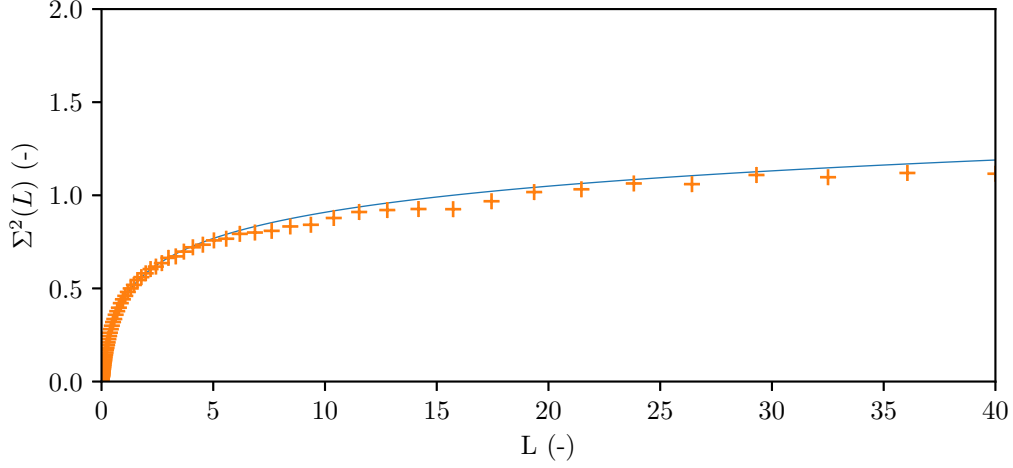


Fig. III.1.5 – Number variance $\Sigma^2(L)$ obtained from 48 matrices of order $M = 3000$ (orange crosses), and compared to $\Sigma_{\text{GOE}}^2(L)$ (solid blue curve).

When dealing with the [RMT](#), and for eigenvalues computed from matrices from the [GOE](#), $\Sigma_{\text{GOE}}^2(L)$ is given by [[Bohigas, 1991](#), C.17 and C.18]:

$$\Sigma_{\text{GOE}}^2(L) = \left[\frac{\text{Si}(\pi L)}{\pi} \right]^2 - \left[\frac{\text{Si}(\pi L)}{\pi} \right] + 2\Sigma_2^2(L) \quad (\text{III.1.20})$$

with:

$$\Sigma_2^2(L) = \frac{1}{\pi^2} (\log(2\pi L) + \gamma + 1 - \cos(2\pi L) - \text{Ci}(2\pi L)) + L \left(1 - \frac{2}{\pi} \text{Si}(2\pi L) \right) \quad (\text{III.1.21})$$

([III.1.20](#)) can be simplified to [[Bohigas, 1991](#), C.20]:

$$\Sigma_{\text{GOE}}^2(L) = \frac{2}{\pi^2} \left[\log(2\pi L) + 1 + \gamma - \frac{\pi^2}{8} \right] + O(L^{-1}) \quad (\text{III.1.22})$$

$\Sigma_{\text{GOE}}^2(L)$ can characterize long-range correlations within unfolded spectrum of matrices from the [GOE](#), and therefore also for chaotic microwave cavities with time symmetry. $\Sigma_{\text{GOE}}^2(L)$ can also be used as a comparative value when it comes to characterize unfolding procedures for spectra obtained through Monte Carlo iterations. Fig. [III.1.5](#) plots $\Sigma^2(L)$ computed from Monte Carlo iterations, as well as $\Sigma_{\text{GOE}}^2(L)$.

III.1.3 The random coupling model (RCM)

III.1.3.1 Introduction

The [random coupling model \(RCM\)](#) is a statistical circuit model. Thus, it helps to find a random impedance $\underline{\underline{Z}}^{\text{cav}}$ or a random admittance matrix $\underline{\underline{Y}}^{\text{cav}}$ of a cavity which statistically describes a given configuration. From, $\underline{\underline{Z}}^{\text{cav}}$ we have:

$$\vec{V} = \underline{\underline{Z}}^{\text{cav}} \vec{I} \quad (\text{III.1.23})$$

where \vec{V} is the voltage source vector applied to the N ports of the system ($\vec{V} = [V_1, V_2, \dots, V_N]$), and \vec{I} is the reaction current vector. A port may be the end of a cable of a transmission line or the input of an antenna for example. The eigenmodes density needs to be high enough in the system to consider

the cavity as a chaotic one [Zheng et al., 2006a]. This is a mandatory requirement to apply the RCM as it integrates the RMT. A criterion will be defined in section III.4.6 to evaluate the chaoticity of a system.

Two behaviors are merged into the RCM. The first one is related to the coupling between ports that would happen in free-space, *i.e.* without boundary conditions that make the system reverberant. For an electronic equipment, this can be done by removing its casing or by placing absorbers against the casing wall [Hemmady, 2006]. This behavior is characterized by a radiation impedance matrix $\underline{\underline{Z}}^{\text{rad}}$ which is frequency-dependent. This impedance may be determined either by simulations, by measurements in an anechoic chamber or by an ad hoc model. The second behavior takes into account the reverberant effects of the cavity due to the casing. The normalized impedance matrix $\underline{\underline{\xi}}$, that depends on the boundary conditions of the system, models the couplings between the ports and the eigenmodes of the cavity. From $\underline{\underline{Z}}^{\text{rad}}$ and $\underline{\underline{\xi}}$, the cavity impedance $\underline{\underline{Z}}^{\text{cav}}$ is defined as [Zheng et al., 2006a]:

$$\underline{\underline{Z}}^{\text{cav}} = \text{j}\Im \left\{ \underline{\underline{Z}}^{\text{rad}} \right\} + \left[\Re \left\{ \underline{\underline{Z}}^{\text{rad}} \right\} \right]^{1/2} \underline{\underline{\xi}} \left[\Re \left\{ \underline{\underline{Z}}^{\text{rad}} \right\} \right]^{1/2} \quad (\text{III.1.24})$$

Symbols $\Re[\cdot]$ and $\Im[\cdot]$ denote the real and imaginary parts of a complex quantity respectively. The deterministic (for a given cavity with fully determined boundary conditions) formulation of $\underline{\underline{\xi}}$ can be expressed as:

$$\underline{\underline{\xi}}(k) = -\frac{\text{j}}{\pi} \sum_{n=1}^M \frac{\Delta k^2 \vec{\Phi}_n \otimes \vec{\Phi}_n^T}{k^2(1 - \text{j}/Q) - k_n^2} \quad (\text{III.1.25})$$

where the summation over n covers the M modes (whose wavenumbers are k_n) taken into account inside the cavity. \otimes refers to the outer product. k is the wavenumber of interest and Δk^2 the mean spacing between two adjacent wavenumbers ($\Delta k^2 = \langle k_{n+1}^2 - k_n^2 \rangle$). Q is the quality factor of the unloaded cavity (without the ports). To obtain (III.1.25), the currents and voltages at the location of the ports are expanded into a basis of eigenfunctions ϕ_n of the cavity such as $(\nabla^2 + k^2)\phi_n = 0$. The full procedure to get (III.1.25) is given in [Zheng et al., 2006b] when there is only one port in the cavity or in [Zheng et al., 2006a] when several ports are present. Appendix C gives key steps to obtain (III.1.25). Equation (III.1.25) may be rewritten as:

$$\underline{\underline{\xi}}(k) = -\frac{\text{j}}{\pi} \sum_M \frac{\vec{\Phi}_n \otimes \vec{\Phi}_n^T}{\frac{k^2}{\Delta k^2} - \frac{k_n^2}{\Delta k^2} - \text{j}\alpha} \quad (\text{III.1.26})$$

where α is the loss factor of the cavity, $\alpha = \frac{k^2}{Q\Delta k^2}$. The set of normalized wavenumbers $\left\{ \tilde{k}_n^2 = \frac{k_n^2}{\Delta k^2} \right\}$ is difficult to assess, as it requires to determine the eigenfrequencies of the configuration. This is a hard problem for cavities which cannot be parametrized by means of separable variables (*i.e.* with complex boundary conditions). In a statistical approach, the interest is not focused on a specific cavity but on a set of various ones. Instead of determining the modes of the cavity, they are randomly drawn in accordance with the RMT [Hemmady, 2006]. Indeed, we remind that WIGNER has shown that the statistics of the eigenlevel spacings of the Hamiltonian of some systems are the same as those of the eigenvalues of random matrices from a given ensemble [Eugene P. Wigner, 1967]. Moreover, the BERRY hypothesis states that, for a chaotic cavity, an infinite sum of isotropic plane waves is a good statistical model to describe the eigenfunctions [Berry, 1977, Gradoni et al., 2014]. The RCM combines these two conceptual features.

The set $\left\{ \frac{k_n^2}{\Delta k^2} \right\}$ will be replaced by quantities provided by the RMT and specifically the eigenlevels $\{E_n\}$ will be changed into $\{\tilde{k}_n^2\}$ ($\tilde{E}_n \rightarrow \tilde{k}_n^2$ after the unfolding procedure). Several unfolding

methods are proposed [Hemmady et al., 2005, Zheng, 2005] and will be detailed in section III.4.2.2. Equation (III.1.25) may be rewritten like [Hemmady, 2006]:

$$\underline{\underline{\xi}} = -\frac{j}{\pi} \underline{\underline{W}} [\underline{\underline{\lambda}} - j\alpha \underline{\underline{1}}]^{-1} \underline{\underline{W}}^T \quad (\text{III.1.27})$$

This expression will be justified in section III.4.2.3. $\underline{\underline{W}}$ is a $M \times N$ real matrix, N is the number of ports in the system and M the number of modes taken into account inside the cavity. $\underline{\underline{W}}$ expresses the coupling of the modes to the ports of the system and its elements are normally distributed ($W_{ij} \sim \mathcal{N}(0, 1)$). $\underline{\underline{\lambda}}$ is a diagonal matrix populated with the eigenvalues of a matrix from the GOE after an unfolding procedure, as presented above. This formulation allows to practically apply the RCM. Indeed, to determine the statistics of $\underline{\underline{Z}}^{\text{cav}}$, a large number of Monte Carlo iterations shall be carried out. For each iteration, a matrix $\underline{\underline{\xi}}$ is randomly drawn (as $\underline{\underline{Z}}^{\text{rad}}$ is deterministic). Equation (III.1.27) is a formulation of equation (III.1.25) that can be easily implemented. However, these iterations may be time-consuming (depending on whether an aperture is considered and on the value of M), therefore some optimizations may be implemented and will be detailed in section III.4.3.2.

The loss factor α , may be assessed by several means. Using the WEYL's formula one can obtain: $\alpha = \frac{k^3 V}{2\pi^2 Q}$, where V is the volume of the cavity, and Q its quality factor [Hemmady et al., 2005]. In section III.5.3, a method to experimentally determine α will be proposed.

We should mention that the matrix $\underline{\underline{\xi}}$ does not take into account the *short-orbit* of the system. The *short-orbits* represent the energy emitted by a port in the system that returns directly to it or to another port of the system, without ergodically sampling the system. Another formulation of $\underline{\underline{\xi}}$ exists to take these *short-orbits* into account [Gradoni et al., 2014] but will not be exposed here.

III.1.3.2 Interest and application of the RCM

The major interest of the RCM is to avoid the determination of the eigenfrequencies of a cavity, which depends on its geometry. Instead, the geometry is assumed to be random, and statistics over a large number of geometries may be evaluated through Monte Carlo iterations. For each Monte Carlo iteration a matrix $\underline{\underline{\xi}}$ is randomly drawn. Moreover, the random couplings between the N ports and the M eigenmodes are set by the random vector $\vec{\Phi}_n$. Then, the free-space behavior contained in $\underline{\underline{Z}}^{\text{rad}}$ is superposed to $\underline{\underline{Z}}^{\text{cav}}$. After some iterations, statistics may be determined such as induced currents $\vec{I} = [I_1, I_2, \dots, I_N]$.

This method allows to take into account many possible cavity geometries including worse cases. Worse cases in *electromagnetic security* (EMSEC) are configurations for which the currents or voltages induced on ports of interest reach extreme values. In other words, extreme values correspond to specific cavity geometry with a given loss factor α for which induced currents or voltages reach extreme values in comparison to other geometries. Thus, right tails of PDF will refer to geometries (equivalently to a set of eigenmodes) that lead to the higher induced voltages or currents. The drawback is that no indication about the geometry that causes an extreme value can be retrieved from the RCM. In section III.4.7 some statistical quantities of interest for EMSEC will be listed.

Three quantities need to be determined to apply the RCM: the free-space impedance matrix $\underline{\underline{Z}}^{\text{rad}}$, the number of modes M taken into account inside the cavity and the loss parameter α . The free-space impedance matrix $\underline{\underline{Z}}^{\text{rad}}$ for all the tested configurations was determined from experimental data acquired by a VNA in free-space (see section III.5). Setting M is a trade-off between the number of modes to consider inside the cavity and the computation time. The choice of M will be suggested in section III.4.5. The parameter α is the most difficult to assess. It characterizes the losses inside the cavity and is frequency-dependent. It will be experimentally determined (see section III.5.3).

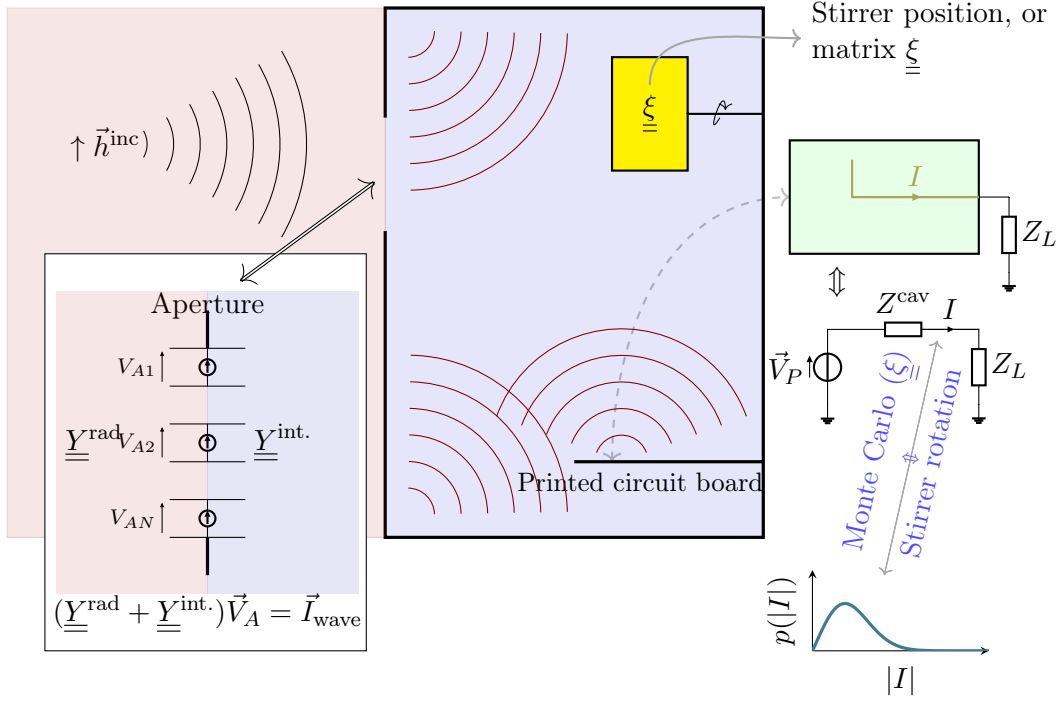


Fig. III.1.6 – Configuration 1 - Coupling between an aperture and an inner element of a desktop computer chassis.

III.1.4 Set up of the RCM for the two configurations of interest

In section I.1, two configurations of interest were mentioned. The first one intends to assess the coupling between a plane wave, through an aperture, to a port inside a cavity. This port may be a wire or a conductor on a PCB. In the second configuration, the coupling between ports in the cavity is evaluated. The aim of this section is to state how the RCM may be applied to both configurations, and which measurement setup will allow to evaluate the generated statistics from the RCM.

III.1.4.1 Configuration 1: plane wave coupling to a port inside a cavity

Fig. III.1.6 depicts the first configuration. It deals with a cavity having a PCB inside. This PCB has a conductor of interest etched on its surface. The cavity has an aperture cut on its front panel. In this scenario, the cavity is aggressed by an electromagnetic wave. Two regions may be defined, outside (in red) and inside (in blue) the cavity. These regions are connected by the aperture. When the cavity is aggressed from the exterior, a part of the incident energy penetrates inside the cavity through the aperture and excites the eigenmodes of the cavity. The coupling of the excited eigenmodes of the cavity on the conductor generates a current I on the PCB.

In order to assess the statistics of the induced current (flowing on a transmission line on the PCB for example) over the space of possible cavity geometries, the set of eigenmodes in the cavity needs to change. When this configuration is studied from the RCM point of view, the set of eigenmodes for a random cavity geometry is determined while drawing a normalized impedance matrix ξ as exposed in the previous section. When this configuration is measured, by means of the desktop computer chassis mock-up, the set of eigenmodes of the cavity is excited by setting a mode-stirrer at a random position inside the cavity. Indeed, it will change the boundary conditions thus, the set of eigenmodes will change. The matrix ξ and the mode-stirrer have the same purpose, to variate the set of eigenmodes in the cavity.

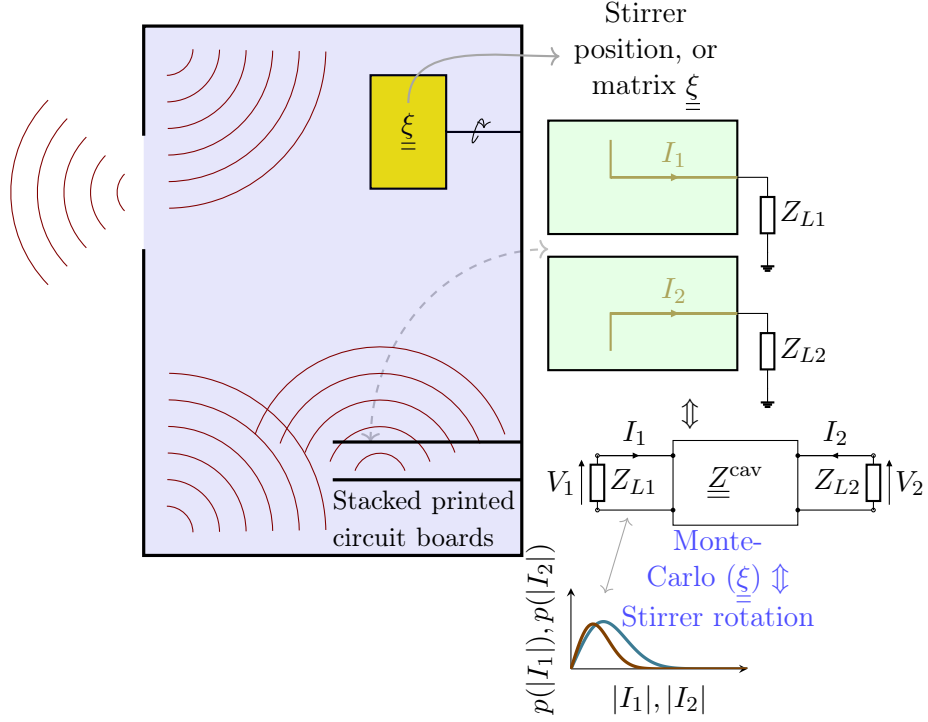


Fig. III.1.7 – Configuration 2 - Coupling between inner elements of a desktop computer chassis.

With the [RCM](#), the statistics of the current are assessed thanks to Monte Carlo iterations. For each iteration, a matrix $\underline{\xi}$ is drawn. When the statistics of the current have to be determined by measurements, one current value is acquired per mode-stirrer position, and statistics are computed from a large number of mode-stirrer angles.

For this configuration, one has to find a way to couple the energy of the incoming electromagnetic wave (located outside the cavity) into the interior of the cavity. In other words, the aperture has to be modeled as a way to link the two regions. A method was proposed in [[Harrington and Mautz, 1976](#)]: both regions were connected to each other thanks to two admittance matrices: $\underline{\underline{Y}}^{\text{rad}}$ for the outside part, and $\underline{\underline{Y}}^{\text{int.}}$ for the internal part of the cavity. This method is reviewed in section [III.2.4](#). The admittance matrix $\underline{\underline{Y}}^{\text{rad}}$ of the exterior region represents the aperture as a set of TE_{n0} modes. The method to obtain $\underline{\underline{Y}}^{\text{rad}}$ will be exposed in section [III.2](#).

The next step is to determine the admittance $\underline{\underline{Y}}^{\text{int.}}$. It stands for the reverberant behavior of the cavity (as previously exposed), and the contribution of the transmission line on the circuit board.

As indicated before, the [RCM](#) superposes the chaotic behavior of a cavity to the free-space behavior (which is deterministic). The free-space behavior is included in Z^{rad} ($\underline{\underline{Z}}^{\text{rad}}$ merges into Z^{rad} as there is only one port in the system). This impedance may be obtained by measuring the impedance of the transmission line with a [VNA](#), or by simulation. In that case, the simulation is much easier to perform than if the cavity was present. By placing the [PCB](#) in the cavity, the impedance seen from a port will become Z^{cav} , which includes Z^{rad} and $\underline{\xi}$.

All these quantities will be used to compute the current I . The full computation procedure with $\underline{\underline{Y}}^{\text{rad}}$, $\underline{\xi}$, Z^{rad} and the incident magnetic field \vec{h}^{inc} is explained in section [III.2.5](#). A comparison between [RCM](#) simulations and experimental data will be exposed in [III.5.7](#)

III.1.4.2 Configuration 2: Coupling between several ports in the cavity

In the second configuration, as depicted in Fig. III.1.7, only the coupling between ports is considered. The quantities of interest are the statistics of the currents flowing on the PCBs. This problem is simpler than the previous one, because there is no interaction with the aperture. The aperture will be taken into account through the loss parameter α included in $\underline{\underline{\xi}}$. Thus, equation (III.1.24) can be directly applied.

The impedance matrix $\underline{\underline{Z}}^{\text{rad}}$ stands for the free-space behavior of the ports associated to boards and can be obtained by measuring the scattering matrix $\underline{\underline{S}}$ of the boards. The relative positions of the boards must stay constant when they are measured and when the boards are placed into the cavity. That configuration will be studied in section III.5.5.

Chapter III.2

Determination of the impedance/admittance of an aperture

Contents

III.2.1	Introduction	102
III.2.2	First estimation	102
III.2.3	Second estimation	104
III.2.3.1	Definition of the modes $e_n(x, y)$	105
III.2.3.2	Integration over k , evaluated by residue computation	106
III.2.3.3	Determination of $G_{mn}^{\text{rad}}(k_0)$	107
III.2.3.4	Link between real and imaginary parts of $Y_{mn}^{\text{rad}}(k_0)$: the KRAMERS-KRONIG's relations	108
III.2.3.5	Determination of $B_{mn}^{\text{rad}}(k_0)$	109
III.2.4	Impedance of an aperture between two regions	109
III.2.5	Mapping of the aperture impedance to the RCM	112
III.2.5.1	Case where $N_P = 1$	115
III.2.5.2	Statistics of the elements of $\underline{\xi}$ when dealing with an aperture	116

III.2.1 Introduction

In this section, two methods will be exposed to determine the radiation impedance $\underline{Z}^{\text{rad}}$ or admittance $\underline{Y}^{\text{rad}}$ of an aperture. This matrix is required to apply the RCM when the statistics of a coupling between an aperture and a port in a cavity need to be determined.

The first method is proposed by [Caudron, 2012], and relies on the BABINET's principle. The second one, proposed by [Antonsen et al., 2011], expands the fields within the aperture and decomposes them as a superposition of modes belonging to an orthonormal basis.

III.2.2 First estimation

In [Caudron, 2012], a method is proposed to compute the impedance of an aperture. It is based on the BABINET's principle written for the impedance (see I.2.2.1.1).

$$Z^{\text{rad}} Z_{\text{planar dipole}} = \frac{\eta^2}{4} \quad (\text{III.2.1})$$

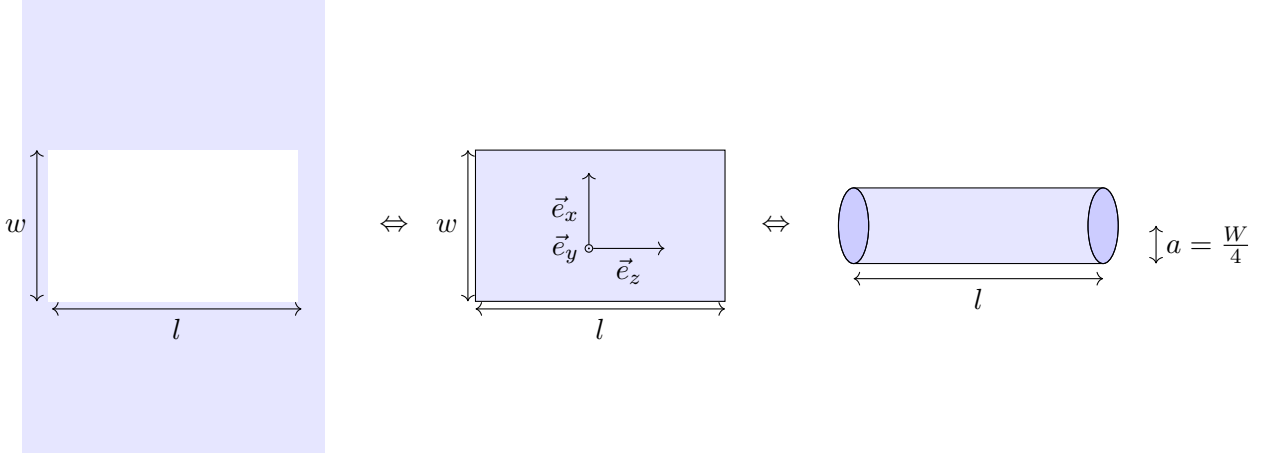


Fig. III.2.1 – Aperture impedance using the BABINET's equivalence principle, and the equivalence between a planar aperture and a wire.

where $Z_{\text{planar dipole}}$ is the impedance of the complementary screen of the aperture.

In [Newman, 1987], it was suggested that a planar antenna of width w and length l is equivalent to a wire dipole of same length and radius a , with $a = w/4$. Fig. III.2.1 shows the three equivalent geometries. Thus, $Z_{\text{planar dipole}}$ is taken to be the same as the input impedance of that wire, $Z_{\text{planar dipole}} = Z_{\text{wire},i}$. To determine $Z_{\text{wire},i}$, it was proposed in [Caudron, 2012] to compute the voltage V_i and the current I_i at the center of the wire, and to use the simple equation:

$$Z_{\text{wire},i} = \frac{V_i}{I_i} \quad (\text{III.2.2})$$

V_i and I_i were obtained by solving the POCKLINGTON's equation [Balanis, 2016, Chap 8.3.3] written using cylindrical coordinates:

$$\int_{-\frac{l}{2}}^{\frac{l}{2}} I_z(z') \left[\left(\frac{\partial^2}{\partial z'^2} + k^2 \right) G(\vec{r}, \vec{r}') \right] dz' = -j\omega\epsilon E_z^i(\rho = a) \quad (\text{III.2.3})$$

assuming that the wire is along the Oz axis, and with:

$$G(\vec{r}, \vec{r}') = \frac{1}{2\pi} \int_0^{2\pi} \frac{e^{-jkR}}{4\pi R} d\phi \quad (\text{III.2.4})$$

$$R = \sqrt{4a^2 \sin^2 \left(\frac{\phi'}{2} \right) + (z - z')^2} \quad (\text{III.2.5})$$

$$\vec{r} = [\rho, \phi, z]^T \quad (\text{III.2.6})$$

$$\vec{r}' = [\rho', \phi', z']^T \quad (\text{III.2.7})$$

\vec{r}' locates the sources, *i.e.* the current density on the wire, and \vec{r} is the observation location. The wire is driven by a magnetic-frill generator [Balanis, 2016, p 446]. It models a source, in the feed gap of the dipole, as a magnetic current density (circularly directed) over an annular aperture where a stands for its inner radius and b the outer one. The relation between the voltage V_i , at the center of the wire, and the field colinear to the wire $E_z^i(\rho = a)$ is given by:

$$E_z^i(\rho = a) = -V_i \left(\frac{k(b^2 - a^2)e^{-jkR_0}}{8 \ln \left(\frac{b}{a} \right) R_0^2} \left\{ 2 \left[\frac{k}{R_0} + j \left(1 - \frac{b^2 - a^2}{2R_0^2} \right) \right] + \frac{a^2}{R_0} \left[\left(\frac{k}{R_0} + j \left(1 - \frac{b^2 + a^2}{2R_0^2} \right) \right) \left(-jk - \frac{2}{R_0} \right) + \left(-\frac{1}{kR_0^2} + j \frac{b^2 + a^2}{R_0^3} \right) \right] \right\} \right) \quad (\text{III.2.8})$$

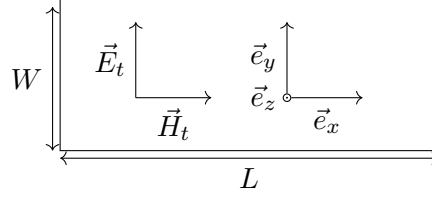


Fig. III.2.2 – Rectangular aperture

where $R_0 = \sqrt{z^2 + a^2}$.

To solve the integro-differential equation (III.2.3) the GALERKIN's technique was employed in [Caudron, 2012].

Such method and magnetic-frill generators are implemented in several full-wave simulation softwares such as [Burke and Poggio, 1981, NEC] and [FEKO]. However, for both simulation softwares, errors appear when considering electrically wide apertures. Here, we deal with apertures of the size of a CD reader. Therefore, it was not possible to move forward with that method. A second method is proposed in the next section.

III.2.3 Second estimation

Another formulation, more general, of the impedance of an aperture is given in [Antonsen et al., 2011]. The field transverse to \vec{e}_z may be expressed as a superposition of modes $\vec{e}_s(x_\perp)$ such as:

$$\vec{E}_t = \sum_s V_s \vec{e}_s(x_\perp) \quad (\text{III.2.9})$$

$$\vec{H}_t = \sum_s I_s \vec{e}_z \wedge \vec{e}_s(x_\perp) \quad (\text{III.2.10})$$

The coordinate system is indicated in Fig. III.2.2. The complete calculus, detailed in the appendix B, yields to the admittance of a planar aperture:

$$Y_{mn}^{\text{rad}}(k_0) = \sqrt{\frac{\epsilon_0}{\mu_0}} \int_{\mathbb{R}^3} \frac{1}{(2\pi)^3} \frac{2j}{k_0(k_0^2 - k^2)} \vec{e}_n \Delta \vec{e}_m^* d^3k \quad (\text{III.2.11})$$

with:

$$\Delta = \begin{pmatrix} k_0^2 - k_y^2 & k_x k_y & 0 \\ k_x k_y & k_0^2 - k_x^2 & 0 \\ 0 & 0 & 0 \end{pmatrix} \quad (\text{III.2.12})$$

\vec{e}_n are the FOURIER transform of the modes. This formulation is valid for any planar geometry. In what follows, the shape of the aperture is supposed to be rectangular (see Fig. III.2.2).

In what follows, we will write:

$$Y_{mn}^{\text{rad}}(k_0) = G_{mn}^{\text{rad}}(k_0) + jB_{mn}^{\text{rad}}(k_0) \quad (\text{III.2.13})$$

III.2.3.1 Definition of the modes $e_n(x, y)$

We assume that the tangential field \vec{E}_\perp at the aperture location is composed of the TE_{n0} modes of a rectangular waveguide [Gradoni et al., 2012].

We call $w(x)$ the gate function defined as:

$$w(x) = \begin{cases} 1, & |x| \leq \frac{1}{2} \\ 0, & \text{otherwise} \end{cases} \quad (\text{III.2.14})$$

We define the not-normalized mode $e'_n(x, y)$:

$$e'_n(x, y) = \sin(k_n x) w\left(\frac{x - L/2}{L}\right) w\left(\frac{y}{W}\right) \quad (\text{III.2.15})$$

where $k_n = \frac{n\pi}{L}$ and we search the normalized mode $e_n(x, y)$, such that:

$$\int \int_{\text{aperture}} |e_n(x, y)|^2 dx dy = 1 \quad (\text{III.2.16})$$

$$\int \int_{\text{aperture}} |e_n(x, y)|^2 dx dy = 1 \Leftrightarrow e_n(x, y) = \frac{e'_n(x, y)}{\sqrt{\int_0^W \int_{-L/2}^{L/2} \sin(k_n x)^2 dx dy}} \quad (\text{III.2.17})$$

$$= \frac{e'_n(x, y)}{\sqrt{\frac{LW}{2}}} \quad (\text{III.2.18})$$

$$= e'_n(x, y) \sqrt{\frac{2}{LW}} \quad (\text{III.2.19})$$

Therefore, the normalized modes are:

$$e_n(x, y) = \sin(k_n x) \sqrt{\frac{2}{LW}} w\left(\frac{x - L/2}{L}\right) w\left(\frac{y}{W}\right) \quad (\text{III.2.20})$$

$$\vec{e}_n(x, y) = e_n \vec{e}_y \quad (\text{III.2.21})$$

III.2.3.1.1 Determination of their Fourier transform

To compute (III.2.11), the FOURIER transform of (III.2.20) must be determined thanks to:

$$\mathcal{F}(e_n(x, y)) = \mathcal{F}(e_n(\vec{x}_\perp)) = \int_{\mathbb{R}^2} e_n(x, y) e^{-j\vec{k}\vec{x}_\perp} dx dy \quad (\text{III.2.22})$$

After calculation, we obtain:

$$\mathcal{F}(e_n(x, y)) = \tilde{e}_n(k_x, k_y) = \tilde{e}_n(\vec{k}_\perp) = \frac{\sqrt{2}\pi n \sqrt{LW} (-1 + (-1)^n e^{ik_x L}) \text{sinc}\left(\frac{k_y W}{2}\right)}{k_x^2 L^2 - \pi^2 n^2} \quad (\text{III.2.23})$$

Thus:

$$\vec{\tilde{e}}_n = \frac{\sqrt{2}\pi n \sqrt{LW} (-1 + (-1)^n e^{ik_x L}) \text{sinc}\left(\frac{k_y W}{2}\right)}{k_x^2 L^2 - \pi^2 n^2} \vec{e}_y \quad (\text{III.2.24})$$

III.2.3.2 Integration over k , evaluated by residue computation

In order to remove the pole in $k = k_0$, we change the variables (k_x, k_y, k_z) of equation (III.2.11) into (k, θ, φ) following:

$$d^3k = k^2 \sin \theta dk d\theta d\varphi \quad (\text{III.2.25})$$

$$k_x = k \sin \theta \cos \varphi \quad (\text{III.2.26})$$

$$k_y = k \sin \theta \sin \varphi \quad (\text{III.2.27})$$

$$k_z = k \cos \theta \quad (\text{III.2.28})$$

$$|\vec{k}| = \sqrt{k_x^2 + k_y^2 + k_z^2} \quad (\text{III.2.29})$$

Thus:

$$Y_{mn}^{\text{rad}}(k_0) = \sqrt{\frac{\epsilon_0}{\mu_0}} \int_0^\pi \int_0^{2\pi} \int_0^\infty \frac{k^2 \sin \theta}{(2\pi)^3} \frac{2j}{k_0(k_0^2 - k^2)} \vec{e}_n \Delta \vec{e}_m^* dk d\theta d\varphi \quad (\text{III.2.30})$$

$$= \int_0^\pi \int_0^{2\pi} \int_0^\infty f(k, \theta, \varphi) dk d\theta d\varphi \quad (\text{III.2.31})$$

with $f(k, \theta, \varphi) = \sqrt{\frac{\epsilon_0}{\mu_0}} \frac{k^2 \sin \theta}{(2\pi)^3} \frac{2j}{k_0(k_0^2 - k^2)} \vec{e}_n \Delta \vec{e}_m^*$.

We derive the residue in $k = k_0$:

$$\text{Res}(f(k, \theta, \varphi), k_0) = \lim_{k \rightarrow k_0} f(k, \theta, \varphi)(k - k_0) \quad (\text{III.2.32})$$

$$= \lim_{k \rightarrow k_0} \sqrt{\frac{\epsilon_0}{\mu_0}} \frac{k^2}{(2\pi)^3} \frac{2j}{k_0(k_0^2 - k^2)} \vec{e}_n \Delta \vec{e}_m^* (k - k_0) \sin \theta \quad (\text{III.2.33})$$

$$= \lim_{k \rightarrow k_0} \sqrt{\frac{\epsilon_0}{\mu_0}} \frac{k^2}{(2\pi)^3} \frac{2j}{k_0(k_0 - k)(k_0 + k)} \vec{e}_n \Delta \vec{e}_m^* (k - k_0) \sin \theta \quad (\text{III.2.34})$$

$$= - \lim_{k \rightarrow k_0} \sqrt{\frac{\epsilon_0}{\mu_0}} \frac{k^2}{(2\pi)^3} \frac{2j}{k_0(k_0 + k)} \vec{e}_n \Delta \vec{e}_m^* \sin \theta \quad (\text{III.2.35})$$

$$= - \sqrt{\frac{\epsilon_0}{\mu_0}} \frac{j}{(2\pi)^3} \vec{e}_n \Delta \vec{e}_m^* \sin \theta \quad (\text{III.2.36})$$

In $k = k_0$, we have $k_0^2 = k_x^2 + k_y^2 + k_z^2$. We can compute:

$$2j\pi \int_0^\pi \int_0^{2\pi} \text{Res}(f(k, \theta, \varphi), k_0) d\theta d\varphi = -2j\pi \int_0^\pi \int_0^{2\pi} \sqrt{\frac{\epsilon_0}{\mu_0}} \frac{j}{(2\pi)^3} \vec{e}_n \Delta \vec{e}_m^* \sin \theta d\theta d\varphi \quad (\text{III.2.37})$$

$$= \sqrt{\frac{\epsilon_0}{\mu_0}} \int_0^\pi \int_0^{2\pi} \frac{1}{(2\pi)^2} \vec{e}_n \Delta \vec{e}_m^* \sin \theta d\theta d\varphi \quad (\text{III.2.38})$$

Using (III.2.12) and (III.2.24):

$$\vec{e}_n \Delta \vec{e}_m^* = \frac{8\pi^2 LmnW(k_0 - k_x)(k_0 + k_x)j^{m-n} \text{sinc}\left(\frac{k_y W}{2}\right)^2 \sin\left(\frac{1}{2}(k_x L + \pi m)\right) \sin\left(\frac{1}{2}(k_x L + \pi n)\right)}{(k_x L - \pi m)(k_x L + \pi m)(k_x L - \pi n)(k_x L + \pi n)} \quad (\text{III.2.39})$$

This term is purely real when $m - n$ is even. In that case, the residue merges with $G_{mn}^{\text{rad}}(k_0)$. $B_{mn}^{\text{rad}}(k_0)$ will be computed thanks to the KRAMERS-KRONIG relations (see section III.2.3.4). Further, it can be demonstrated that when $m - n$ is odd, the integral (III.2.38) equals zero.

III.2.3.3 Determination of $G_{mn}^{\text{rad}}(k_0)$

For $m - n$ even:

$$G_{mn}^{\text{rad}}(k_0) = \sqrt{\frac{\epsilon_0}{\mu_0}} \int_0^\pi \int_0^{2\pi} \frac{\sin \theta}{(2\pi)^2} \vec{e}_n \Delta \vec{e}_m^* d\theta d\varphi \quad (\text{III.2.40})$$

III.2.3.3.1 Change of integration variables

We perform another change of integration variables (θ, φ) to (k_x, k_y) . It allows to analytically compute the integral of $G_{mn}^{\text{rad}}(k_0)$ over k_y . We have:

$$k_x^2 + k_y^2 = k_0^2 \sin^2 \theta (\cos^2 \varphi + \sin^2 \varphi) = k_0^2 \sin^2 \theta \quad (\text{III.2.41})$$

with:

$$\theta = \arctan \left(\frac{\sqrt{k_x^2 + k_y^2}}{k_z} \right) = \arctan \left(\frac{\sqrt{k_x^2 + k_y^2}}{\sqrt{k_0^2 - k_x^2 - k_y^2}} \right) \quad (\text{III.2.42})$$

and:

$$\varphi = \arctan \left(\frac{k_y}{k_x} \right) \quad (\text{III.2.43})$$

We can now determine the new limits of the integral. When θ goes from 0 to π , $\sin^2(\theta)$ oscillates from 0 to 1. Thus:

$$k_x^2 + k_y^2 \leq k_0^2 \Rightarrow -\sqrt{k_0^2 - k_x^2} \leq k_y \leq \sqrt{k_0^2 - k_x^2} \quad (\text{III.2.44})$$

and,

$$k_x^2 \leq k_0^2 \Rightarrow -k_0 \leq k_x \leq k_0 \quad (\text{III.2.45})$$

The Jacobian determinant of the transformation is:

$$|J| = \left| \begin{array}{cc} \frac{d\theta}{dk_x} & \frac{d\theta}{dk_y} \\ \frac{d\varphi}{dk_x} & \frac{d\varphi}{dk_y} \end{array} \right| = \left| \begin{array}{cc} \frac{k_x}{\sqrt{k_x^2 + k_y^2} \sqrt{k_0^2 - k_x^2 - k_y^2}} & \frac{k_y}{\sqrt{k_x^2 + k_y^2} \sqrt{k_0^2 - k_x^2 - k_y^2}} \\ -\frac{k_y}{k_x^2 + k_y^2} & \frac{k_x}{k_x^2 + k_y^2} \end{array} \right| = \frac{1}{\sqrt{k_x^2 + k_y^2} \sqrt{k_0^2 - k_x^2 - k_y^2}} \quad (\text{III.2.46})$$

Using the equality: $\sin(\arctan(x)) = \frac{x}{\sqrt{1+x^2}}$, we get $\sin \theta = \sin \left(\arctan \left(\frac{\sqrt{k_x^2 + k_y^2}}{k_z} \right) \right) = \frac{\sqrt{k_x^2 + k_y^2}}{k_0}$,

At the end, we obtain:

$$\begin{aligned} G_{mn}^{\text{rad}}(k_0) &= \sqrt{\frac{\epsilon_0}{\mu_0}} \int_{-k_0}^{k_0} \int_{-\sqrt{k_0^2 - k_x^2}}^{\sqrt{k_0^2 - k_x^2}} \frac{1}{(2\pi)^2} \vec{e}_n \Delta \vec{e}_m^* |J| \sin \theta dk_x dk_y \\ &= \sqrt{\frac{\epsilon_0}{\mu_0}} \int_{-k_0}^{k_0} \int_{-\sqrt{k_0^2 - k_x^2}}^{\sqrt{k_0^2 - k_x^2}} \frac{1}{(2\pi)^2} \vec{e}_n \Delta \vec{e}_m^* \frac{1}{k_0} \frac{1}{\sqrt{k_0^2 - k_x^2 - k_y^2}} dk_x dk_y \end{aligned} \quad (\text{III.2.47})$$

III.2.3.3.2 Integration over k_y

It is possible to compute analytically the integral (III.2.47) over k_y thanks to an algebraic computation software [Wolfram Research, Inc., 2018], which leads to:

$$G_{mn}^{\text{rad}}(k_0) = \int_{-k_0}^{k_0} \frac{A(B-C)}{D} dk_x \quad (\text{III.2.48})$$

where

$$A = j^{m-n} LmnW(k_0 - k_x)(k_0 + k_x) \sin\left(\frac{1}{2}(k_x L + \pi m)\right) \sin\left(\frac{1}{2}(k_x L + \pi n)\right) \quad (\text{III.2.49})$$

$$B = \frac{\pi \left(\pi W \sqrt{k_0^2 - k_x^2} \mathbf{H}_0 \left(\sqrt{k_0^2 - k_x^2} W \right) - 2 \right) J_1 \left(\sqrt{k_0^2 - k_x^2} W \right)}{W \sqrt{k_0^2 - k_x^2}} \quad (\text{III.2.50})$$

$$C = \pi \left(\pi \mathbf{H}_1 \left(\sqrt{k_0^2 - k_x^2} W \right) - 2 \right) J_0 \left(\sqrt{k_0^2 - k_x^2} W \right) \quad (\text{III.2.51})$$

$$D = 60\pi k_0(k_x L - \pi m)(k_x L + \pi m)(k_x L - \pi n)(k_x L + \pi n) \quad (\text{III.2.52})$$

$\mathbf{H}_0(x)$ and $\mathbf{H}_1(x)$ are STRUVE's functions of order 0 and 1, and J_0 and J_1 are BESSEL's functions of first kind (order 0 and 1 respectively).

As we did not find a way to analytically integrate (III.2.48), a numerical integration over k_x was run (see section III.3.3).

III.2.3.4 Link between real and imaginary parts of $Y_{mn}^{\text{rad}}(k_0)$: the KRAMERS-KRONIG's relations

A general admittance Y may be written as:

$$Y(\omega) = G(\omega) + jB(\omega) \quad (\text{III.2.53})$$

Where $G(\omega)$ is the conductance and $B(\omega)$ is the susceptance. The real and imaginary parts of an admittance are linked together by the KRAMERS-KRONIG relations ([Van Kampen and Lurçat, 1961]):

$$G(\omega) = \frac{1}{\pi} P \int_{-\infty}^{\infty} \frac{B(\omega')}{\omega' - \omega} d\omega' \quad (\text{III.2.54})$$

$$B(\omega) = -\frac{1}{\pi} P \int_{-\infty}^{\infty} \frac{G(\omega')}{\omega' - \omega} d\omega' \quad (\text{III.2.55})$$

where P stands for CAUCHY principal value. (III.2.54) and (III.2.55) may also be written:

$$G(\omega) = \frac{2}{\pi} P \int_0^{\infty} \frac{\omega' B(\omega')}{\omega'^2 - \omega^2} d\omega' \quad (\text{III.2.56})$$

$$B(\omega) = -\frac{2\omega}{\pi} P \int_0^{\infty} \frac{G(\omega')}{\omega'^2 - \omega^2} d\omega' \quad (\text{III.2.57})$$

Those two equations are set by the causality necessity $Y(-\omega) = Y(\omega)^*$. These relations will be applied to compute $B_{mn}^{\text{rad}}(k_0)$.

III.2.3.5 Determination of $B_{mn}^{\text{rad}}(k_0)$

Thanks to (III.2.57), and by replacing ω by $k_0 c$, and ω' by $k c$:

$$B_{mn}^{\text{rad}}(k_0) = -\frac{2k_0}{\pi} P \int_0^\infty \frac{G_{mn}^{\text{rad}}(k)}{k^2 - k_0^2} dk = \frac{2k_0}{\pi} P \int_0^\infty \frac{G_{mn}^{\text{rad}}(k)}{k_0^2 - k^2} dk \quad (\text{III.2.58})$$

The product $\frac{2k_0}{k_0^2 - k^2} \vec{e}_n \Delta \vec{e}_m^*$ (obtain from (III.2.58) with the expression of $G_{mn}^{\text{rad}}(k)$ given in equation (III.2.47)) yields a contribution in k_0^{-1} that adds an inductive part that would not be taken into account by the transformation the equation (III.2.58). Thus, an additional term $B_{mn}^{\text{rad,ms}}(k_0)$ is added to (III.2.58), giving:

$$B_{mn}^{\text{rad}}(k_0) = \frac{2k_0}{\pi} P \int_0^\infty \frac{G_{mn}^{\text{rad}}(k)}{k_0^2 - k^2} dk + B_{mn}^{\text{rad,ms}}(k_0) \quad (\text{III.2.59})$$

This term has the expression [Gradoni et al., 2015]:

$$B_{mn}^{\text{rad,ms}}(k_0) = \sqrt{\frac{\epsilon_0}{\mu_0}} \int_{\mathbb{R}^3} \vec{e}_n \vec{e}_m^* \frac{2k_x^2}{k^2 k_0 (2\pi)^3} dk_x dk_y dk_z \quad (\text{III.2.60})$$

III.2.3.5.1 Integration of $B_{mn}^{\text{rad,ms}}(k_0)$ over k_z

By replacing \vec{e}_n and \vec{e}_m^* by their expressions given in equation (III.2.24), we get:

$$B_{mn}^{\text{rad,ms}}(k_0) = \int_{\mathbb{R}^3} \frac{k_x^2 L m n W j^{m-n} \text{sinc}\left(\frac{k_y W}{2}\right)^2 \sin\left(\frac{1}{2}(k_x L + \pi m)\right) \sin\left(\frac{1}{2}(k_x L + \pi n)\right)}{60\pi^2 k^2 k_0 (k_x L - \pi m)(k_x L + \pi m)(k_x L - \pi n)(k_x L + \pi n)} dk_x dk_y dk_z \quad (\text{III.2.61})$$

The integration over k_z , thanks to an algebraic computation software [Wolfram Research, Inc., 2018], gives:

$$B_{mn}^{\text{rad,ms}}(k_0) = \frac{m n L W j^{m-n}}{60\pi k_0} \int_{\mathbb{R}^2} \frac{k_x^2 \sin\left(\frac{1}{2}(k_x L + \pi m)\right) \sin\left(\frac{1}{2}(k_x L + \pi n)\right)}{(\pi m - k_x L)(k_x L + \pi m)(\pi n - k_x L)(k_x L + \pi n)} \frac{\text{sinc}\left(\frac{k_y W}{2}\right)^2}{\sqrt{k_x^2 + k_y^2}} dk_x dk_y \quad (\text{III.2.62})$$

This integral cannot be analytically computed over k_x and k_y .

The quantities $G_{mn}^{\text{rad}}(k_0)$, $B_{mn}^{\text{rad}}(k_0)$ and $B_{mn}^{\text{rad,ms}}(k_0)$ will be numerically computed in the next section.

The next step, as presented in section III.1.4, is to bind this aperture admittance to the admittance of the cavity $\underline{Y}^{\text{int}}$. Moreover, the plane wave will be modeled as an equivalent current vector \vec{I}^{inc} on the aperture (see Fig. III.2.3a).

III.2.4 Impedance of an aperture between two regions

This section takes up a method proposed initially in [Harrington and Mautz, 1976]. It aims to give a general formulation for aperture problems.

The studied configuration consists of two regions separated by a perfect conductor with a planar aperture. These regions are coupled through that aperture. In region 1, on the left side of the aperture, remote impressed sources \vec{J}^{inc} and \vec{M}^{inc} create an electromagnetic field \vec{h}^{inc} that can couple onto the aperture as presented in Fig. III.2.3a. Region 2, on the right side of the aperture, is open to infinity. The problem is split into two subproblems, and for each of these an equivalent system is set by applying the equivalent principle as exposed in [Balanis, 2012, sec. 7.8]. The fields inside the imaginary volume are considered as null.

In region 1 (see Fig. III.2.3b), just to the left of the aperture, the electric field is $\vec{E}_{(1)}^{\text{tot}}|_{z=0-}$. By impressing an equivalent surfacic magnetic current density \vec{M}_A , the field in the original problem, *i.e.* \vec{E}^{tot} , is recovered since. \vec{M}_A can be expressed as:

$$\vec{M}_A = \vec{e}_z \wedge \vec{E}_{(1)}^{\text{tot}}|_{z=0} \quad (\text{III.2.63})$$

The fields are null on the right of the aperture from the region 1 point of view. The total fields \vec{E}^{tot} and \vec{H}^{tot} are expressed as the sum of the electric/magnetic field impressed by the source \vec{J}^{inc} and \vec{M}^{inc} , and the field created by the equivalent surfacic current density \vec{M}_A :

$$\vec{E}_{(1)}^{\text{tot}} = 2\vec{e}^{\text{inc}} e^{-j\vec{k}\vec{x}_\perp} + \vec{E}(\vec{M}_A) \quad (\text{III.2.64})$$

$$\vec{H}_{(1)}^{\text{tot}} = 2\vec{h}^{\text{inc}} e^{-j\vec{k}\vec{x}_\perp} + \vec{H}(\vec{M}_A) \quad (\text{III.2.65})$$

For region 2 (see Fig. III.2.3c), and just to the right of the aperture, a surfacic magnetic current density \vec{M}'_A is added.

$$\vec{M}'_A = -\vec{e}_z \wedge \vec{E}_{(2)}^{\text{tot}}|_{z=0+} \quad (\text{III.2.66})$$

The fields are null on the left side of the aperture from the region 2 point of view. Then the tangential part of the electric field must be continuous at the aperture boundary. On the left, the tangential part writes $\vec{e}_z \wedge \vec{E}_{(1)}^{\text{tot}}|_{z=0}$, and on the right, $\vec{e}_z \wedge \vec{E}_{(2)}^{\text{tot}}|_{z=0+}$. Thus:

$$\vec{e}_z \wedge \vec{E}_{(1)}^{\text{tot}}|_{z=0} = \vec{e}_z \wedge \vec{E}_{(2)}^{\text{tot}}|_{z=0+} \quad (\text{III.2.67})$$

$$\vec{M}_A = -\vec{M}'_A \quad (\text{III.2.68})$$

So, the total field in region 2 can be written as:

$$\vec{E}_{(2)}^{\text{tot}} = \vec{E}(\vec{M}'_A) = \vec{E}(-\vec{M}_A) = -\vec{E}(\vec{M}_A) \quad (\text{III.2.69})$$

$$\vec{H}_{(2)}^{\text{tot}} = \vec{H}(\vec{M}'_A) = \vec{H}(-\vec{M}_A) = -\vec{H}(\vec{M}_A) \quad (\text{III.2.70})$$

The continuity of the tangential part of the magnetic field gives:

$$\vec{H}_{(1)}^{\text{tot}}|_{\text{tan}} = \vec{H}_{(2)}^{\text{tot}}|_{\text{tan}} \quad (\text{III.2.71})$$

$$2\vec{h}^{\text{inc}} e^{-j\vec{k}^{\text{inc}}\vec{x}_\perp} + \vec{H}_{(1)}^{\text{tot}}(\vec{M}_A)|_{\text{tan}} = -\vec{H}_{(2)}^{\text{tot}}(\vec{M}_A)|_{\text{tan}} \quad (\text{III.2.72})$$

$$\vec{H}_{(1)}^{\text{tot}}(\vec{M}_A)|_{\text{tan}} + \vec{H}_{(2)}^{\text{tot}}(\vec{M}_A)|_{\text{tan}} = -2\vec{h}^{\text{inc}} e^{-j\vec{k}^{\text{inc}}\vec{x}_\perp} \quad (\text{III.2.73})$$

The problem is solved by applying the MoM [Balanis, 2012, Chap. 12.2.8]. The expansion functions (or basis functions) are the same as those used to model the field at the aperture in the previous section (*i.e.* $\vec{e}_z \wedge \vec{e}_s(\vec{x}_\perp)$, see (III.2.10)). The surfacic magnetic current density \vec{M}_A may be expanded onto the basis:

$$\vec{M}_A = \sum_s V_s \vec{e}_z \wedge \vec{e}_s(\vec{x}_\perp) \quad (\text{III.2.74})$$

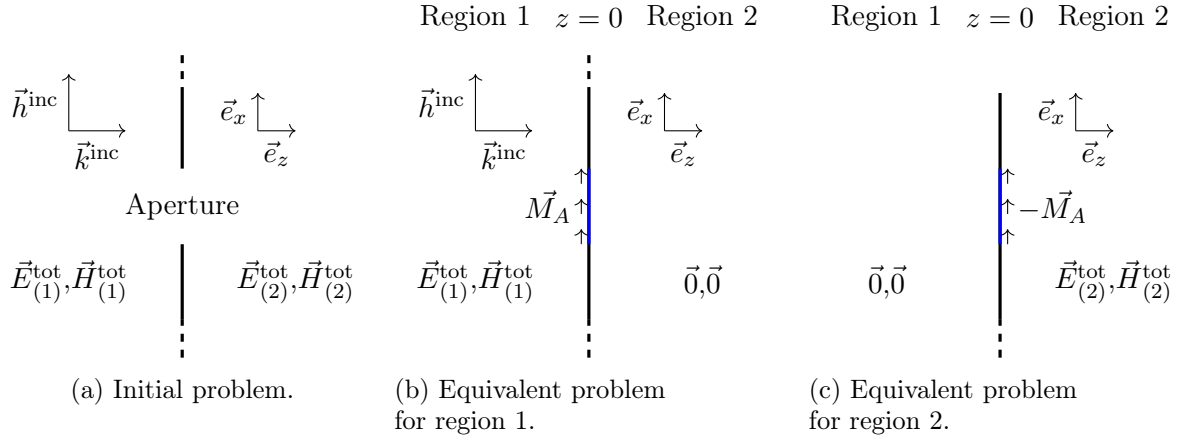


Fig. III.2.3 – Initial and equivalent problems for the problem of two regions separated by a planar aperture.

Thus, thanks to the linearity of the operators $\vec{H}_{(1)}^{\text{tot}}$ and $\vec{H}_{(2)}^{\text{tot}}$, the equation (III.2.73) can be rewritten as :

$$\sum_s V_s \vec{H}_{(1)}^{\text{tot}}(\vec{e}_z \wedge \vec{e}_s(x_\perp))|_{\text{tan}} + \sum_s V_s \vec{H}_{(2)}^{\text{tot}}(\vec{e}_z \wedge \vec{e}_s(x_\perp))|_{\text{tan}} = -2\vec{h}^{\text{inc}} e^{-j\vec{k}^{\text{inc}} \vec{x}_\perp} \quad (\text{III.2.75})$$

The next step is to project (III.2.75) on the weighting functions (or testing functions). We take these weighting functions to be the same as the expansion functions. This method merges with the GALERKIN technique, and we define a scalar product:

$$\langle A, B \rangle = \iint_{\mathbb{R}^2} AB \, dx dy \quad (\text{III.2.76})$$

Then:

$$\sum_s V_s \langle \vec{e}_z \wedge \vec{e}_s'(x_\perp), \vec{H}_{(1)}^{\text{tot}}(\vec{e}_z \wedge \vec{e}_s(x_\perp))|_{\text{tan}} \rangle + \sum_s V_s \langle \vec{e}_z \wedge \vec{e}_s'(x_\perp), \vec{H}_{(2)}^{\text{tot}}(\vec{e}_z \wedge \vec{e}_s(x_\perp))|_{\text{tan}} \rangle = \langle \vec{e}_z \wedge \vec{e}_s'(x_\perp), -2\vec{h}^{\text{inc}} e^{-j\vec{k}^{\text{inc}} \vec{x}_\perp} \rangle \quad (\text{III.2.77})$$

By putting it in a matrix form:

$$\underline{\underline{Y}}|_{z=0-} = \left[\langle \vec{e}_z \wedge \vec{e}_s'(x_\perp), \vec{H}_{(1)}^{\text{tot}}(\vec{e}_z \wedge \vec{e}_s(x_\perp))|_{\text{tan}} \rangle \right]_{N \times N} \quad (\text{III.2.78})$$

$$\underline{\underline{Y}}|_{z=0+} = \left[\langle \vec{e}_z \wedge \vec{e}_s'(x_\perp), \vec{H}_{(2)}^{\text{tot}}(\vec{e}_z \wedge \vec{e}_s(x_\perp))|_{\text{tan}} \rangle \right]_{N \times N} \quad (\text{III.2.79})$$

$$\vec{I}^{\text{inc}} = [\langle \vec{e}_z \wedge \vec{e}_s'(x_\perp), -\vec{h}^{\text{inc}} e^{-j\vec{k}^{\text{inc}} \vec{x}_\perp} \rangle]_{N \times 1} \quad (\text{III.2.80})$$

equation (III.2.77) becomes:

$$\left(\underline{\underline{Y}}|_{z=0-} + \underline{\underline{Y}}|_{z=0+} \right) \vec{V} = 2\vec{I}^{\text{inc}} \quad (\text{III.2.81})$$

where N is the number of modes taken into account over the aperture.

Equation (III.2.81) may be modeled as two networks connected in parallel (see Fig. III.2.4). These networks are driven by a set of current sources \vec{I}^{inc} . The advantage of this formulation is that the two regions are independantly modeled by $\underline{\underline{Y}}|_{z=0-}$ and $\underline{\underline{Y}}|_{z=0+}$.

Each row of \vec{I}^{inc} writes $(\vec{e}_s'(x_\perp))$ is replaced by $\vec{e}_s(x_\perp)$ for clarity):

$$I_s^{\text{inc}} = \langle \vec{e}_z \wedge \vec{e}_s(x_\perp), -\vec{h}^{\text{inc}} e^{-j\vec{k}^{\text{inc}} \vec{x}_\perp} \rangle \quad (\text{III.2.82})$$

$$I_s^{\text{inc}} = \iint_{\mathbb{R}^2} (\vec{e}_z \wedge \vec{e}_s(x_\perp)) \cdot (-\vec{h}^{\text{inc}}) e^{-j\vec{k}^{\text{inc}} \vec{x}_\perp} dx dy \quad (\text{III.2.83})$$

$$I_s^{\text{inc}} = -\vec{h}^{\text{inc}} \cdot \left(\vec{e}_z \wedge \left(\iint_{\mathbb{R}^2} \vec{e}_s(x_\perp) e^{-j\vec{k}^{\text{inc}} \vec{x}_\perp} \right) \right) dx dy \quad (\text{III.2.84})$$

By noticing that:

$$\iint_{\mathbb{R}^2} \vec{e}_s(\vec{x}_\perp) e^{-j\vec{k}^{\text{inc}} \vec{x}_\perp} dx dy = \vec{e}_s(\vec{k}_\perp^{\text{inc}}) \quad (\text{III.2.85})$$

where $\vec{e}_s(\vec{k}_\perp^{\text{inc}})$ is the same as in (III.2.23), we have

$$I_s^{\text{inc}} = -\vec{h}^{\text{inc}} \cdot \left(\vec{e}_z \wedge \left(\vec{e}_s(\vec{k}_\perp^{\text{inc}}) \right) \right) \quad (\text{III.2.86})$$

Thanks to the triple product property $a \cdot (b \wedge c) = b \cdot (c \wedge a) = c \cdot (a \wedge b)$, (III.2.86) becomes:

$$I_s^{\text{inc}} = -\vec{e}_z \cdot \left(\vec{e}_s(\vec{k}_\perp^{\text{inc}}) \wedge \vec{h}^{\text{inc}} \right) \quad (\text{III.2.87})$$

For a normal incidence (with $\vec{h}^{\text{inc}} = h^{\text{inc}} \vec{e}_x$) of the plane wave, we have:

$$\vec{e}_s(\vec{k}_\perp^{\text{inc}}) = \vec{e}_s(\vec{0}) = -\frac{\sqrt{2}((-1)^s - 1)\sqrt{LW}}{\pi s} \vec{e}_y \quad (\text{III.2.88})$$

thus:

$$I_s^{\text{inc}} = \frac{\sqrt{2}(1 - (-1)^s)\sqrt{LW}}{\pi s} h^{\text{inc}} \quad (\text{III.2.89})$$

To solve this MoM problem, \vec{V} needs to be computed. \vec{V} is obtained by inverting (III.2.81), and \vec{V} is:

$$\vec{V} = 2(\underline{\underline{Y}}|_{z=0^-} + \underline{\underline{Y}}|_{z=0^+})^{-1} \vec{I}^{\text{inc}} \quad (\text{III.2.90})$$

In the considered problem, the coupling between a plane wave and a cavity through an aperture, the matrix $\underline{\underline{Y}}|_{z=0^-}$ is the admittance matrix $\underline{\underline{Y}}^{\text{rad}}$ of the aperture as determined earlier. In the same way, $\underline{\underline{Y}}|_{z=0^+}$ is the admittance that models the interior of the cavity. Equation (III.2.90) becomes then:

$$\vec{V} = 2(\underline{\underline{Y}}^{\text{int.}} + \underline{\underline{Y}}^{\text{rad}})^{-1} \vec{I}^{\text{inc}} \quad (\text{III.2.91})$$

with $\vec{I}^{\text{inc}} = [I_1^{\text{inc}}, I_2^{\text{inc}}, \dots, I_N^{\text{inc}}]^T$.

III.2.5 Mapping of the aperture impedance to the RCM

In section III.2.3, the admittance $\underline{\underline{Y}}^{\text{rad}}$ of a rectangular aperture has been determined and, in the previous section, a way to merge two regions, modeled by two admittance matrices, and separated by an aperture, has been proposed. The last step is to apply these two results to get an enhanced version of the RCM that includes the admittance $\underline{\underline{Y}}^{\text{rad}}$. This work has been firstly proposed in [Antonsen et al., 2011] and better explained in [Gradoni et al., 2015], but with few details only and some approximations.

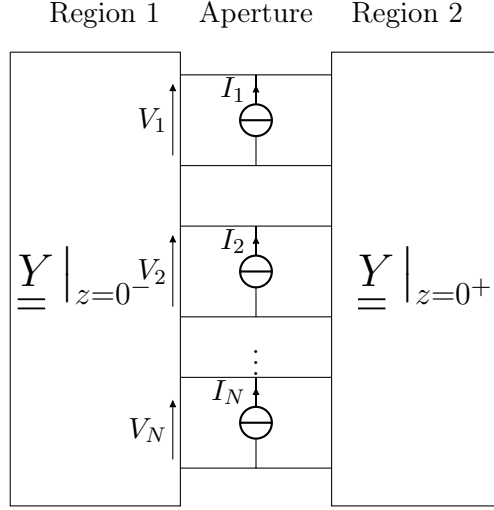


Fig. III.2.4 – Circuit model of the aperture, between two regions.

We have carried out as rigorously as possible calculations to bind these results and to obtain the expression of $\underline{\underline{Y}}^{\text{int}}$.

The studied cavity is composed of an aperture modeled by $\underline{\underline{Y}}^{\text{rad}}$ and of a set of ports (wire, PCB, etc.). $N_A + N_P$ equations are set up, where N_A is the number of modes required to model the aperture, and N_P is the number of ports connected to the cavity. We define the source vectors $\vec{\phi}$ and $\vec{\psi}$ of the system:

$$\vec{\phi} = \begin{pmatrix} \vec{V}_A \\ \vec{I}_P \end{pmatrix} \quad (\text{III.2.92})$$

$$\vec{\psi} = \begin{pmatrix} \vec{I}_A \\ \vec{V}_P \end{pmatrix} \quad (\text{III.2.93})$$

\vec{V}_A and \vec{V}_P are vectors containing the voltage of either the modes in the aperture \vec{V}_A (as defined in (III.2.91)) or the ports in the cavity \vec{V}_P (cables, PCBs, etc.), and respectively we have the associated currents \vec{I}_A and \vec{I}_P . Starting with the hybrid block matrix of the system $\underline{\underline{T}}$ we have [Antonsen et al., 2011]:

$$\vec{\psi} = \underline{\underline{T}} \vec{\phi} \quad (\text{III.2.94})$$

We can apply the RCM to formulate $\underline{\underline{T}}$:

$$\underline{\underline{T}} = j\Im \left\{ \underline{\underline{U}} \right\} + \left[\Re \left\{ \underline{\underline{U}} \right\} \right]^{1/2} \underline{\underline{\xi}} \left[\Re \left\{ \underline{\underline{U}} \right\} \right]^{1/2} = \begin{pmatrix} \underline{\underline{T}}_{1,1} & \underline{\underline{T}}_{1,2} \\ \underline{\underline{T}}_{2,1} & \underline{\underline{T}}_{2,2} \end{pmatrix} \quad (\text{III.2.95})$$

where $\underline{\underline{U}}$ is a block diagonal matrix defined as:

$$\underline{\underline{U}} = \begin{pmatrix} \underline{\underline{Y}}^{\text{rad}} & 0 \\ 0 & \underline{\underline{Z}}^{\text{rad}} \end{pmatrix} \quad (\text{III.2.96})$$

Here, we assume that there is no direct coupling between the aperture and the ports. $\underline{\underline{Y}}^{\text{rad}}$ stands for the admittance of the aperture and $\underline{\underline{Z}}^{\text{rad}}$ is the impedance of the ports. The size of $\underline{\underline{Y}}^{\text{rad}}$ is $(N_A \times N_A)$,

and that of $\underline{\underline{Z}}^{\text{rad}}$ is $(N_P \times N_P)$. $\underline{\underline{U}}$ is then of size $(N_A + N_P) \times (N_A + N_P)$. In [Gradoni et al., 2015] $\underline{\underline{\xi}}$ is expanded:

$$\underline{\underline{\xi}} = \underline{\underline{\xi}}_{AP} \cdot \underline{\underline{\xi}}_{AP}^T = \begin{pmatrix} \underline{\underline{\xi}}_A \\ \underline{\underline{\xi}}_P \end{pmatrix} \cdot \begin{pmatrix} \underline{\underline{\xi}}_A^T & \underline{\underline{\xi}}_P^T \end{pmatrix} = \begin{pmatrix} \underline{\underline{\xi}}_A & \underline{\underline{\xi}}_A \cdot \underline{\underline{\xi}}_P^T \\ \underline{\underline{\xi}}_P \cdot \underline{\underline{\xi}}_A^T & \underline{\underline{\xi}}_P \end{pmatrix} \quad (\text{III.2.97})$$

where

$$\underline{\underline{\xi}}_A = \underline{\underline{\xi}}_A \cdot \underline{\underline{\xi}}_A^T \quad (\text{III.2.98})$$

and

$$\underline{\underline{\xi}}_P = \underline{\underline{\xi}}_P \cdot \underline{\underline{\xi}}_P^T \quad (\text{III.2.99})$$

However, that formulation was not clear in [Antonsen et al., 2011] nor in [Gradoni et al., 2015] and raised an issue that will be discussed later. To solve the problem, $N_A + N_P$ equations need to be solved. The blocks of $\underline{\underline{T}}$ may be written as:

$$T_{1,1}_{N_A \times N_A} = \underline{\underline{Y}}^{\text{cav}} = j\Im \left\{ \underline{\underline{Y}}^{\text{rad}} \right\} + \left[\Re \left\{ \underline{\underline{Y}}^{\text{rad}} \right\} \right]^{1/2} \underline{\underline{\xi}}_A \left[\Re \left\{ \underline{\underline{Y}}^{\text{rad}} \right\} \right]^{1/2} \quad (\text{III.2.100})$$

$$T_{2,2}_{N_P \times N_P} = \underline{\underline{Z}}^{\text{cav}} = j\Im \left\{ \underline{\underline{Z}}^{\text{rad}} \right\} + \left[\Re \left\{ \underline{\underline{Z}}^{\text{rad}} \right\} \right]^{1/2} \underline{\underline{\xi}}_P \left[\Re \left\{ \underline{\underline{Z}}^{\text{rad}} \right\} \right]^{1/2} \quad (\text{III.2.101})$$

$$T_{1,2}_{N_A \times N_P} = \left[\Re \left\{ \underline{\underline{Y}}^{\text{rad}} \right\} \right]^{1/2} \underline{\underline{\xi}}_A \underline{\underline{\xi}}_P^T \left[\Re \left\{ \underline{\underline{Z}}^{\text{rad}} \right\} \right]^{1/2} \quad (\text{III.2.102})$$

$$T_{2,1}_{N_P \times N_A} = \left[\Re \left\{ \underline{\underline{Z}}^{\text{rad}} \right\} \right]^{1/2} \underline{\underline{\xi}}_P \underline{\underline{\xi}}_A^T \left[\Re \left\{ \underline{\underline{Y}}^{\text{rad}} \right\} \right]^{1/2} \quad (\text{III.2.103})$$

We assume that the aperture is illuminated by a plane wave, thus \vec{h}^{inc} is known as well as \vec{I}^{inc} . The aperture currents \vec{I}_A may be expressed as a sum of \vec{I}^{inc} (the contribution of the plane wave) and $-\underline{\underline{Y}}^{\text{rad}} \vec{V}_A$ (the contribution of the ports inside the cavity):

$$\vec{I}_A = 2\vec{I}^{\text{inc}} - \underline{\underline{Y}}^{\text{rad}} \vec{V}_A \quad (\text{III.2.104})$$

Putting everything together leads to the equation [Antonsen et al., 2011]:

$$\begin{pmatrix} \underline{\underline{Y}}^{\text{rad}} & 0 \\ 0 & \underline{\underline{Z}}^{\text{L}} \end{pmatrix} \cdot \begin{pmatrix} \vec{V}_A \\ \vec{I}_P \end{pmatrix} + \underline{\underline{T}} \cdot \begin{pmatrix} \vec{V}_A \\ \vec{I}_P \end{pmatrix} = \begin{pmatrix} 2\vec{I}^{\text{inc}} \\ \vec{0} \end{pmatrix} \quad (\text{III.2.105})$$

where $\underline{\underline{Z}}^{\text{L}}$ is a diagonal matrix, which elements represent the characteristic impedance of the ports (Usually $\underline{\underline{Z}}^{\text{L}} = 50I$).

From (III.2.105) we get N_A aperture equations:

$$\underline{\underline{Y}}^{\text{rad}} \vec{V}_A + \underline{\underline{T}}_{1,1} \vec{V}_A + \underline{\underline{T}}_{1,2} \vec{I}_P = 2\vec{I}^{\text{inc}} \quad (\text{III.2.106})$$

$$(\underline{\underline{Y}}^{\text{rad}} + \underline{\underline{Y}}^{\text{cav}}) \vec{V}_A + \left[\Re \left\{ \underline{\underline{Y}}^{\text{rad}} \right\} \right]^{1/2} \underline{\underline{\xi}}_A \underline{\underline{\xi}}_P^T \left[\Re \left\{ \underline{\underline{Z}}^{\text{rad}} \right\} \right]^{1/2} \vec{I}_P = 2\vec{I}^{\text{inc}} \quad (\text{III.2.107})$$

and N_P port equations:

$$\underline{\underline{Z}}^L \vec{I}_P + \underline{\underline{T}}_{2,1} \vec{V}_A + \underline{\underline{T}}_{2,2} \vec{I}_P = \vec{0} \quad (\text{III.2.108})$$

$$(\underline{\underline{Z}}^L + \underline{\underline{Z}}^{\text{cav}}) \vec{I}_P + \left[\Re \left\{ \underline{\underline{Z}}^{\text{rad}} \right\} \right]^{1/2} \vec{\xi}_P \vec{\xi}_A^T \left[\Re \left\{ \underline{\underline{Y}}^{\text{rad}} \right\} \right]^{1/2} \vec{V}_A = \vec{0} \quad (\text{III.2.109})$$

To isolate \vec{I}_P , we can write:

$$\vec{I}_P = -(\underline{\underline{Z}}^L + \underline{\underline{Z}}^{\text{cav}})^{-1} \left[\Re \left\{ \underline{\underline{Z}}^{\text{rad}} \right\} \right]^{1/2} \vec{\xi}_P \vec{\xi}_A^T \left[\Re \left\{ \underline{\underline{Y}}^{\text{rad}} \right\} \right]^{1/2} \vec{V}_A \quad (\text{III.2.110})$$

\vec{V}_A may be linked by \vec{I}^{inc} by injecting (III.2.110) in (III.2.107):

$$\begin{aligned} 2\vec{I}^{\text{inc}} &= (\underline{\underline{Y}}^{\text{rad}} + \underline{\underline{Y}}^{\text{cav}}) \vec{V}_A \\ &\quad - \left[\Re \left\{ \underline{\underline{Y}}^{\text{rad}} \right\} \right]^{1/2} \vec{\xi}_A \vec{\xi}_P^T \left[\Re \left\{ \underline{\underline{Z}}^{\text{rad}} \right\} \right]^{1/2} (\underline{\underline{Z}}^L + \underline{\underline{Z}}^{\text{cav}})^{-1} \left[\Re \left\{ \underline{\underline{Z}}^{\text{rad}} \right\} \right]^{1/2} \vec{\xi}_P \vec{\xi}_A^T \left[\Re \left\{ \underline{\underline{Y}}^{\text{rad}} \right\} \right]^{1/2} \vec{V}_A \\ 2\vec{I}^{\text{inc}} &= \left(\underline{\underline{Y}}^{\text{rad}} + \underline{\underline{Y}}^{\text{cav}'} \right) \vec{V}_A \end{aligned} \quad (\text{III.2.111})$$

with:

$$\underline{\underline{Y}}^{\text{cav}'} = \underline{\underline{Y}}^{\text{cav}} - \left[\Re \left\{ \underline{\underline{Y}}^{\text{rad}} \right\} \right]^{1/2} \vec{\xi}_A \vec{\xi}_P^T \left[\Re \left\{ \underline{\underline{Z}}^{\text{rad}} \right\} \right]^{1/2} (\underline{\underline{Z}}^L + \underline{\underline{Z}}^{\text{cav}})^{-1} \left[\Re \left\{ \underline{\underline{Z}}^{\text{rad}} \right\} \right]^{1/2} \vec{\xi}_P \vec{\xi}_A^T \left[\Re \left\{ \underline{\underline{Y}}^{\text{rad}} \right\} \right]^{1/2} \quad (\text{III.2.112})$$

\vec{V}_A can be deduced from (III.2.111):

$$\vec{V}_A = 2 \left(\underline{\underline{Y}}^{\text{rad}} + \underline{\underline{Y}}^{\text{cav}'} \right)^{-1} \vec{I}^{\text{inc}} \quad (\text{III.2.113})$$

\vec{I}_P is obtained by calculating \vec{V}_A from (III.2.113), and injecting it in (III.2.110). The admittance of the interior of the cavity $\underline{\underline{Y}}^{\text{int.}}$, merges with $\underline{\underline{Y}}^{\text{cav}'}$.

III.2.5.1 Case where $N_P = 1$

The above equations may be simplified when $N_P = 1$ which corresponds to configuration 1 (see section III.1.4.1). Equations (III.2.109) and (III.2.107) become respectively:

$$(Z_L + Z^{\text{cav}}) I_P + \sqrt{R^{\text{rad}}} \cdot \xi_P \xi_A^T \cdot \left[\Re \left\{ \underline{\underline{Y}}^{\text{rad}} \right\} \right]^{1/2} \vec{V}_A = 0 \quad (\text{III.2.114})$$

$$(\underline{\underline{Y}}^{\text{cav}} + \underline{\underline{Y}}^{\text{rad}}) \vec{V}_A + \left[\Re \left\{ \underline{\underline{Y}}^{\text{rad}} \right\} \right]^{1/2} \vec{\xi}_A \xi_P \sqrt{R^{\text{rad}}} I_P = 2\vec{I}^{\text{inc}} \quad (\text{III.2.115})$$

where $Z^{\text{rad}} = R^{\text{rad}} + jX^{\text{rad}}$, and $Z^{\text{cav}} = jX^{\text{rad}} + R^{\text{rad}} \xi_P$ is the scalar cavity impedance (see Fig. III.2.5).

Then, (III.2.114) may be inverted, leading to:

$$I_P = -\frac{\sqrt{R^{\text{rad}}}}{Z_L + Z^{\text{cav}}} \xi_P \xi_A^T \left[\Re \left\{ \underline{\underline{Y}}^{\text{rad}} \right\} \right]^{1/2} \vec{V}_A \quad (\text{III.2.116})$$

Inserting (III.2.116) in (III.2.115) yields to:

$$(\underline{\underline{Y}}^{\text{int.}} + \underline{\underline{Y}}^{\text{rad}}) \vec{V}_A = 2\vec{I}^{\text{inc}} \quad (\text{III.2.117})$$

where:

$$\underline{\underline{Y}}^{\text{int.}} = \underline{\underline{Y}}^{\text{cav}} - \frac{R^{\text{rad}}}{Z_L + Z^{\text{cav}}} \left[\Re \left\{ \underline{\underline{Y}}^{\text{rad}} \right\} \right]^{1/2} \xi_P^2 \xi_A \xi_A^T \left[\Re \left\{ \underline{\underline{Y}}^{\text{rad}} \right\} \right]^{1/2} \quad (\text{III.2.118})$$

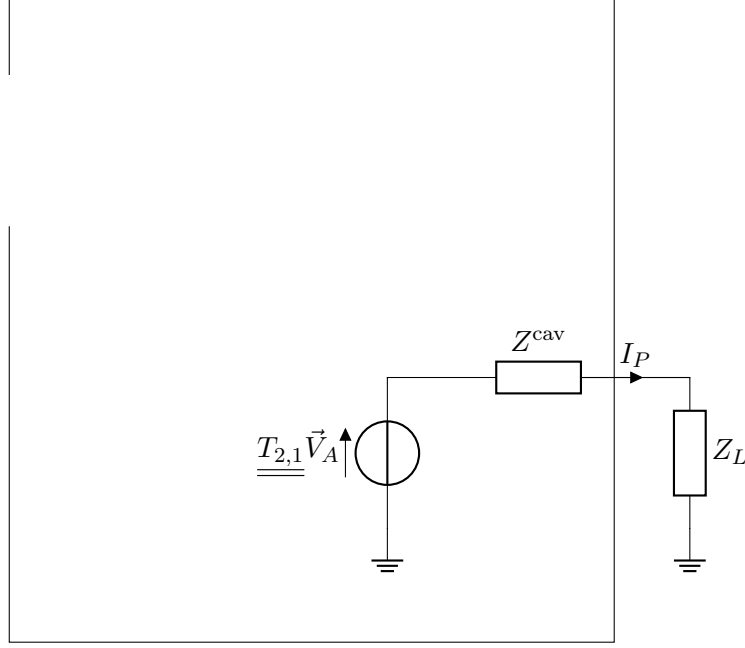


Fig. III.2.5 – Circuit model to compute I_P from \vec{V}_A when $N_P = 1$

III.2.5.2 Statistics of the elements of $\underline{\underline{\xi}}$ when dealing with an aperture

Previously, an expression of $\underline{\underline{\xi}}_1$ was given:

$$\underline{\underline{\xi}}_1 = \vec{\xi}_{AP} \cdot \vec{\xi}_{AP}^T \quad (\text{III.2.119})$$

Later, in section III.4.4, we will see that $\underline{\underline{\xi}}_2$ must take the following form:

$$\underline{\underline{\xi}}_2 = -\frac{j}{\pi} \underline{\underline{W}} [\underline{\underline{\lambda}} - j\underline{\underline{\alpha}} \underline{\underline{1}}]^{-1} \underline{\underline{W}}^T \quad (\text{III.2.120})$$

$\underline{\underline{W}}$ is a matrix whose elements are standard normal distributed, $\underline{\underline{\lambda}}$ a real diagonal matrix, and α a scalar.

For instance, if three modes are considered in the cavity and three ports in the system, $[\underline{\underline{\lambda}} - j\underline{\underline{\alpha}} \underline{\underline{1}}]^{-1}$, $\underline{\underline{W}}$ and $\underline{\underline{\xi}}$ can be written like:

$$[\underline{\underline{\lambda}} - j\underline{\underline{\alpha}} \underline{\underline{1}}]^{-1} = \begin{pmatrix} \frac{1}{\lambda_1 - j\alpha} & 0 & 0 \\ 0 & \frac{1}{\lambda_2 - j\alpha} & 0 \\ 0 & 0 & \frac{1}{\lambda_3 - j\alpha} \end{pmatrix} \quad (\text{III.2.121})$$

$$\underline{\underline{W}} = \begin{pmatrix} w_{11} & w_{12} & w_{13} \\ w_{21} & w_{22} & w_{23} \\ w_{31} & w_{32} & w_{33} \end{pmatrix} \quad (\text{III.2.122})$$

$$\underline{\underline{\xi}}_2 = \begin{pmatrix} \frac{w_{11}^2}{\lambda_1 - j\alpha} + \frac{w_{12}^2}{\lambda_2 - j\alpha} + \frac{w_{13}^2}{\lambda_3 - j\alpha} & \frac{w_{11}w_{21}}{\lambda_1 - j\alpha} + \frac{w_{12}w_{22}}{\lambda_2 - j\alpha} + \frac{w_{13}w_{23}}{\lambda_3 - j\alpha} & \frac{w_{11}w_{31}}{\lambda_1 - j\alpha} + \frac{w_{12}w_{32}}{\lambda_2 - j\alpha} + \frac{w_{13}w_{33}}{\lambda_3 - j\alpha} \\ \frac{w_{11}w_{21}}{\lambda_1 - j\alpha} + \frac{w_{12}w_{22}}{\lambda_2 - j\alpha} + \frac{w_{13}w_{23}}{\lambda_3 - j\alpha} & \frac{w_{21}^2}{\lambda_1 - j\alpha} + \frac{w_{22}^2}{\lambda_2 - j\alpha} + \frac{w_{23}^2}{\lambda_3 - j\alpha} & \frac{w_{21}w_{31}}{\lambda_1 - j\alpha} + \frac{w_{22}w_{32}}{\lambda_2 - j\alpha} + \frac{w_{23}w_{33}}{\lambda_3 - j\alpha} \\ \frac{w_{11}w_{31}}{\lambda_1 - j\alpha} + \frac{w_{12}w_{32}}{\lambda_2 - j\alpha} + \frac{w_{13}w_{33}}{\lambda_3 - j\alpha} & \frac{w_{21}w_{31}}{\lambda_1 - j\alpha} + \frac{w_{22}w_{32}}{\lambda_2 - j\alpha} + \frac{w_{23}w_{33}}{\lambda_3 - j\alpha} & \frac{w_{31}^2}{\lambda_1 - j\alpha} + \frac{w_{32}^2}{\lambda_2 - j\alpha} + \frac{w_{33}^2}{\lambda_3 - j\alpha} \end{pmatrix} \quad (\text{III.2.123})$$

There is no obvious way to equal the formulations $\underline{\underline{\xi}}_2$ and $\underline{\underline{\xi}}_1$. However, in [Gradoni et al., 2015] the authors indicate that the elements of ξ_{AP}^{\rightarrow} should have the same statistical properties as the off-diagonal elements of $\underline{\underline{\xi}}_2$. Therefore, in what follows, the matrix $\underline{\underline{\xi}}$ will be constructed in such a way that the statistical properties of the elements ξ_{ij_1} and ξ_{ij_2} are the same.

Chapter III.3

Numerical computation of the aperture admittance

Contents

III.3.1	Introduction	118
III.3.2	Numerical error estimation	118
III.3.3	Integration of G_{mn}^{rad} over k_x	119
III.3.4	Integration of $B_{mn}^{\text{rad},ms}$ over k_x and k_y	119
III.3.5	Computation of B_{mn}^{rad} by means of the HILBERT transform	122
III.3.5.1	On-diagonal terms	122
III.3.5.2	Off-diagonal terms	123
III.3.6	Impedance and admittance	123

III.3.1 Introduction

This chapter presents how the aperture impedance proposed by [Antonsen et al., 2011] is numerically computed as well as some other numerical results.

Z_{mn}^{rad} is computed for an aperture with a width $W = 146.1$ mm and a length L of 41.3 mm. The size of this aperture is set from the front face of a CD reader. As the computation of some integrals is more and more complicated as n (or m) increases, a tradeoff has to be decided and 29 modes in the aperture are considered. They take into account all the resonances into the aperture for a study up to 27 GHz.

III.3.2 Numerical error estimation

The library [GNU Scientific Library \(GSL\)](#), which is a general purpose library [Galassi et al., 2007], is used. Before coming to the obtained results, an overview of a stopping criterion for the integration is defined. The library aims at computing the integral I :

$$I = \int_a^b f(x)dx \quad (\text{III.3.1})$$

with the following goal:

$$|RESULT - I| \leq \max(epsabs, epsrel|I|) \quad (\text{III.3.2})$$

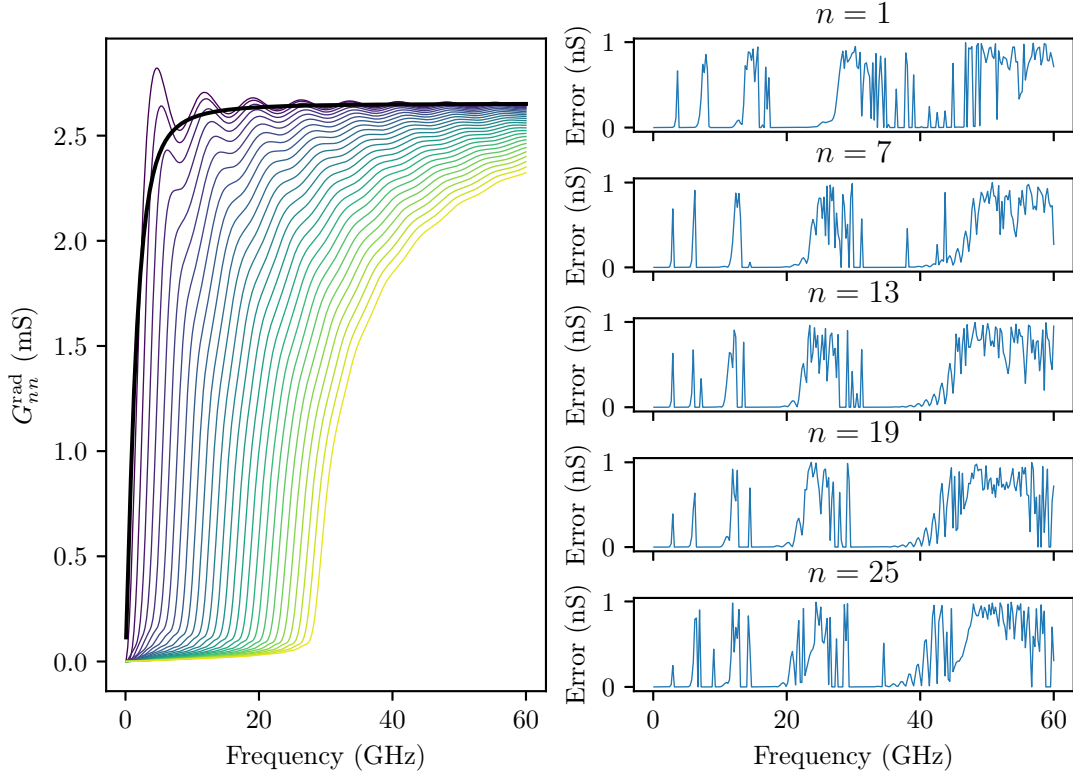


Fig. III.3.1 – G_{mn}^{rad} on the left (from $n = 1$ (purple) to $n = 29$ (yellow)), and the associated estimated error on the right. The solid black curve corresponds to the asymptotic behavior (which will be used in III.3.5.1).

where *RESULT* is the numerical estimation computed by the library, *epsrel* is the relative error and *epsabs* is the absolute error. The library tries to assess the absolute error *ABSEERR* by estimating $|RESULT - I|$ such that:

$$|RESULT - I| \leq ABSEERR \leq \max(epsabs, epsrel|I|) \quad (\text{III.3.3})$$

The algorithm stops as soon as equation (III.3.3) holds. In what follows, the absolute error is plotted. For some cases, the requested error cannot be reached because of roundoff errors.

III.3.3 Integration of G_{mn}^{rad} over k_x

G_{mn}^{rad} was computed by numerical integration of (III.2.48). In (III.2.48), the special STRUVE and BESSEL functions are used. Implementations of these functions were found in [Brun and Rademakers, 1997]. Computing G_{mn}^{rad} requires a few seconds to reach an absolute error of $\pm 1 \times 10^{-9}$ S. The results for on-diagonal terms are depicted in Fig. III.3.1 and in Fig. III.3.2 for off-diagonal terms.

III.3.4 Integration of $B_{mn}^{\text{rad},ms}$ over k_x and k_y

This integral cannot be analytically evaluated, thus a numerical integration will be performed. As a reminder, the expression of $B_{nm}^{\text{rad},ms}(k_0)$ is given in (III.2.62).

In order to minimize the computation time, the number of operations need to be limited. We can

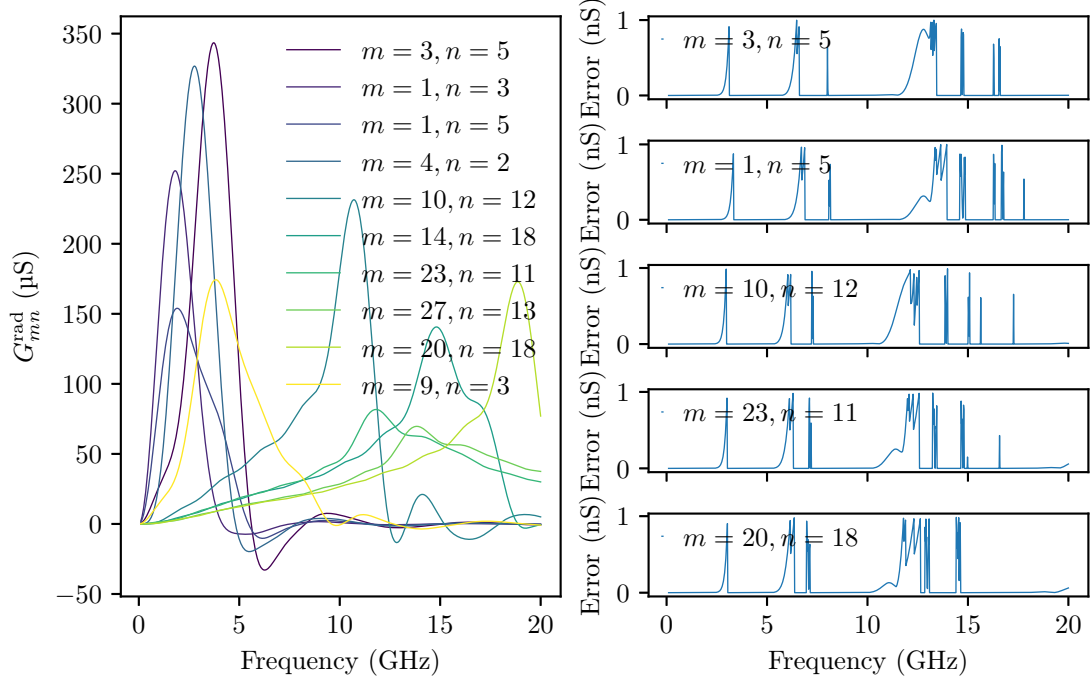


Fig. III.3.2 – G_{mn}^{rad} for some pair (m, n) on the left and the associated estimated error on the right.

write (III.2.62) as:

$$B_{nm}^{\text{rad}, \text{ms}}(k_0) = A \int_{\mathbb{R}} \left(f_1(k_x) \left(\int_{\mathbb{R}} f_2(k_x, k_y) dk_y \right) \right) dk_x \quad (\text{III.3.4})$$

$$= A \int_{\mathbb{R}} f_1(k_x) f_3(k_x) dk_x \quad (\text{III.3.5})$$

with :

$$A = \frac{mnLWj^{m-n}}{60\pi k_0} \quad (\text{III.3.6})$$

$$f_1(k_x) = \frac{k_x^2 \sin\left(\frac{1}{2}(k_x L + \pi m)\right) \sin\left(\frac{1}{2}(k_x L + \pi n)\right)}{(\pi m - k_x L)(k_x L + \pi m)(\pi n - k_x L)(k_x L + \pi n)} \quad (\text{III.3.7})$$

$$f_2(k_x, k_y) = \frac{\text{sinc}\left(\frac{k_y W}{2}\right)^2}{\sqrt{k_x^2 + k_y^2}} \quad (\text{III.3.8})$$

$$f_3(k_x) = \int_{\mathbb{R}} f_2(k_x, k_y) dk_y \quad (\text{III.3.9})$$

As the computation time of $f_1(k_x)$ is higher than that of $f_2(k_x, k_y)$, we limit the number of calls to $f_1(k_x)$ by starting the integration of k_y given k_x . The routine `gsl_integration_qagi` dedicated to infinite intervals from the GNU Scientific Library [Galassi et al., 2007] was used. The relative error specified was close to 10^{-7} . In order to speed up the computation, several frequencies were computed in parallel. It took approximately 300s to compute $B_{mn}^{\text{rad}, \text{ms}}$ for a single frequency on an up to date desktop computer.

Fig. III.3.3 and Fig. III.3.4 illustrate the computation of $B_{mn}^{\text{rad}, \text{ms}}$ for on and off-diagonal terms, and Fig. III.3.5a and Fig. III.3.5b the corresponding errors.

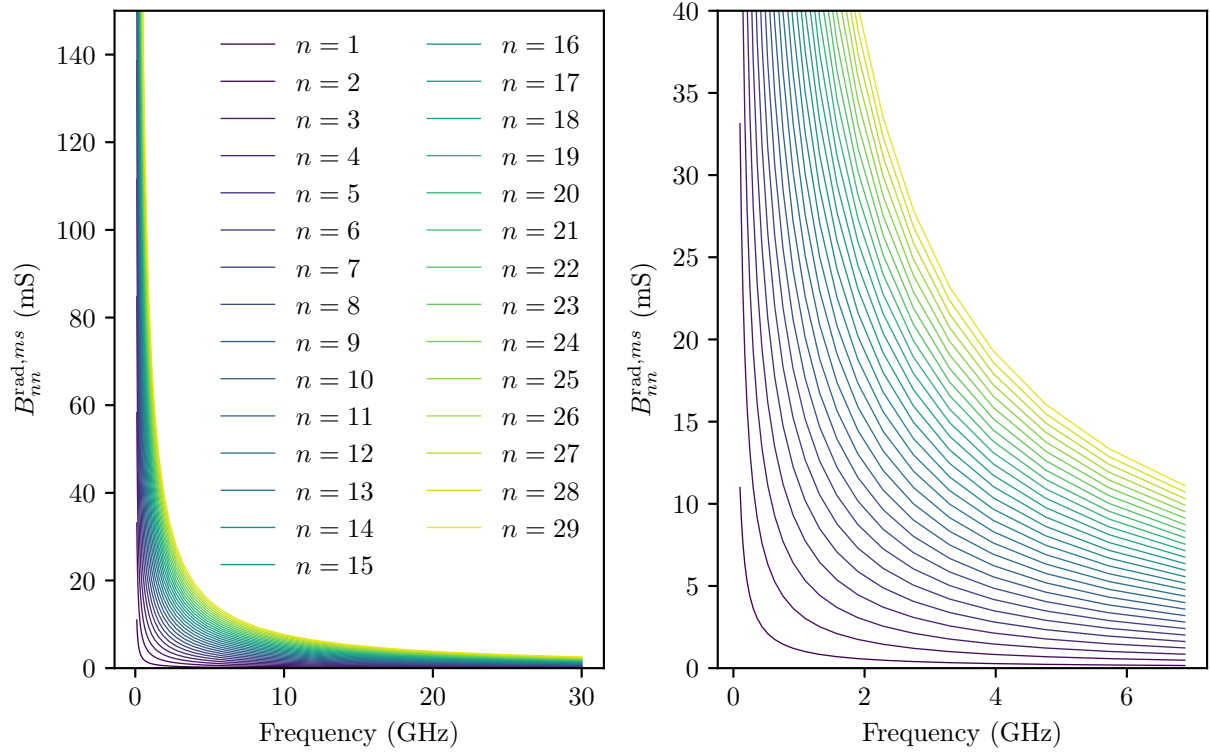


Fig. III.3.3 – Plot of $B_{nn}^{\text{rad},ms}$, with an enlargement on the right for low frequencies.

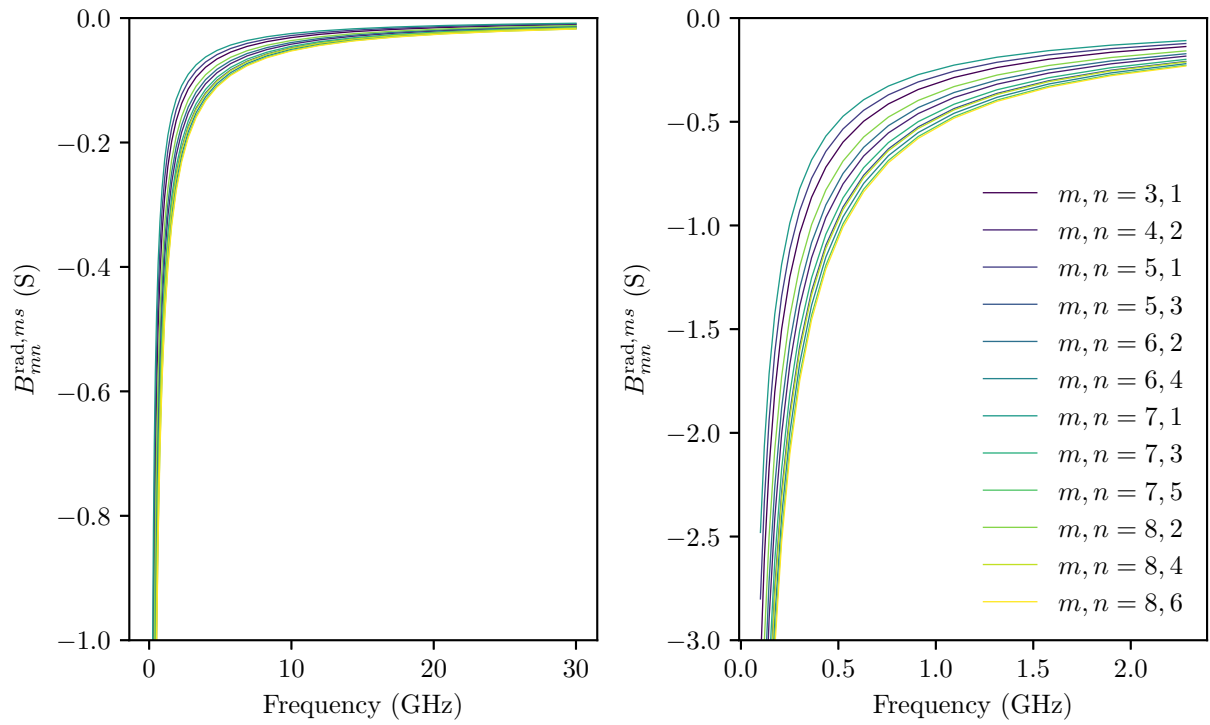


Fig. III.3.4 – $B_{mn}^{\text{rad},ms}$ for some pair (m, n) , with an enlargement on the right for low frequencies.

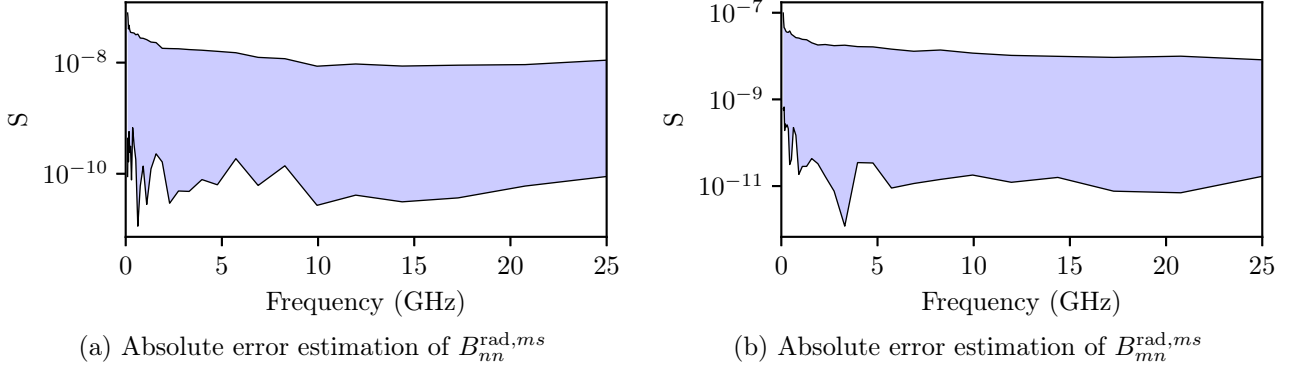


Fig. III.3.5 – Absolute error estimation of $B_{nn}^{\text{rad},ms}$ and $B_{mn}^{\text{rad},ms}$.

III.3.5 Computation of B_{nn}^{rad} by means of the HILBERT transform

III.3.5.1 On-diagonal terms

To evaluate $B_{nn}^{\text{rad}}(k_0)$, thanks to the KRAMERS-KRONIG relations. We need to compute principal value integrals. As it was impossible to compute $G_{nn}^{\text{rad}}(k_0)$ analytically, $G_{nn}^{\text{rad}}(k_0)$ has been discretized and numerically integrated. We notice that computing $B_{nn}^{\text{rad}}(k_0)$ is equivalent to compute the HILBERT transform of $G_{nn}^{\text{rad}}(k_0)$. To compute the HILBERT transform of a discretized signal, the following procedure may be adopted. If $x_a(\cdot)$ is the discrete analytic signal of the discrete signal $x(\cdot)$, and $y(\cdot)$ its HILBERT transform, we can write:

$$x_a(\cdot) = \mathcal{F}^{-1}(\mathcal{F}(x(\cdot))2U) = x(\cdot) + jy(\cdot) \quad (\text{III.3.10})$$

where $\mathcal{F}(f)$ and $\mathcal{F}^{-1}(f)$ are respectively the direct and inverse FOURIER transform of the function f , and U is the step function. By taking the imaginary parts of equation (III.3.10) we get $\mathcal{H}(\cdot) = \Im[\mathcal{F}^{-1}(\mathcal{F}(x(\cdot))2U)] = y(\cdot)$ [Duoandikoetxea and Zuazo, 2001, Chap 3].

But, as $G_{nn}^{\text{rad}}(k)$ has a constant component, see Fig. III.3.1, we cannot compute $B_{nn}^{\text{rad}}(k)$ directly, we need to remove its constant part first.

We define $G_{nn}^{\text{rad},m}(k_0)$ to have the same asymptotic behavior as $G_{nn}^{\text{rad}}(k_0)$ (black curve in Fig. III.3.1):

$$G_{nn}^{\text{rad},m}(k_0) = \frac{1}{\eta_0} \frac{k_0 W}{2} \frac{1}{\sqrt{1 + \left(\frac{k_0 W}{2}\right)^2}} \quad (\text{III.3.11})$$

By using the KRAMERS-KRONIG relations, we get:

$$B_{nn}^{\text{rad},m}(k_0) = \frac{2k_0}{\pi} \text{P} \int_0^\infty \frac{G_{nn}^{\text{rad},m}(k)}{k_0^2 - k^2} dk = \frac{k_0 W \log \left(\frac{\sqrt{k_0^2 W^2 + 4} - 2}{\sqrt{k_0^2 W^2 + 4} + 2} \right)}{120\pi^2 \sqrt{k_0^2 W^2 + 4}} \quad (\text{III.3.12})$$

$G_{nn}^{\text{rad},m}(k_0)$ and $B_{nn}^{\text{rad},m}(k_0)$ are presented in Fig. III.3.6. This asymptotic function is subtracted from $G_{nn}^{\text{rad}}(k_0)$, then the HILBERT transform is computed, and $B_{nn}^{\text{rad}}(k_0)$ is added. Thus, we can write:

$$\Delta G_{nn}^{\text{rad}}(k_0) = G_{nn}^{\text{rad}}(k_0) - G_{nn}^{\text{rad},m}(k_0) \quad (\text{III.3.13})$$

$$\Delta B_{nn}^{\text{rad}}(k_0) = \mathcal{H}[\Delta G_{nn}^{\text{rad}}(k)](k_0) \quad (\text{III.3.14})$$

$$B_{nn}^{\text{rad}}(k_0) = B_{nn}^{\text{rad},m}(k_0) + \Delta B_{nn}^{\text{rad}}(k_0) + B_{nn}^{ms}(k_0) \quad (\text{III.3.15})$$

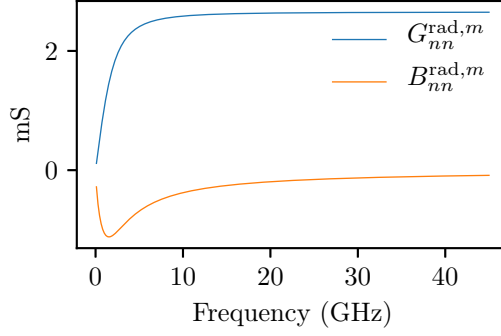


Fig. III.3.6 – $G_{nn}^{\text{rad},m}$ and $B_{nn}^{\text{rad},m}$

III.3.5.2 Off-diagonal terms

As there is no constant component on the off-diagonal terms of $G^{\text{rad}}(k_0)$, we directly compute:

$$B_{mn}^{\text{rad}}(k_0) = \mathcal{H}[G_{mn}^{\text{rad}}(k)](k_0) + B_{mn}^{\text{ms}}(k_0) \quad (\text{III.3.16})$$

The results are presented in Fig. III.3.7b.

III.3.6 Impedance and admittance

We now have the real and imaginary parts of $Y_{mn}^{\text{rad}}(k_0) = G_{mn}^{\text{rad}}(k_0) + jB_{mn}^{\text{rad}}(k_0)$. In Fig. III.3.8 and Fig. III.3.9, the eigenfrequencies of the modes at the aperture may be identified. It can be noticed that two consecutive eigenfrequencies are separated by 1.05 GHz. This fact is useful to assess the number of modes to take into account a given maximum frequency. For example, for a study up to 27 GHz we need to take into account $\frac{27}{1.05} \approx 26$ modes.

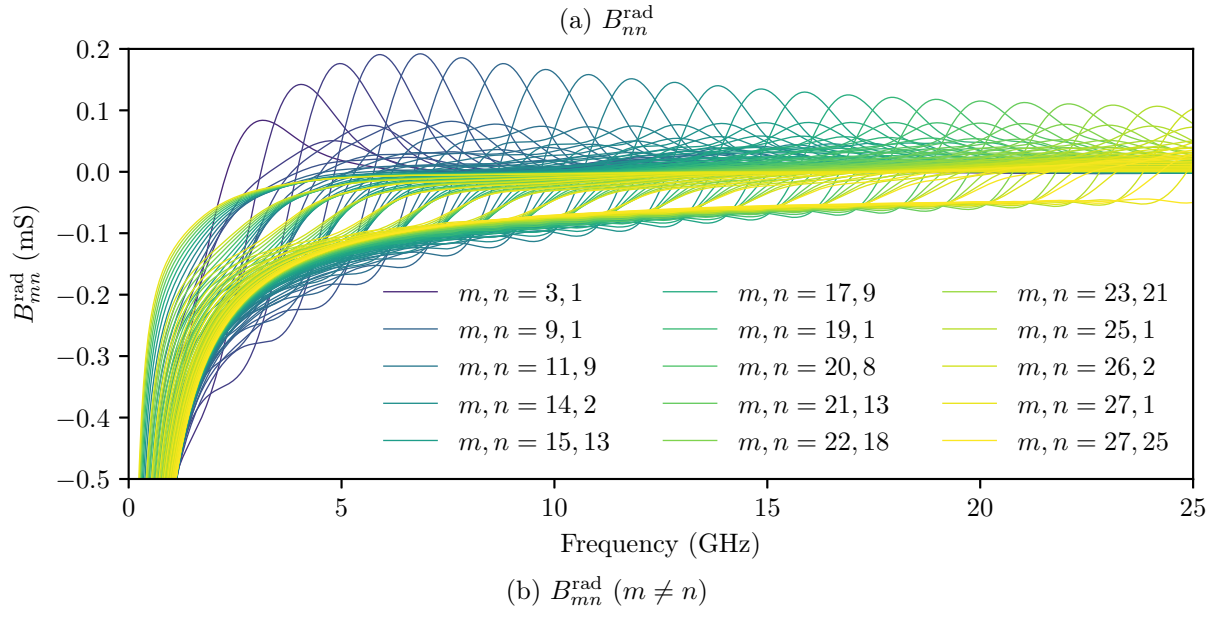
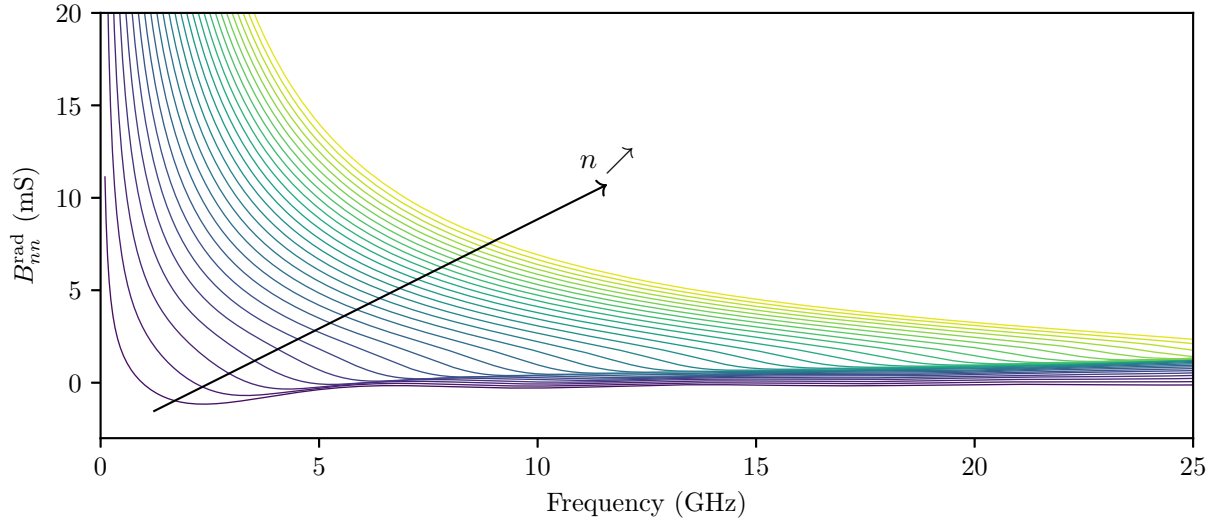


Fig. III.3.7 – Plot of B_{mn}^{rad}

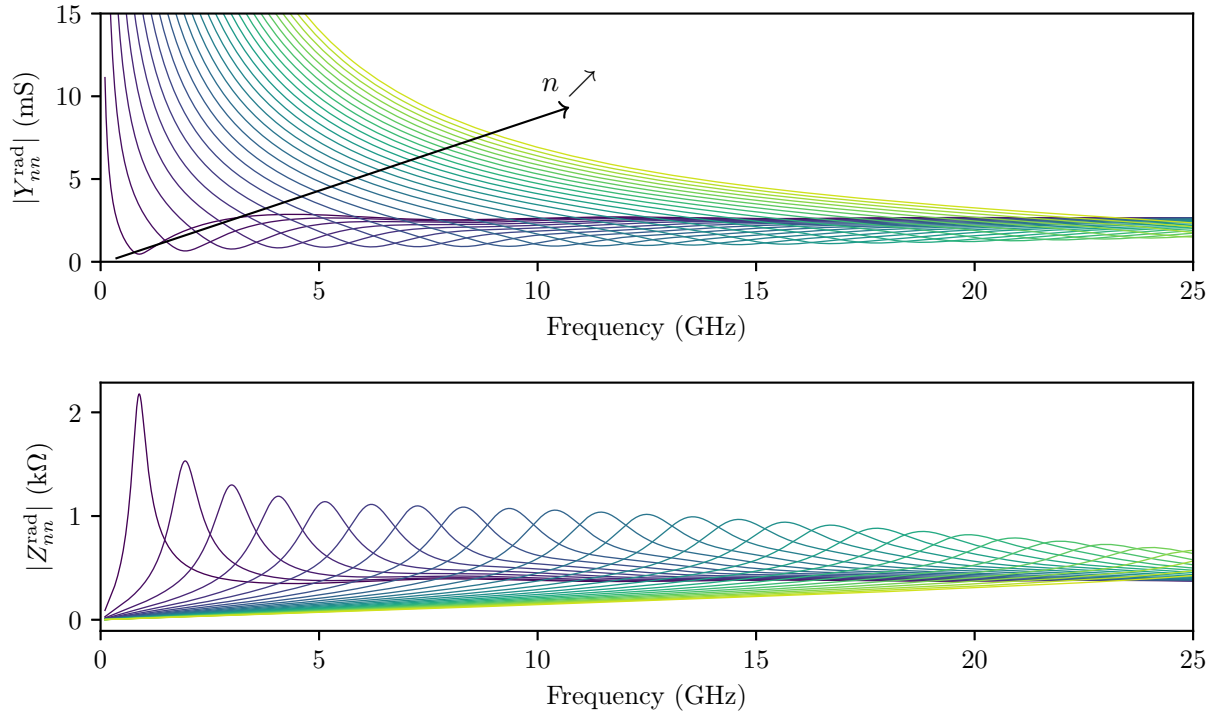


Fig. III.3.8 – Plots of $|Y_{nn}^{rad}(k_0)|$ and $|Z_{nn}^{rad}(k_0)|$, on-diagonal terms

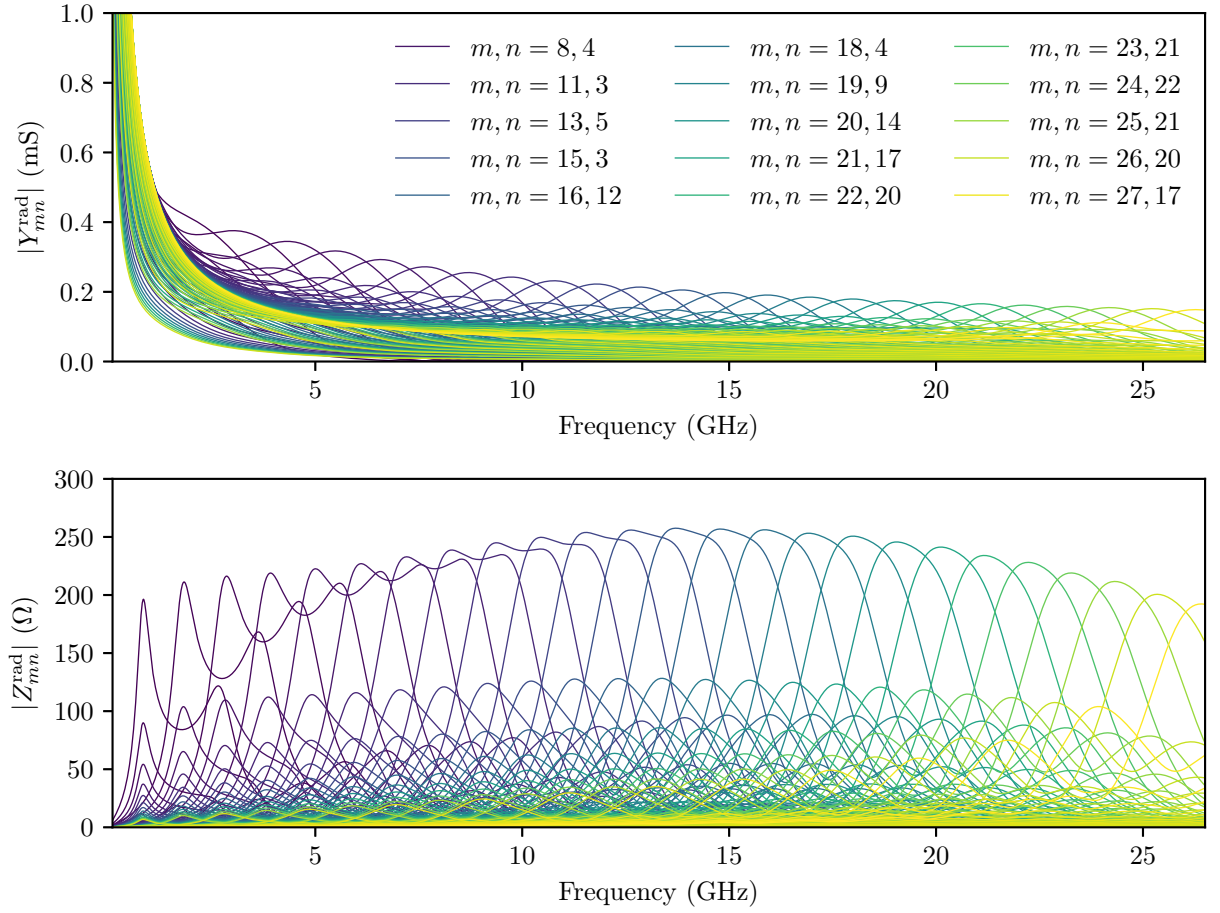


Fig. III.3.9 – $|Y_{mn}^{rad}(k_0)|$ and $|Z_{mn}^{rad}(k_0)|$, off diagonal terms

Chapter III.4

Monte-Carlo simulations

Contents

III.4.1	Introduction	126
III.4.2	Elements statistics of the normalized impedance matrix $\underline{\xi}$	127
III.4.2.1	Frequency dependency	127
III.4.2.2	Statistical representation of $\frac{k^2}{\Delta k^2}$	128
III.4.2.3	Matricial formulation of $\underline{\xi}$	129
III.4.3	RCM implementation	131
III.4.3.1	Developed programs	131
III.4.3.2	Implementation optimizations	132
III.4.4	Statistics of the elements of the normalized impedance matrix $\underline{\Xi}$	134
III.4.5	Relation between the variance of Ξ_{ii}, Ξ_{ij} and α	135
III.4.6	Chaoticity of the random normalized impedance matrix $\underline{\Xi}$	136
III.4.7	Statistical quantity of interest for EMSEC	137
III.4.8	First RCM application	141
III.4.8.1	Setup	141
III.4.8.2	Results	142
III.4.9	Conclusion	147

III.4.1 Introduction

The aims of this chapter are to illustrate how the **RCM** is practically applied, and how statistics of coupled quantities are determined through Monte-Carlo iterations. The normalized impedance matrix $\underline{\xi}$ will first be expressed in a convenient way to perform Monte-Carlo iterations. Then, various implementations of programs dedicated to the **RCM** will be exposed, and some software optimizations will be proposed. As the **RCM** applies only to chaotic system, a criterion based on the properties of $\underline{\xi}$ will be given. Afterwards, statistical quantities of interest for the **EMSEC** will be introduced as well as their implementation. Finally, the **RCM** will be applied on a simple case: the study of the coupling of two weakly coupled ports inside a cavity.

III.4.2 Elements statistics of the normalized impedance matrix $\underline{\underline{\xi}}$

III.4.2.1 Frequency dependency

In what follows, a statistical and practical formulation of the [RCM](#) will be detailed in order to run Monte-Carlo iterations. Equation (III.4.1) formulates the normalized impedance $\underline{\underline{\xi}}$, and includes the eigenmodes of a cavity:

$$\underline{\underline{\xi}}(k) = -\frac{j}{\pi} \sum_{n=1}^{\infty} \frac{\Delta k^2 \vec{\Phi}_n \otimes \vec{\Phi}_n^T}{k^2(1 - j/Q_{\text{unloaded}}) - k_n^2} \quad (\text{III.4.1})$$

It is important to have in mind that Δk^2 is the mean spacing between two adjacent wavenumbers k^2 (associated to two successive eigenmodes k_n and k_{n+1}) and $\vec{\Phi}$ statistically models the couplings between the ports and the eigenmodes. It is then possible to define a loss factor α defined as the following ratio [[Hemmady, 2006](#)]:

$$\alpha = \frac{k^2}{\Delta k^2 Q_{\text{unloaded}}} \quad (\text{III.4.2})$$

where Q_{unloaded} is the quality factor of the cavity without the ports of the systems. It describes the spectral overlap. This parameter can be expressed as:

$$Q_{\text{unloaded}} = \omega \frac{E}{P_d} \quad (\text{III.4.3})$$

where E is the total energy stored in the cavity and P_d the dissipated power throughout the cavity. In (III.4.2), α is estimated for a Q_{unloaded} quality factor that does not take into account for the losses into the cavity ports. Remind that ports may be ends of transmission lines or cables for example. However, the contribution of the losses in ports is commonly neglected and the overall quality factor of the cavity Q approximated by $Q \approx Q_{\text{unloaded}}$ [[Hemmady, 2006](#)]. For an undermoded cavity, the spectrum of the eigenfrequencies is discrete and $\alpha \ll 1$. On the other hand, for an overmoded cavity with overlapping modes, $\alpha \gg 1$. Equation (III.4.1) may be rewritten in such a way that:

$$\underline{\underline{\xi}}(k) = -\frac{j}{\pi} \sum_M \frac{\vec{\Phi}_n \otimes \vec{\Phi}_n^T}{\frac{k^2}{\Delta k^2} - \frac{k_n^2}{\Delta k^2} - j\alpha} \quad (\text{III.4.4})$$

Moreover, at the wavenumber of interest k , only the eigenmodes (associated to k_n) near k impact $\underline{\underline{\xi}}$. Similar arguments are employed when dealing with the computation of [GREEN's](#) functions of cavities (see [[Wu and Chang, 1988](#)]), where only a few modes are considered around a given frequency to accelerate the convergence of the computation. If M eigenmodes are considered around k , equation (III.4.4) can be written as:

$$\underline{\underline{\xi}}(k) = -\frac{j}{\pi} \sum_{n=-\frac{M}{2}}^{\frac{M}{2}} \frac{\vec{\Phi}_n \otimes \vec{\Phi}_n^T}{\frac{k^2}{\Delta k^2} - \frac{k_n^2}{\Delta k^2} - j\alpha} \quad (\text{III.4.5})$$

From a statistical point of view, the frequency dependence may be dropped out (α is considered constant near k), and:

$$\underline{\underline{\xi}}(k) = -\frac{j}{\pi} \sum_{n=-\frac{M}{2}}^{\frac{M}{2}} \frac{\vec{\Phi}_n \otimes \vec{\Phi}_n^T}{\frac{k^2}{\Delta k^2} - \frac{k_n^2}{\Delta k^2} - j\alpha} \Leftrightarrow \underline{\underline{\xi}}(0) = \underline{\underline{\xi}} = -\frac{j}{\pi} \sum_{n=-\frac{M}{2}}^{\frac{M}{2}} \frac{\vec{\Phi}_n \otimes \vec{\Phi}_n^T}{-\frac{k_n^2}{\Delta k^2} - j\alpha} \quad (\text{III.4.6})$$

The next step is to statistically determine the quantity $\frac{k_n^2}{\Delta k^2}$.

III.4.2.2 Statistical representation of $\frac{k_n^2}{\Delta k^2}$

Three different approaches may be employed to compute $\frac{k_n^2}{\Delta k^2}$. They are all related to properties of the random matrices drawn from the [gaussian orthogonal ensemble \(GOE\)](#). Thus, in what follows, the term $\frac{k_n^2}{\Delta k^2}$ will be replaced by $\tilde{\lambda} = \frac{\lambda}{\Delta(\lambda)}$, where λ are the eigenvalues of matrices from the [GOE](#) and $\Delta(\lambda)$ the mean spacing between two consecutive eigenvalues. These eigenvalues λ are associated to the random variable Λ and $\tilde{\lambda}$ to the random variable $\tilde{\Lambda}$ respectively. Drawbacks and benefits of each approach will now be exposed.

Method 1 The random variable S_n associated to the normalized eigenvalues spacing s_n ($s_n = \frac{\lambda_{n+1} - \lambda_n}{\Delta(\lambda)}$) is given by the WIGNER surmises, and its [PDF](#) is defined by:

$$p_{S_n}(s_n) = \frac{\pi s_n}{2} e^{-\frac{\pi}{4} s_n^2} \quad (\text{III.4.7})$$

The quantity $\frac{\lambda_n}{\Delta(\lambda)}$ may be expressed as a sum over the n previous spacings $\{s_i\}$ as:

$$\tilde{\lambda} = \frac{\lambda_n}{\Delta(\lambda)} = \frac{1}{\Delta(\lambda)} \sum_{i=1}^n (\lambda_{i+1} - \lambda_i) = \sum_{i=1}^n s_i \quad (\text{III.4.8})$$

The main advantage is that its computation is really straightforward and fast. The drawback of this method is that there is no guarantee that long range correlations between the eigenvalues spacings is as predicted by the [RMT](#). Indeed, from the [RMT](#), it is known that spacings s_n are correlated over a long distance in n [[Zheng, 2005](#)].

To generate random samples from the WIGNER surmises, one can benefit from the RAYLEIGH distribution. If X and Y are two random variables (associated to their [PDF](#) $f_X(x)$ and $f_Y(y)$) and $Y = cX$ where c is a scalar number, then $\mathbb{E}[Y] = \mathbb{E}[cX] = \int_{\mathbb{R}} cx f_X(x) dx = \int_{\mathbb{R}} y f_X(\frac{y}{c}) \frac{dy}{c}$, thus $f_Y(y) = \frac{1}{c} f_X(\frac{y}{c})$.

Let $R \sim \text{RAYLEIGH}(\sqrt{2})$ be a random variable, so its [PDF](#) is $f_R(r) = \frac{r}{2} e^{-\frac{r^2}{4}}$. If the random variable W is as $W \sim \frac{R}{\sqrt{\pi}}$, then its [PDF](#) is $f_W(r) = \sqrt{\pi} f_R(r\sqrt{\pi}) = \frac{\sqrt{\pi} r}{2} e^{-\frac{\pi r^2}{4}}$ which is the [PDF](#) of the WIGNER surmises. As scientific tools (Python, MATLAB, etc.) usually propose RAYLEIGH random generators, random values from the WIGNER surmises may be generated by scaling values from these random generator by $\frac{1}{\sqrt{\pi}}$.

Another solution is to use the inverse transform sampling. The idea is to take advantage of uniform random generator which distribution is $\mathcal{U}(0, 1)$, and to apply these random numbers to the inverse [CDF](#) of the target distribution, which leads to $S_n \sim \sqrt{-4 \ln U}$, with $U \sim \mathcal{U}(0, 1)$ [[Devroye, 2006](#)].

Method 2 The M eigenvalues $\lambda_{i\text{GOE}}$ (with $i \in [1, M]$) of matrices of size M from the [GOE](#) are distributed as a WIGNER's semi circle law [[Zheng, 2005](#)]. The average spacing $\Delta(\lambda_{\text{GOE}})$ near the eigenvalue $\lambda_{i\text{GOE}}$ is:

$$\Delta(\lambda_{i\text{GOE}}) = \frac{\pi}{\sqrt{2M - \lambda_{i\text{GOE}}^2}} \mathbb{1}_{[-\sqrt{2M}, \sqrt{2M}]}(\lambda_{i\text{GOE}}) \quad (\text{III.4.9})$$

As $\Delta \approx \frac{\sqrt{2M}}{\pi}$ near $\lambda_{i\text{GOE}} = 0$, it is possible to drop out the dependency of $\Delta(\lambda)$ ($\Delta(\lambda) \rightarrow \Delta$) in ([III.4.9](#)) for the middle M eigenvalues. Then λ is scaled as:

$$\tilde{\lambda} = \frac{\lambda}{\Delta} = \frac{\lambda \sqrt{2M}}{\pi} \quad (\text{III.4.10})$$

This method refers to an unfolding procedure as exposed in section III.1.2.2.3. It is sometimes applied to compute the eigenvalues from a matrix of size M' from the GOE ensemble and to select the middle M eigenvalues (M' was set to $5M$ in [Hemmady et al., 2012]). The advantage is that the long-range correlations are guaranteed. The downside is that $4M$ eigenvalues are lost whereas the computation of eigenvalues of large matrices is time-consuming.

Method 3 The last method is an unfolding procedure which consists in applying the CDF of the eigenvalues distribution ($p_\Lambda(\lambda) = \sqrt{2M - \lambda^2}/(M\pi)$) to the computed eigenvalues λ .

If X and Y are two random variables where Y is computed as the composition of X by its CDF, *i.e.* $Y = F_X(X)$, then the CDF of Y is:

$$\begin{aligned} F_Y(y) &= \mathbb{P}[Y \leq y] \\ &= \mathbb{P}[F_X(x) \leq y] \\ &= \mathbb{P}[x \leq F_X^{-1}(y)] \\ &= F_X(F_X^{-1}(y)) \mathbf{1}_{F_X(S)}(y) \\ &= y \mathbf{1}_{F_X(S)}(y) \end{aligned} \tag{III.4.11}$$

where S is the support of the random variable X . Especially, if $\Lambda' = F_\Lambda(\Lambda)$, then $F_{\Lambda'}(\lambda') = \lambda' \mathbf{1}_{[0,1]}(\lambda')$ thus $\Lambda' \sim \mathcal{U}(0, 1)$ (uniform distribution between 0 and 1). A scaling process on Λ' will enforce a uniform spacing between the eigenvalues λ' and leads to a set of scaled values $\tilde{\lambda}$.

$$\tilde{\lambda}_i = M\lambda'_i - \frac{M}{2} = MF_\Lambda(\lambda_{i\text{GOE}}) - \frac{M}{2} \tag{III.4.12}$$

where the CDF of Λ is:

$$F_\Lambda(\lambda_{i\text{GOE}}) = \int_{-\infty}^{\lambda_{i\text{GOE}}} \frac{1}{M\pi} \sqrt{2M - \lambda'^2} d\lambda' = \frac{1}{2} + \frac{1}{\pi} \sin^{-1} \left(\frac{\lambda_{i\text{GOE}}}{\sqrt{2M}} \right) + \frac{\lambda_{i\text{GOE}}}{2\pi M} \sqrt{2M - \lambda_{i\text{GOE}}^2} \tag{III.4.13}$$

To sum up, the complete procedure is: to first compute the eigenvalues $\lambda_{i\text{GOE}}$ a matrix from the GOE, then to calculate $\lambda'_i = F_\Lambda(\lambda_{i\text{GOE}})$ and to finally scale $\tilde{\lambda}_i$ as $\tilde{\lambda}_i = MF_\Lambda(\lambda_{i\text{GOE}}) - \frac{M}{2}$. This way, the mean value of the eigenvalue spacings remains constant all along the spectrum. However, long-range correlations of the eigenvalues need to be verified.

We can now consider these methods with the quantities exposed in section III.1.2.2.3. Remind that the eigenvalues $\tilde{\lambda}$ should be uniformly distributed. Fig. III.4.1 shows plots of the eigenvalue distributions computed with the three methods. We obtain similar results, and we note that method 1 produces a fluctuating distribution. We now consider the mean eigenvalue spacings $\langle \tilde{s}_n \rangle$ that should be reduced to unity. Fig. III.4.2 depicts $\langle \tilde{s}_n \rangle$ for 2000 Monte-Carlo iterations and method 3 produces the lowest standard deviation for $\langle \tilde{s}_n \rangle$. Then, the number variance (as exposed in section III.1.2.2.3) is shown in Fig. III.4.3. Method 1 does not ensure, even for short intervals L , a number variance close to the expected one for chaotic systems. Method 2 is valid for $L < 15$, and method 3 whatever L is.

From this comparison, we notice that method 3 is the most capable to model chaotic systems, and we have selected it to model our chaotic systems.

III.4.2.3 Matricial formulation of ξ

We now consider that the eigenmodes of the cavity are issued from the random matrix theory by method 3 described previously. To be numerically evaluated, equation (III.4.1) should be rewritten

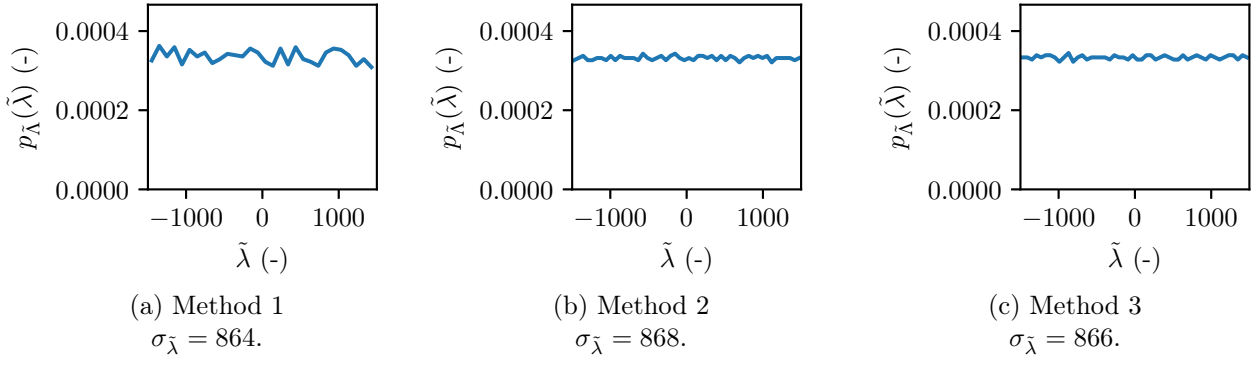


Fig. III.4.1 – Comparison of the three methods to compute $\tilde{\lambda} = \frac{\lambda}{\Delta}$, for $M = 3000$ eigenvalues computed. The obtained distribution should be $\sim \mathcal{U}(-M, M)$ and $p_{\tilde{\lambda}}(\tilde{\lambda}) = \frac{1}{M} \mathbb{1}_{[-\frac{M}{2}, \frac{M}{2}]}(\tilde{\lambda})$ and $\frac{1}{M} = 3.333 \times 10^{-4}$. For the method 2, the middle M eigenvalues were selected in a matrix of size $M' = 15000$. We remark that all the standard deviation values $\sigma_{\tilde{\lambda}}$ for the three methods are close to each other. The theoretical standard deviation here is $\frac{3000}{2\sqrt{3}} = 866$ (standard deviation of a uniform distribution on the range $[-M, M]$).

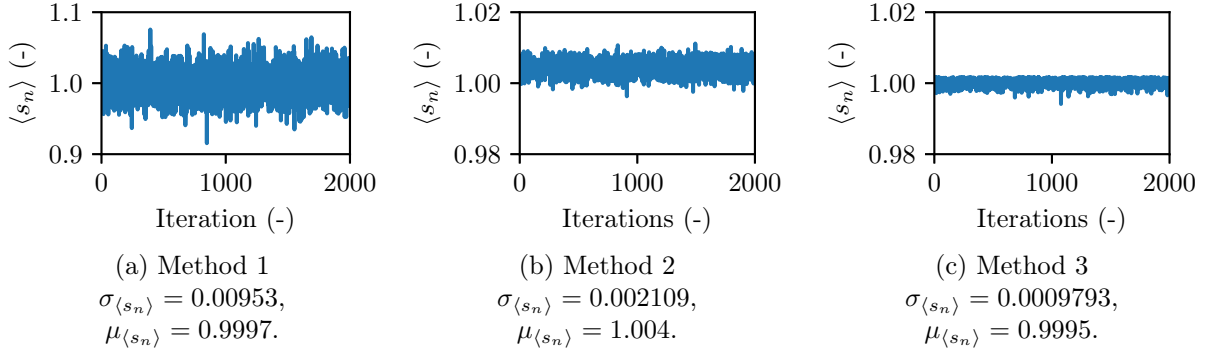


Fig. III.4.2 – Comparison of the three methods to compute $\langle s_n \rangle$ for a matrix $M = 600$. The spacings were computed for matrices of size $M = 600$ (thus 599 spacings), and the mean spacing $\langle s_n \rangle$ was computed for 2000 Monte-Carlo iterations. Remark that the right axes for method 1 has not the same scale.

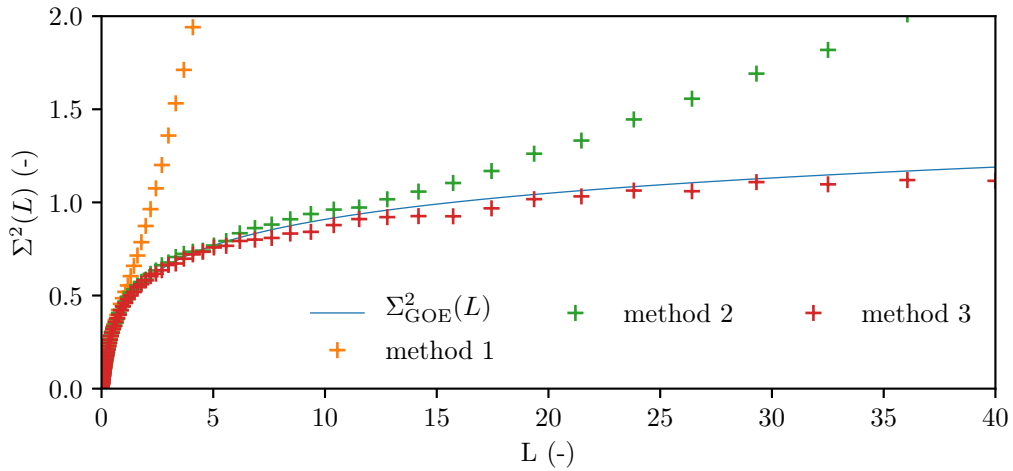


Fig. III.4.3 – Number variance $\Sigma^2(L)$ obtained from 48 matrices of size $M = 3000$ for the three methods, compared to $\Sigma_{\text{GOE}}^2(L)$ (solid blue curve).

as [Hemmady et al., 2005]:

$$\underline{\underline{\xi}} = -\frac{j}{\pi} \underline{\underline{W}} [\underline{\underline{\lambda}} - j\alpha \underline{\underline{1}}]^{-1} \underline{\underline{W}}^T \quad (\text{III.4.14})$$

where $\underline{\underline{W}}$ is a $M \times N$ real matrix, N is the number of ports in the system and M the number of modes taken into account in the cavity. The elements of $\underline{\underline{W}}$ are normally distributed $\mathcal{N}(0, 1)$. $\underline{\underline{W}}$ takes into account the coupling of the modes onto the ports of the system. The diagonal matrix $\underline{\underline{\lambda}}$ is populated with values computed from method 3 ($\lambda_{ii} = MF_{\Lambda}(\lambda_{i\text{GOE}}) - \frac{M}{2}$), where $\lambda_{i\text{GOE}}$ represents the M eigenvalues of a matrix from the [GOE](#).

III.4.3 RCM implementation

The formulation (III.4.14) of the normalized impedance matrix $\underline{\underline{\xi}}$ needs to be now efficiently implemented to compute induced currents or coupled voltages. This section will focus on the softwares that have been developed and on optimizations that allow performance gains.

III.4.3.1 Developed programs

Several programs have been developed along this PhD to efficiently implement the [RCM](#). The first one computes the eigenvalues of matrices from the [GOE](#), which are the on-diagonal elements of the matrix $\underline{\underline{\lambda}}$. As $\underline{\underline{\lambda}}$ is not configuration dependent, it is possible to precompute a large number of eigenvalues from the [GOE](#). Moreover, as the calculus involved in the computing of eigenvalues is time-consuming, these precomputed values will reduce in a very significant way the time needed to get the induced current (or coupled voltages) from the [RCM](#). This software was run several times to compute eigenvalues for matrices size M between $M = 10$ to $M = 3000$. We remind that M denotes the number of modes considered in the cavity. Two million of matrices for a given size M were randomly drawn from the [GOE](#) and their eigenvalues were stored in appropriate files.

Two other programs are dedicated to apply the [RCM](#). One to compute the currents or voltages within a cavity (*i.e.* without the coupling of a plane wave to an aperture) that implements equation (III.1.24). The inputs of this program are the loss factor α , the file that stores eigenvalues of random matrices from the [GOE](#), the radiation impedance matrix $\underline{\underline{Z}}^{\text{rad}}$ and the number of Monte-Carlo iterations to run. Another program implements equations (III.2.110) to compute \vec{I}_P , (III.2.113) to compute \vec{V}_A , (III.2.112) to compute $\underline{\underline{Y}}^{\text{cav}}$ and (III.1.24) to compute $\underline{\underline{Z}}^{\text{cav}}$. It takes as inputs: the loss parameter α , the number of modes in the cavity M , the admittance $\underline{\underline{Y}}^{\text{rad}}$ of the aperture, the impedance of the ports $\underline{\underline{Z}}^{\text{rad}}$, the characteristic impedance $\underline{\underline{Z}}^L$, and the source vector \vec{I}^{inc} . All these matrices and vectors are frequency dependent. The random values used to compute matrices $\underline{\underline{Z}}^{\text{cav}}$ and $\underline{\underline{Y}}^{\text{cav}}$, which account for a random geometry, are randomly drawn at each iteration and for each frequency. A schematic diagram of this computation is depicted in Fig. III.4.4.

The outputs of these two programs are either a set of vectors \vec{I} (or \vec{V}) or histograms of the vectors elements and a set of outliers (for extreme values). When histograms are needed, one histogram is computed per frequency, and all the histograms are computed with the same bin edges and bin count. Thus, the histogram for a given frequency range is obtained by a simple addition of histograms and a normalization step. Histograms for the real part, the imaginary part and the modulus of the elements of \vec{I}_P may be stored.

The determination of the loss factor α is mandatory to apply the [RCM](#). Several methods can be employed and will be exposed later. One of these is a fitting process which uses the elements $\xi_{ij\alpha}$ of

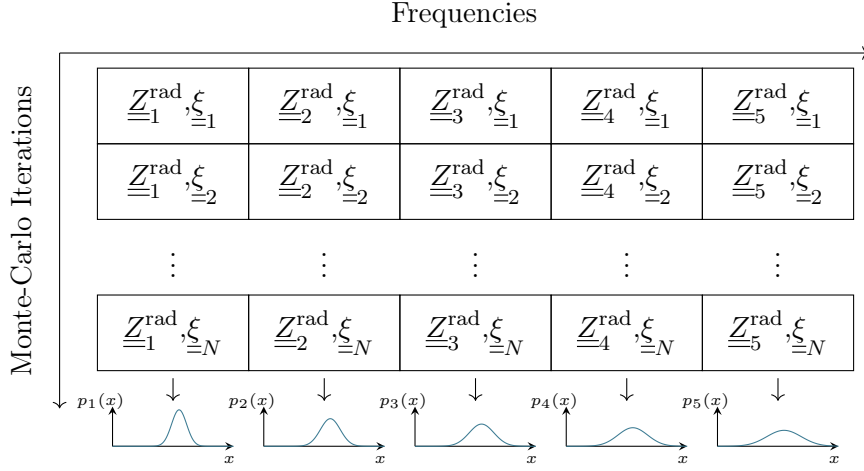


Fig. III.4.4 – Computation process of the statistics of \vec{I}_P with N iterations (vertical axis). Each cell corresponds to an evaluation of \vec{I}_P , computed from $\underline{\xi}_{\underline{n}}$ (n th-iteration) and with $\underline{Z}_{\underline{i}}^{\text{rad}}$ (corresponding to the i th-frequency). $\underline{\xi}_{\underline{n}}$ is not randomly drawn for each frequency, but only for each Monte-Carlo iteration. Likewise as with a stirrer, where a measurement along a given frequency bandwidth is performed for a given rotation angle. For each frequency f_i , a histogram $p_i(x)$ is computed.

the random matrix. A program is in charge of computing many matrices $\underline{\xi}_{\alpha}$ from equation (III.4.14) and for different values of α . Then, from $\underline{\xi}_{\alpha}$, the PDF of the elements $\xi_{ij\alpha}$ are assessed by means of a kernel density estimation (KDE) [Wand and Jones, 1994] and then stored. A KDE is related to histograms, but can be endowed with continuity or smoothness properties. A random sample is not considered as an increment in a histogram bin, but as a function (kernel). Then, all the functions are averaged to determine the KDE. Even if several kernels may be applied (triangle, uniform, negative exponential, gaussian, etc.), the gaussian kernel is classically adopted (as in this work). These statistical distributions will be used to fit the elements $\xi_{ij}^{\text{Measured}}$ obtained experimentally in order to determine the loss parameter α .

Finally, a tool was developed to efficiently compute some properties of scattering matrix eigenvalues of the normalized impedance matrix $\underline{\xi}$. These properties, that will be detailed in section III.4.6, are related to the assessment of the chaoticity of a system.

III.4.3.2 Implementation optimizations

To obtain reliable probability density functions (in order to compute probabilities of rare events, for example), numerous draws must be carried out. With a naive implementation of (III.4.14), thousands of draws are calculated within a few hours. To reduce the computation time, optimizations of several kinds need to be carried out.

First, the use of a programming language that is compiled and not interpreted (like Python or MATLAB) increases the performances. Moreover, calling libraries dedicated to efficient matrix computations results in a performance gain. It was chosen to take advantage of the *Math Kernel Library* (MKL) from Intel®. This library, dedicated to Intel® processors, allows efficient operations on matrices. It contains functions to compute products, eigenvalues/eigenvectors, inverse, etc. of matrices. The element type of the matrices may be real or complex, and their representations may have single or double

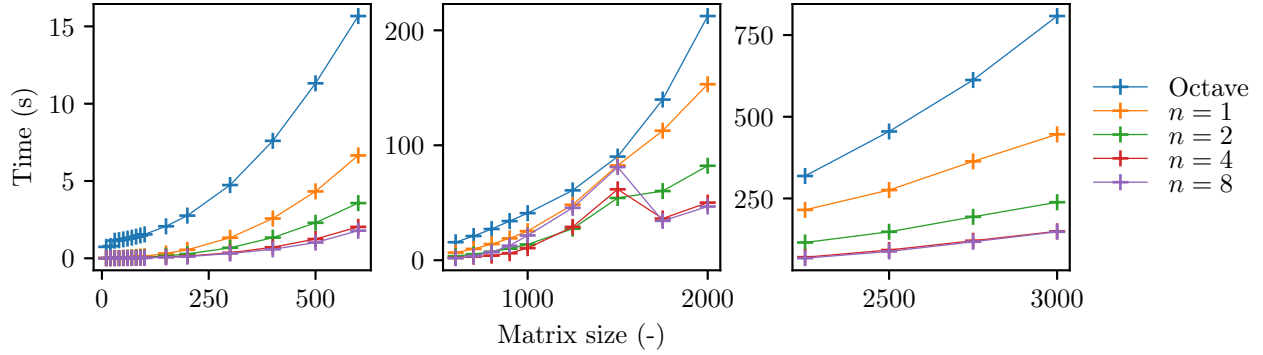


Fig. III.4.5 – CPU time required to compute the eigenvalues of matrices from the GOE (based on 10 runs). Octave refers to the implementation proposed by the authors of the RCM¹ and runs with [Eaton et al., 2017, Octave], and n is the number of threads used to compute the eigenvalues using the listed optimizations. Note that for $n > 4$ there is no performance gain as the computer has only 4 physical cores.

precision. In addition, the matrices may have different properties (general, symmetric or hermitian). To perform an operation (*i.e.* eigenvalues computation, product), the function specialized in a given matrix type (element type, element precision and property of the matrix) needs to be called. In this way, problem specific acceleration is used, leading to reduce computation time. For operations that occur while using the RCM, many matrices are symmetric such as $\underline{\underline{Y}}^{\text{cav}}$, $\underline{\underline{Y}}^{\text{rad}}$, $\underline{\underline{Z}}^{\text{cav}}$ and $\underline{\underline{Z}}^{\text{rad}}$. Most of the matrices having complex elements and double precision was chosen for all the matrices (*i.e.* 8 B per matrix element of real matrices and 16 B for complex ones). We explain how the Math Kernel Library (MKL) is employed for three steps that occur while using the RCM:

- Eigenvalues of a real symmetric matrix $\underline{\underline{M}}$: the function `dsyevd` is used, which implements the divide and conquer algorithm. This algorithm is dedicated to real symmetric matrices;
- Square root of a real symmetric matrix $\left[\underline{\underline{A}}\right]^{1/2}$: by using the `dsyevd` function, the matrix $\underline{\underline{A}}$ is diagonalized ($\underline{\underline{A}} = \underline{\underline{B}} \underline{\underline{\lambda}} \underline{\underline{B}}^{-1}$). Then, the square root of the elements of $\underline{\underline{\lambda}}$ are taken, to get $\underline{\underline{\lambda}}^{1/2}$. Then, we compute $\underline{\underline{B}} \underline{\underline{\lambda}}^{1/2} \underline{\underline{B}}^{-1}$ by using the function `zgemm` (product of general complex matrices);
- Inverse of a matrix $\left[\underline{\underline{A}}\right]^{-1}$: first the LU factorization of the matrix $\underline{\underline{A}} = \underline{\underline{L}} \underline{\underline{U}}$ is performed thanks to the function `zgetrf`. Then, the backward and forward substitutions are computed by the function `zgetri`.

Moreover, random numbers are needed to populate the random matrices. Samples points are needed from gaussian and RAYLEIGH distributions. The routines `vdRngGaussian` and `vdRngRayleigh` fulfill that purpose.

GSL, another library, is used to compute histograms. Indeed, it is sometimes not possible to store all the vectors \vec{I} as it would require too much disk storage, thus only histograms are stored. To create a histogram, a number of bins and a range have to be specified. To estimate this range, some Monte-Carlo iterations are processed. Then, the first and last percentiles are computed, used as lower and upper bounds and the outliers are stored.

¹Reference page for the RCM: <http://anlage.umd.edu/RCM/>.

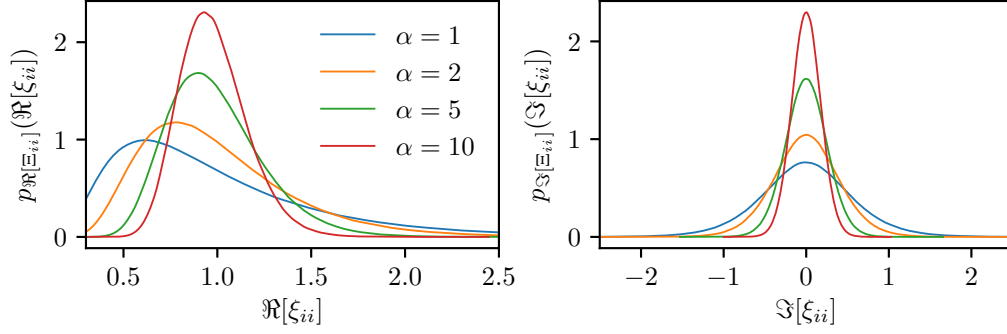


Fig. III.4.6 – PDFs of the real and imaginary part of the on-diagonal elements of the random variable $\underline{\Xi}$. By construction, all the on-diagonal elements of $\underline{\Xi}$ follow the same random variable.

All the developed programs are designed to be multithreaded, allowing to split the computations and to process them in parallel. This requires to design the programs in such a way that resources are well dispatched between the different threads. Though, it is important to avoid the use of hyperthreading technology to be able to take full advantage of the CPU caches. Fig. III.4.5 shows the performance gains to compute 300 matrices $\underline{\lambda}$ for different matrix sizes M .

Some matrices have large dimensions leading to a high computation cost when it comes to multiply matrices. By noticing that the matrix $[\underline{\lambda} - j\alpha \mathbf{1}]^{-1}$ is diagonal, it is possible to reduce the computational complexity from $O(M^2N)$ to $O(MN)$ for the computation of the product \underline{W} by $[\underline{\lambda} - j\alpha \mathbf{1}]^{-1}$.

By putting all these optimizations together, it is possible to obtain induced currents and coupled voltages within less than 4 minutes with thousands of draws for the matrix $\underline{Z}^{\text{cav}}$. These results have been obtained on an Intel(R) Core(TM) i7-4770 CPU (3.40 GHz) with 32 GB of random access memory and a Solid-state drive (SSD) disk. It is worth noting that the throughput of read and write operations on the disks has a very significant impact on the performances.

III.4.4 Statistics of the elements of the normalized impedance matrix $\underline{\Xi}$

We now have at our disposal several tools to compute the matrix samples. From now, the normalized impedance matrix $\underline{\xi}$ is associated to the random matrix $\underline{\Xi}$, and $\underline{\Xi}_{ij}$ refers to the random variable associated to the elements of the random matrix $\underline{\Xi}$. We can draw several sample points to analyse the statistics of elements of $\underline{\Xi}$. Fig. III.4.6 and Fig. III.4.7 show the statistics of on-diagonal and off-diagonal elements of the matrix $\underline{\Xi}$. These statistics have been computed with $N = 2$ ports in the system (*i.e.* $\underline{\Xi}$ is a 2 by 2 random matrix), with $M = 600$ eigenvalues considered in the reverberant environment, and for different loss factors α . Method 3 was applied to produce these results. For each run, a new realization of \underline{W} and $\underline{\lambda}$ was drawn. These PDFs have been assessed from two million Monte-Carlo computations of (III.4.14). These PDFs are similar to those found in the literature [Gradoni et al., 2014].

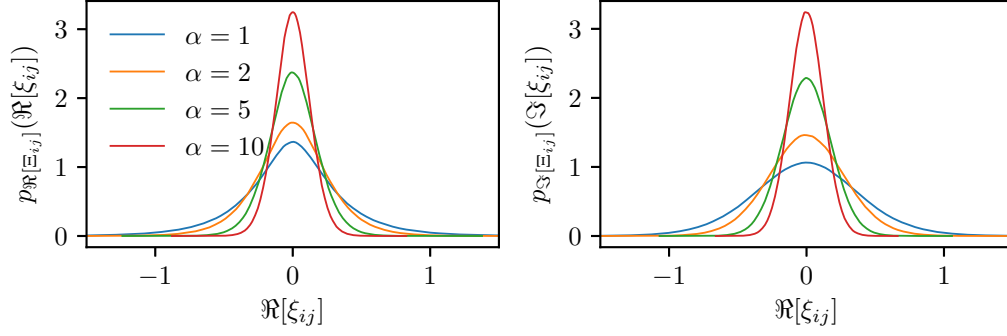


Fig. III.4.7 – PDFs of the real and imaginary part of the off-diagonal elements of the random variable Ξ . By construction, all the off-diagonal elements of Ξ follow the same random variable.

III.4.5 Relation between the variance of Ξ_{ii} , Ξ_{ij} and α

A general formulation of the loss factor α is $\alpha = \frac{k^2}{\Delta k^2 Q}$. More convenient expressions are given in [Hemmady, 2006] depending on the type of the cavity. For a 2D cavity (*i.e.* a cavity with one dimension very small compared to the two others), α is expressed as:

$$\alpha = \frac{k_0^2 A}{4\pi Q} \quad (\text{III.4.15})$$

where A is the area of the cavity. For a 3D cavity, the loss factor is given by:

$$\alpha = \frac{k_0^3 V}{2\pi^2 Q} \quad (\text{III.4.16})$$

where V is the volume of the cavity.

To assess the order of magnitude of α , the quality factor of the cavity of interest needs to be quantified. The total quality factor Q may be expressed as:

$$\frac{1}{Q} = \sum_{i=1}^N \frac{1}{Q_i} \quad (\text{III.4.17})$$

where each Q_i accounts for a loss mechanism. In [Liu et al., 1983] the following formula is given to determine the quality factor Q_{wall} associated to the losses in the walls of a cuboid cavity:

$$Q_{\text{wall}} = \frac{V}{S} \frac{3}{2} \frac{1}{\delta} \frac{1}{1 + \frac{3\pi}{8k_0} \left(\frac{1}{a} + \frac{1}{b} + \frac{1}{c} \right)} \quad (\text{III.4.18})$$

where a, b and c are the dimensions of the cavity, V its volume ($V = abc$) and S its surface ($S = 2(ab + ac + bc)$ for a cuboid). Note that $Q_{\text{wall}} \propto \sqrt{f}$ in equation (III.4.18) when f is large enough. δ , the skin depth of the wall material, is:

$$\delta = \sqrt{\frac{2}{\omega \mu_0 \mu_r \sigma}} \quad (\text{III.4.19})$$

where σ is the conductivity of the material. In the case of the computer chassis mock-up, made of steel, $\sigma = 1 \times 10^6 \text{ S m}^{-1}$. If there is an aperture on the wall of the cavity, its quality factor $Q_{\text{ap.}}$ is [Hill, 2009]:

$$Q_{\text{ap.}} = \frac{4\pi}{\lambda \langle \sigma_{\text{ap.}} \rangle_{\Omega}} \quad (\text{III.4.20})$$

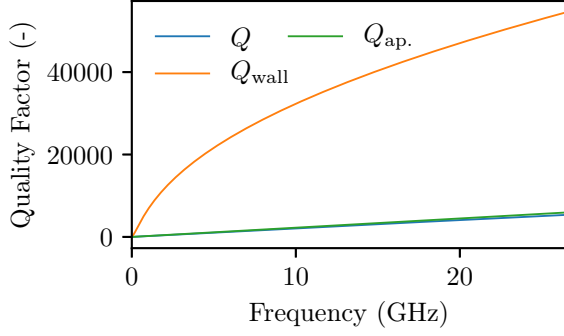


Fig. III.4.8 – Evolution of the total quality factor Q of the computer chassis mock-up.

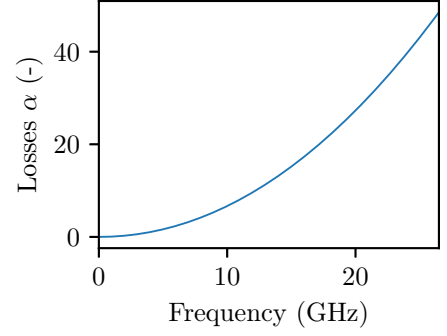


Fig. III.4.9 – Evolution of the loss factor α of the computer chassis mock-up.

where $\langle \sigma_{\text{ap.}} \rangle_{\Omega}$ is the mean absorption cross section of the aperture over 4π sr. $\langle \sigma_{\text{ap.}} \rangle_{\Omega}$ is not frequency dependent for large apertures compared to the wavelength, and $Q_{\text{ap.}} \propto f$. For a circular aperture, $\langle \sigma_{\text{ap.}} \rangle_{\Omega} = \frac{\pi a^2}{2}$ where a is the radius. If we consider a rectangular aperture, $\langle \sigma_{\text{ap.}} \rangle_{\Omega}$ may be taken to be approximately equal to the surface of the aperture (*i.e.* 14 cm \times 4 cm for the aperture of the mock-up), and $Q_{\text{ap.}}$ may be determined.

The quality factor Q of the mock-up may finally be plotted. Fig. III.4.8 shows the evolution of Q_{wall} , $Q_{\text{ap.}}$ and Q with the frequency. We observe that Q is dominated by the losses due to the aperture. Then, from equation (III.4.16), the RCM loss factor α is plotted in Fig. III.4.9. For an actual configuration, this reasoning does not apply as all the losses are not included, such as, in PCBs or cables. However, it gives a lower boundary for the loss factor α .

In [Zheng et al., 2006b] it was demonstrated that the variance of the elements of Ξ are related to the loss parameter α by the following expressions:

$$\text{Var} [\Re [\Xi_{ii}]] = \text{Var} [\Im [\Xi_{ii}]] = \frac{1}{\pi\alpha} \quad (\text{III.4.21})$$

$$\text{Var} [\Re [\Xi_{ij}]] = \text{Var} [\Im [\Xi_{ij}]] = \frac{1}{2\pi\alpha} \quad (\text{III.4.22})$$

As the developed tools allow to easily generate numerous matrices Ξ , it is achievable to test these assumptions, by computing the estimated variance. In [Hemmady, 2006] it is argued that these relations hold only for $\alpha \geq 5$. This conclusion was based on experimental data acquired onto a 2D cavity. The quantity $\text{Var}[\Re[\Xi_{11}]] \times \alpha\pi$ should stay equal to 1 as α increases.

Fig. III.4.10 shows the evolution of $\text{Var}[\Re[\Xi_{11}]] \times \alpha\pi$ according to α and for $\alpha < 11$. We observe that the equality (III.4.21) holds as soon as $\alpha \geq 5$. However, in Fig. III.4.11, one remarks that the equality (III.4.21) does not hold for all α and for all M .

In the literature, two matrix sizes are found: $M = 600$ in [Gradoni et al., 2015], and $M = 200$ in [Zheng et al., 2006b]. These two values are sufficiently large for $\alpha \leq 100$ (as soon as $\alpha > 100$, then $\text{Var} [\Re [\Xi_{ii}]] < 0.98$). For $M = 3000$, $\text{Var} [\Re [\Xi_{ii}]] < 0.98$ as soon as $\alpha = 600$.

For the empty mock-up, it has been estimated that $\alpha_{\text{max}} \approx 40$, thus setting M to 600 should be sufficient. In any case, when applying the RCM, M has to be set in consideration of α .

III.4.6 Chaoticity of the random normalized impedance matrix Ξ

The RCM applies only to chaotic systems. Some properties of chaotic systems are related to the eigenvalues of the scattering matrix \underline{s} associated to the normalized impedance matrix Ξ . \underline{s} is computed

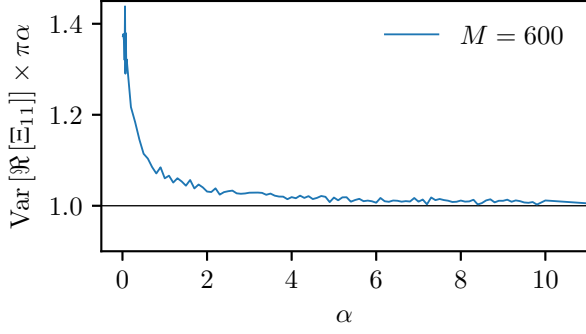


Fig. III.4.10 – Evolution of $\text{Var}[\Re[\Xi_{11}]] \times \alpha\pi$ as α increases from 0 to 11. Ξ was computed from $M = 600$ eigenvalues.

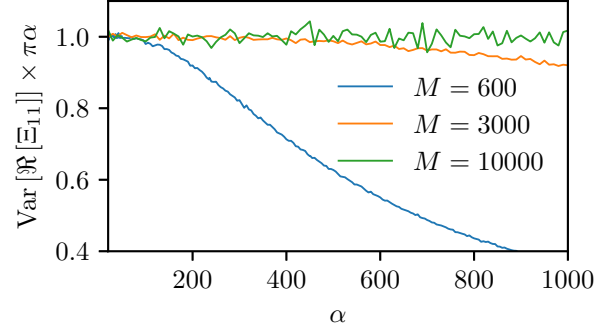


Fig. III.4.11 – Evolution of $\text{Var}[\Re[\Xi_{11}]] \times \alpha\pi$ as α increases from 50 to 100. Three matrix sizes were considered. The variance $\text{Var}[\Re[\Xi_{11}]]$ was computed from 2 millions sample points for $M = 600$ and $M = 3000$ and for 10000 sample points for $M = 10000$.

as:

$$\underline{s} = (\underline{\Xi} + \underline{1})(\underline{\Xi} - \underline{1})^{-1} \quad (\text{III.4.23})$$

\underline{s} may be diagonalized and its eigenvalues may be expressed as moduli and phases:

$$\underline{s} = \underline{U} \begin{pmatrix} |\lambda_1|e^{j\phi_1} & \dots & 0 \\ \vdots & \ddots & \vdots \\ 0 & \dots & |\lambda_N|e^{j\phi_N} \end{pmatrix} \underline{U}^{-1} \quad (\text{III.4.24})$$

where the columns of \underline{U} are the eigenvectors of \underline{s} .

Based on the DYSON circular ensemble [Dyson, 1962, Brouwer, 1995, Hemmady et al., 2005], and for a chaotic system, the random variable Φ , associated to the distribution of the phases $[\phi_1; \dots; \phi_N]$ of \underline{s} , and the random variable Λ related to the distribution of the modulus $[\lambda_1; \dots; \lambda_N]$ of \underline{s} should be independent. Thus, we have:

$$p_\Lambda(\lambda) = \mathbb{P}[\Lambda = \lambda | \Phi = \phi] = \mathbb{P}[\Lambda = \lambda] \quad (\text{III.4.25})$$

Moreover, Φ follows a uniform distribution, thus its PDF is:

$$p(\phi) = \frac{1}{2\pi} \mathbb{1}_{[-\pi, \pi]}(\phi) \quad (\text{III.4.26})$$

From these properties, the polar 2D histogram of the eigenvalues has rotational invariance. As the formulation of $\underline{\Xi}$ given in (III.4.14) considers that the system is chaotic, the properties aforementioned must be ensured. Fig. III.4.12 displays 2D histograms of the real and imaginary parts of the eigenvalues for two random matrices \underline{s} computed from two random matrices $\underline{\Xi}$ with different loss parameter α (1 and 10). It can be observed that the modulus and phase of the eigenvalues are indeed independent. It validates the ability of the random variable $\underline{\Xi}$ to describe a chaotic behavior.

III.4.7 Statistical quantity of interest for electromagnetic security (EMSEC)

Three statistical quantities of interest, related to EMSEC problematics, will be exposed in this section. In the next section, these three quantities will be used in application of the RCM.

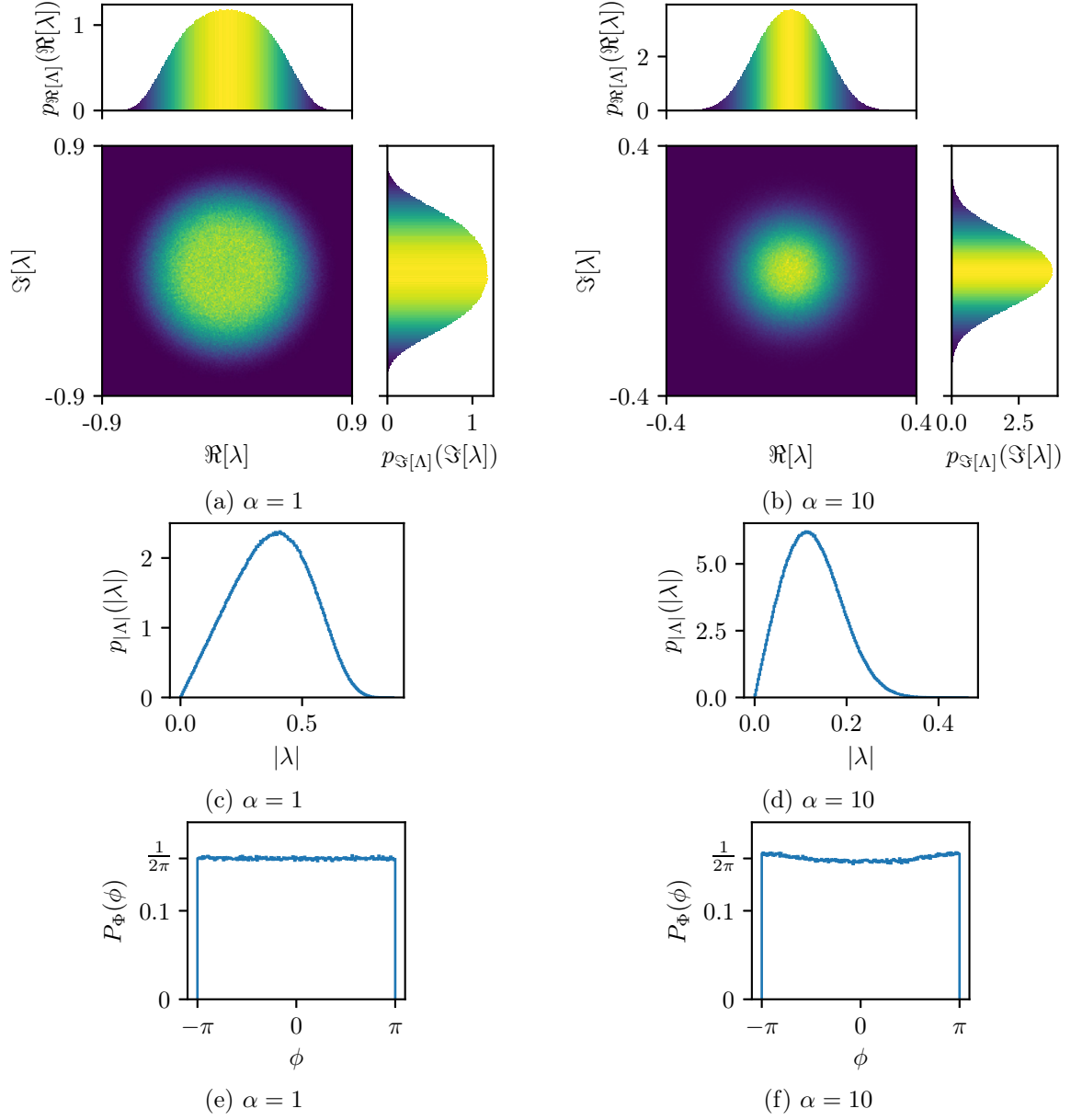


Fig. III.4.12 – Statistics of the eigenvalues of \underline{s} for two alpha values ($\alpha = 1$ for Fig. III.4.12a, Fig. III.4.12c and Fig. III.4.12e and $\alpha = 10$ for Fig. III.4.12b, Fig. III.4.12d and Fig. III.4.12f). In addition to the 2D histograms, the assessed PDF of Λ and Φ are plotted.

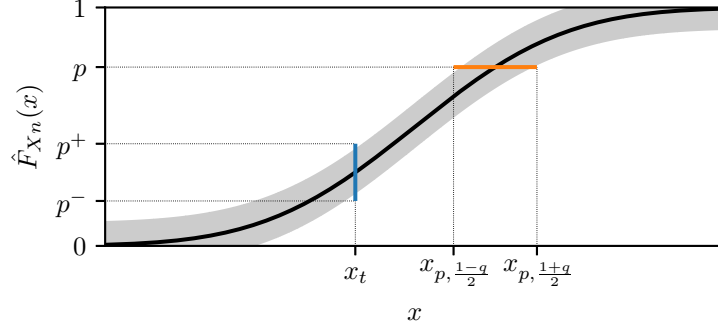


Fig. III.4.13 – Confidence intervals at x_t for the empirical CDF $\hat{F}_{Xn}(x_t)$, the confidence interval of the quantile $x_{p\%}$.

n	$1 - \alpha_{\text{risk}} = 90\%$	$1 - \alpha_{\text{risk}} = 95\%$	$1 - \alpha_{\text{risk}} = 99\%$
100	0.122	0.136	0.163
1000	0.0387	0.0429	0.0515
10000	0.0122	0.0136	0.0163

Table III.4.1 – ε for several couples n /confidence interval, computed from equation (III.4.29). $1 - \alpha_{\text{risk}}$ is the probability that the interval contains the true CDF $F_X(x)$

Probability to exceed a limit For EMSEC, a valuable quantity is the probability that a physical quantity, whose random variable is X , exceeds a given threshold. This information is related to its CDF $F_X(x)$ defined as:

$$F_X(x) = \mathbb{P}[X \leq x] \quad (\text{III.4.27})$$

Sample values of the random variable X may be generated through Monte-Carlo iterations. Then, from this sample an empirical CDF of X can be obtained. Let $X_1, \dots, X_j, \dots, X_n$ be independent and identically distributed (iid) random variables with a common CDF $F_X(x)$ associated to the n random draws. The empirical CDF is then defined as the estimator $\hat{F}_{Xn}(x)$ such that:

$$\hat{F}_{Xn}(x) = \frac{1}{n} \sum_{k=1}^n \mathbf{1}_{\{X_k \leq x\}} \quad (\text{III.4.28})$$

where $\mathbf{1}_E$ is the indicator of the event E .

The probability that a sample point x exceeds the threshold x_t is thus $1 - \hat{F}_{Xn}(x_t)$. As the estimator $\hat{F}_{Xn}(x)$ depends on the number of sample points n , $\hat{F}_{Xn}(x_t)$ also depends of n . It is thus relevant to determine a confidence band such that: $p^- \leq \hat{F}_{Xn}(x_t) \leq p^+$ (see Fig. III.4.13). The range is given by the DVORETZKY-KIEFER-WOLFOWITZ (DKW) inequality [Dvoretzky et al., 1956]. It states that the empirical CDF $\hat{F}_{Xn}(x)$ is bounded as:

$$\hat{F}_{Xn}(x) - \varepsilon \leq F_X(x) \leq \hat{F}_{Xn}(x) + \varepsilon, \text{ where } \varepsilon = \sqrt{\frac{1}{2n} \ln \left(\frac{2}{\alpha_{\text{risk}}} \right)} \quad (\text{III.4.29})$$

at a specified confidence level $1 - \alpha_{\text{risk}}$. This inequality also confirms that the convergence rate of the empirical CDF is of \sqrt{n} .

Quantile Another useful information is the quantity x_p (namely the p quantile) for which $F_X(x_p) = p$. This quantity is associated to the risk at $p\%$ to observe a sample point x greater than x_p . Imagine

that a risk of 5% is accepted for a device to malfunction, the quantity x_p is determined from $F_X(x_p)$ (X may be a current for example). During the design stage of that device, its constitutive components must be chosen in such a way that their functioning is guaranteed when the device is stressed by an interference which value is lower than x_p .

Again, as the underlying CDF $F_X(x)$ is unknown, the estimator $\hat{F}_{X_n}(x)$ is used, and a confidence interval at $q\%$ must be determined (see Fig. III.4.13), such as $x_{p, \frac{1-q}{2}} \leq x_p \leq x_{p, \frac{1+q}{2}}$. This problem is not trivial, and no close solutions is available. A general confidence interval may be given by the following procedure [Conover, 1999, p145-148]. General, because it is not asymptotic (n does not need to be large), and non parametric as no information about the underlying distribution law is required. Let X_i^* be the i th order statistic (*i.e.* i th-smallest value of a statistical sample). Then the CDF of the i th order statistic is:

$$\begin{aligned} F_{X_i^*}(x) &= \mathbb{P}[X_i^* \leq x] \\ &= \sum_{k=i}^n \binom{n}{k} \mathbb{P}[X_1 \leq x, \dots, X_k \leq x, X_{k+1} > x, \dots, X_n > x] \\ &= \sum_{k=i}^n \binom{n}{k} \mathbb{P}[F(x)]^k [1 - F(x)]^{n-k} = \sum_{k=i}^n C_n^k \mathbb{P}[F(x)]^k [1 - F(x)]^{n-k} \end{aligned} \quad (\text{III.4.30})$$

From (III.4.30), one can then show that:

$$\mathbb{P}[X_i^* \leq q_p \leq X_j^*] = \sum_{k=i}^{j-1} C_n^k p^k (1-p)^{n-k} \quad (\text{III.4.31})$$

A corollary is that if i and j are such as $\sum_{k=i}^{j-1} C_n^k p^k (1-p)^{n-k} = 1 - \alpha$, then $[X_{(i)}, X_{(j)}]$ is a confidence interval. Practically, the estimator $\hat{F}(x)$ is used instead of $F(x)$. This procedure is implemented in the **EnvStat** R package [Millard, 2013] (R is a programming language dedicated to statistics [R Core Team, 2018]), and the routine **eqnpar** may be employed.

Re-sampling techniques can also provide quantiles with confidence intervals. The bootstrap is one of these. From an initial sample of size n , L random re-samplings with replacement of size n are created. From the L samples, a bootstrap distribution of the quantity of interest (mean, quantile, etc.) is computed. Several formulations are available and not all of these are appropriate to compute quantiles and confidence intervals. Among all the bootstrap methods dedicated to confidence intervals (basic, percentile, Studentized, etc. [Efron and Tibshirani, 1986]), the **bias-corrected and accelerated (BCa)** bootstrap is one that works well for a variety of parameters, including quantiles [Efron, 1987]. Moreover, the **BCa** is appropriate for skewed distributions and is a second-order method (more accurate). [Canty and Ripley, 2017] is an implementation in R of numerous bootstrap methods, and espacially the **BCa** one.

Threshold models If one applies the **RCM** to lossy cavities ($\alpha \gg 50$), or when an aperture of large size (compared to the wavelength) is considered, Monte-Carlo iterations may then be time-consuming when it comes to determine extreme quantiles (99%, 99‰). To avoid this, it is possible to apply threshold models from the extreme value theory [Coles et al., 2001].

If X is a random variable with a CDF $F_X(x)$, the probability to exceed a high threshold u is then:

$$\begin{aligned} \mathbb{P}[X > u + y \mid X > u] &= \frac{\mathbb{P}[X > u + y \cap X > u]}{\mathbb{P}[X > u]} \\ &= \frac{1 - F_X(u + y)}{1 - F_X(u)} \end{aligned} \quad (\text{III.4.32})$$

Usually $F_X(x)$ is unknown. However, if u is large enough, and from the extreme values theory [Coles et al., 2001]:

$$H(y) = 1 - \mathbb{P}[X > u + y \mid X > u] \quad (\text{III.4.33})$$

with $H(y)$ defined as:

$$H(y) = \begin{cases} 1 - \left(1 + \frac{\zeta y}{\tilde{\sigma}}\right)^{-1/\zeta} & \text{for } \zeta \neq 0, \\ 1 - \exp\left(-\frac{y}{\tilde{\sigma}}\right) & \text{for } \zeta = 0. \end{cases} \quad (\text{III.4.34})$$

where $\tilde{\sigma} = \sigma + \zeta(u - \mu)$. ζ , σ and μ are parameters that need to be determined. The family of distributions $H(y)$ is the generalized PARETO family.

Sample values gathered from Monte-Carlo iterations that are greater than u may be fitted to (III.4.34). To estimate the parameters ζ , σ and μ a solution is to maximize the likelihood associated to $H(y)$.

A complex problem is to determine the lowest threshold u from which it is possible to fit the tail of a sample (from which extreme quantiles need to be assessed) to the generalized PARETO distribution. In [Coles et al., 2001, chap. 4.3.4] a procedure is proposed. It consists in estimating the parameters ζ and σ (with their confidence intervals) for several thresholds u . Indeed, if a **generalized PARETO distribution (GPD)** models the excesses of a threshold u , then, from equation (III.4.32), this same distribution (with identical parameters) will model the excesses for threshold greater than u . Finally, u is chosen as low as possible while ensuring that the estimated parameters remain constant over a range of threshold u and with a reasonable confidence interval. Again, the R package **ismev** [Heffernan and Stephenson, 2018] allows to practically deal with extreme values.

III.4.8 First RCM application

The goal of this section is to highlight how a **RCM** application is set up and how to configure the sources. Moreover, the statistical quantities aforementioned will be applied to the **RCM** results.

III.4.8.1 Setup

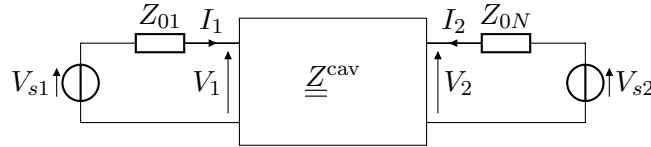


Fig. III.4.14 – Sources of the impedance $\underline{Z}^{\text{cav}}$.

We recall that, from the **RCM** and without apertures considered as ports, the cavity impedance $\underline{Z}^{\text{cav}}$ is:

$$\underline{Z}^{\text{cav}} = j\Im \left\{ \underline{Z}^{\text{rad}} \right\} + \left[\Re \left\{ \underline{Z}^{\text{rad}} \right\} \right]^{1/2} \xi \left[\Re \left\{ \underline{Z}^{\text{rad}} \right\} \right]^{1/2} \quad (\text{III.4.35})$$

Fig. III.4.14 shows the circuit model for a two-port system. Let \vec{V}_s be the source vector defined as $\vec{V}_s = [V_{s1}, \dots, V_{sN}]^T$, $\vec{V} = [V_1, \dots, V_N]^T$ be the voltages across the ports, $\vec{I} = [I_1, \dots, I_N]^T$ be the currents that flow into the ports, and Z_{01}, \dots, Z_{0N} be the impedances of the sources. Current and voltage are assumed to be peak values (not RMS values). The current vector \vec{I} may be expressed from

the source vector \vec{V}_s . Indeed, we have $\vec{V} = \underline{\underline{Z}}^{\text{cav}} \vec{I}$ and:

$$\vec{V}_s = \begin{bmatrix} Z_{01} & \dots & 0 \\ \vdots & \ddots & \vdots \\ 0 & \dots & Z_{0N} \end{bmatrix} \vec{I} + \vec{V} = \left(\begin{bmatrix} Z_{01} & \dots & 0 \\ \vdots & \ddots & \vdots \\ 0 & \dots & Z_{0N} \end{bmatrix} + \underline{\underline{Z}}^{\text{cav}} \right) \vec{I} \quad (\text{III.4.36})$$

If $Z_{0i} = Z_0$, then $\vec{V}_s = (Z_0 \underline{\underline{I}} + \underline{\underline{Z}}^{\text{cav}}) \vec{I}$ and:

$$\vec{I} = (Z_0 \underline{\underline{I}} + \underline{\underline{Z}}^{\text{cav}})^{-1} \vec{V}_s \quad (\text{III.4.37})$$

If each source is defined from its input impedance and by an injected power P_i (as for a [VNA](#)), then $V_{si} = \sqrt{2Z_{0i}P_i} = \sqrt{2Z_0P_i}$.

For this first [RCM](#) application, let's consider a simple two-port lossy attenuator circuit defined by the scattering matrix:

$$\underline{\underline{S}} = \begin{bmatrix} 0 & e^{-g} \\ e^{-g} & 0 \end{bmatrix} \quad (\text{III.4.38})$$

Its attenuation A is $A = 20 \log_{10}(e^{-g}) = \frac{-20g}{\ln 10}$, and its impedance matrix $\underline{\underline{Z}}^{\text{rad}}$ is expressed as:

$$\underline{\underline{Z}}^{\text{rad}} = Z_0^{1/2} (\underline{\underline{I}} + \underline{\underline{S}})(\underline{\underline{I}} - \underline{\underline{S}})^{-1} Z_0^{-1/2} \quad (\text{III.4.39})$$

We now place this circuit inside a cavity with random boundary conditions and we want to determine the statistics of the magnitude of the current vector at the port 2 when a power $P = 10$ dBm is applied to port 1 (thus $\vec{V}_s = [\sqrt{2Z_0P}, 0]^T$).

III.4.8.2 Results

A sample of 4000 values of the magnitude current $|I_2|$ was generated. As there was only one current of interest, the subscript 2 could be dropped. Fig. [III.4.15](#) shows the empirical [CDF](#) $\hat{F}_{|I|_{360}}(|i|)$ obtained for $n = 360$ Monte-carlo iterations. Four simulations were run with four different loss factors α (1, 20, 50 and 100). The attenuation A was set to 60 dB to simulate a low coupling between the two ports. From the DKT inequality, a confidence band around $\hat{F}_{|I|_{360}}(|i|)$ was added for two confidence levels ($1 - \alpha_{\text{rist}} = 95\%$ and $1 - \alpha_{\text{rist}} = 99\%$). An intended outcome is confirmed: as α increases, the probability $\hat{F}_{|I|_{360}\alpha}(|i|)$ decrease such that $\hat{F}_{|I|_{360}\alpha=10}(|i|) \geq \hat{F}_{|I|_{360}\alpha=50}(|i|) \geq \hat{F}_{|I|_{360}\alpha=100}(|i|)$.

Several techniques were used to determine the extreme quantiles and their confidence intervals. The results are listed in Table. [III.4.2](#). The extreme quantiles (95%, 97.5%, 99% and 99.9%) were determined from the initial sample and from a fitting to the [GPD](#). Then, the [BCa](#) bootstrap and the general purpose method (explained in section [III.4.7](#)) have provided the confidence intervals. Bootstrap distributions were obtained from 10000 re-samplings. The [BCa](#) bootstrap generates narrower intervals than the general purpose technique. Yet, it requires more computation time (≈ 1 min for a statistic, like a quantile for example). Fig. [III.4.16](#) depicts the bootstrap distributions obtained to determine the quantiles 95% and 99%. It highlights that the bootstrap distributions are not always normal (thus not every bootstrap techniques can be employed).

The threshold model has been also applied to fit the tail of the distribution of the current magnitude. Fig. [III.4.17](#) presents the fitting procedure for two loss factors. It first consists in the

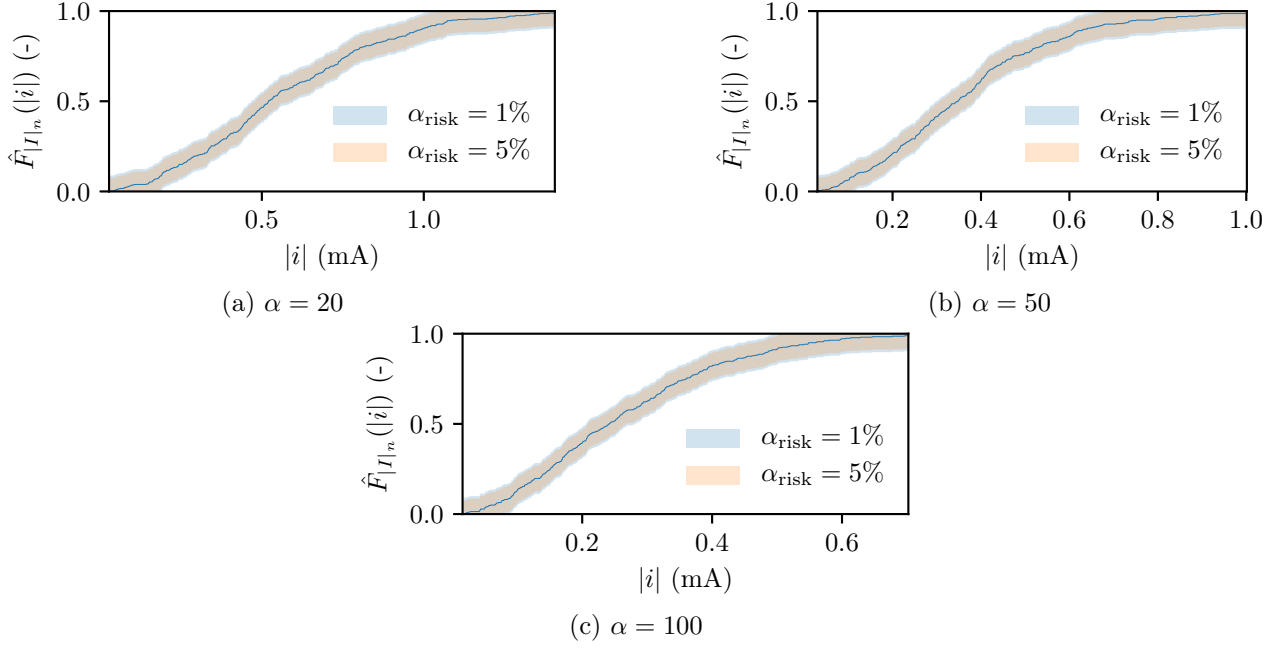


Fig. III.4.15 – Empirical CDF $\hat{F}_{|I|_{360}}(|i|)$ for two loss factors α .

determination of the parameters ζ and σ within a given threshold range $|i|_t \in [|i|_{t\min}, |i|_{t\max}]$. ζ and σ are set as soon as they remain constant (over $|i|_t$) while $|i|_t$ increases. Fig. III.4.17 shows the quantile-quantile plot of the empirical distribution, defined as all the sample values greater than $|i|_t$, and the quantile of the GPD. A good agreement is observed. The column EV in Table. III.4.2 lists the extreme quantiles determined from the fitted GPD.

Finally, it is worthwhile to study the impact of the error on α for the quantiles $|i|_{p\%}$. Indeed, α may be assessed with a substantial uncertainty. Table. III.4.3 lists relative errors δ on $|i|_{p\%}$ for several quantiles, several loss factors and six errors e . We observe that the order of magnitude of the relative errors computed for a given error e does not depend on α . Moreover, when α is estimated with an error of $\pm 10\%$, the relative errors relies within the range $\pm 5\%$.

		$ i _{p\%}$		BCa Bootstrap			Conover [1999]		
α	p	E	EV	Interval	Len.	Shape	Interval	Len.	Shape
1	95%	4.19	4.17	[4.11, 4.27]	154.0	0.979	[4.12, 4.27]	153.0	1.19
	97.5%	4.55	4.57	[4.46, 4.65]	184.0	1.17	[4.47, 4.66]	190.0	1.43
	99%	4.89	4.99	[4.83, 5.00]	175.0	1.69	[4.83, 5.06]	224.0	2.61
	99.9%	5.72	5.70	[5.55, 5.95]	401.0	1.46	[5.59, 6.17]	583.0	3.47
20	95%	1.08	1.08	[1.06, 1.10]	38.8	1.46	[1.06, 1.10]	41.8	1.78
	97.5%	1.21	1.20	[1.16, 1.24]	74.6	0.501	[1.17, 1.24]	74.3	0.600
	99%	1.34	1.35	[1.30, 1.39]	94.7	1.15	[1.30, 1.41]	110.0	1.91
	99.9%	1.70	1.67	[1.57, 1.81]	234.0	0.817	[1.59, 1.88]	286.0	1.55
50	95%	0.722	0.723	[0.708, 0.734]	25.7	0.793	[0.708, 0.734]	25.4	0.840
	97.5%	0.799	0.800	[0.777, 0.831]	53.8	1.47	[0.779, 0.833]	54.3	1.79
	99%	0.917	0.902	[0.889, 0.941]	52.0	0.878	[0.891, 0.952]	61.5	1.34
	99.9%	1.15	1.16	[1.03, 1.36]	337.0	1.62	[1.05, 1.38]	333.0	2.08
100	95%	0.549	0.548	[0.533, 0.570]	36.6	1.38	[0.534, 0.571]	37.0	1.46
	97.5%	0.616	0.618	[0.602, 0.636]	34.7	1.49	[0.603, 0.640]	37.4	1.87
	99%	0.703	0.702	[0.673, 0.723]	50.5	0.690	[0.676, 0.733]	57.5	1.14
	99.9%	0.839	0.878	[0.810, 0.970]	160.0	4.61	[0.821, 1.07]	249.0	13.2

Table III.4.2 – Confidence intervals for several quantiles $|i|_{p\%}$ for four loss factors α and for two methods: Bootstrap and a general method. All the quantities are in mA but the interval length (column Len.) which is in μA . E refers to the quantile determined from the sample, and EV from a fitting with the [GPD](#) (see Fig. [III.4.17](#)). The probability p' of the [GPD](#) and the probability p are related by $p' = \frac{p - \hat{F}_{|I|}(|i|_t)}{1 - \hat{F}_{|I|}(|i|_t)}$, where $|i|_t$ is the threshold from which a [GPD](#) is fitted. Then the quantile is determined by use of the inverse [CDF](#) of the [GPD](#). The shape, computed as $\frac{|i|_{p\% \text{ up}} - |i|_{p\%}}{|i|_{p\%} - |i|_{p\% \text{ lo}}}$, indicates the dissymmetry of the confidence interval. Confidence intervals computed from the [BCa](#) bootstrap method produce narrower and more symmetric interval than the general method (most of the time), and especially for high quantiles (99.9%). Moreover, the higher $p\%$ is, the wider and the most dissymmetric the confidence interval is. All these statistical quantities have been computed from an initial sample of size 4000.

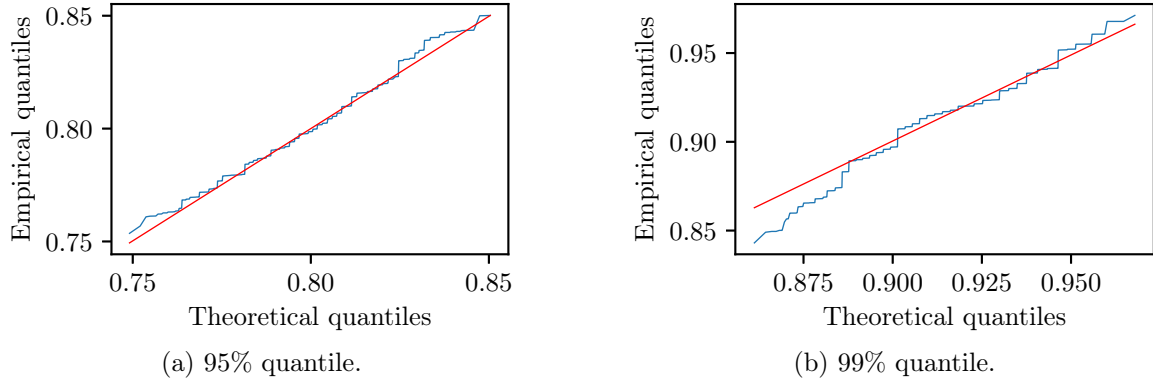
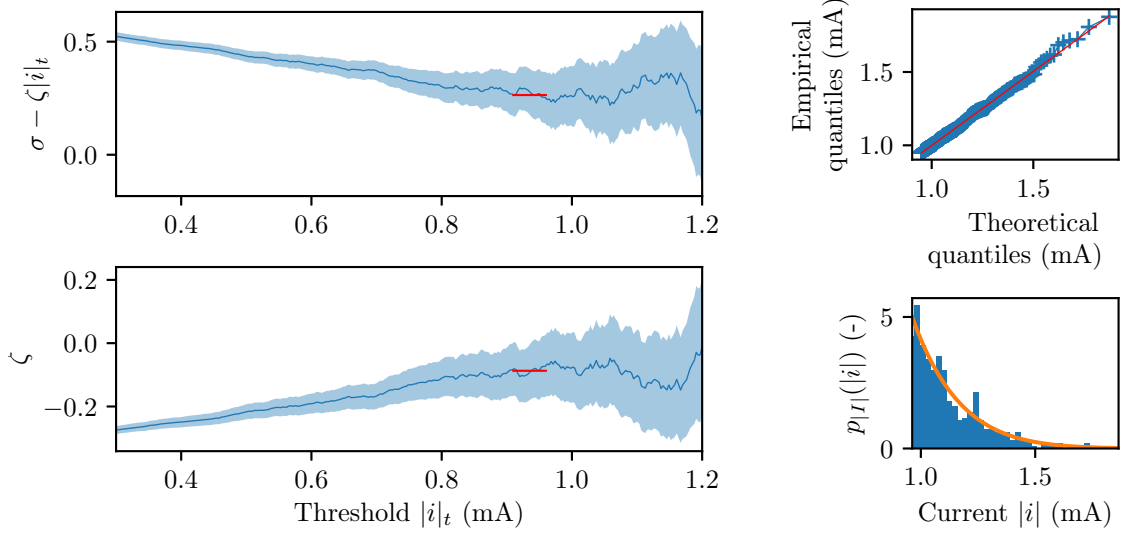


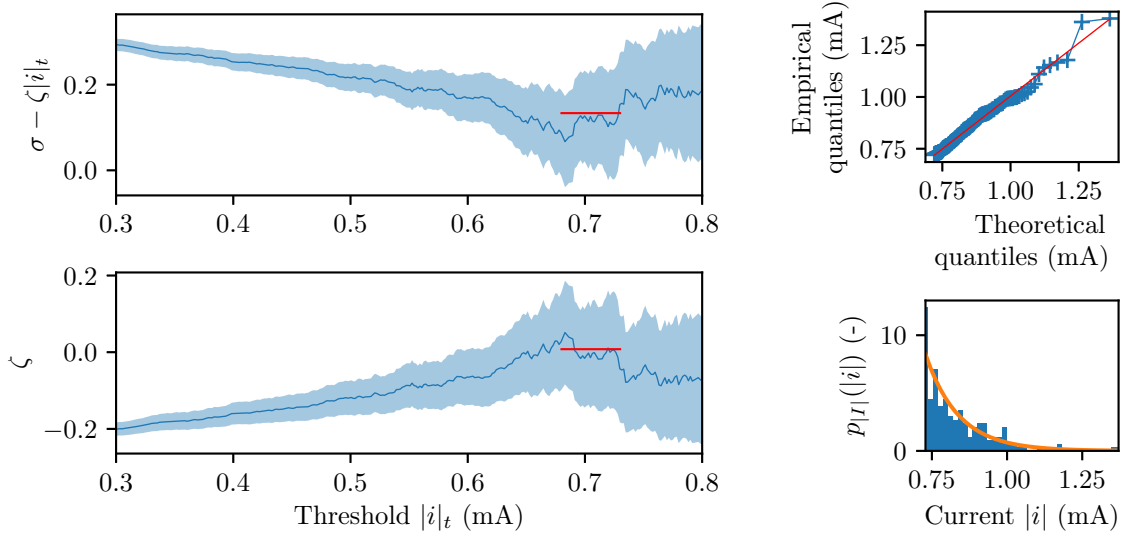
Fig. III.4.16 – Quantile-quantile plots (Q-Q plots): quantiles from the bootstrap distribution against quantiles from a normal distribution of the statistical quantity of interest, here the 95% and 99% quantile. The standard deviation and the mean of the normal distribution are obtained from the bootstrap distribution. We observe that for the 95% quantile, the bootstrap distribution agrees with a normal distribution. However for the 99% quantile the normality assumption does not apply (see the left tail). The quantiles are computed with $\alpha = 20$, from a sample of 4000 elements, and from 10000 bootstrap samples.

	$\alpha = 1$							$\alpha = 20$						
		$\pm 1\%$		$\pm 5\%$		$\pm 10\%$			$\pm 1\%$		$\pm 5\%$		$\pm 10\%$	
p	$ i _{p\%}$	δ_-	δ_+	δ_-	δ_+	δ_-	δ_+	$ i _{p\%}$	δ_-	δ_+	δ_-	δ_+	δ_-	δ_+
50 %	2.09	1.15	0.61	3.54	0.30	5.99	-2.66	0.53	0.03	-0.53	2.45	-1.87	5.74	-3.98
95 %	4.22	-0.19	-0.06	1.69	-2.30	3.93	-3.78	1.10	1.14	-0.48	3.49	-2.62	6.17	-4.11
97.5 %	4.59	0.11	0.06	2.48	-1.90	4.27	-3.20	1.22	0.95	-0.71	3.47	-3.22	5.98	-3.39
99 %	4.99	1.24	-0.09	2.72	-1.04	4.64	-3.00	1.35	1.82	0.05	4.31	-1.82	7.86	-2.77
99.9 %	5.80	-0.34	-0.57	1.98	0.30	2.62	-1.66	1.68	0.67	-2.51	0.49	-1.06	4.40	-4.01
	$\alpha = 50$							$\alpha = 100$						
		$\pm 1\%$		$\pm 5\%$		$\pm 10\%$			$\pm 1\%$		$\pm 5\%$		$\pm 10\%$	
p	$ i _{p\%}$	δ_-	δ_+	δ_-	δ_+	δ_-	δ_+	$ i _{p\%}$	δ_-	δ_+	δ_-	δ_+	δ_-	δ_+
50 %	0.35	0.75	-0.09	2.57	-1.22	5.13	-3.74	0.26	0.63	-1.56	2.13	-2.77	4.76	-4.24
95 %	0.73	-0.34	-2.04	1.67	-3.08	3.92	-4.58	0.54	0.63	-0.12	1.34	-2.23	3.29	-2.84
97.5 %	0.82	-1.32	-2.82	1.17	-2.98	3.77	-5.15	0.61	-0.01	-0.71	0.78	-3.33	3.62	-4.52
99 %	0.92	-0.97	-3.29	0.26	-3.53	2.23	-5.74	0.68	0.99	0.22	2.12	-2.06	3.68	-3.16
99.9 %	1.14	-1.10	-4.09	-1.89	-3.41	-0.88	-5.57	0.83	7.08	3.96	4.17	0.29	5.69	-1.64

Table III.4.3 – Influence on the quantiles $|i|_{p\%}$ of the error on α . For the four values α (1, 20, 50 and 100), the quantiles $|i|_{p\%}$ were computed. For each value α , six errors e are considered $\pm 1\%$, $\pm 5\%$ and $\pm 10\%$, and the quantiles $|i_e|_{p\%}$ are calculated. Thus six simulations were run with a loss factor of $(1 + e)\alpha$. The relative errors were computed as $\delta_{\pm} = \frac{|i_e|_{p\%} - |i|_{p\%}}{|i|_{p\%}}$ and are expressed in percent. The quantiles are expressed in mA. δ_- refers to a negative error, i.e. $(1 + e)\alpha < \alpha$, and δ_+ to a positive one, i.e. $(1 + e)\alpha > \alpha$.



(a) $\alpha = 20$, $|i|_t = 0.95$ mA ($\hat{F}_{|I|}(|i|_t) = 89.9\%$, $\zeta = -0.0872$ and $\sigma = -0.0872$ and 405 sample values above $|i|_t$).



(b) $\alpha = 50$, $|i|_t = 0.72$ mA ($\hat{F}_{|I|}(|i|_t) = 94.8\%$, $\zeta = 0.00789$ and $\sigma = 0.00789$ and 206 sample values above $|i|_t$).

Fig. III.4.17 – Fitting process of the tail of the current magnitude to the GPD. On the left, variations of ζ and σ according to the threshold $|i|_t$ with a confidence interval. As explained in section III.4.7, the lowest constant part (flagged by the red lines) allows to select the parameters ζ and σ . On the right, the quantile-quantile plots and the histograms show a good agreement between the tail (which starts at $|i|_t$) of the current distribution and the GPD (with $\mu = u = |i|_t$, see equation (III.4.34)). Both samples ($\alpha = 20$ and $\alpha = 50$) contain 4000 sample values. The extreme quantiles determined from the GPD are listed on Table. III.4.2.

III.4.9 Conclusion

This section was dedicated to the implementation of the [random coupling model \(RCM\)](#). The expression of a convenient matrix formulation of the normalized impedance $\underline{\underline{\xi}}$ was validated. Several methods were implemented to express $\frac{k_n^2}{\Delta k^2}$ and were compared. Some clues were given in order to efficiently implement the RCM into a compiled language, allowing to significantly reduce the computation time of the Monte-Carlo iterations. Then, the link between the variance of the elements of $\underline{\underline{\xi}}$ and α was confronted to Monte-Carlo simulation. It was highlighted that the number M of modes taken into account in the cavity should be sufficiently high for lossy environments. This result was not found in any available paper. A criterion to characterize the chaoticity of a system was exposed and is based on the eigenvalues of the normalized impedance $\underline{\underline{\xi}}$. Finally, some relevant statistic tools for the [electromagnetic security \(EMSEC\)](#) were presented. The developed tools have been used to model low couplings in a lossy system between two ports. The extreme quantiles were determined using several methods and with coherent results.

The last chapter of this part is devoted to compare [RCM](#) simulations to experimental data.

Chapter III.5

Measurements

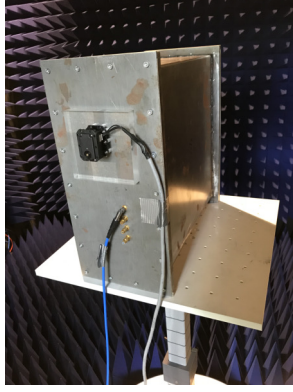
Contents

III.5.1	Introduction	148
III.5.2	Use of a small stirrer to generate a chaotic environment	149
III.5.3	Methods to determine the parameters of the RCM	149
III.5.4	First comparison: monopoles	150
III.5.4.1	Evaluation of the chaoticity of the system	150
III.5.4.2	Fitting of the loss parameter α and the probability density function of the induced voltages	151
III.5.5	Second comparison: printed circuit boards	151
III.5.5.1	Tested configurations	152
III.5.5.2	Computing of the experimental results	152
III.5.5.3	Computing of the RCM results	153
III.5.5.4	Discussion	155
III.5.6	Effects of absorbers on the magnitude of induced currents	158
III.5.7	Coupling between the aperture and the internal ports	159
III.5.7.1	Determination of RCM parameters when applied with apertures	159
III.5.7.2	Results	160
III.5.8	Conclusion	161

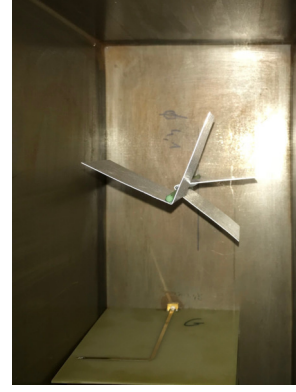
III.5.1 Introduction

In order to validate the RCM approach, several measurements were performed for three configurations. At first, the coupling between two monopoles was studied. Then, the coupling between stacked PCBs was investigated. Finally, the setup has been installed to determine couplings between an aperture and PCBs.

In the first two cases, the statistics of the coupled voltages or currents on PCBs were evaluated. In order to do this, a small stirrer was designed and installed inside the cavity. The statistic of the currents is assessed by acquiring scattering matrices for a frequency sweep and for a full rotation (360°) of the stirrer at each frequency step. For each pair (frequency, stirrer position), a scattering matrix is measured and stored. Then the current can be determined from the scattering matrix.



(a) Servomotor outside the cavity.



(b) Stirrer inside the cavity.

Fig. III.5.1 – Stirrer and servomotor.

III.5.2 Use of a small stirrer to generate a chaotic environment

To compare measurements with the [RCM](#), the measured system has to be chaotic. In order to generate a large number of mode topologies in the cavity (BERRY hypothesis), a stirrer rotates inside the cavity. The statistics of quantities of interest (voltages or currents) will then be assessed from sample values acquired for frequency sweeps and stirrer rotations. Thus, statistics are determined over the ensemble of a large number of geometries of cavities.

A small stirrer has been designed and manufactured in order to function inside a computer cavity. Its shape has been designed to have as few symmetries as possible (Fig. [III.5.1b](#)). The stirrer is rotated thanks to a servomotor (Fig. [III.5.1a](#)) controlled by a *Raspberry Pi* (a nano-computer board¹). The *Raspberry Pi* (inside the anechoic chamber) is connected to a desktop computer (outside the anechoic chamber) by an optical fiber. This setup allows to rotate precisely the stirrer. Moreover, the position of the stirrer in the cavity has been determined to maximize the chaoticity in the cavity.

III.5.3 Methods to determine the parameters of the [RCM](#)

Three quantities have to be determined to apply the [RCM](#): the free-space impedance matrix $\underline{\underline{Z}}^{\text{rad}}$, the number of modes M taken into account inside the cavity and the loss parameter α . The free-space impedance matrix $\underline{\underline{Z}}^{\text{rad}}$ has been determined from experimental data acquired by a [VNA](#) in free-space for all the tested configuration (see Fig. [III.5.3](#) for the monopoles and Fig. [III.5.9a](#) for a stacking of [PCBs](#)). Setting M is a trade-off between the number of modes to consider in the cavity and the computation time. In the previous section, it was highlighted that setting $M = 600$ was sufficient and allows to take into account the losses inside the mock-up.

The parameter α is the most tricky to assess. It characterizes the losses inside the cavity and is frequency dependent. Several techniques may be applied to evaluate it, as explained in [[Hemmady, 2006](#), [Gil et al., 2016](#)], based on experimental data. The first method consists in computing (from equation ([III.4.14](#))) and storing the [PDFs](#) of the elements of $\underline{\underline{\xi}}_{\alpha}$ for different values of α . Then, from the acquired data, $\underline{\underline{\xi}}^{\text{Measured}}$ is computed by inverting ([III.1.24](#)) as:

$$\underline{\underline{\xi}}^{\text{Measured}} = \Re [\underline{\underline{Z}}^{\text{rad}}]^{\frac{1}{2}} (\underline{\underline{Z}}^{\text{cav}} - \Im [\underline{\underline{Z}}^{\text{rad}}]) \Re [\underline{\underline{Z}}^{\text{rad}}]^{\frac{1}{2}} \quad (\text{III.5.1})$$

A fitting process then allows to match the elements of $\underline{\underline{\xi}}^{\text{Measured}}$ with the elements of the matrices $\underline{\underline{\xi}}_{\alpha=\alpha_{\min}}, \dots, \underline{\underline{\xi}}_{\alpha=\alpha_{\max}}$. The best fit determines the value of α .

¹<https://www.raspberrypi.org/>



Fig. III.5.2 – A monopole attached to the front panel.

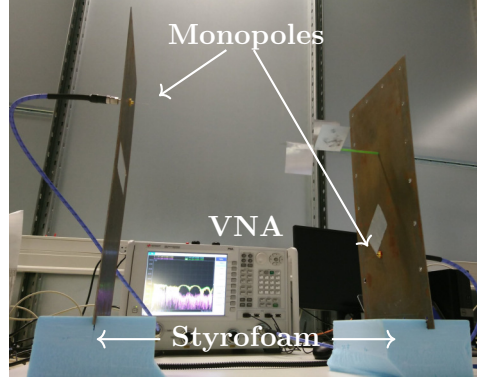


Fig. III.5.3 – Setup to measure the free-space impedance $\underline{\underline{Z}}^{\text{rad}}$ between the two monopoles. Two blocks of styrofoam are used as stands.

The second method computes α from [Gil et al., 2016]:

$$\text{Var} [\Re [\xi_{ii}^{\text{Measured}}]] = \text{Var} [\Im [\xi_{ii}^{\text{Measured}}]] = \frac{1}{\pi \alpha_{ii}} \quad (\text{III.5.2})$$

$$\text{Var} [\Re [\xi_{ij}^{\text{Measured}}]] = \text{Var} [\Im [\xi_{ij}^{\text{Measured}}]] = \frac{1}{2\pi \alpha_{ij}} \quad (\text{III.5.3})$$

and:

$$\alpha = \frac{1}{N^2} \sum_{i,j} \alpha_{ij} \quad (\text{III.5.4})$$

The benefit of this latter method is that no $\underline{\underline{\xi}}_{\alpha}$ matrix needs to be computed. However, it is important to note that for both methods, the determination of α relies on experimental data. Both methods were applied in this work. A comparison between these two methods can also be found in [Gil et al., 2016].

III.5.4 First comparison: monopoles

The first practical application of the RCM concerns the coupling between two monopoles that are mounted inside the cavity. Both monopoles are composed of a 46 mm long wire soldered to a bulkhead through hole SMA connector (see Fig. III.5.2). This configuration is similar to that presented in [Gil et al., 2016]. The free-space impedance $\underline{\underline{Z}}^{\text{rad}}$ is measured by means of a VNA (see Fig. III.5.3). The free-space scattering parameters are summed up in Fig. III.5.4. Then, the scattering matrix $\underline{\underline{S}}$ between the two monopoles placed in the computer chassis mock-up is measured between 5 and 26.5 GHz, and for 360 stirrer angular positions.

III.5.4.1 Evaluation of the chaoticity of the system

As mentioned above, the RCM applies only for chaotic systems. In [Hemmady et al., 2005, Dyson, 1962] a method is developed to determine if a system is chaotic or not. It is based on the eigenvalues properties of the normalized scattering matrix of the system. It states that the phase of the eigenvalues has to be uniformly distributed, and that the phase and magnitude of the eigenvalues have to be independent. From the normalized impedance $\underline{\underline{\xi}}$, the normalized scattering matrix is computed and

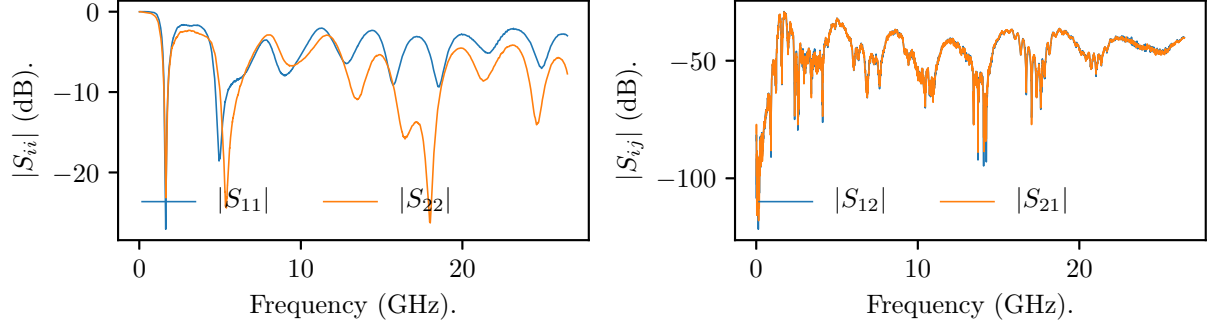


Fig. III.5.4 – Scattering parameters of the two monopoles, measured in free-space.

diagonalized:

$$\underline{\underline{s}} = (\underline{\underline{\xi}}^{\text{Measured}} - \underline{\underline{1}})(\underline{\underline{\xi}}^{\text{Measured}} + \underline{\underline{1}})^{-1} \quad (\text{III.5.5})$$

$$\underline{\underline{s}} = \underline{\underline{U}} \begin{pmatrix} |\lambda_1| e^{j\phi_{\lambda_1}} & \dots & 0 \\ \vdots & \ddots & \vdots \\ 0 & \dots & |\lambda_N| e^{j\phi_{\lambda_N}} \end{pmatrix} \underline{\underline{U}}^{-1} \quad (\text{III.5.6})$$

where $\underline{\underline{U}}$ is the basis change matrix.

Fig. III.5.5 depicts histograms of the real and imaginary parts of the eigenvalues of $\underline{\underline{s}}$ and of their phases. As the 2D histogram is rotation invariant and as $P(\Phi_{\lambda_s})$ is uniformly distributed ($P(\Phi_{\lambda_s}) \approx \mathbb{1}_{[-\pi, \pi]}(\Phi_{\lambda_s}) \frac{1}{2\pi}$), we can conclude that the system is chaotic. Thus, the RCM can be applied.

III.5.4.2 Fitting of the loss parameter α and the probability density function of the induced voltages

At the center of the four frequency ranges of 5 GHz for which the chaoticity of the system has been evaluated (*i.e.* 7.5, 12.5, 17.5 and 22.5 GHz), the loss parameter α has been determined. As explained previously, a fitting process allows to fit the PDF of the elements of $\underline{\underline{\xi}}^{\text{Measured}}$ to the elements of $\underline{\underline{\xi}}_\alpha$. Frequency samples within a bandwidth of 500 MHz acquired for 360 stirrer positions were gathered to compute the PDF of the elements of $\underline{\underline{\xi}}^{\text{Measured}}$. Fig. III.5.6 depicts the PDF of the real part of ξ_{ij} and the fitted PDF associated to a given loss parameter α_{fit} . We can notice that α_{fit} increases when the frequency increases. This phenomenon confirms the results given in [Gil et al., 2016].

We highlight the fact that fitting only the off-diagonal elements (ξ_{12} and ξ_{21}) gives better results when it comes to compute the induced voltages, when compared to experimental data. Fig. III.5.7 shows the comparison between the PDF of the induced voltages computed from experimental data and the PDF obtained from RCM simulations. A good agreement can be noticed for the four frequencies. Moreover, we observe that the induced voltages decrease with frequency.

α was finally determined for the whole frequency range and is plotted in Fig. III.5.8. As expected, α increases with the frequency, and its order of magnitude is in coherence with the assessment set in section III.4.5.

III.5.5 Second comparison: printed circuit boards

In this section, we will assess the probabilities of occurrence of induced currents at one end of microstrip transmission lines. These transmission lines are printed on circuit boards that are stacked together and placed into a cavity with changing boundary conditions (by use of the mode-stirrer). These

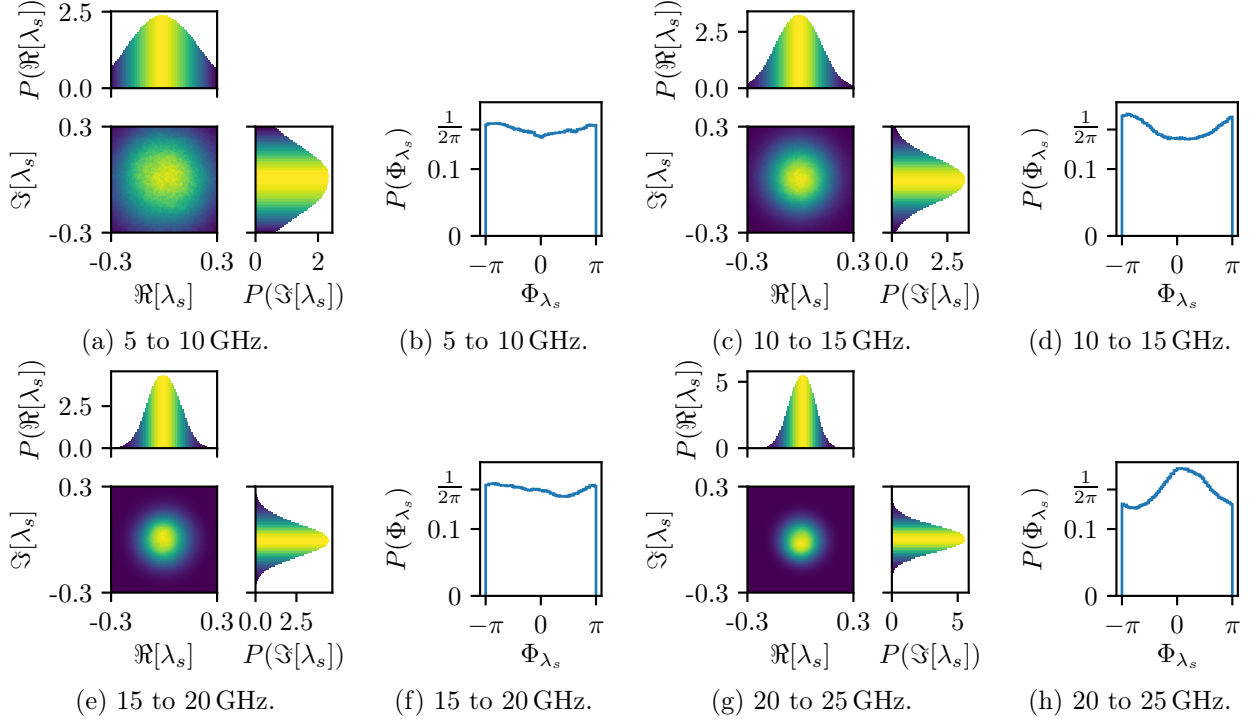


Fig. III.5.5 – 2D histograms of the real $\Re[\lambda_s]$ and imaginary $\Im[\lambda_s]$ parts of the eigenvalues of the matrix $\underline{\underline{S}}$ (Fig. III.5.5a, Fig. III.5.5c, Fig. III.5.5e and Fig. III.5.5g), and the distribution $P(\Phi_{\lambda_s})$ of the phase of the eigenvalues of $\underline{\underline{S}}$ (Fig. III.5.5b, Fig. III.5.5d, Fig. III.5.5f and Fig. III.5.5h).

configurations can be representative of a computer chassis in which cables are not constrained (*i.e.* that they can move), or when a heavy load is placed on top of an equipment resulting into a mechanical deformation that changes the boundary conditions of the problem. This may also obviously occur when additional elements are integrated inside the chassis. One aim would be to provide placement rules of the boards inside the chassis, to minimize, if possible, the probability of coupling due to a current that exceeds a given threshold.

III.5.5.1 Tested configurations

Several stacking configurations (Table III.5.1) composed of a maximum of four PCBs (see Fig. II.1.15 in section II.1.4.1) are considered. On each board a microstrip transmission line (characteristic impedance 50Ω) is printed, terminated at one end by a bulkhead through hole SMA connector (that also allows to hold the PCB in the mock-up) and at the other end by a 50Ω load (surface mount resistor and via). Position 1 corresponds to the board at the bottom of the stacking, and position 4 to the highest location (Fig. III.5.9d). Two consecutive positions are separated by a 2 cm gap (like in a real desktop computer). These configurations were chosen to allow to test the RCM with configurations that present different spacing between the boards (multiple of 2 cm), thus different modal configurations of the electromagnetic field within the stacking.

III.5.5.2 Computing of the experimental results

The scattering matrix $\underline{\underline{S}}$ between the ports of the system has been measured from 5 to 26.5 GHz with a step of 1 MHz (16501 frequency samples), and for 360 stirrer positions. Using $\underline{\underline{S}}$, the corresponding

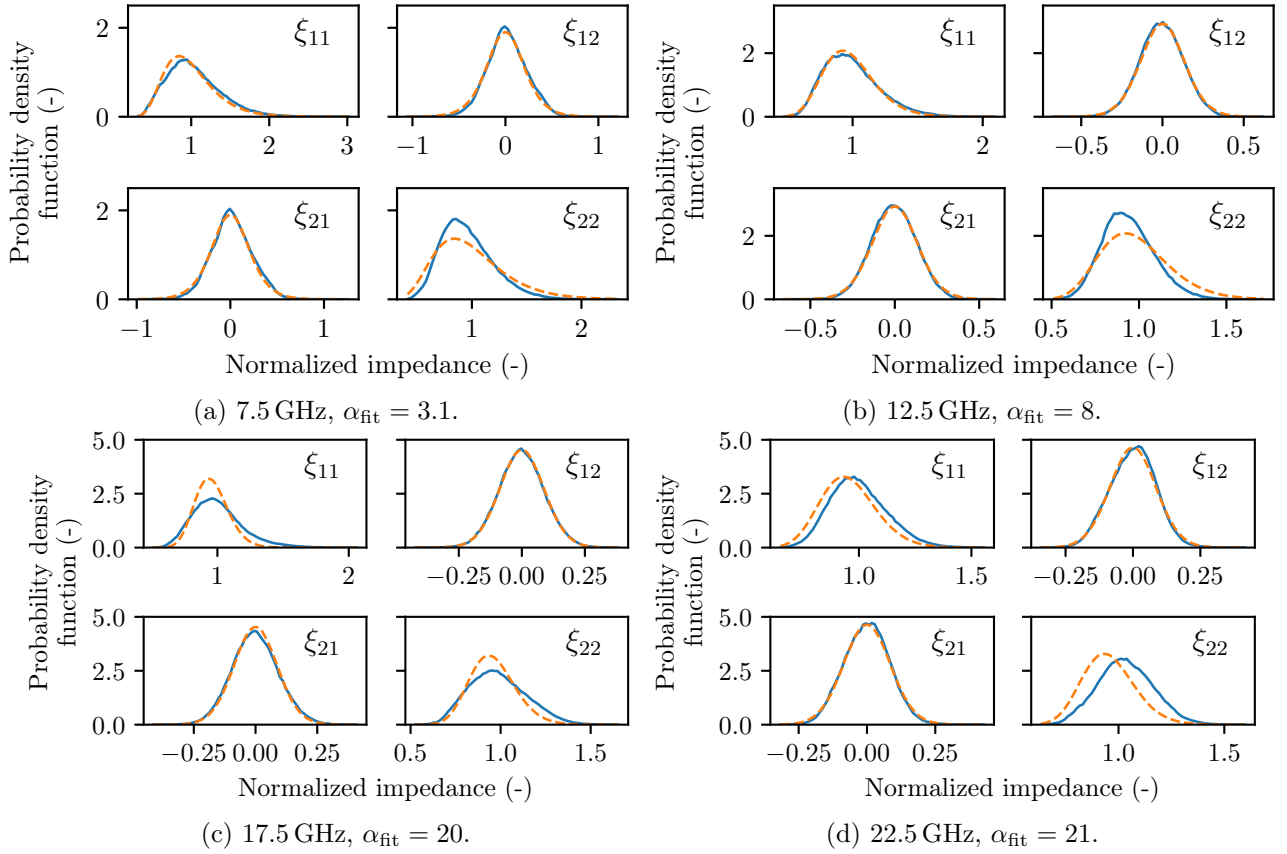


Fig. III.5.6 – Probability density functions of the real part of the elements ξ_{ij} from $\xi_{ij}^{\text{Measured}}$ (blue curves) and from ξ_{ij}^{α} (dashed orange curves).

impedance matrix $\underline{\underline{Z}}^{\text{Measures}}$ is calculated as:

$$\underline{\underline{Z}}^{\text{Measures}} = \left[\underline{\underline{Z}}_0 \underline{\underline{1}} \right]^{\frac{1}{2}} (\underline{\underline{1}} + \underline{\underline{S}})(\underline{\underline{1}} - \underline{\underline{S}})^{-1} \left[\underline{\underline{Z}}_0 \underline{\underline{1}} \right]^{\frac{1}{2}} \quad (\text{III.5.7})$$

Then the current vector \vec{I}^{RCM} is computed from (III.4.37). Fig. III.5.10 and Fig. III.5.11 show the CDFs $|I_{a,Cb}^{\text{Measure}}|$ of the measured current amplitudes. a corresponds to the port index number, and b to the configuration number (see Table III.5.1). In Fig. III.5.10 the power (10 dBm) is injected into port index #1 and in Fig. III.5.11 into the port index #2.

III.5.5.3 Computing of the RCM results

The matrices $\underline{\underline{Z}}^{\text{rad}}$ have been measured in free space (see Fig. III.5.9a) for the five configurations. The loss parameter α has been determined from equations (III.5.2) and (III.5.3) using $\xi_{ij}^{\text{Measured}}$ (computed from $\underline{\underline{Z}}^{\text{Measures}}$ with equation (III.5.1)), as $\alpha = \frac{1}{N^2} \sum_{i,j} \alpha_{i,j}$ with N the number of ports in the system. Then, from (III.1.24), 360×16501 matrices $\underline{\underline{Z}}^{\text{cav}}$ have been computed as well as the port currents vector \vec{I}^{RCM} (from equation (III.4.37)). Depending on N , the time needed to compute the 5940360 vectors \vec{I}^{RCM} varies from 40s to 3 min. Fig. III.5.10 and Fig. III.5.11 display the CDF $|I_{a,Cb}^{\text{RCM}}|$ of the simulated current amplitudes.

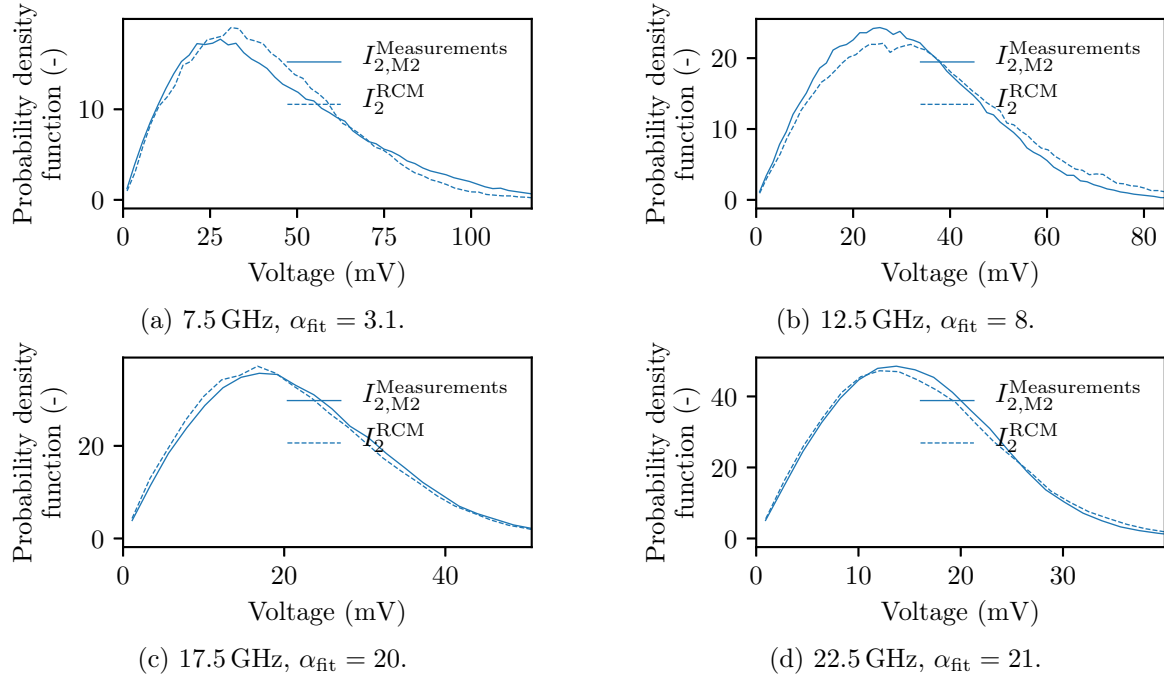


Fig. III.5.7 – Comparison between the probability density functions of the magnitude of the induced voltages on port 2 measured and simulated by the RCM. These PDF are computed within a frequency bandwidth of 500 MHz, and with a constant loss factor α_{fit} .

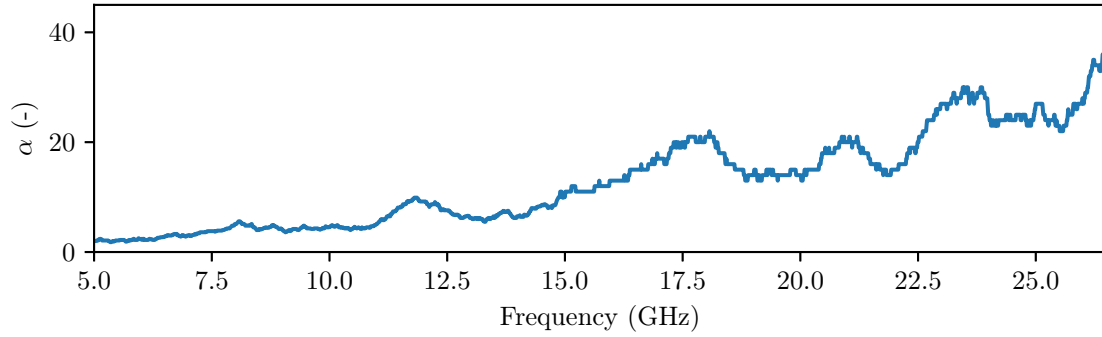


Fig. III.5.8 – Variation of the loss factor α inside the cavity versus the frequency.

Configuration	Number of port N	Position 1	Position 2	Position 3	Position 4
$C1$	4	Meander #1	Straight #2	L right #3	L left #4
$C2$	4	L right #1	Meander #2	L left #3	Straight #4
$C3$	2	L right #1	-	-	L left #2
$C4$	2	L right #1	-	L left #2	-
$C5$	3	Meander #1	Straight #2	-	L left #3

Table III.5.1 – The five configurations considered. The number prefixed by the symbol # corresponds to the port index of the system.

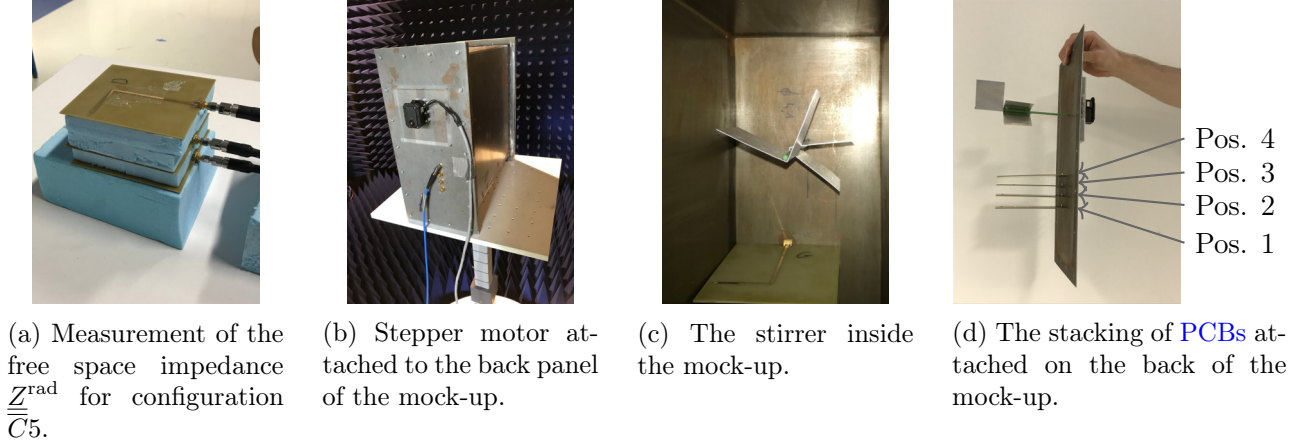


Fig. III.5.9 – Illustrations of the experimental set-up.

Configuration	Source port index	Position 1		Position 2		Position 3		Position 4	
		M	RCM	M	RCM	M	RCM	M	RCM
$C1$	#1	Source		925	789	327	321	333	319
$C1$	#2	927	787	Source		802	706	307	310
$C2$	#1	Source		883	785	321	303	336	299
$C2$	#2	884	785	Source		791	733	298	301
$C3$	#1	Source		-	-	-	-	524	375
$C3$	#2	525	374	-	-	-	-	Source	
$C4$	#1	Source		-	-	595	416	-	-
$C4$	#2	594	407	-	-	Source		-	-
$C5$	#1	Source		946	659	-	-	358	332
$C5$	#2	948	658	Source		-	-	534	408

Table III.5.2 – 95% percentile in μA for the five configurations with source location at port indexes #1 or #2. Fig. III.5.9d indicates the four positions. Grey cells refer to line of sight configurations.

III.5.5.4 Discussion

The results depend on the existence of a line of sight configuration between the source board and the other ones. The line of sight case appears for example when the source port index is #1 and the measurement port index is #2, or when the source port index is #2 and the measurement port indexes are #1 and #3. There is a good agreement between the CDF of the simulated data and the measured ones. In the line of sight case, the probability of having higher current is greater than when the source and the destination ports are not in a line of sight. In [Flintoft et al., 2016, Parker et al., 2016c,a,b], the same problem (stacking of PCB) was considered, also from an experimental point of view, and an equivalent conclusion was raised. For boards not in a line of sight, the RCM and the measurement data are in even better agreement.

The higher the voltage and current magnitudes are, the higher the threat for the confidentiality of the information that an equipment processes, is. Hence, we analyze high percentiles of the induced currents. Table III.5.2 lists the 95% percentiles for the five configurations, for two port source indexes (#1 and #2) and for both experimental and simulation data. When the source port is not in line of

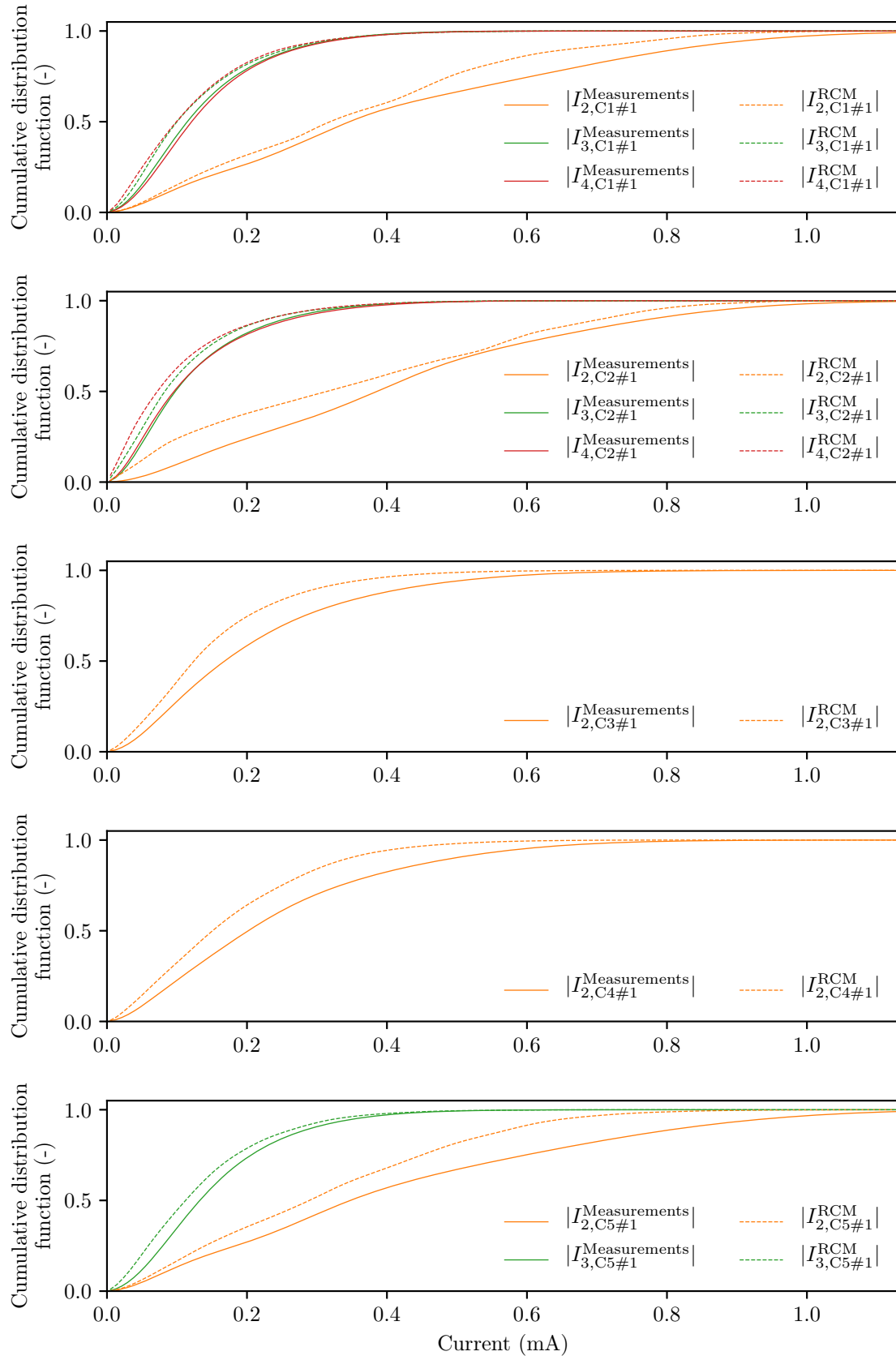


Fig. III.5.10 – CDFs of induced currents for the five configurations. The source is connected to port #1.

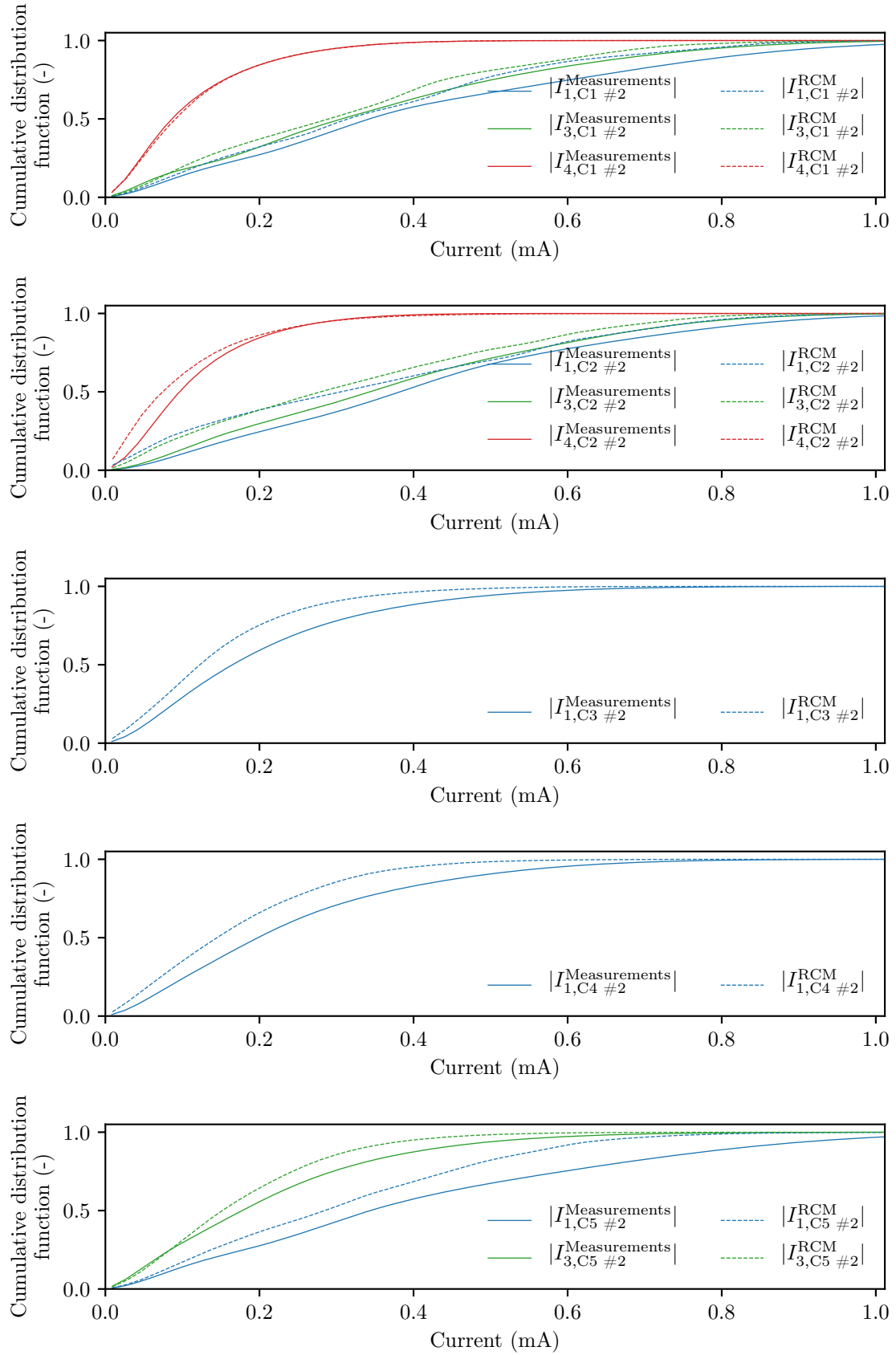


Fig. III.5.11 – CDFs of induced currents for the five configurations. The source is connected to port #2.

Absorbers	with		without	
	M	RCM	M	RCM
95% percentile	82	124	372	352

Table III.5.3 – 95% percentile in μA for the configuration *C5* with and without absorbers. The source is located at port index #1.

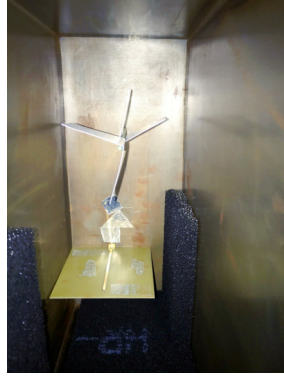


Fig. III.5.12 – Absorbers placed at the bottom of the mock-up.

sight with the destination port, then the two percentiles (Measurements/[RCM](#)) are close.

Moreover, for all the configurations, the probability to obtain a given current amplitude is higher for the [RCM](#) than for the experimental data (*i.e.* $|I^{\text{Measurements}}| < |I^{\text{RCM}}|$ for all the configurations). Thus, [RCM](#) simulations tend to slightly overestimate the magnitude of the coupled currents.

III.5.6 Effects of absorbers on the magnitude of induced currents

If the risk assessment process unveils that the magnitude of the induced current is too high in an electronic equipment (regarding the 95% percentile for example), some countermeasures may be set up. One of these is the insertion of absorbers in the equipment. The impact of this operation will now be studied.

The boards are placed in the mock-up according to configuration *C5* (see table [III.5.1](#)). The information provided by the manufacturer indicates that the absorbers (referenced as HR-25) have a reflection coefficient lower than -20 dB from 10 GHz to 60 GHz . They were placed on the bottom of the mock-up and the surface they occupy by these is approximately of 1100 cm^2 or 0.11 m^2 (see Fig. [III.5.12](#)).

The [CDF](#) are depicted in Fig. [III.5.13](#), and again the 95% percentiles are listed in Table. [III.5.3](#). Without the absorbers, the 95% percentile is $p_{95\%, |I_{3, \text{without absorbers}}^{\text{Measurements}}|} = 372\text{ }\mu\text{A}$ for the measurement data and $p_{95\%, |I_{3, \text{without absorbers}}^{\text{RCM}}|} = 352\text{ }\mu\text{A}$ for the [RCM](#) simulations. And with the absorbers, we have $p_{95\%, |I_{3, \text{with absorbers}}^{\text{Measurements}}|} = 82\text{ }\mu\text{A}$ and $p_{95\%, |I_{3, \text{with absorbers}}^{\text{RCM}}|} = 124\text{ }\mu\text{A}$. Thus, adding a surface of 1100 cm^2 into the mock-up mitigates the magnitude of the induced current between 9.1 dB (experimental data) and 13.1 dB ([RCM](#) simulations).

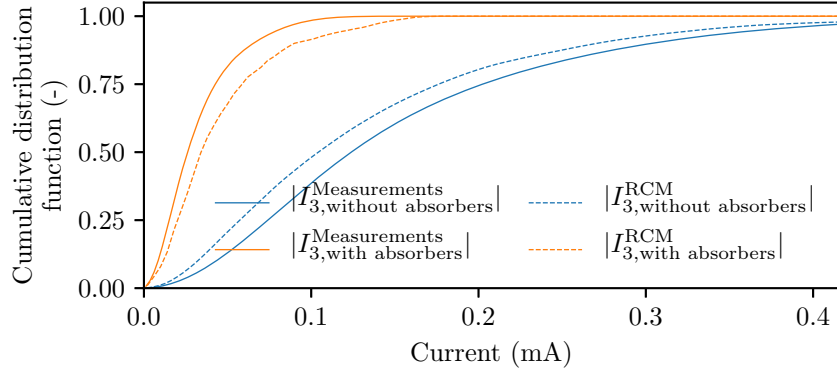


Fig. III.5.13 – Induced currents with and without absorbers in the mock-up.

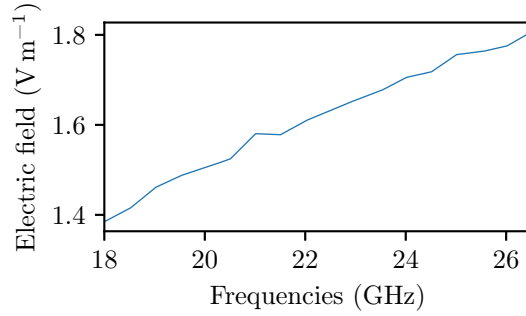


Fig. III.5.14 – Assessment of the electric field at the aperture location.

III.5.7 Coupling between the aperture and the internal ports

III.5.7.1 Determination of **RCM** parameters when applied with apertures

This section reminds the quantities that are required to apply the **RCM** when the coupling between one or several ports and an aperture needs to be determined and how they were determined.

The free-space impedance of the ports $\underline{\underline{Z}}^{\text{rad}}$: it was measured in free-space for all the studied configurations similarly to the configuration without the aperture.

The aperture admittance $\underline{\underline{Y}}^{\text{rad}}$: it was computed as explained in chapter III.2, and numerically evaluated in chapter III.3. It takes into account an incident plane wave of frequency up to ≈ 27 GHz.

The aperture source vector \vec{I}^{inc} : \vec{I}^{inc} depends on the electric field \vec{E}^{inc} at the aperture and on the dimensions of the aperture. It is possible to express the electric field $\vec{E}^{\text{inc}}(\vec{r} = D\vec{e}_r)$ at the aperture as :

$$\vec{E}^{\text{inc}}(\vec{r} = D\vec{e}_r) = |E^{\text{inc}}(\vec{r} = D\vec{e}_r)| e^{-jkD} \vec{e}_y \quad (\text{III.5.8})$$

with

$$|E^{\text{inc}}(\vec{r} = D\vec{e}_r)| = \frac{\eta k}{4\pi} \frac{1}{D} \frac{|V_0|}{Z_0} \frac{1}{|AF|} \quad (\text{III.5.9})$$

where \vec{r} is the observer location and D its distance from the transmitting antenna, k the wavenumber, $|V_0|$ the supplied voltage to the antenna, and Z_0 the characteristic impedance of the **VNA**. The full calculus is detailed in appendix D. The output power P of the **VNA** was set to its maximum value,

Configuration	Number of port N	Position 1	Position 2	Position 3	Position 4
A1	1	Straight #2	-	-	-
A2	1	-	-	-	L right #2
A3	2	Straight #2	-	-	L right #3
A4	3	L right #2	Meander #3	-	L right #4

Table III.5.4 – The four considered configurations. The number prefixed by the symbol # corresponds to the port index of the system. The source antenna is at the port index #1.

which is $P = 10 \text{ dBm}$, and $|V_0| = \sqrt{2PZ_0}$. Fig. III.5.14 shows the electric field magnitude at the aperture location which is at a distance $D = 4.28 \text{ m}$ from the source antenna. A 25 dB gain horn antenna (reference AF-INFO LB-42-25) was chosen. Its frequency range is from 18 to 26.5 GHz. Then, from equation (III.2.89), the current input vector at the aperture location \vec{I}^{inc} is determined. We assume that the field at the aperture is a plane wave, thus:

$$\vec{H}^{\text{inc}} = \frac{\vec{e}_z \wedge \vec{E}^{\text{inc}}}{\eta} = H^{\text{inc}} \vec{e}_x \quad (\text{III.5.10})$$

We then compute the components of \vec{I}^{inc} as:

$$I_s^{\text{inc}} = \frac{\sqrt{2}(1 - (-1)^s) \sqrt{LW}}{\pi s} H^{\text{inc}} \quad (\text{III.5.11})$$

$$= \frac{\sqrt{2}(1 - (-1)^s) \sqrt{LW}}{4\pi^2 n s} \frac{k}{D} \frac{|V_0|}{Z_0} \frac{1}{|AF|} \quad (\text{III.5.12})$$

The loss parameter α : Again, as α is not easy to determine, it was computed from experimental data as explained in section III.5.7.1. The port index #1 of the VNA was connected to the source antenna, and the full scattering matrix was acquired. Scattering matrices $\underline{\underline{S}}$ have the form:

$$\underline{\underline{S}} = \begin{pmatrix} S_{1,1} & S_{1,2} & \cdots & S_{1,N+1} \\ S_{2,1} & \begin{pmatrix} S_{2,2} & \cdots & S_{2,N+1} \\ \vdots & \ddots & \vdots \\ S_{N+1,2} & \cdots & S_{N+1,N+1} \end{pmatrix} \\ \vdots & \\ S_{N+1,1} & \end{pmatrix} \quad (\text{III.5.13})$$

The sub-matrix $\underline{\underline{S}}_p$ related to the interaction between the N ports, is identified in blue in equation (III.5.13). From $\underline{\underline{S}}_p$, one can compute its associated impedance matrix $\underline{\underline{Z}}_p^{\text{cav}}$ (from equation (III.5.7)). Then, the normalized impedance ξ_p is determined (from equation (III.5.1)), and α can be determined either from the variance of its elements (equations (III.5.2) and (III.5.3)), or by a fitting process.

The number of modes M : As, there is no reason to change the value of M , we set $M = 600$ as previously.

III.5.7.2 Results

Four configurations have been considered and are listed in Table. III.5.4. As we had at our disposal a four ports VNA, it was not possible to consider configurations with more than three PCBs because one port was dedicated to the antenna.

Concerning the [RCM](#) simulations, it took ≈ 10 min to execute each of these [RCM](#) simulations. This duration does not include the time needed to numerically compute $\underline{\underline{Y}}^{\text{rad}}$.

At the time of writing this report, it was not possible to present a comparison, because the measurement data were not validated, as the voltages/currents measured are too abnormal compared to the [RCM](#) results. A measurement campaign dealing with the coupling between the [PCBs](#) inside the chassis and a plane wave through the aperture is planned in the near future, as soon as possible.

III.5.8 Conclusion

Four applications of the [RCM](#) have been proposed. The first one was relative to the coupling between two monopoles. From experimental data, the chaoticity of the system of interest has been assessed between 5 and 25 GHz, and we could conclude that this system could be considered as chaotic in that frequency range. The loss parameter α was then determined for some frequencies by a fitting process. Finally, the [RCM](#) was applied and the probability density functions of the induced voltages, for experimental and simulated data, was compared with good agreements.

The second application was about the stacking of several [PCBs](#) having microstrip transmission lines. Induced currents were investigated by means of [CDFs](#) computed from [RCM](#) simulations and from experimental data. The results have revealed two behaviors depending on whether the boards are in line of sight or not. Comparison between the [RCM](#) simulations and experimental data has shown a good agreement for all the tested configurations.

The third study was about the effect of placing absorbers in the mock-up, and we have highlighted that adding a surface of 1100 cm^2 in the mock-up reduces the 95% percentile by a factor between 9.1 dB ([RCM](#) simulations) and 13.1 dB (measurements).

The last study was considering the couplings between a plane wave and one or several [PCBs](#) fitted inside the desktop computer chassis. The analytical expressions of the required parameters have been proposed. However, it is not possible to propose a comparison. Further experiments are required and will be planned as soon as possible.

Conclusion

The study of electromagnetic phenomena is valuable for the [information system security \(INFOSEC\)](#). Indeed, it was highlighted that multiple threats, against the information security, result from [electromagnetic interferences \(EMI\)](#). Specifically, one of these threats is their potential coupling to inner elements of electronic equipment chassis. Depending on the [EMI](#) spectrum occupancy and on the chassis geometry, couplings can be strong on account of resonances. Different scenarios that could reduce information security, involving [EMI](#) and reverberant environments, were enumerated. A study of these couplings was thus conducted on a generic desktop computer chassis. That chassis was described by means of three different models.

The first model was used to experiment the other two, and is the actual instantiation of a computer chassis mock-up with common dimensions. The mock-up was first designed, then manufactured and, finally, validated. The second model aimed to simulate the mock-up with a full-wave simulation model by using a commercial time-domain solver. From the obtained results, it was possible to determine couplings between an aperture and several simple [printed circuit boards \(PCBs\)](#). The third model is based on the [random matrix theory \(RMT\)](#) and takes the form of a sophisticated circuit model. It is referred to as the [random coupling model \(RCM\)](#).

[EMSEC](#) analysis for the full-wave simulation model

The simulation model allowed to accurately compute the electric field inside the empty cavity at several positions and with different aperture locations. The model was then fitted with simple [PCBs](#). An antenna factor was used to compare a set of measurements with the simulated data. It was defined as the ratio of the electric field strength, at the aperture, to the voltage generated by this field, at the end of transmission lines printed on the circuit boards. At first, a stacking of two [PCBs](#) was considered. The moving difference (between measurements and simulations results) of antenna factors, averaged over 40 MHz, was computed. For this configuration, the results stay within a ± 10 dB interval. Finally, a stacking of four [PCBs](#) was considered. In this case, the moving difference of averaged values was in the range ± 17 dB. Thus, a larger uncertainty is observed when the number of stacked [PCBs](#) increases.

From an [electromagnetic security \(EMSEC\)](#) perspective, although the uncertainty of this moving difference is large, its knowledge can be an input for a risk assessment process. It can be used as a level of confidence. Indeed, one can determine from it a safety margin in order to mitigate the coupling risks. This safety margin may be used to select electronic components, that meet requirements. Furthermore, when considering an [intentional electromagnetic interference \(IEMI\)](#) towards a sensitive information system, it could help to determine a restricted area, around this information system, which guarantees that the couplings would not exceed a given threshold. Indeed, the free-space propagation between the [IEMI](#) source and the target system would not allow the aggression to reach a given level.

Consider an application close to the studied model, for which a risk assessment process highlights that the couplings between an aperture and PCBs inside a cavity must remain below a given threshold. This could be a desktop computer, with a plastic cover at the location of a DVD drive, and two stacked PCBs that process sensitive information. It is then possible to run a full-wave simulation and to determine the antenna factor between the incident electric field and the voltage under investigation. If the obtained antenna factor added with the uncertainty (10 dB in our example) is above the threshold, then mitigating procedures must be engaged. The design of the PCB may be modified to reduce the coupling or the losses within the cavity can be increased (by adding absorbers for example).

As a main drawback, this procedure can be time-consuming to determine coupled currents and voltages for randomized boundary conditions, especially for cavities whose inner shapes cannot be clearly determined.

EMSEC analysis for the RCM

We have illustrated that the RCM is able to quickly simulate complex reverberant environments by providing statistical quantities when the free-space impedance matrix and the cavity losses are available. The RCM relies on the RMT, and the eigenmodes in reverberant environments are randomized. The inner shape of a cavity is thus, also randomized. Multiple statistical quantities of interest were exposed, and their implementation were detailed. They are all related to right tails of the probability density functions (PDFs).

This study has shown that to mitigate couplings between two sensitive devices, it is necessary to interleave other non sensitive buffer boards between them. Furthermore, if the risk assessment process reveals that the magnitude of the induced current is still too high (regarding the 95% percentile for example), the insertion of absorbers inside the chassis could help to meet the requirements.

A possible application workflow, related to EMSEC, is the following one. Consider the design of a new electronic equipment installed within a chassis. Inside it, a board processing sensitive information generates parasitic signals which couple onto a given cable. Previously, a risk analysis process or a user feedback, determined that these parasitic signals must not exceed a given threshold. The first step would be to determine the free space impedance matrix $\underline{\underline{Z}}^{\text{rad}}$ between the board and the cable, from a full-wave simulation software for example. Then, the quality factor Q (or the loss factor α) of the cavity should be assessed for a frequency range depending on the spectral occupancy of the parasitic signals. Finally, the RCM may be applied to determine at which voltage/current magnitude the 95% percentile is reached.

We remind the straightforward application previously exposed, that is relative to encryption devices which are dedicated to encipher sensitive data. In such devices, the signal that carries the plaintext (not enciphered) information penetrates the device via a cable, then the information is enciphered and this generated signal exits the equipment through another cable. It is thus mandatory to prevent couplings of the signal containing the plaintext (that may radiate inside the equipment chassis) to the conductor that carries the ciphered data. Indeed, if this happened, the information confidentiality would not be guaranteed anymore as a parasitic signal, correlated to the plaintext, may be superposed on the outgoing signal. In such a case, advantage may be taken from the RCM, as the designer of such specific equipment has the full knowledge about its constitutive elements since the making is managed from scratch. The quantities $\underline{\underline{Z}}^{\text{rad}}$ and α may thus be easily accessed.

Let us consider another situation where a server is used to run sensitive information system (*i.e.* data storage, active directory, etc.). An integrator will select [commercial off-the-shelf \(COTS\)](#) elements (casing, hard drive, processor, ethernet controller, etc.) and will arrange these pieces of hardware together. Here, one does not control the hardware design of these elements but needs to guarantee low couplings between two inner components like the processor and the ethernet controller. For this case, $\underline{\underline{Z}}^{\text{rad}}$ and α are difficult to obtain, and it thus requires an additional modeling work.

Future works

The study of the [IEMI](#) coupling through apertures inside a casing is valuable as these couplings can have an impact on the disponibility of an information system, but also on the processed information integrity. Thus, the comparison between the [RCM](#) simulations and measurements should be completed. This comparison would allow to qualify the selected approach. In addition, a study to take into account aperture of arbitrary shape could be relevant as only rectangular apertures were considered for now.

The impact, on the extreme quantiles, of adding absorber materials inside cavities was exposed. It would be of high interest to determine the relation between the quantity of absorber materials, in terms of occupied surface in the cavity, to the drop of the extreme quantiles. From that relation, it would be possible to determine the amount of absorber materials that need to be inserted inside the cavity to meet the [EMSEC](#) requirements.

If the losses cannot be changed in a given cavity, it would be relevant to determine the relative arrangement between the system ports, in order to minimize the couplings. In order to do this, the free-space impedance could be determined from a full-wave simulation software, for several relative arrangements. The [RCM](#) could then be applied to select the arrangement that gives the lowest couplings, in terms of extreme quantiles for example.

Moreover, in this study, only a small cavity (400 mm×440 mm×170 mm) was investigated. However, other practical applications and different scales may be considered. We can imagine applying the [RCM](#) to server racks where equipment with multiple purposes are stacked. In that type of configuration, and from the [EMSEC](#) point of view, the mitigation of couplings between equipment is mandatory.

Bibliography of the author

- Houchouas, V., Darces, M., Hélier, M., Cottais, E., and Lopes Esteves, J. (2020a). Application du modèle de couplages aléatoires pour l'évaluation de probabilités d'occurrence de courants induits. *20ème Colloque International et Exposition sur la Compatibilité ÉlectroMagnétique*.
- Houchouas, V., Chatelon, Y., Cottais, E., Darces, M., Hélier, M., and Lopes Esteves, J. (2019). Estimation statistique de couplages au sein de châssis d'équipements électroniques. In *Journée thématique do GdR ondes « Sécurité des systèmes électroniques et communicants »*.
- Houchouas, V., Darces, M., Bourey, N., Cottais, E., Chatelon, Y., and Hélier, M. (2018). Comparison between simulation and measurement of EMI inside a computer chassis mock-up. In *2018 International Symposium on Electromagnetic Compatibility (EMC EUROPE)*, pages 551–555.
- Houchouas, V., Lopes Esteves, J., Cottais, E., Kasmi, C., and Armstrong, K. (2017). Immunity assessment of a servomotor exposed to an intentional train of rf pulses. In *2017 International Symposium on Electromagnetic Compatibility - EMC EUROPE*, pages 1–5.
- Houchouas, V., Kasmi, C., Lopes Esteves, J., and Valembois, P. (2016). Caractérisation logicielle de la susceptibilité d'un capteur de température de PC pour la CEM et la SSI. In *18ème Colloque International et Exposition sur la Compatibilité ÉlectroMagnétique*, volume 18, page 245, Rennes, France.
- Houchouas, V., Kasmi, C., Lopes Esteves, J., and Coiffard, D. (2015a). Experimental comparison of mode-stirrer geometries for EMC. *ASIAEM*.
- Houchouas, V., Kasmi, Chaouki, Lopes, Esteves, José, and Coiffard, Damien (2015b). Experimental comparison of mode-stirrer geometries based on the susceptibility testing of cots information systems in regards of the criticality of effects. *SDAN*.
- Haddad, P., Kasmi, C., Lopes Esteves, J., and Houchouas, V. (2016). Electromagnetic harmonic attack on transient effect ring oscillator based true random number generator. In *Hardware Security Conference & Training 2016*, The Hague, Netherlands.

To be published: journal article and conference papers

- Houchouas, V., Darces, M., Hélier, M., Cottais, E., and Lopes Esteves, J. (2020d). Applications of the random coupling model to assess induced currents or voltages in reverberant environment. *PIER C*.
- Houchouas, V., Darces, M., Hélier, M., Cottais, E., and Lopes Esteves, J. (2020c). Applications of the random coupling model for stacked printed circuit boards. *EMC Europe and URSI GASS, Rome, september 2020*.

Bibliography

- HiPOW: Protection of Critical Infrastructure against High Power Microwave Threat, 2012a.
- SECRET: SECurity of Railways against Electromagnetic aTtacks, 2012b.
- STRUCTURES: Strategies for the impRovement of critical infrastrUCTure Resilience to Electromagnetic attackS, 2012c. URL <https://cordis.europa.eu/project/id/285257>.
- CST Studio Suite user manual*, 2020.
- A. K. Agrawal, H. J. Price, and S. H. Gurbaxani. Transient response of multiconductor transmission lines excited by a nonuniform electromagnetic field. *IEEE Transactions on Electromagnetic Compatibility*, EMC-22(2):119–129, 1980. ISSN 0018-9375. doi: 10.1109/TEM.1980.303824.
- Y. Alhassid and C. H. Lewenkopf. Statistical distributions of level widths and conductance peaks in irregularly shaped quantum dots. *Phys. Rev. Lett.*, 75:3922–3925, Nov 1995. doi: 10.1103/PhysRevLett.75.3922. URL <https://link.aps.org/doi/10.1103/PhysRevLett.75.3922>.
- T. M. Antonsen, G. Gradoni, S. Anlage, and E. Ott. Statistical characterization of complex enclosures with distributed ports. In *2011 IEEE International Symposium on Electromagnetic Compatibility*, pages 220–225, Aug 2011. doi: 10.1109/ISEMC.2011.6038313.
- R. Azaro, S. Caorsi, M. Donelli, and G. L. Gragnani. Evaluation of the effects of an external incident electromagnetic wave on metallic enclosures with rectangular apertures. *Microwave and Optical Technology Letters*, 28(5):289–293, 2001. ISSN 1098-2760. doi: 10.1002/1098-2760(20010305)28:5<289::AID-MOP1021>3.0.CO;2-T. URL [http://dx.doi.org/10.1002/1098-2760\(20010305\)28:5<289::AID-MOP1021>3.0.CO;2-T](http://dx.doi.org/10.1002/1098-2760(20010305)28:5<289::AID-MOP1021>3.0.CO;2-T).
- R. Azaro, S. Caorsi, M. Donelli, and G. L. Gragnani. A circuital approach to evaluating the electromagnetic field on rectangular apertures backed by rectangular cavities. *IEEE Transactions on Microwave Theory and Techniques*, 50(10):2259–2266, 2002. ISSN 0018-9480. doi: 10.1109/TMTT.2002.803434.
- M. G. Backstrom and K. G. Lovstrand. Susceptibility of electronic systems to high-power microwaves: Summary of test experience. *IEEE Transactions on Electromagnetic Compatibility*, 46(3):396–403, 2004. ISSN 0018-9375. doi: 10.1109/TEM.2004.831814. URL <http://ieeexplore.ieee.org/lpdocs/epic03/wrapper.htm?arnumber=1325794>.
- Constantine A Balanis. *Advanced engineering electromagnetics*. John Wiley & Sons, 2012.
- Constantine A Balanis. *Antenna theory: analysis and design*. John Wiley & Sons, 2016.
- Carl E Baum, Tom K Liu, and Fred M Tesche. On the analysis of general multiconductor transmission-line networks. *Interaction Note*, 350(6):467–547, 1978.

- I. Belokour and J. LoVetri. A 2d-transmission line model for the EM field estimation inside enclosures with apertures. In *2002 IEEE International Symposium on Electromagnetic Compatibility*, volume 1, pages 424–429 vol.1, 2002. doi: 10.1109/ISEMC.2002.1032516.
- Michael V. Berry. Regular and irregular semiclassical wavefunctions. *Journal of Physics A: Mathematical and General*, 10(12):2083, 1977.
- Philippe Besnier and Bernard Démoulin. *Electromagnetic reverberation chambers*. John Wiley & Sons, 2013.
- H. A. Bethe. Theory of diffraction by small holes. *Phys. Rev.*, 66:163–182, Oct 1944. doi: 10.1103/PhysRev.66.163. URL <http://link.aps.org/doi/10.1103/PhysRev.66.163>.
- O. Bohigas, M. J. Giannoni, and C. Schmit. Characterization of chaotic quantum spectra and universality of level fluctuation laws. *Phys. Rev. Lett.*, 52:1–4, Jan 1984. doi: 10.1103/PhysRevLett.52.1. URL <https://link.aps.org/doi/10.1103/PhysRevLett.52.1>.
- Oriol Bohigas. Random matrix theories and chaotic dynamics. Technical report, Paris-11 Univ., 1991.
- A. Boutar, A. Reineix, C. Guiffaut, and G. Andrieu. An efficient analytical method for electromagnetic field to transmission line coupling into a rectangular enclosure excited by an internal source. *IEEE Transactions on Electromagnetic Compatibility*, 57(3):565–573, June 2015. ISSN 1558-187X. doi: 10.1109/TEMC.2014.2386913.
- C J Bouwkamp. Diffraction theory. *Reports on Progress in Physics*, 17(1):35–100, jan 1954. doi: 10.1088/0034-4885/17/1/302. URL <https://doi.org/10.1088/2F0034-4885/2F17%2F1%2F302>.
- Claudio Bozzato, Riccardo Focardi, and Francesco Palmarini. Shaping the glitch: Optimizing voltage fault injection attacks. *IACR Transactions on Cryptographic Hardware and Embedded Systems*, 2019(2):199–224, Feb. 2019. doi: 10.13154/tches.v2019.i2.199-224. URL <https://tches.iacr.org/index.php/TCHES/article/view/7390>.
- S. Bronckers, G. Vandersteen, G. van der Plas, and Y. Rolain. On the p+ guard ring sizing strategy to shield against substrate noise. In *2007 IEEE Radio Frequency Integrated Circuits (RFIC) Symposium*, pages 753–756, June 2007. doi: 10.1109/RFIC.2007.380992.
- Piet Wibertus Brouwer. Generalized circular ensemble of scattering matrices for a chaotic cavity with nonideal leads. *Physical Review B*, 51(23):16878–16884, Jun 1995. ISSN 1095-3795. doi: 10.1103/physrevb.51.16878. URL <http://link.aps.org/doi/10.1103/PhysRevB.51.16878>.
- Rene Brun and Fons Rademakers. Root—an object oriented data analysis framework. *Nuclear Instruments and Methods in Physics Research Section A: Accelerators, Spectrometers, Detectors and Associated Equipment*, 389(1-2):81–86, 1997.
- Christian Bruns. *Three-dimensional simulation and experimental verification of a reverberation chamber*. PhD thesis, ETH Zurich, 2005.
- Gerald J Burke and Andrew J Poggio. Numerical electromagnetics code (nec)-method of moments. 1981.
- C. Butler, Y. Rahmat-Samii, and R. Mittra. Electromagnetic penetration through apertures in conducting surfaces. *IEEE Transactions on Antennas and Propagation*, 26(1):82–93, January 1978. ISSN 0018-926X. doi: 10.1109/TAP.1978.1141788.

- R. Callan, A. Zajic, and M. Prvulovic. A practical methodology for measuring the side-channel signal available to the attacker for instruction-level events. In *2014 47th Annual IEEE/ACM International Symposium on Microarchitecture*, pages 242–254, Dec 2014. doi: 10.1109/MICRO.2014.39.
- Giovanni Camurati, Sebastian Poeplau, Marius Muench, Tom Hayes, and Aurélien Francillon. Screaming channels: When electromagnetic side channels meet radio transceivers. In *Proceedings of the 2018 ACM SIGSAC Conference on Computer and Communications Security, CCS '18*, page 163–177, New York, NY, USA, 2018. Association for Computing Machinery. ISBN 9781450356930. doi: 10.1145/3243734.3243802. URL <https://doi.org/10.1145/3243734.3243802>.
- Angelo Canty and B. D. Ripley. *boot: Bootstrap R (S-Plus) Functions*, 2017. R package version 1.3-20.
- U. Carlberg, P. S. Kildal, A. Wolfgang, O. Sotoudeh, and C. Orlenius. Calculated and measured absorption cross sections of lossy objects in reverberation chamber. *IEEE Transactions on Electromagnetic Compatibility*, 46(2):146–154, 2004. ISSN 0018-9375. doi: 10.1109/TEM.2004.826878.
- W. P. Carpes, L. Pichon, and A. Razek. Analysis of the coupling of an incident wave with a wire inside a cavity using an FEM in frequency and time domains. *IEEE Transactions on Electromagnetic Compatibility*, 44(3):470–475, 2002. ISSN 0018-9375. doi: 10.1109/TEM.2002.801767.
- F. Caudron, A. Ouslimani, R. Vézinet, A. Kasbari, J. L. Lavergne, and J. S. Borrod. Study of the front door coupling into a complicated enclosure. In *2010 International Symposium on Signals, Systems and Electronics*, volume 1, pages 1–4, 2010. doi: 10.1109/ISSSE.2010.5607139.
- François Caudron. *Etude fondamentale des effets liés aux agressions micro-ondes de fortes puissances et du chaos sur l'électronique (composants, circuits et systèmes)*. Cergy-Pontoise, 2012. URL <http://www.theses.fr/2012CERG0663>.
- Stuart Coles, Joanna Bawa, Lesley Trenner, and Pat Dorazio. *An introduction to statistical modeling of extreme values*, volume 208. Springer, 2001.
- R. Collin. *Field Theory of Guided Waves*, pages i–xii. Wiley-IEEE Press, 1991. ISBN 9780470544648. doi: 10.1109/9780470544648.fmatter. URL <http://ieeexplore.ieee.org/xpl/articleDetails.jsp?arnumber=5265765>.
- Committee on National Security Systems. Nstissam tempest 2-95; red / black installation guidance, 1995.
- W.J Conover. *Practical nonparametric statistics*. Wiley series in probability and statistics 1999: 9. Wiley, 3ed. edition, 1999.
- Emmanuel Cottais, José Lopes Esteves, and Chaouki Kasmi. Second order soft-tempest in rf front-ends: Design and detection of polyglot modulations. In *2018 International Symposium on Electromagnetic Compatibility (EMC EUROPE)*, pages 166–171, Aug 2018. doi: 10.1109/EMCEurope.2018.8485134.
- CST. *SMD Resistor Modelling - Wilkinson Power Divider*, 2016.
- C. Dembowski, B. Dietz, H.-D. Gräf, A. Heine, T. Papenbrock, A. Richter, and C. Richter. Experimental test of a trace formula for a chaotic three-dimensional microwave cavity. *Phys. Rev. Lett.*, 89:064101, Jul 2002. doi: 10.1103/PhysRevLett.89.064101. URL <https://link.aps.org/doi/10.1103/PhysRevLett.89.064101>.
- Luc Devroye. Nonuniform random variate generation. *Handbooks in operations research and management science*, 13:83–121, 2006.

- T. Dubois, J. J. Laurin, J. Raoult, and S. Jarrix. Effect of low and high power continuous wave electromagnetic interference on a microwave oscillator system: From VCO to PLL to QPSK receiver. *IEEE Transactions on Electromagnetic Compatibility*, 56(2):286–293, 2014. ISSN 0018-9375. doi: 10.1109/TEM.2013.2280670.
- Javier Duoandikoetxea and Javier Duoandikoetxea Zuazo. *Fourier analysis*, volume 29. American Mathematical Soc., 2001.
- A. Dvoretzky, J. Kiefer, and J. Wolfowitz. Asymptotic minimax character of the sample distribution function and of the classical multinomial estimator. *Ann. Math. Statist.*, 27(3):642–669, 09 1956. doi: 10.1214/aoms/1177728174. URL <https://doi.org/10.1214/aoms/1177728174>.
- Freeman J. Dyson. A brownian-motion model for the eigenvalues of a random matrix. *Journal of Mathematical Physics*, 3(6):1191–1198, nov 1962. doi: 10.1063/1.1703862. URL <https://doi.org/10.1063/1.1703862>.
- John W. Eaton, David Bateman, Søren Hauberg, and Rik Wehbring. *GNU Octave version 4.2.1 manual: a high-level interactive language for numerical computations*, 2017. URL <https://www.gnu.org/software/octave/doc/v4.2.1/>.
- B. Efron and R. Tibshirani. Bootstrap methods for standard errors, confidence intervals, and other measures of statistical accuracy. *Statist. Sci.*, 1(1):54–75, 02 1986. doi: 10.1214/ss/1177013815. URL <https://doi.org/10.1214/ss/1177013815>.
- Bradley Efron. Better bootstrap confidence intervals. *Journal of the American Statistical Association*, 82(397):171–185, 1987. ISSN 01621459. URL <http://www.jstor.org/stable/2289144>.
- Gilles Montambaux Eric Akkermans. *Mesoscopic physics of electrons and photons*. Cambridge University Press, 1 edition, 2007.
- Eugene P. Wigner. Random matrices in physics. *SIAM Review*, 9(1):1–23, 1967. URL <http://www.jstor.org/stable/2027409>.
- EM FEKO. Software & systems sa,(pty) ltd, 32 techno lane. *Technopark, Stellenbosch*, 7600.
- I. D. Flintoft, S. L. Parker, S. J. Bale, A. C. Marvin, J. F. Dawson, and M. P. Robinson. Measured average absorption cross-sections of printed circuit boards from 2 to 20 GHz. *IEEE Transactions on Electromagnetic Compatibility*, 58(2):553–560, 2016. ISSN 0018-9375. doi: 10.1109/TEM.2016.2515658.
- Ronald M. Foster. A reactance theorem. *Bell System Technical Journal*, 3(2):259–267, Apr 1924. doi: 10.1002/j.1538-7305.1924.tb01358.x. URL <http://dx.doi.org/10.1002/j.1538-7305.1924.tb01358.x>.
- Mark Galassi, Jim Davies, James Theiler, Brian Gough, Gerard Jungman, Patrick Alken, Michael Booth, and Fabrice Rossi. Gnu scientific library, 2007. URL <https://www.gnu.org/software/gsl/>.
- Daniel Genkin, Lev Pachmanov, Itamar Pipman, and Eran Tromer. Ecdh key-extraction via low-bandwidth electromagnetic attacks on pcs. In *Cryptographers’ Track at the RSA Conference*, pages 219–235. Springer, 2016.
- J. Gil Gil, Z. B. Drikas, T. D. Andreadis, and S. M. Anlage. Prediction of induced voltages on ports in complex, three-dimensional enclosures with apertures, using the random coupling model. *IEEE Transactions on Electromagnetic Compatibility*, 58(5):1535–1540, Oct 2016. ISSN 0018-9375. doi: 10.1109/TEM.2016.2580301.

- Travis Goodspeed and Sergey Bratus. Polyglots and chimeras in digital radio modes. In *REcon 2015, Montreal, Canada*, 2015.
- G. Gradoni, T. M. Antonsen, S. M. Anlage, and E. Ott. A statistical model for the excitation of cavities through apertures. *IEEE Transactions on Electromagnetic Compatibility*, 57(5):1049–1061, Oct 2015. ISSN 0018-9375. doi: 10.1109/TEMPC.2015.2421346.
- Gabriele Gradoni, Thomas M Antonsen, Steven Anlage, and Edward Ott. Theoretical analysis of apertures radiating inside wave chaotic cavities. In *Electromagnetic Compatibility (EMC EUROPE), 2012 International Symposium on*, pages 1–6. IEEE, 2012.
- Gabriele Gradoni, Jen-Hao Yeh, Bo Xiao, Thomas M. Antonsen, Steven M. Anlage, and Edward Ott. Predicting the statistics of wave transport through chaotic cavities by the random coupling model: A review and recent progress. *Wave Motion*, 51(4):606 – 621, 2014. ISSN 01652125. doi: <https://doi.org/10.1016/j.wavemoti.2014.02.003>. URL <http://www.sciencedirect.com/science/article/pii/S0165212514000250>.
- Gabriele Gradoni, Thomas M Antonsen, and Edward Ott. Random coupling model for the radiation of irregular apertures. *Radio Science*, 50(7):678–687, 2015.
- Frank Gronwald. *Antenna theory in resonating systems derived from fundamental electromagnetism*. PhD thesis, Otto-von-Guericke-Universität Magdeburg, Universitätsbibliothek, 2006.
- Jean-Baptiste Gros. *Statistiques spatiales des cavités chaotiques ouvertes : applications aux cavités électromagnétiques*. PhD thesis, École doctorale Sciences fondamentales et appliquées (Nice), 2014. URL <http://www.theses.fr/2014NICE4150>. Thèse de doctorat dirigée par Legrand, Olivier et Mortessagne, Fabrice Physique Nice 2014.
- Jean-Baptiste Gros, Olivier Legrand, Fabrice Mortessagne, Elodie Richalot, and Kamardine Selemanni. Universal behaviour of a wave chaos based electromagnetic reverberation chamber. *Wave Motion*, 51:664–672, 2014. doi: 10.1016/j.wavemoti.2013.09.006. URL <https://hal.archives-ouvertes.fr/hal-00800526>.
- Thomas Guhr, Axel Müller-Groeling, and Hans A Weidenmüller. Random-matrix theories in quantum physics: common concepts. *Physics Reports*, 299(4-6):189–425, 1998.
- K. C. Gupta. *Microstrip Lines and Slotlines*. Artech House Antennas and Propagation Library. Artech House Publishers, 2 edition, 1996.
- Mordechai Guri, Assaf Kachlon, Ofer Hasson, Gabi Kedma, Yisroel Mirsky, and Yuval Elovici. Gsmem: Data exfiltration from air-gapped computers over GSM frequencies. In *24th USENIX Security Symposium (USENIX Security 15)*, pages 849–864, Washington, D.C., August 2015. USENIX Association. ISBN 978-1-931971-232. URL <https://www.usenix.org/conference/usenixsecurity15/technical-sessions/presentation/guri>.
- Mordechai Guri, Matan Monitz, and Yuval Elovici. Usbee: air-gap covert-channel via electromagnetic emission from usb. In *2016 14th Annual Conference on Privacy, Security and Trust (PST)*, pages 264–268. IEEE, 2016.
- Fritz Haake. Quantum signatures of chaos, 3th edition. In *Quantum Coherence in Mesoscopic Systems*, pages 583–595. Springer, 2010.
- Patrick Haddad, Chaouki Kasmi, José Lopes Esteves, and Valentin Houchouas. Electromagnetic harmonic attack on transient effect ring oscillator based true random number generator. In *Hardware Security Conference & Training 2016*, The Hague, Netherlands, 2016.

- R Harrington and J Mautz. A generalized network formulation for aperture problems. *IEEE Transactions on Antennas and Propagation*, 24(6):870–873, 1976.
- Yuichi Hayashi, Naofumi Homma, Mamoru Miura, Takafumi Aoki, and Hideaki Sone. A threat for tablet pcs in public space: Remote visualization of screen images using em emanation. In *Proceedings of the 2014 ACM SIGSAC Conference on Computer and Communications Security, CCS '14*, pages 954–965, New York, NY, USA, 2014. ACM. ISBN 978-1-4503-2957-6. doi: 10.1145/2660267.2660292. URL <http://doi.acm.org/10.1145/2660267.2660292>.
- Janet E. Heffernan and Alec G. Stephenson. *ismev: An Introduction to Statistical Modeling of Extreme Values*, 2018. URL <https://CRAN.R-project.org/package=ismev>. R package version 1.42.
- Sameer Hemmady, Xing Zheng, Thomas M Antonsen Jr, Edward Ott, and Steven M Anlage. Universal statistics of the scattering coefficient of chaotic microwave cavities. *Physical Review E*, 71(5):056215, 2005.
- Sameer Hemmady, Thomas M. Antonsen, Edward Ott, and Steven M. Anlage. Statistical prediction and measurement of induced voltages on components within complicated enclosures: A wave-chaotic approach. 54(4):758–771, 2012. ISSN 0018-9375, 1558-187X. doi: 10.1109/TEMPC.2011.2177270. URL <http://ieeexplore.ieee.org/lpdocs/epic03/wrapper.htm?arnumber=6122500>.
- Sameer Dileep Hemmady. *A wave-chaotic approach to predicting and measuring electromagnetic field quantities in complicated enclosures*. PhD thesis, University of Maryland, 2006. URL <http://drum.lib.umd.edu/handle/1903/3979>.
- D. A. Hill. Plane wave integral representation for fields in reverberation chambers. *IEEE Transactions on Electromagnetic Compatibility*, 40(3):209–217, Aug 1998. ISSN 0018-9375. doi: 10.1109/15.709418.
- David A Hill. *Electromagnetic fields in cavities: deterministic and statistical theories*, volume 35. John Wiley & Sons, 2009.
- R. Hoad, N.J. Carter, D. Herke, and S.P. Watkins. Trends in EM susceptibility of IT equipment. *IEEE Transactions on Electromagnetic Compatibility*, 46(3):390–395, 2004. ISSN 0018-9375. doi: 10.1109/TEMPC.2004.831815. URL <http://ieeexplore.ieee.org/lpdocs/epic03/wrapper.htm?arnumber=1325793>.
- Richard Hoad and Iain Sutherland. The forensic utility of detecting disruptive electromagnetic interference. In *Proceedings of 6th European Conference on Information Warfare and Security*, page 77, 2007.
- Valentin Houchouas, Chaouki Kasmi, José Lopes Esteves, and Philippe Valembois. Caractérisation logicielle de la susceptibilité d’un capteur de température de PC pour la CEM et la SSI. In *18ème Colloque International et Exposition sur la Compatibilité ÉlectroMagnétique*, volume 18, page 245, Rennes, France, 2016.
- Valentin Houchouas, José Lopes Esteves, Emmanuel Cottais, Chaouki Kasmi, and Keith Armstrong. Immunity assessment of a servomotor exposed to an intentional train of rf pulses. In *2017 International Symposium on Electromagnetic Compatibility - EMC EUROPE*, pages 1–5, Sep. 2017. doi: 10.1109/EMCEurope.2017.8094785.
- Michael Hutter and Jörn-Marc Schmidt. The temperature side channel and heating fault attacks. In *International Conference on Smart Card Research and Advanced Applications*, pages 219–235. Springer, 2013.

- International Electrotechnical Commission. IEC 61508 functional safety of electrical/electronic/programmable electronic safety-related systems, 2010.
- John David Jackson. Classical electrodynamics, 3rd edition, 1999. URL <http://www.wiley.com/WileyCDA/WileyTitle/productCd-047130932X.html>.
- I. Junqua, L. Guibert, and J. Parmantier. Assessment of high frequency coupling in a generic object by the power balance method. In *2007 18th International Zurich Symposium on Electromagnetic Compatibility*, pages 397–400, Sep. 2007. doi: 10.1109/EMCZUR.2007.4388279.
- I. Junqua, J.P. Parmantier, F. Issac, and W. Quenum. Evaluation of RF Transfer Functions Between the Outside and the Inside of Building Rooms. In *AMEREM 2014*, ALBUQUERQUE, United States, July 2014a. URL <https://hal-onera.archives-ouvertes.fr/hal-01068728>.
- I. Junqua, J.P. Parmantier, F. Issac, and W. Quenum. Application of electromagnetic topology and power balance concepts to radio frequency couplings into buildings. (625), 2014b. URL <http://www.ece.unm.edu/summa/notes/In/IN625.pdf>.
- Isabelle Junqua. *Pénétration des ondes électromagnétiques haute fréquence dans des systèmes : analyse et évaluation par l'approche Power Balance*. PhD thesis, Université de Lille 1, 2010. URL <http://www.theses.fr/2010LIL10053>. Thèse de doctorat dirigée par Degauque, Pierre Électronique Lille 1 2010.
- Isabelle Junqua, Jean-Philippe Parmantier, and François Issac. A network formulation of the power balance method for high-frequency coupling. *Electromagnetics*, 25(7-8):603–622, 2005. doi: 10.1080/02726340500214845. URL <http://dx.doi.org/10.1080/02726340500214845>.
- C. Kasmi, D. Coiffard, M. Hélier, and M. Darces. Performance analysis of a power network counter-tempest filter in realistic cabling scenarios. In *2014 International Symposium on Electromagnetic Compatibility*, pages 1166–1169, Sep. 2014a. doi: 10.1109/EMCEurope.2014.6931079.
- C. Kasmi, J. Lopes-Esteves, N. Picard, M. Renard, B. Beillard, E. Martinod, J. Andrieu, and M. Lalande. Event logs generated by an operating system running on a cots computer during iemi exposure. *IEEE Transactions on Electromagnetic Compatibility*, 56(6):1723–1726, Dec 2014b. ISSN 1558-187X. doi: 10.1109/TEMPC.2014.2357060.
- C Kasmi, J Lopes-Esteves, and M Renard. Automation of the immunity testing of COTS computers by the instrumentation of the internal sensors and involving the operating system logs – technical report. *System Design & Assessment Note*, 2014. URL <http://www.ece.unm.edu/summa/notes/index.html>.
- Chaouki Kasmi and José Lopes Esteves. Whisper in the wire: Voice command injection reloaded. *Hack In Paris*, 2016.
- Paul Kocher, Joshua Jaffe, and Benjamin Jun. Differential power analysis. In *Annual International Cryptology Conference*, pages 388–397. Springer, 1999.
- T. Konefal, J. F. Dawson, A. C. Marvin, M. P. Robinson, and S. J. Porter. A fast multiple mode intermediate level circuit model for the prediction of shielding effectiveness of a rectangular box containing a rectangular aperture. 47(4):678–691, 2005. ISSN 0018-9375. doi: 10.1109/TEMPC.2005.853715.
- L. Kovalevsky, R. S. Langley, and A. Barbarulo. Method for determining statistical mean and variance of electromagnetic energy transmission between coupled cavities. In *2014 International Symposium*

- on *Electromagnetic Compatibility*, pages 1007–1011, Sep. 2014. doi: 10.1109/EMCEurope.2014.6931050.
- L. Kovalevsky, R. S. Langley, and S. Caro. Prediction of the electromagnetic field distribution in a typical aircraft using the statistical energy analysis. In *2016 ESA Workshop on Aerospace EMC (Aerospace EMC)*, pages 1–6, May 2016. doi: 10.1109/AeroEMC.2016.7504577.
- U. Kuhl, M. Martínez-Mares, R. A. Méndez-Sánchez, and H.-J. Stöckmann. Direct processes in chaotic microwave cavities in the presence of absorption. *Physical Review Letters*, 94(14), apr 2005. doi: 10.1103/physrevlett.94.144101. URL <https://doi.org/10.1103/physrevlett.94.144101>.
- M. G. Kuhn. Compromising emanations of LCD TV sets. *IEEE Transactions on Electromagnetic Compatibility*, 55(3):564–570, June 2013. ISSN 1558-187X. doi: 10.1109/TEMPC.2013.2252353.
- Markus G. Kuhn. Electromagnetic eavesdropping risks of flat-panel displays. In David Martin and Andrei Serjantov, editors, *Privacy Enhancing Technologies*, pages 88–107, Berlin, Heidelberg, 2005. Springer Berlin Heidelberg. ISBN 978-3-540-31960-3.
- Markus G Kuhn and Ross J Anderson. Soft tempest: Hidden data transmission using electromagnetic emanations. In *International Workshop on Information Hiding*, pages 124–142. Springer, 1998.
- D. F. Kune, J. Backes, S. S. Clark, D. Kramer, M. Reynolds, K. Fu, Y. Kim, and W. Xu. Ghost talk: Mitigating EMI signal injection attacks against analog sensors. In *2013 IEEE Symposium on Security and Privacy*, pages 145–159, May 2013. doi: 10.1109/SP.2013.20.
- C. Lange and M. Leone. Broadband circuit model for electromagnetic-interference analysis in metallic enclosures. *IEEE Transactions on Electromagnetic Compatibility*, PP(99):1–8, 2017. ISSN 0018-9375. doi: 10.1109/TEMPC.2017.2709079.
- R. S. Langley and V. Cotoni. The ensemble statistics of the vibrational energy density of a random system subjected to single point harmonic excitation. *The Journal of the Acoustical Society of America*, 118(5):3064–3076, 2005. doi: 10.1121/1.2046827. URL <https://doi.org/10.1121/1.2046827>.
- D. Lecointe, W. Tabbara, and J. L. Lasserre. Aperture coupling of electromagnetic energy to a wire inside a rectangular metallic cavity. In *IEEE Antennas and Propagation Society International Symposium 1992 Digest*, pages 1571–1574 vol.3, 1992. doi: 10.1109/APS.1992.221737.
- Dominique Lecointe. *Determination du couplage d’une onde electromagnetique avec un cable situe dans une cavite metallique*. PhD thesis, Université Pierre et Marie Curie Paris 6, 1995. URL <http://www.theses.fr/1995PA066137>. Thèse de doctorat dirigée par TABBARA, W. Sciences appliquées Paris 6 1995.
- Ho Seong Lee, Jong-Gwan Yook, and Kyohong Sim. An information recovery technique from radiated electromagnetic fields from display devices. In *2016 Asia-Pacific International Symposium on Electromagnetic Compatibility (APEMC)*, volume 01, pages 473–475, May 2016. doi: 10.1109/APEMC.2016.7522772.
- Christophe Lemoine. *Contribution à l’analyse statistique des mesures en chambre réverbérante à brassage de modes : Applications à la détermination de l’efficacité de brassage et de l’incertitude de mesure dans un contexte CEM et radiofréquence*. PhD thesis, Institut national des sciences appliquées de Rennes, 2008. URL <http://www.theses.fr/2008ISAR0007>. Thèse de doctorat dirigée par Drissi, M’hamed Électronique Rennes, INSA 2008.

- Harold Levine and Julian Schwinger. On the theory of electromagnetic wave diffraction by an aperture in an infinite plane conducting screen. *Communications on Pure and Applied Mathematics*, 3(4): 355–391, 1950.
- Bing-Hope Liu, David C. Chang, and MaMark T. *Eigenmodes and the composite quality factor of a reverberating chamber*. Number 1066. 1983.
- J Lopes Esteves, E Cottais, and C Kasmi. A ghost in your transmitter analyzing polyglot signals for physical layer covert channels detection. *Hardware. io, The Hague, The Netherlands*, 2017.
- Paolo Maistri, Regis Leveugle, Lilian Bossuet, Alain Aubert, Viktor Fischer, Bruno Robisson, Nicolas Moro, Philippe Maurine, Jean-Max Dutertre, and Mathieu Lisart. ElectroMagnetic Analysis and Fault Injection onto Secure Circuits. In *VLSI-SoC: Very Large Scale Integration - System-on-Chip*, Mexico, Mexico, October 2014. doi: 10.1109/VLSI-SoC.2014.7004182. URL <https://hal-emse.ccsd.cnrs.fr/emse-01099025>.
- D. Mansson, T. Nilsson, R. Thottappillil, and M. Backstrom. Propagation of uwb transients in low-voltage installation power cables. *IEEE Transactions on Electromagnetic Compatibility*, 49(3):585–592, Aug 2007. ISSN 1558-187X. doi: 10.1109/TEMPC.2007.902186.
- Michel Mardiguian. *Controlling Radiated Emissions by Design*. Springer International Publishing, 3 edition, 2014. ISBN 978-3-319-04770-6, 978-3-319-04771-3.
- Martin Marinov. TempestSDR. <https://github.com/martinmarinov/TempestSDR>, 2016. URL <https://github.com/martinmarinov/TempestSDR>. [Online; accessed 31-december-2019].
- F. Marliani and A. Ciccolella. Computationally efficient expressions of the dyadic green’s function for rectangular enclosures - abstract *. *Journal of Electromagnetic Waves and Applications*, 14(12):1635–1636, 2000. doi: 10.1163/156939300X00428. URL <https://doi.org/10.1163/156939300X00428>.
- Madan Lal Mehta. *Random Matrices, 3rd Edition*, volume 142. Elsevier, 2004. URL <http://store.elsevier.com/Random-Matrices/Madan-Lal-Mehta/isbn-9780120884094/>.
- Steven P. Millard. *EnvStats: An R Package for Environmental Statistics*. Springer-Verlag New York, 2 edition, 2013.
- Brian S Mitchell. *Appendix 8: Electrical Conductivity of Selected Materials*, pages 893–899. John Wiley & Sons, Ltd, 2004. ISBN 9780471473350. doi: 10.1002/0471473359.app8. URL <https://onlinelibrary.wiley.com/doi/abs/10.1002/0471473359.app8>.
- Nicolas Moro, Amine Dehbaoui, Karine Heydemann, Bruno Robisson, and Emmanuelle Encrenaz. Electromagnetic fault injection: towards a fault model on a 32-bit microcontroller. In *2013 Workshop on Fault Diagnosis and Tolerance in Cryptography*, pages 77–88. IEEE, 2013.
- E. Newman. The equivalent separation(s) for the self-impedance of thin strips. *IEEE Transactions on Antennas and Propagation*, 35(1):110–113, January 1987. ISSN 0018-926X. doi: 10.1109/TAP.1987.1143976.
- Myun-Joo Park, Jongkuk Park, and Sangwook Nam. Efficient calculation of the green’s function for the rectangular cavity. *IEEE Microwave and Guided Wave Letters*, 8(3):124–126, 1998. ISSN 1051-8207. doi: 10.1109/75.661136.
- Y. M. Park, Y. Lee, J. So, C. Cheon, Y. S. Chung, and H. K. Jung. Electromagnetic topology combined with mode matching for the electromagnetic field penetration analysis of an aperture backed cavity. In *2009 IEEE International Symposium on Electromagnetic Compatibility*, pages 121–126, 2009. doi: 10.1109/ISEMC.2009.5284664.

- S. L. Parker, I. D. Flintoft, A. C. Marvin, J. F. Dawson, S. J. Bale, M. P. Robinson, M. Ye, C. Wan, and M. Zhang. Changes in a printed circuit board's absorption cross section due to proximity to walls in a reverberant environment. In *2016 IEEE International Symposium on Electromagnetic Compatibility (EMC)*, pages 818–823, 2016a. doi: 10.1109/ISEMC.2016.7571755.
- S. L. Parker, I. D. Flintoft, A. C. Marvin, J. F. Dawson, S. J. Bale, M. P. Robinson, M. Ye, C. Wan, and M. Zhang. Predicting shielding effectiveness of populated enclosures using absorption cross section of PCBs. In *2016 International Symposium on Electromagnetic Compatibility - EMC EUROPE*, pages 324–328, 2016b. doi: 10.1109/EMCEurope.2016.7739305.
- S. L. Parker, I. D. Flintoft, A. C. Marvin, J. F. Dawson, S. J. Bale, M. P. Robinson, Ming Ye, Changyong Wan, and Mengze Zhang. Absorption cross section measurement of stacked PCBs in a reverberation chamber. In *2016 Asia-Pacific International Symposium on Electromagnetic Compatibility (APEMC)*, volume 01, pages 991–993, 2016c. doi: 10.1109/APEMC.2016.7522925.
- Jean-Jacques Quisquater and David Samyde. Electromagnetic analysis (ema): Measures and counter-measures for smart cards. In Isabelle Attali and Thomas Jensen, editors, *Smart Card Programming and Security*, pages 200–210, Berlin, Heidelberg, 2001. Springer Berlin Heidelberg. ISBN 978-3-540-45418-2.
- R Core Team. *R: A Language and Environment for Statistical Computing*. R Foundation for Statistical Computing, Vienna, Austria, 2018. URL <https://www.R-project.org/>.
- A. Rabat, P. Bonnet, K. E. K. Drissi, and S. Girard. Analytical models for electromagnetic coupling of an open metallic shield containing a loaded wire. *IEEE Transactions on Electromagnetic Compatibility*, 59(5):1634–1637, Oct 2017. ISSN 1558-187X. doi: 10.1109/TEMC.2017.2661579.
- A. Rabat, P. Bonnet, K. E. K. Drissi, and S. Girard. Analytical formulation for shielding effectiveness of a lossy enclosure containing apertures. *IEEE Transactions on Electromagnetic Compatibility*, 60(5):1384–1392, Oct 2018. ISSN 1558-187X. doi: 10.1109/TEMC.2017.2764327.
- F. Rachidi. A review of field-to-transmission line coupling models with special emphasis to lightning-induced voltages on overhead lines. *IEEE Transactions on Electromagnetic Compatibility*, 54(4): 898–911, 2012. ISSN 0018-9375. doi: 10.1109/TEMC.2011.2181519.
- S. Radu, F. Solorzano, and J. Poore. EMI problems in video frame buffers design. In *Electromagnetic Compatibility, 2003 IEEE International Symposium on*, volume 1, pages 388–393 vol.1, Aug 2003. doi: 10.1109/ISEMC.2003.1236627.
- A. Richter. *Playing Billiards with Microwaves — Quantum Manifestations of Classical Chaos*, pages 479–523. Springer New York, New York, NY, 1999. ISBN 978-1-4612-1544-8. doi: 10.1007/978-1-4612-1544-8_20. URL https://doi.org/10.1007/978-1-4612-1544-8_20.
- Pierre-Michel Ricordel and Emmanuel Duponchelle. Risques associés aux signaux parasites compromettants: le cas des câbles dvi et hdmi. In *Sur la sécurité des Technologies de l'Information et des Communications (SSTIC)*, 2018.
- M. P. Robinson, J. D. Turner, D. W. P. Thomas, J. F. Dawson, M. D. Ganley, A. C. Marvin, S. J. Porter, T. M. Benson, and C. Christopoulos. Shielding effectiveness of a rectangular enclosure with a rectangular aperture. *Electronics Letters*, 32(17):1559–1560, 1996. ISSN 0013-5194. doi: 10.1049/el:19961030.

- M. P. Robinson, T. M. Benson, C. Christopoulos, J. F. Dawson, M. D. Ganley, A. C. Marvin, S. J. Porter, and D. W. P. Thomas. Analytical formulation for the shielding effectiveness of enclosures with apertures. *IEEE Transactions on Electromagnetic Compatibility*, 40(3):240–248, 1998. ISSN 0018-9375. doi: 10.1109/15.709422.
- Frank Sabath. Classification of electromagnetic effects at system level. In *Ultra-Wideband, Short Pulse Electromagnetics 9*, pages 325–333. Springer, 2010. URL http://link.springer.com/chapter/10.1007/978-0-387-77845-7_38.
- D. B. Seidel. Aperture excitation of a wire in a rectangular cavity. *IEEE Transactions on Microwave Theory and Techniques*, 26(11):908–914, 1978. ISSN 0018-9480. doi: 10.1109/TMTT.1978.1129513.
- Jayaprakash Selvaraj. Intentional electromagnetic interference attack on sensors and actuators. 2018.
- J. Shim, D. G. Kam, J. H. Kwon, and J. Kim. Circuit modeling and measurement of shielding effectiveness against oblique incident plane wave on apertures in multiple sides of rectangular enclosure. *IEEE Transactions on Electromagnetic Compatibility*, 52(3):566–577, Aug 2010. ISSN 1558-187X. doi: 10.1109/TEMPC.2009.2039483.
- Eng Swee Siah, K. Sertel, J. L. Volakis, V. V. Liepa, and R. Wiese. Coupling studies and shielding techniques for electromagnetic penetration through apertures on complex cavities and vehicular platforms. *IEEE Transactions on Electromagnetic Compatibility*, 45(2):245–257, 2003. ISSN 0018-9375. doi: 10.1109/TEMPC.2003.810814.
- Sergei P Skorobogatov and Ross J Anderson. Optical fault induction attacks. In *International workshop on cryptographic hardware and embedded systems*, pages 2–12. Springer, 2002.
- Paul So, Steven M. Anlage, Edward Ott, and Robert N. Oerter. Wave chaos experiments with and without time reversal symmetry: GUE and GOE statistics. *Physical Review Letters*, 74(14):2662–2665, apr 1995. doi: 10.1103/physrevlett.74.2662. URL <https://doi.org/10.1103/physrevlett.74.2662>.
- G. Spadacini, S. A. Pignari, and F. Marliani. Closed-form transmission line model for radiated susceptibility in metallic enclosures. *IEEE Transactions on Electromagnetic Compatibility*, 47(4):701–708, Nov 2005. ISSN 1558-187X. doi: 10.1109/TEMPC.2005.857875.
- J. Stein, H.-J. Stöckmann, and U. Stoffregen. Microwave studies of billiard green functions and propagators. *Phys. Rev. Lett.*, 75:53–56, Jul 1995. doi: 10.1103/PhysRevLett.75.53. URL <https://link.aps.org/doi/10.1103/PhysRevLett.75.53>.
- Hans-Jürgen Stöckmann. *Quantum chaos: An introduction*. Cambridge University Press, illustrated edition edition, 1999.
- G. B. Tait, R. E. Richardson, M. B. Slocum, M. O. Hatfield, and M. J. Rodriguez. Reverberant microwave propagation in coupled complex cavities. *IEEE Transactions on Electromagnetic Compatibility*, 53(1):229–232, 2011. ISSN 0018-9375. doi: 10.1109/TEMPC.2010.2051442.
- C. Taylor, R. Satterwhite, and C. Harrison. The response of a terminated two-wire transmission line excited by a nonuniform electromagnetic field. *IEEE Transactions on Antennas and Propagation*, 13(6):987–989, 1965. ISSN 0018-926X. doi: 10.1109/TAP.1965.1138574.
- Erik Thiele. Tempest for Eliza. <http://www.erikyyy.de/tempest/>, 2001. URL <http://www.erikyyy.de/tempest/>. [Online; accessed 31-december-2019].

- Adrian Thillard. *Countermeasures to side-channel attacks and secure multi-party computation*. PhD thesis, 2016. URL <http://www.theses.fr/2016PSLEE053>. Thèse de doctorat dirigée par Prouff, Emmanuel et Vergnaud, Damien Informatique Paris Sciences et Lettres 2016.
- Niek Timmers, Albert Spruyt, and Marc Witterman. Controlling pc on arm using fault injection. In *2016 Workshop on Fault Diagnosis and Tolerance in Cryptography (FDTC)*, pages 25–35. IEEE, 2016.
- S. V. Tkachenko, R. Rambousky, and J. B. Nitsch. Electromagnetic field coupling to a thin wire located symmetrically inside a rectangular enclosure. *IEEE Transactions on Electromagnetic Compatibility*, 55(2):334–341, April 2013. ISSN 1558-187X. doi: 10.1109/TEMPC.2012.2216532.
- S. van de Beek, R. Vogt-Ardatjew, and F. Leferink. Intentional electromagnetic interference through saturation of the RF front end. In *2015 Asia-Pacific Symposium on Electromagnetic Compatibility (APEMC)*, pages 132–135, 2015. doi: 10.1109/APEMC.2015.7175304.
- Wim Van Eck. Electromagnetic radiation from video display units: An eavesdropping risk? *Computers & Security*, 4(4):269–286, 1985. ISSN 0167-4048.
- NG Van Kampen and François Lurçat. Causalité et relations de kramers-kronig. *J. Phys. Radium*, 22(3):179–191, 1961.
- Alexander Vogt. *Analysis of electromagnetic interference in server casings*. PhD thesis, Technical University of Hamburg, Germany, 2016. URL <http://d-nb.info/1107059844>.
- Alexander Vogt, Heinz-D Brüns, Qi Wu, Frank Gronwald, and Christian Schuster. A measurement setup for quantification of electromagnetic interference in metallic casings. *IEEE Transactions on Electromagnetic Compatibility*, 57(6):1354–1364, 2015. ISSN 0018-9375. doi: 10.1109/TEMPC.2015.2452295.
- Martin Vuagnoux and Sylvain Pasini. Compromising electromagnetic emanations of wired and wireless keyboards. In *USENIX security symposium*, pages 1–16, 2009. URL http://static.usenix.org/event/sec09/tech/full_papers/sec09_attacks.pdf.
- Matt P Wand and M Chris Jones. *Kernel smoothing*. Chapman and Hall/CRC, 1994.
- Harald Welte. OsmocomBB-a tool for GSM protocol level security. In *Sur la sécurité des Technologies de l'Information et des Communications (SSTIC)*, 2010.
- John Wishart. The generalised product moment distribution in samples from a normal multivariate population. *Biometrika*, 20A(1/2):32, jul 1928. doi: 10.2307/2331939. URL <https://doi.org/10.2307/2331939>.
- Wolfram Research, Inc. Mathematica, Version 11.3, 2018. Champaign, IL, 2018.
- D. I. Wu and D. C. Chang. A hybrid representation of the green’s function in an overmoded rectangular cavity. *IEEE Transactions on Microwave Theory and Techniques*, 36(9):1334–1342, Sep. 1988. ISSN 1557-9670. doi: 10.1109/22.3680.
- P. Xiao, P. A. Du, D. Ren, and B. L. Nie. A hybrid method for calculating the coupling to PCB inside a nested shielding enclosure based on electromagnetic topology. *IEEE Transactions on Electromagnetic Compatibility*, 58(6):1701–1709, 2016. ISSN 0018-9375. doi: 10.1109/TEMPC.2016.2588505.
- M. Yin and P. Du. An improved circuit model for the prediction of the shielding effectiveness and resonances of an enclosure with apertures. *IEEE Transactions on Electromagnetic Compatibility*, 58(2):448–456, April 2016. ISSN 1558-187X. doi: 10.1109/TEMPC.2016.2517163.

- Youqian Zhang and Kasper Rasmussen. Detection of electromagnetic interference attacks on sensor systems. In *IEEE Symposium on Security and Privacy (S&P)*, May 2020.
- Xing Zheng. *Statistics of impedance and scattering matrices in microwave chaotic cavities: the random coupling model*. phdthesis, 2005. URL <http://drum.lib.umd.edu/handle/1903/2920>.
- Xing Zheng, Thomas M. Antonsen, and Edward Ott. Statistics of impedance and scattering matrices of chaotic microwave cavities with multiple ports. *Electromagnetics*, 26(1):37–55, 2006a. URL <http://www.tandfonline.com/doi/abs/10.1080/02726340500214902>.
- Xing Zheng, Thomas M Antonsen, and Edward Ott. Statistics of impedance and scattering matrices in chaotic microwave cavities: Single channel case. *Electromagnetics*, 26(1):3–35, 2006b.

Part IV

Appendix

Appendix A

Tables of the mock-up deformations

Mode	f_{mnp}	f_0	f_1	δ_{f_1}	f_2	δ_{f_2}	f_3	δ_{f_3}	f_4	δ_{f_4}
011	506.80	506.45	507.49	-2.06‰	508.51	-4.08‰	509.52	-6.07‰	510.51	-8.03‰
021	778.14	777.60	778.22	-0.79‰	778.83	-1.58‰	779.43	-2.36‰	780.04	-3.13‰
012	823.84	823.27	823.87	-0.72‰	824.45	-1.43‰	825.04	-2.14‰	825.61	-2.84‰
110	945.92	945.27	939.67	5.92‰	934.09	11.82‰	928.55	17.69‰	923.03	23.53‰
101	958.73	958.07	952.55	5.77‰	947.04	11.52‰	941.55	17.24‰	936.09	22.94‰
022	1013.6	1012.9	1013.2	-0.31‰	1009.6	3.26‰	1006.0	6.83‰	1002.4	10.39‰
111	1017.5	1016.8	1013.3	3.45‰	1011.7	5.08‰	1009.1	7.61‰	1006.5	10.14‰
111	1017.5	1016.8	1014.3	2.54‰	1013.8	3.03‰	1014.2	2.60‰	1014.6	2.18‰
031	1089.3	1088.6	1089.0	-0.39‰	1089.4	-0.78‰	1089.8	-1.17‰	1090.2	-1.54‰
120	1115.1	1114.3	1110.4	3.52‰	1106.5	7.02‰	1102.6	10.51‰	1098.7	13.98‰

Table A.1 – 20 first eigenfrequencies (in MHz) of the cavity with deformations on the right and left sides from 1 to 4 mm. f_{mnp} is the theoretical eigenfrequency computed from equation (II.1.2). δ_{f_r} was computed as $\delta_{f_r} = \frac{f_0 - f_i}{f_0}$, where f_0 is the eigenfrequency without any deformation computed from the eigenmode solver.

Mode	f_5	δ_{f_5}	f_6	δ_{f_6}	f_7	δ_{f_7}	f_8	δ_{f_8}	f_9	δ_{f_9}
011	511.49	-9.95‰	512.45	-11.85‰	513.39	-13.71‰	514.32	-15.55‰	515.24	-17.35‰
021	780.63	-3.90‰	781.22	-4.66‰	781.81	-5.41‰	782.39	-6.16‰	782.96	-6.89‰
012	826.18	-3.53‰	826.75	-4.22‰	827.31	-4.90‰	827.86	-5.57‰	828.41	-6.24‰
110	917.54	29.33‰	912.10	35.09‰	906.69	40.81‰	901.33	46.48‰	896.01	52.11‰
101	930.66	28.61‰	925.27	34.24‰	919.91	39.83‰	914.59	45.38‰	909.32	50.88‰
022	998.77	13.95‰	995.18	17.49‰	991.61	21.02‰	988.04	24.53‰	984.50	28.04‰
111	1004.0	12.66‰	1001.4	15.18‰	998.85	17.69‰	996.30	20.20‰	993.76	22.69‰
111	1015.0	1.76‰	1015.5	1.34‰	1015.9	0.92‰	1016.3	0.51‰	1016.7	0.10‰
031	1090.6	-1.91‰	1091.0	-2.27‰	1087.3	1.18‰	1083.5	4.64‰	1079.8	8.08‰
120	1094.9	17.43‰	1091.1	20.86‰	1091.4	20.55‰	1091.8	20.21‰	1092.2	19.87‰

Table A.2 – 20 first eigenfrequencies (in MHz) of the cavity with deformations on the right and left sides from 5 to 9 mm.

Mode	f_{mnp}	f_0	f_1	δ_{f_1}	f_2	δ_{f_2}	f_3	δ_{f_3}	f_4	δ_{f_4}
011	506.80	506.45	507.25	-1.59‰	508.07	-3.20‰	508.89	-4.82‰	509.72	-6.46‰
021	778.14	777.60	778.04	-0.56‰	778.47	-1.12‰	778.92	-1.69‰	779.36	-2.27‰
012	823.84	823.27	825.26	-2.41‰	827.25	-4.83‰	829.26	-7.27‰	831.29	-9.73‰
110	945.92	945.27	944.42	0.89‰	943.56	1.81‰	942.67	2.74‰	941.77	3.70‰
101	958.73	958.07	958.50	-0.45‰	958.93	-0.90‰	959.37	-1.35‰	959.81	-1.81‰
022	1013.6	1012.9	1014.2	-1.31‰	1014.2	-1.34‰	1012.9	-0.02‰	1011.6	1.31‰
111	1017.5	1016.8	1015.6	1.26‰	1015.6	1.25‰	1016.9	-0.08‰	1018.0	-1.12‰
111	1017.5	1016.8	1017.1	-0.28‰	1017.4	-0.55‰	1017.7	-0.83‰	1018.3	-1.42‰
031	1089.3	1088.6	1088.9	-0.27‰	1089.2	-0.55‰	1089.5	-0.83‰	1089.8	-1.11‰
120	1115.1	1114.3	1113.7	0.55‰	1113.1	1.11‰	1112.4	1.69‰	1111.8	2.29‰

Table A.3 – 20 first eigenfrequencies (in MHz) of the cavity with deformations on the top and bottom sides from 1 to 4 mm.

Mode	f_5	δ_{f_5}	f_6	δ_{f_6}	f_7	δ_{f_7}	f_8	δ_{f_8}	f_9	δ_{f_9}
011	510.55	-8.11‰	511.40	-9.78‰	512.25	-11.46‰	513.11	-13.15‰	513.97	-14.86‰
021	779.81	-2.85‰	780.27	-3.43‰	780.73	-4.02‰	781.20	-4.62‰	781.67	-5.23‰
012	833.32	-12.20‰	835.37	-14.69‰	837.43	-17.19‰	839.50	-19.71‰	841.59	-22.25‰
110	940.84	4.69‰	939.88	5.69‰	938.91	6.73‰	937.91	7.78‰	936.89	8.86‰
101	960.25	-2.28‰	960.70	-2.75‰	961.16	-3.22‰	961.61	-3.70‰	962.08	-4.18‰
022	1010.2	2.68‰	1008.8	4.06‰	1007.3	5.48‰	1005.9	6.91‰	1004.4	8.37‰
111	1018.3	-1.40‰	1018.6	-1.69‰	1018.9	-1.98‰	1019.2	-2.27‰	1019.5	-2.57‰
111	1019.7	-2.77‰	1021.0	-4.13‰	1022.4	-5.50‰	1023.8	-6.88‰	1025.2	-8.27‰
031	1090.1	-1.39‰	1090.4	-1.68‰	1090.7	-1.96‰	1091.0	-2.25‰	1091.3	-2.55‰
120	1111.1	2.91‰	1110.4	3.55‰	1109.6	4.20‰	1108.9	4.87‰	1108.1	5.56‰

Table A.4 – 20 first eigenfrequencies (in MHz) of the cavity with deformations on the top and bottom sides from 5 to 9 mm.

Appendix B

Admittance of an aperture

The instantaneous electric and magnetic fields may be written as:

$$\vec{\mathcal{E}}(x, y, z, t) = \Re[\vec{E}(x, y, z)e^{j\omega t}] = \Re[\vec{E}e^{j\omega t}] \quad (\text{B.1})$$

$$\vec{\mathcal{H}}(x, y, z, t) = \Re[\vec{H}(x, y, z)e^{j\omega t}] = \Re[\vec{H}e^{j\omega t}] \quad (\text{B.2})$$

Then, generalized MAXWELL's equations for time-harmonic electromagnetic fields in free space are [Balanis, 2012]:

$$\vec{\text{curl}}\vec{E} = -j\omega\mu_0\vec{H} - \vec{M} \quad (\text{B.3})$$

$$\vec{\text{curl}}\vec{H} = j\omega\epsilon_0\vec{E} + \vec{J} \quad (\text{B.4})$$

$$\text{div}\vec{E} = \frac{\rho_e}{\epsilon_0} \quad (\text{B.5})$$

$$\text{div}\vec{H} = \frac{\rho_m}{\mu_0} \quad (\text{B.6})$$

where:

- \vec{E} is the electric field intensity;
- \vec{H} is the magnetic field intensity;
- \vec{J} is the electric current density;
- \vec{M} is the magnetic current density;
- ρ_e is the electric charge density;
- ρ_m is the magnetic charge density.

The divergence of (B.4) gives:

$$\text{div } \vec{\text{curl}}\vec{H} = j\omega\epsilon_0\text{div } \vec{E} + \text{div}\vec{J} \quad (\text{B.7})$$

From vector analysis, if \vec{A} is a field vector, then:

$$\text{div } \vec{\text{curl}}\vec{A} = 0 \quad (\text{B.8})$$

Which leads to the electric charge conservation equation:

$$\text{div} \vec{J} + j\omega\epsilon_0 \text{div} \vec{E} = 0 \quad (\text{B.9})$$

$$\text{div} \vec{E} = \frac{\text{div} \vec{J}}{-j\omega\epsilon_0} = \frac{j \text{div} \vec{J}}{\omega\epsilon_0} \quad (\text{B.10})$$

Because of the symmetry of MAXWELL's equation, we also have:

$$\text{div} \vec{\text{curl}} \vec{E} = -j\omega\mu_0 \text{div} \vec{H} - \text{div} \vec{M} \quad (\text{B.11})$$

$$\text{div} \vec{H} = \frac{j \text{div} \vec{M}}{\omega\mu_0} \quad (\text{B.12})$$

We can then express the electric field \vec{E} from the electric current density \vec{J} and the magnetic current density \vec{M} :

$$\vec{\text{curl}} \vec{\text{curl}} \vec{E} = -j\omega\mu_0 \vec{\text{curl}} \vec{H} - \vec{\text{curl}} \vec{M} \quad (\text{B.13})$$

$$\overrightarrow{\text{grad}} \text{div} \vec{E} - \Delta \vec{E} = -j\omega\mu_0 j\omega\epsilon_0 \vec{E} - j\omega\mu_0 \vec{J} - \vec{\text{curl}} \vec{M} \quad (\text{B.14})$$

where:

$$k_0 = \frac{\omega}{c} = \omega\sqrt{\epsilon_0\mu_0} \quad (\text{B.15})$$

thus:

$$\overrightarrow{\text{grad}} \frac{j \text{div} \vec{J}}{\omega\epsilon_0} - \Delta \vec{E} = k_0^2 \vec{E} - j\omega\mu_0 \vec{J} - \vec{\text{curl}} \vec{M} \quad (\text{B.16})$$

$$(\Delta + k_0^2) \vec{E} = \overrightarrow{\text{grad}} \frac{j \text{div} \vec{J}}{\omega\epsilon_0} + j\omega\mu_0 \vec{J} + \vec{\text{curl}} \vec{M} \quad (\text{B.17})$$

And for the magnetic field \vec{H} :

$$\vec{\text{curl}} \vec{\text{curl}} \vec{H} = j\omega\epsilon_0 \vec{\text{curl}} \vec{E} + \vec{\text{curl}} \vec{J} \quad (\text{B.18})$$

$$\overrightarrow{\text{grad}} \text{div} \vec{H} - \Delta \vec{H} = -j\omega\epsilon_0 j\omega\mu_0 \vec{H} - j\omega\epsilon_0 \vec{M} + \vec{\text{curl}} \vec{J} \quad (\text{B.19})$$

$$\overrightarrow{\text{grad}} \frac{j \text{div} \vec{M}}{\omega\mu_0} - \Delta \vec{H} = k_0^2 \vec{H} - j\omega\epsilon_0 \vec{M} + \vec{\text{curl}} \vec{J} \quad (\text{B.20})$$

$$(\Delta + k_0^2) \vec{H} = \overrightarrow{\text{grad}} \frac{j \text{div} \vec{M}}{\omega\mu_0} + j\omega\epsilon_0 \vec{M} - \vec{\text{curl}} \vec{J} \quad (\text{B.21})$$

In our problem, there is no electric current density:

$$\vec{J} = \vec{0} \quad (\text{B.22})$$

Rearranging (B.21) gives:

$$(\Delta + k_0^2) \vec{H} = \frac{j}{\omega\mu_0} \left[\overrightarrow{\text{grad}} \text{div} \vec{M} + k_0^2 \vec{M} \right] \quad (\text{B.23})$$

We define the FOURIER transform of a function $f \in L_1(\mathbb{R}^3)$ as:

$$\tilde{f}(\xi_1, \xi_2, \xi_3) = \mathcal{F}(f)(\xi_1, \xi_2, \xi_3) = \int_{\mathbb{R}^3} f(x) e^{-j(\sum_{i=1}^3 x_i \xi_i)} d^3x \quad (\text{B.24})$$

with the following property:

$$\mathcal{F}\left(\frac{\partial f}{\partial x_i}\right)(\xi_1, \xi_2, \xi_3) = j\xi_i \tilde{f}(\xi_1, \xi_2, \xi_3) \quad (\text{B.25})$$

If $\mathcal{F}(A(x, y, z)) = \tilde{A}(k_x, k_y, k_z)$, then

$$\mathcal{F}\left(\frac{\partial A}{\partial x}\right) = jk_x \tilde{A} \quad (\text{B.26})$$

Then, we can express $\Delta \vec{H}$, from k_x , k_y and k_z .

$$\Delta \vec{H} = \nabla^2 H_x \vec{e}_x + \nabla^2 H_y \vec{e}_y + \nabla^2 H_z \vec{e}_z \quad (\text{B.27})$$

$$\mathcal{F}(\Delta \vec{H}|_x) = -k_x^2 \tilde{H}_x - k_y^2 \tilde{H}_x - k_z^2 \tilde{H}_x = -(k_x^2 + k_y^2 + k_z^2) \tilde{H}_x \quad (\text{B.28})$$

$$\mathcal{F}(\Delta \vec{H}|_y) = -(k_x^2 + k_y^2 + k_z^2) \tilde{H}_y \quad (\text{B.29})$$

$$\mathcal{F}(\Delta \vec{H}|_z) = -(k_x^2 + k_y^2 + k_z^2) \tilde{H}_z \quad (\text{B.30})$$

$$\mathcal{F}(\Delta \vec{H}) = -(k_x^2 + k_y^2 + k_z^2)(\tilde{H}_x \vec{e}_x + \tilde{H}_y \vec{e}_y + \tilde{H}_z \vec{e}_z) \quad (\text{B.31})$$

Assuming that $k^2 = k_x^2 + k_y^2 + k_z^2$, we have:

$$\mathcal{F}(\Delta \vec{H}) = -k^2 \vec{H} \quad (\text{B.32})$$

Thus, the FOURIER transform of equation (B.23) gives:

$$(k_0^2 - k^2) \vec{H} = \frac{j}{\omega \mu_0} [\overrightarrow{\text{grad}} \text{div} \vec{M} + k_0^2 \vec{M}] \quad (\text{B.33})$$

$\mathcal{F}(\overrightarrow{\text{grad}} \text{div} \vec{M})$, may be expressed as a product of a matrix by a vector $\vec{M} = [\tilde{M}_x, \tilde{M}_y, \tilde{M}_z]^T$:

$$\text{div} \vec{M} = \frac{\partial M_x}{\partial x} + \frac{\partial M_y}{\partial y} + \frac{\partial M_z}{\partial z} \quad (\text{B.34})$$

$$\mathcal{F}(\text{div} \vec{M}) = jk_x \tilde{M}_x + jk_y \tilde{M}_y + jk_z \tilde{M}_z \quad (\text{B.35})$$

$$\overrightarrow{\text{grad}} [\text{div} \vec{M}]_x = \frac{\partial \text{div} \vec{M}}{\partial x} \vec{e}_x = \left(\frac{\partial^2 M_x}{\partial x^2} + \frac{\partial^2 M_x}{\partial x \partial y} + \frac{\partial^2 M_x}{\partial x \partial z} \right) \vec{e}_x \quad (\text{B.36})$$

$$\overrightarrow{\text{grad}} [\text{div} \vec{M}]_y = \frac{\partial \text{div} \vec{M}}{\partial y} \vec{e}_y = \left(\frac{\partial^2 M_y}{\partial x^2} + \frac{\partial^2 M_y}{\partial x \partial y} + \frac{\partial^2 M_y}{\partial x \partial z} \right) \vec{e}_y \quad (\text{B.37})$$

$$\overrightarrow{\text{grad}} [\text{div} \vec{M}]_z = \frac{\partial \text{div} \vec{M}}{\partial z} \vec{e}_z = \left(\frac{\partial^2 M_z}{\partial x^2} + \frac{\partial^2 M_z}{\partial x \partial y} + \frac{\partial^2 M_z}{\partial x \partial z} \right) \vec{e}_z \quad (\text{B.38})$$

At the end, by taking the FOURIER transform of equations (B.36) to (B.38), we obtain:

$$\mathcal{F}(\overrightarrow{\text{grad}} \text{div} \vec{M}) = - \begin{pmatrix} k_x^2 & k_x k_y & k_x k_z \\ k_x k_y & k_y^2 & k_y k_z \\ k_x k_z & k_y k_z & k_z^2 \end{pmatrix} \vec{M} \quad (\text{B.39})$$

Thus, equation (B.33) becomes:

$$(k_0^2 - k^2) \vec{H} = \frac{j}{\omega \mu_0} \begin{pmatrix} k_0^2 - k_x^2 & -k_x k_y & -k_x k_z \\ -k_x k_y & k_0^2 - k_y^2 & -k_y k_z \\ -k_x k_z & -k_y k_z & k_0^2 - k_z^2 \end{pmatrix} \vec{M} \quad (\text{B.40})$$

From the surface equivalence theorem (HUYGENS's principle), we can replace the field at the aperture by a magnetic current density:

$$\vec{M} = 2\vec{e}_z \wedge \vec{E}_t \delta_S \quad (\text{B.41})$$

where S described the surface of the aperture (Figure III.2.2), and e_s is a basis of modes.

Thus :

$$\vec{M} = 2\vec{e}_z \wedge \sum_s V_s \vec{e}_s(\vec{x}_\perp) \delta_S \quad (\text{B.42})$$

As the modes have only orthogonal components, we can write:

$$\vec{e}_s = e_{sx} \vec{e}_x + e_{sy} \vec{e}_y \quad (\text{B.43})$$

$$\tilde{\vec{e}}_s = \tilde{e}_{sx} \vec{e}_x + \tilde{e}_{sy} \vec{e}_y \quad (\text{B.44})$$

Thus:

$$\vec{M} = 2\vec{e}_z \wedge \sum_s V_s (\tilde{e}_{sx} \vec{e}_x + \tilde{e}_{sy} \vec{e}_y) = 2 \sum_s V_s (\tilde{e}_{sx} \vec{e}_y - \tilde{e}_{sy} \vec{e}_x) \quad (\text{B.45})$$

$$\tilde{M}_x = -2 \sum_s V_s \tilde{e}_{sy} \quad (\text{B.46})$$

$$\tilde{M}_y = 2 \sum_s V_s \tilde{e}_{sx} \quad (\text{B.47})$$

$$\tilde{M}_z = 0 \quad (\text{B.48})$$

By inserting the components of \vec{M} in (B.40) as:

$$\vec{H} = \frac{j}{\omega \mu_0 (k_0^2 - k^2)} \begin{pmatrix} k_0^2 - k_x^2 & -k_x k_y & -k_x k_z \\ -k_x k_y & k_0^2 - k_y^2 & -k_y k_z \\ -k_x k_z & -k_y k_z & k_0^2 - k_z^2 \end{pmatrix} \begin{pmatrix} -2 \sum_s V_s \tilde{e}_{sy} \\ 2 \sum_s V_s \tilde{e}_{sx} \\ 0 \end{pmatrix} \quad (\text{B.49})$$

We can also write the orthogonal components \vec{H}_\perp of \vec{H} as (see equation (III.2.10)):

$$\vec{H}_\perp = \tilde{H}_x \vec{e}_x + \tilde{H}_y \vec{e}_y = \sum_s I_s \vec{e}_z \wedge \vec{e}_s = \sum_s I_s \vec{e}_z \wedge (\tilde{e}_{sx} \vec{e}_x + \tilde{e}_{sy} \vec{e}_y) \quad (\text{B.50})$$

$$\tilde{H}_x = - \sum_s I_s \tilde{e}_{sy} \quad (\text{B.51})$$

$$\tilde{H}_y = \sum_s I_s \tilde{e}_{sx} \quad (\text{B.52})$$

Thus:

$$\sum_s I_s \tilde{e}_{sy} = \frac{2j}{\omega \mu_0 (k_0^2 - k^2)} \left[(k_0^2 - k_x^2) \sum_s V_s \tilde{e}_{sy} + k_y k_x \sum_s V_s \tilde{e}_{sx} \right] \quad (\text{B.53})$$

$$\sum_s I_s \tilde{e}_{sx} = \frac{2j}{\omega \mu_0 (k_0^2 - k^2)} \left[k_x k_y \sum_s V_s \tilde{e}_{sy} + (k_0^2 - k_y^2) \sum_s V_s \tilde{e}_{sx} \right] \quad (\text{B.54})$$

Leading to:

$$\sum_s I_s \vec{e}_s = \frac{2j}{\omega \mu_0 (k_0^2 - k^2)} \begin{pmatrix} k_0^2 - k_y^2 & k_x k_y \\ k_x k_y & k_0^2 - k_x^2 \end{pmatrix} \sum_s V_s \vec{e}_s \quad (\text{B.55})$$

We want to find an admittance $Y_{s's}^{\text{rad}}$, expressed as $I_{s'} = \sum_s Y_{s's}^{\text{rad}} V_s$. We take the inverse 3D FOURIER transform of (B.55):

$$\sum_s I_s \vec{e}_s = \frac{1}{(2\pi)^3} \int_{\mathbb{R}^3} \frac{2j}{\omega \mu_0 (k_0^2 - k^2)} \begin{pmatrix} k_0^2 - k_y^2 & k_x k_y \\ k_x k_y & k_0^2 - k_x^2 \end{pmatrix} \sum_s V_s \vec{e}_s e^{j\vec{k} \cdot \vec{x}_\perp} d^3 k \quad (\text{B.56})$$

We then define the inner product between two modes as:

$$\langle \vec{e}_s, \vec{e}_{s'} \rangle = \int_{\text{aperture}} \vec{e}_s \vec{e}_{s'}^* dx dy \quad (\text{B.57})$$

in space, and in the FOURIER basis:

$$\langle \vec{e}_s, \vec{e}_{s'} \rangle = \int_{\mathbb{R}^2} \vec{e}_s \vec{e}_{s'}^* dk_x dk_y \quad (\text{B.58})$$

At $z = 0$, $\vec{x} = \vec{x}_\perp$, after projecting onto $\vec{e}_{s'}^*$, we have:

$$I_{s'} = \int_{\mathbb{R}^2} \vec{e}_{s'}^* \left(\frac{1}{(2\pi)^3} \int_{\mathbb{R}^3} \frac{2j}{\omega \mu_0 (k_0^2 - k^2)} \begin{pmatrix} k_0^2 - k_y^2 & k_x k_y \\ k_x k_y & k_0^2 - k_x^2 \end{pmatrix} \sum_s V_s \vec{e}_s e^{j\vec{k} \cdot \vec{x}_\perp} d^3 k \right) dx dy \quad (\text{B.59})$$

Thanks to FUBINI, we can switch the integration of the inner product and the integration of the inverse FOURIER transform:

$$I_{s'} = \int_{\mathbb{R}^3} \frac{2j}{\omega\mu_0(k_0^2 - k^2)} \left(\frac{1}{(2\pi)^3} \sum_s V_s \vec{e}_s \begin{pmatrix} k_0^2 - k_y^2 & k_x k_y \\ k_x k_y & k_0^2 - k_x^2 \end{pmatrix} \int_{\mathbb{R}^2} \vec{e}_{s'}^* e^{j\vec{k} \cdot \vec{x}_\perp} dx dy \right) d^3k \quad (\text{B.60})$$

We can notice that:

$$\int_{\mathbb{R}^2} \vec{e}_{s'}^* e^{j\vec{k} \cdot \vec{x}_\perp} dx dy = \left(\int_{\mathbb{R}^2} \vec{e}_{s'} e^{-j\vec{k} \cdot \vec{x}_\perp} dx dy \right)^* = \vec{e}_{s'}^* \quad (\text{B.61})$$

Thus:

$$I_{s'} = \int_{\mathbb{R}^3} \frac{2j}{\omega\mu_0(k_0^2 - k^2)} \left(\frac{1}{(2\pi)^3} \sum_s V_s \vec{e}_s \begin{pmatrix} k_0^2 - k_y^2 & k_x k_y \\ k_x k_y & k_0^2 - k_x^2 \end{pmatrix} \vec{e}_{s'}^* \right) d^3k \quad (\text{B.62})$$

$$= \sum_s V_s \int_{\mathbb{R}^3} \frac{2j}{\omega\mu_0(k_0^2 - k^2)} \left(\frac{1}{(2\pi)^3} \vec{e}_s \begin{pmatrix} k_0^2 - k_y^2 & k_x k_y \\ k_x k_y & k_0^2 - k_x^2 \end{pmatrix} \vec{e}_{s'}^* \right) d^3k \quad (\text{B.63})$$

$$= \sum_s V_s Y_{s's}^{\text{rad}} \quad (\text{B.64})$$

And we finally have the expression of the admittance of the aperture:

$$Y_{s's}^{\text{rad}} = \int_{\mathbb{R}^3} \frac{2j}{\omega\mu_0(k_0^2 - k^2)} \left(\frac{1}{(2\pi)^3} \vec{e}_s \begin{pmatrix} k_0^2 - k_y^2 & k_x k_y \\ k_x k_y & k_0^2 - k_x^2 \end{pmatrix} \vec{e}_{s'}^* \right) d^3k \quad (\text{B.65})$$

$$= \frac{2j}{\omega\mu_0(2\pi)^3} \int_{\mathbb{R}^3} \frac{1}{(k_0^2 - k^2)} \left(\vec{e}_s \begin{pmatrix} k_0^2 - k_y^2 & k_x k_y \\ k_x k_y & k_0^2 - k_x^2 \end{pmatrix} \vec{e}_{s'}^* \right) d^3k \quad (\text{B.66})$$

with:

$$\frac{1}{\omega\mu_0} = \frac{1}{\eta_0 k_0} = \sqrt{\frac{\epsilon_0}{\mu_0}} \frac{1}{k_0} \quad (\text{B.67})$$

Appendix C

Derivation of the Random coupling model

Contents

C.1	Introduction	189
C.2	Derivation of the RCM in two dimensions	189
C.3	Statistical representation	191
C.4	Radiation impedance as a deterministic quantity	193
C.5	Generalisation to the multiple port case	195
C.5.1	Deterministic approach	195
C.5.2	Statistical approach	195

C.1 Introduction

This appendix is relative to the derivation of the [random coupling model \(RCM\)](#). At first the RCM was set for 2D cavities in [Zheng, 2005], then the results were generalized for 3D cavities in [Hemmady, 2006]. We will briefly remind the calculation steps that were well exposed in these two references. Some additional details will be given for these succinctly described steps. We will only consider two dimension cavities here.

C.2 Derivation of the RCM in two dimensions

Let us consider a closed 2D cavity with several ports connected to it. The cavity consists of two plates spaced by a gap h . The cavity is sealed at its edges. The electric field is considered constant in the z direction $\vec{E}(x, y, z, t) = E_z(\vec{x}, t)\vec{e}_z$ with $\vec{x} = x\vec{e}_x + y\vec{e}_y$, and $\vec{B}(\vec{x}, t) = [B_x, B_y, 0]^T = \mu_0\vec{H}(\vec{x}, t)$. Thus, the voltage between the top and the bottom plates is $V_T(\vec{x}, t) = -hE_z(\vec{x}, t)$. The surface current density flowing on the plates is:

$$\vec{J}_s(\vec{x}, t) = \vec{H}(\vec{x}, t) \wedge \vec{e}_z \quad (\text{C.1})$$

and the surfacic charge density on the plates is:

$$\rho_s(\vec{x}, t) = -\epsilon_0 E_z(\vec{x}, t) \quad (\text{C.2})$$

Equation (C.1) can be expressed in terms of localized current sources as: $\vec{J}_s(\vec{x}, t) = \sum_i I_i(t) u_i(\vec{x}) \vec{e}_\perp$ (with $\vec{e}_z \cdot \vec{e}_\perp = 0$), where $u_i(\vec{x})$ describes the distribution of the current in the vicinity $((x - x_i)^2 + (y - y_i)^2 < l_i^2)$, where l_i is much smaller than the cavity dimensions) of the i -th port of the system.

This profile function is normalized such as: $\iint_{\mathbb{R}^2} u_i(\vec{x}) dxdy = 1$. In a single port system, we have $\vec{J}_s(\vec{x}, t) = I(t)u(\vec{x})\vec{e}_\perp$.

Applying the charge conservation equation to this system leads to:

$$\frac{\partial \rho_s(\vec{x}, t)}{\partial t} + \text{div}(\vec{J}_s(\vec{x}, t)) = I(t)u(\vec{x}) \quad (\text{C.3})$$

by time derivating (C.3), we obtain:

$$\frac{\partial^2 \rho_s(\vec{x}, t)}{\partial t^2} + \frac{\partial}{\partial t} \text{div}(\vec{J}_s(\vec{x}, t)) = \frac{\partial I(t)}{\partial t} u(\vec{x}) \quad (\text{C.4})$$

$$\frac{\partial^2}{\partial t^2} (-\epsilon_0 E_z(\vec{x}, t)) + \text{div} \left(\frac{\partial \vec{H}(\vec{x}, t)}{\partial t} \wedge \vec{e}_z \right) = \frac{\partial I(t)}{\partial t} u(\vec{x}) \quad (\text{C.5})$$

From the FARADAY's law we get:

$$\frac{\partial \vec{H}(\vec{x}, t)}{\partial t} = -\frac{1}{\mu_0} \overrightarrow{\text{curl}} \vec{E}(\vec{x}, t)$$

and from vector calculus:

$$\begin{aligned} \frac{\partial \vec{H}(\vec{x}, t)}{\partial t} \wedge \vec{e}_z &= -\frac{1}{\mu_0} \overrightarrow{\text{curl}} \vec{E}(\vec{x}, t) \wedge \vec{e}_z \\ &= -\frac{1}{\mu_0} \left((\vec{e}_z \cdot \text{div}) \vec{E}(\vec{x}, t) - \overrightarrow{\text{grad}}(\vec{E}(\vec{x}, t) \cdot \vec{e}_z) \right) \\ &= \frac{1}{\mu_0} \overrightarrow{\text{grad}} E_z(\vec{x}, t) \end{aligned}$$

thus:

$$\frac{\partial^2}{\partial t^2} (-\epsilon_0 E_z(\vec{x}, t)) + \frac{1}{\mu_0} \text{div} \overrightarrow{\text{grad}} E_z(\vec{x}, t) = \frac{\partial I(t)}{\partial t} u(\vec{x}) \quad (\text{C.6})$$

by multiplying by $h\mu_0$:

$$\frac{1}{c^2} \frac{\partial^2 V_T(\vec{x}, t)}{\partial t^2} - \nabla^2 V_T(\vec{x}, t) = h\mu_0 u(\vec{x}) \frac{\partial I(t)}{\partial t} \quad (\text{C.7})$$

Assuming that we have $I = \hat{I}e^{j\omega t}$ and $V_T = \hat{V}_T e^{j\omega t}$:

$$\begin{aligned} -\omega^2 \frac{1}{c^2} \hat{V}_T(\vec{x}) - \nabla^2 \hat{V}_T(\vec{x}) &= j\omega h\mu_0 u(\vec{x}) \hat{I} \\ (\nabla^2 + k^2) \hat{V}_T(\vec{x}) &= -jkh\eta_0 u(\vec{x}) \hat{I} \end{aligned} \quad (\text{C.8})$$

with $c^2 = \frac{1}{\mu_0 \epsilon_0}$, $k = \frac{\omega}{c}$ and $\eta_0 = \mu_0 c = 1/\epsilon_0 c = \sqrt{\mu_0/\epsilon_0}$.

One has now to define the port voltage $V(t)$, to be able to determine an impedance. $V(t)$ is given by:

$$V(t) = \iint_{\mathbb{R}^2} u(\vec{x}) V_T(\vec{x}, t) dxdy \quad (\text{C.9})$$

which correspond to the weighted average of $V_T(\vec{x}, t)$.

Then, $\hat{V}_T(\vec{x})$ may be expanded onto a basis of eigenfunctions of the closed cavity like:

$$\hat{V}_T = \sum_n c_n \phi_n(\vec{x}) \quad (\text{C.10})$$

With $(\nabla^2 + k_n^2)\phi_n(\vec{x}) = 0$, $\iint_{\mathbb{R}^2} \phi_i(\vec{x})\phi_j(\vec{x})dxdy = \delta_{ij}$ and $\phi_n(\vec{x}) = 0$ at the cavity boundaries. From equation (C.9), and with, $V = \hat{V}e^{j\omega t}$, we get:

$$\begin{aligned} \hat{V} &= \iint_{\mathbb{R}^2} u(\vec{x}) \sum_n c_n \phi_n(\vec{x})dxdy \\ &= \sum_n c_n \iint_{\mathbb{R}^2} u(\vec{x}) \phi_n(\vec{x})dxdy \\ &= \sum_n c_n \langle u(\vec{x}) \phi_n(\vec{x}) \rangle \end{aligned} \quad (\text{C.11})$$

By mutiplying (C.8) by $\phi_n(\vec{x})$ and integrating it with respect to x and y :

$$\begin{aligned} \iint_{\mathbb{R}^2} \phi_n(\vec{x})(\nabla^2 + k^2) \sum_m c_m \phi_m(\vec{x})dxdy &= -jkh\eta_0 \iint_{\mathbb{R}^2} u(\vec{x})\phi_n(\vec{x})\hat{I}dxdy \\ \sum_m c_m (-k_m^2 + k^2) \iint_{\mathbb{R}^2} \phi_n(\vec{x})\phi_m(\vec{x})dxdy &= -jkh\eta_0 \iint_{\mathbb{R}^2} u(\vec{x})\phi_n(\vec{x})\hat{I}dxdy \\ c_n (k^2 - k_n^2) &= -jkh\eta_0 \langle u(\vec{x})\phi_n(\vec{x}) \rangle \hat{I} \end{aligned} \quad (\text{C.12})$$

where $k_n = \frac{\omega_n}{c}$ is the wavenumber related to the mode $\phi_n(\vec{x})$. Then from (C.11) and (C.12):

$$\begin{aligned} \hat{V} &= \sum_n c_n \langle u(\vec{x})\phi_n(\vec{x}) \rangle \\ &= -j \sum_n \frac{kh\eta_0 \langle u(\vec{x})\phi_n(\vec{x}) \rangle^2}{k^2 - k_n^2} \hat{I} = Z\hat{I} \end{aligned} \quad (\text{C.13})$$

Which leads to a definition of the impedance for a two dimension cavity expressed as a sum over a high number of eigenmodes of the cavity.

$$Z = -j \sum_n \frac{kh\eta_0 \langle u(\vec{x})\phi_n(\vec{x}) \rangle^2}{k^2 - k_n^2} \quad (\text{C.14})$$

C.3 Statistical representation

The definition of the impedance given in (C.14) is deterministic. Indeed, the modes (wave numbers k_n^2 and eigenfunctions $\phi_n(\vec{x})$) need to be determined. This is not a trivial problem as it requires to fully know the geometry of the system as well as the materials. To circumvent this problem, the modes are replaced by random quantities.

The eigenfunctions of the cavity may be expressed as a random superposition of N plane waves (BERRY's hypothesis) as:

$$\phi_n(\vec{x}) \simeq \sum_{i=1}^N \frac{1}{\sqrt{N}} \alpha_i \exp(jk_n \vec{e}_i \cdot \vec{x} + j\beta_i) \quad (\text{C.15})$$

with:

$$\vec{k}_n = k_n \begin{pmatrix} \cos \theta_i \\ \sin \theta_i \end{pmatrix} = k_n \vec{e}_i \quad (\text{C.16})$$

where α_i , β_i and θ_i are random variables.

We will now determine the variance of $\langle u(\vec{x})\phi_n(\vec{x}) \rangle$. In equation (C.16), k_n is set to be known, but not θ_i which is taken to be uniformly distributed ($\theta_i \sim \mathcal{U}(0, 2\pi)$). From (C.15) we can compute $\langle u\phi_n \rangle$:

$$\sqrt{N}\langle u\phi_n \rangle = \iint_{\mathbb{R}^2} u(\vec{x})\phi_n(\vec{x})dxdy \quad (\text{C.17})$$

$$= \iint_{\mathbb{R}^2} u(\vec{x}) \left(\sum_{i=1}^N \alpha_i \exp(jk_n \vec{e}_i \cdot \vec{x} + j\beta_i) \right) dxdy \quad (\text{C.18})$$

$$= \sum_{i=1}^N \alpha_i \iint_{\mathbb{R}^2} u(\vec{x}) \exp(jk_n \vec{e}_i \cdot \vec{x} + j\beta_i) dxdy \quad (\text{C.19})$$

$$= \sum_{i=1}^N \alpha_i \tilde{u}^*(\vec{k}_n) e^{j\beta_i} \quad (\text{C.20})$$

where $\tilde{u}^*(\vec{k}_n) = \iint_{\mathbb{R}^2} u(\vec{x}) \exp(jk_n \vec{e}_i \cdot \vec{x} + j\beta_i) dxdy$ is the FOURIER transform of $u(\vec{x})$.

From the central limit theorem, the quantity $\langle u\phi_n \rangle$ is a gaussian random variable with a mean value of 0. Its variance needs now to be determined. As $\text{Var}[\langle u\phi_n \rangle] = \text{E}[\langle u\phi_n \rangle^2] = \text{E}[\langle u\phi_n \rangle \langle u\phi_n \rangle^*]$, we start to compute $\langle u\phi_n \rangle \langle u\phi_n \rangle^*$:

$$N\langle u\phi_n \rangle \langle u\phi_n \rangle^* = \left(\sum_{i=1}^N \alpha_i \tilde{u}^*(k_n \vec{e}_i) e^{j\beta_i} \right) \left(\sum_{k=1}^N \alpha_k \tilde{u}^*(k_n \vec{e}_k) e^{j\beta_k} \right)^* \quad (\text{C.21})$$

$$= \sum_{i=1}^N \alpha_i^2 \tilde{u}^*(k_n \vec{e}_i) \tilde{u}(k_n \vec{e}_i) e^{j\beta_i} e^{-j\beta_i} + \sum_{i=1}^N \alpha_i \tilde{u}^*(k_n \vec{e}_i) e^{j\beta_i} \left(\sum_{\substack{k=1 \\ k \neq i}}^N \alpha_k \tilde{u}(k_n \vec{e}_k) e^{-j\beta_k} \right) \quad (\text{C.22})$$

$$= \sum_{i=1}^N \alpha_i^2 |\tilde{u}^*(k_n \vec{e}_i)|^2 + \sum_{i=1}^N \sum_{\substack{k=1 \\ k \neq i}}^N \alpha_i \alpha_k \tilde{u}^*(k_n \vec{e}_i) \tilde{u}(k_n \vec{e}_k) e^{j(\beta_i - \beta_k)} \quad (\text{C.23})$$

Then the variance is derived (α_i , β_i and θ_i are now random variables):

$$\begin{aligned}
N\text{Var}[\langle u\phi_n \rangle] &= N \mathbb{E} [\langle u\phi_n \rangle^2] = N \mathbb{E} [\langle u\phi_n \rangle \langle u\phi_n \rangle^*] \\
&= \mathbb{E} \left[\sum_{i=1}^N \alpha_i^2 |\tilde{u}^*(k_n \vec{e}_i)|^2 + \sum_{i=1}^N \sum_{\substack{k=1 \\ k \neq j}}^N \alpha_i \alpha_k \tilde{u}^*(k_n \vec{e}_i) \tilde{u}(k_n \vec{e}_k) e^{j(\beta_i - \beta_k)} \right] \\
&= \mathbb{E} \left[\sum_{i=1}^N \alpha_i^2 |\tilde{u}^*(k_n \vec{e}_i)|^2 \right] + \mathbb{E} \left[\sum_{i=1}^N \sum_{\substack{k=1 \\ k \neq i}}^N \alpha_i \alpha_k \tilde{u}^*(k_n \vec{e}_i) \tilde{u}(k_n \vec{e}_k) e^{j(\beta_i - \beta_k)} \right] \\
&= \sum_{i=1}^N \mathbb{E} [\alpha_i^2] \mathbb{E} [|\tilde{u}^*(k_n \vec{e}_i)|^2] + \sum_{i=1}^N \sum_{\substack{k=1 \\ k \neq i}}^N \mathbb{E} [\alpha_i] \mathbb{E} [\alpha_k] \mathbb{E} [\tilde{u}^*(k_n \vec{e}_i) \tilde{u}(k_n \vec{e}_k)] \mathbb{E} [e^{j(\beta_i - \beta_k)}] \\
&\tag{C.24}
\end{aligned}$$

$$= \frac{1}{A} \sum_{i=1}^N \mathbb{E} [|\tilde{u}^*(k_n \vec{e}_i)|^2] \tag{C.25}$$

As θ_i is uniformly distributed (*i.e.* $\theta_i \sim \mathcal{U}(0, 2\pi)$), the probability density function of θ_i is $p_{\theta_j}(\theta_i) = \frac{1}{2\pi} 1_{[0, 2\pi]}(\theta_i)$, and the expectation of $|\tilde{u}^*(k_n \vec{e}_i)|^2$ is

$$\mathbb{E} [|\tilde{u}^*(k_n \vec{e}_i)|^2] = \int_0^{2\pi} \frac{1}{2\pi} |\tilde{u}^*(k_n \vec{e}_i)|^2 d\theta_i \tag{C.26}$$

By taking the limit when N tends to infinity, which corresponds to superposition of an infinity of plane waves, we get:

$$\text{Var} [\langle u\phi_n \rangle] = \frac{1}{NA} \sum_{i=1}^N \mathbb{E} [|\tilde{u}^*(k_n \vec{e}_i)|^2] \tag{C.27}$$

$$= \frac{1}{A} \int_0^{2\pi} \frac{1}{2\pi} |\tilde{u}^*(\vec{k}_n)|^2 d\theta \tag{C.28}$$

C.4 Radiation impedance as a deterministic quantity

The quantity $\langle u\phi_n \rangle^2$ is now fully determined, then it can be replaced by w_n^2 multiplied by a scaling factor as shown below. We take w_n to be a gaussian random variable with its mean equal to 0. This scaling factor corresponds to the free space impedance of the ports of the system. In [Zheng et al., 2006b], it is shown that the impedance cavity can take the following form:

$$\hat{V} = Z\hat{I} = -\frac{j}{\pi} \sum_n^{\infty} \Delta \frac{R_R(k_n) w_n^2}{k^2 - k_n^2} \hat{I} \tag{C.29}$$

where $\Delta = \frac{4\pi}{A}$, is the mean spacing between two consecutive eigenvalues, and

$$R_R(k) = \frac{kh\eta_0}{4} \int_0^{2\pi} |\tilde{u}^*(\vec{k}_n)|^2 d\theta \tag{C.30}$$

We can verify that, $kh\eta_0 \langle u\phi_n \rangle^2$ (equation (C.14)) and $\frac{1}{\pi} \Delta R_R(k_n) w_n^2$ (equation (C.29)) have the same variance.

We remind the following statistical properties: if $X \sim \mathcal{N}(\mu, \sigma)$, then $\mathbb{E}[X] = \mu$, and $\text{Var}[X] = \sigma^2$. Moreover $X^2 \sim \sigma^2 \chi^2(1)$, $\mathbb{E}[\chi^2(1)] = 1$ and $\text{Var}[\chi^2(1)] = 2$ thus $\text{Var}[X^2] = 2\sigma^4$.

Thus, from one side, $\langle u\phi_n \rangle \sim \mathcal{N}\left(0, \sqrt{\frac{1}{A} \int_0^{2\pi} \frac{1}{2\pi} \left| \tilde{u}^*(\vec{k}_n) \right|^2 d\theta}\right)$, then:

$$\text{Var}[\langle u\phi_n \rangle^2] = 2 \text{Var}[\langle u\phi_n \rangle]^2 \quad (\text{C.31})$$

$$= 2 \left(\frac{1}{A} \int_0^{2\pi} \frac{1}{2\pi} \left| \tilde{u}^*(\vec{k}_n) \right|^2 d\theta \right)^2 \quad (\text{C.32})$$

and from the other side:

$$\text{Var} \left[\left(\frac{1}{A} \int_0^{2\pi} \frac{1}{2\pi} \left| \tilde{u}^*(\vec{k}_n) \right|^2 d\theta \right) w_n^2 \right] = \left(\frac{1}{A} \int_0^{2\pi} \frac{1}{2\pi} \left| \tilde{u}^*(\vec{k}_n) \right|^2 d\theta \right)^2 \text{Var} [w_n^2] \quad (\text{C.33})$$

$$= 2 \left(\frac{1}{A} \int_0^{2\pi} \frac{1}{2\pi} \left| \tilde{u}^*(\vec{k}_n) \right|^2 d\theta \right)^2 \quad (\text{C.34})$$

We then argue that the assertion holds, and equations (C.14) (with (C.28)) and (C.29) have the same variance and mean value.

If we remove the side boundaries of the cavity, then the eigenfrequencies are not discrete but continuous. In this case, we can express an impedance $Z_R(k)$ which is taken to be a free-space impedance for the port. From (C.29), we get, as the step between two consecutive eigenfrequencies tends to zero, the following result:

$$Z_R(k) = \lim_{\alpha \rightarrow \infty} -\frac{j}{\pi} \sum_{n=1}^{\alpha N} \frac{\Delta}{\alpha} \frac{R_R(k_n)}{k^2 - k_n^2} \quad (\text{C.35})$$

$$= -\frac{j}{\pi} \int_0^\infty \frac{R_R(k_n)}{k^2 - k_n^2} dk_n^2 \quad (\text{C.36})$$

From the KRAMERS-KRÖNING relations we get $X_R(k)$:

$$\Re[-jZ_R(k)] = X_R(k) = \mathcal{P} \left(-\frac{1}{\pi} \int_0^\infty \frac{R_R(k)}{k^2 - k_n^2} dk_n^2 \right) \quad (\text{C.37})$$

with $X_R(k) = \Im[Z_R(k)]$.

Then, Z is expressed as a mean value \bar{Z} and a fluctuating part \tilde{Z} :

$$Z = \bar{Z} + \tilde{Z} \quad (\text{C.38})$$

As $\mathbb{E}[w_n^2] = 0$, and from equation (C.29):

$$\bar{Z} = -\frac{j}{\pi} \sum_n^\infty \mathbb{E} \left[\Delta \frac{R_R(k_n) w_n^2}{k^2 - k_n^2} \right] = -\frac{j}{\pi} \sum_n^\infty \Delta \frac{R_R(k_n)}{k^2 - k_n^2} \quad (\text{C.39})$$

Then, (C.39) may be approximated by (C.37), with Δ the mean spacing between eigenvalues, and:

$$\bar{Z} = jX_R(k) \quad (\text{C.40})$$

Finally, (C.38) may be rewritten like [Zheng et al., 2006b]:

$$Z = \bar{Z} + \tilde{Z} = j(X_R(k) + R_R(k)\xi) \quad (\text{C.41})$$

with:

$$\xi = -\frac{1}{\pi} \sum_{n=1}^N \frac{1}{\Delta} \frac{w_n^2}{k^2 - k_n^2} = -\frac{1}{\pi} \sum_{n=1}^N \frac{w_n^2}{\tilde{k}^2 - \tilde{k}_n^2} \quad (\text{C.42})$$

where: $\tilde{k}^2 = \frac{k^2}{\Delta}$ and $\tilde{k}_n^2 = \frac{k_n^2}{\Delta}$.

C.5 Generalisation to the multiple port case

C.5.1 Deterministic approach

Equation (C.8) may be changed to:

$$(\nabla^2 + k^2)V_T(t) = -jkh\eta_0 \sum_{i=1}^M u_i(\vec{x}) \hat{I}_i \quad (\text{C.43})$$

Where the phasor voltage is defined as in (C.9):

$$V_i = \sum_j Z_{ij} \hat{I}_j = \iint_{\mathbb{R}^2} u_i(\vec{x}) V_T(\vec{x}, t) dx dy \equiv \langle u_i \hat{V}_T \rangle \quad (\text{C.44})$$

Thus, the cavity impedance is given by:

$$\underline{\underline{Z}} = -jkh\eta_0 \sum_n \frac{\vec{\phi}_n \otimes \vec{\phi}_n^T}{k^2 - k_n^2} \quad (\text{C.45})$$

where:

$$\vec{\phi}_n = \begin{bmatrix} \langle u_1 \phi_n \rangle \\ \langle u_2 \phi_n \rangle \\ \vdots \\ \langle u_M \phi_n \rangle \end{bmatrix} \quad (\text{C.46})$$

C.5.2 Statistical approach

From the BERRY's hypothesis, we argue that the vector $\vec{\phi}_n$ is composed of Gaussian elements with zero mean. For a given eigenfunction ϕ_n , and depending on the location of the ports (linked to $u_i(\vec{x})$), two $\langle u_a \phi_n \rangle$ and $\langle u_b \phi_n \rangle$ may be correlated. Indeed, for two close port locations, the correlation function of the random plane wave superpositions leads to $\psi(\vec{r}, \vec{r}') = \text{E}[\phi_n(\vec{r})\phi_n(\vec{r}')] \propto J_0(k|\vec{x} - \vec{x}_i|)$ [Alhassid and Lewenkopf, 1995, Zheng et al., 2006b].

To take into account this, the correlation $\vec{\phi}_n$ is changed to:

$$\vec{\phi}_n = \underline{\underline{L}}(k_n) \vec{w}_n \quad (\text{C.47})$$

The excitation of a given port by an eigenmode depends on its geometry and on the structure of the eigenfunction in the vicinity of this port. As for the 2D case, and from the BERRY's hypothesis, the random superposition of plane waves is taken into account by \vec{w}_n . Then, $\underline{\underline{L}}(k_n)$ is relative to the port geometry.

Equation (C.45) becomes:

$$\underline{\underline{Z}} = -jkh\eta_0 \sum_n \frac{\underline{\underline{L}}(k_n) \vec{w}_n \vec{w}_n^T \underline{\underline{L}}^T(k_n)}{k^2 - k_n^2} \quad (\text{C.48})$$

As for the 2D situation with a single port, we compute the expectation of $\underline{\underline{Z}}$:

$$\text{E} [\underline{\underline{Z}}] = -j \int_0^\infty \frac{kh\eta_0}{\Delta} \frac{\underline{\underline{L}}(k_n) \text{E} [\vec{w}_n \vec{w}_n^T] \underline{\underline{L}}^T(k_n)}{k^2 - k_n^2} dk_n^2 \quad (\text{C.49})$$

$$= \underline{\underline{Z}}_R(k) \quad (\text{C.50})$$

$$= \underline{\underline{R}}_R(k) + j\underline{\underline{X}}_R(k) \quad (\text{C.51})$$

With this formulation, $R_R(k)$ becomes [Zheng, 2005]:

$$\underline{\underline{R}}_R(k) = \frac{\pi kh\eta_0}{\Delta} \underline{\underline{L}}(k) \underline{\underline{L}}^T(k) \quad (\text{C.52})$$

Thus (C.48) becomes:

$$\underline{\underline{Z}} = j\underline{\underline{X}}_R - \frac{j}{\pi} \sum_n \frac{1}{\Delta} \frac{\underline{\underline{R}}_R(k_n)^{\frac{1}{2}} \vec{w}_n \vec{w}_n^T \underline{\underline{R}}_R(k_n)^{\frac{1}{2}}}{k^2 - k_n^2} \quad (\text{C.53})$$

$$= j\underline{\underline{X}}_R + \left[\underline{\underline{R}}_R^{\frac{1}{2}} \right] \left[-\frac{j}{\pi} \sum_n \frac{1}{\Delta} \frac{\vec{w}_n \vec{w}_n^T}{k^2 - k_n^2} \right] \left[\underline{\underline{R}}_R^{\frac{1}{2}} \right] \quad (\text{C.54})$$

$$= j\underline{\underline{X}}_R + \left[\underline{\underline{R}}_R^{\frac{1}{2}} \right] \underline{\underline{\xi}} \left[\underline{\underline{R}}_R^{\frac{1}{2}} \right] \quad (\text{C.55})$$

Appendix D

Determination of the antenna factor from experimental data, and of the electric field from the antenna factor

Contents

D.1	Determination of the electric field strength at a distance D from an antenna using its antenna factor AF.	197
D.2	Determination of the antenna factor with two identical antennas	199

In this appendix, a formula is set to determine the field strength at a distance D using the antenna factor of an antenna. Moreover, the procedure to measure the antenna factor AF with two identical antennas is recalled. This expression is used to determine the field at the location of an aperture, as needed in [III.5.7](#).

The antenna factor is defined as the ratio of the field illuminating an antenna \vec{E}_{inc} to the voltage that this field generates across the impedance of the receiver Z_0 .

$$AF = \frac{|\vec{E}_{\text{inc}}|}{|V_s|} \quad (\text{D.1})$$

Fig. [D.1a](#) depicts the studied configuration.

D.1 Determination of the electric field strength at a distance D from an antenna using its antenna factor AF .

The electric field $\vec{E}(\vec{r})$, in the far field region, may be expressed as [[Balanis, 2016](#)]:

$$\vec{E}(\vec{r}) = -j \frac{e^{-jk\vec{r}}}{4\pi|\vec{r}|} \begin{bmatrix} 0 \\ \eta k R_\theta(\theta, \phi) + k F_\theta(\theta, \phi) \\ \eta k R_\phi(\theta, \phi) + k F_\phi(\theta, \phi) \end{bmatrix} = -j \frac{\eta k}{4\pi} \frac{e^{-jk\vec{r}}}{|\vec{r}|} \vec{F}_\perp(\theta, \phi) \quad (\text{D.2})$$

where the quantities $R_\theta(\theta, \phi)$ and $F_\theta(\theta, \phi)$ are related to the electric and magnetic sources that are responsible for the field. η is the free space impedance ($\eta = 120\pi \Omega$), \vec{r} is the position of interest, and

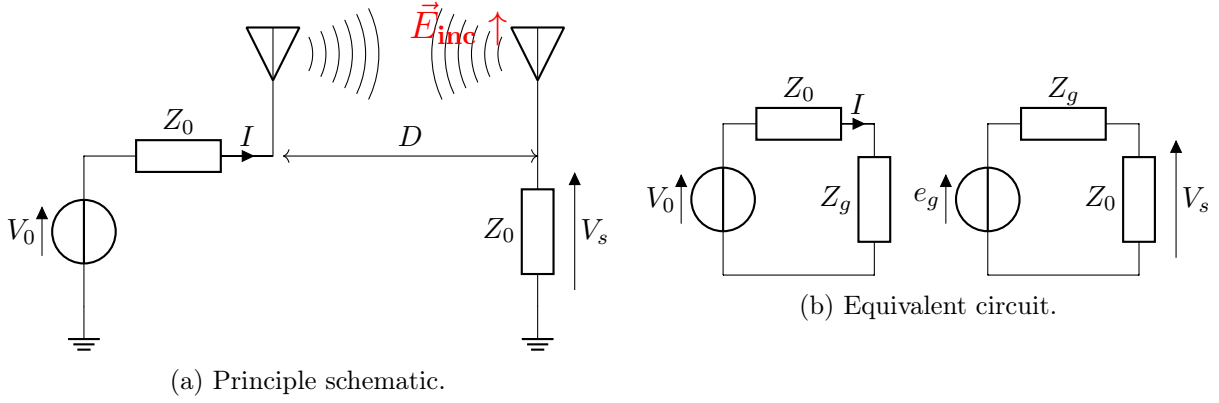


Fig. D.1 – Principle schematic and equivalent circuit.

k is the wavenumber.

At the receiving antenna, the effective length l_e allows to determine the open circuit voltage V_{oc} when the antenna is illuminated by a plane wave. When there is a perfect polarization matching between the antenna and incident electric field, the voltage across the impedance of the receiver Z_0 may be express as:

$$V_s = e_g \frac{Z_0}{Z_0 + Z_g} = E_{inc} l_e \frac{Z_0}{Z_0 + Z_g} \quad (D.3)$$

Then:

$$AF = \left| \frac{E_{inc}}{V_s} \right| = \frac{|Z_0 + Z_g|}{Z_0} \frac{1}{|l_e|} \quad (D.4)$$

At the transmitting antenna, the electric field E_{inc} produced by the current I through the antenna input impedance Z_g is:

$$E_{inc} = j \frac{\eta k}{4\pi} \frac{e^{-jk r_i}}{r_i} I l_e = j \frac{\eta k}{4\pi} \frac{e^{-jk r_i}}{r_i} \frac{V_0}{Z_0 + Z_g} l_e \quad (D.5)$$

In case of a perfect polarization, the electric field at the location of the receiving antenna is:

$$E_{inc} = j \frac{\eta k}{4\pi} \frac{e^{-jk D}}{D} I l_e \quad (D.6)$$

$$= j \frac{\eta k}{4\pi} \frac{e^{-jk D}}{D} \frac{V_0}{Z_0 + Z_g} l_e \quad (D.7)$$

$$= j \frac{\eta k}{4\pi} \frac{e^{-jk D}}{D} \frac{V_0}{Z_0} \frac{Z_0}{Z_0 + Z_g} l_e \quad (D.8)$$

And the electric field strength $|E_{inc}|$ is expressed as:

$$|E_{inc}| = \frac{\eta k}{4\pi} \frac{1}{D} \frac{|V_0|}{Z_0} \frac{1}{|AF|} \quad (D.9)$$

D.2 Determination of the antenna factor with two identical antennas

Let us use two identical antennas with the same antenna factor. If we rewrite equation (D.3) for the receiving antenna, and injecting equation D.8 that gives the electric field at a distance D of a transmitting antenna (configuration shown in Fig. D.1a), we obtain:

$$V_s = E_{\text{inc}} l_e \frac{Z_0}{Z_0 + Z_g} \quad (\text{D.10})$$

$$= j \frac{\eta k}{4\pi} \frac{e^{-jkD}}{D} \frac{V_0 Z_0}{(Z_0 + Z_g)^2} |l_e|^2 \quad (\text{D.11})$$

Then:

$$\frac{V_s}{V_0} = j \frac{\eta k}{4\pi} \frac{e^{-jkD}}{D} \frac{Z_0}{(Z_0 + Z_g)^2} |l_e|^2 \quad (\text{D.12})$$

If we take the module of (D.12), we have:

$$\left| \frac{V_s}{V_0} \right| = \frac{\eta k}{4\pi} \frac{1}{D} \frac{Z_0}{(Z_0 + Z_g)^2} |l_e|^2 \quad (\text{D.13})$$

$$\left| \frac{V_s}{V_0} \right| = \frac{\eta k}{4\pi} \frac{1}{D} \frac{1}{Z_0 A F^2} \quad (\text{D.14})$$

Then:

$$A F^2 = \frac{\eta k}{4\pi} \frac{1}{D} \frac{1}{Z_0} \left| \frac{V_0}{V_s} \right| \quad (\text{D.15})$$

$$A F = \sqrt{\frac{\eta k}{4\pi} \frac{1}{D} \frac{1}{Z_0} \left| \frac{V_0}{V_s} \right|} \quad (\text{D.16})$$

Thanks to a vector network analyzer, the ratio $\left| \frac{V_s}{V_0} \right|$ is acquired as:

$$|S_{21}| = \frac{\sqrt{\frac{|V_s|^2}{Z_0}}}{\sqrt{\frac{|V_0|^2}{Z_0}}} = \left| \frac{V_s}{V_0} \right| \quad (\text{D.17})$$

Finally, the antenna factor of two identical antennas may be determined from the acquisition of the forward voltage gain S_{21} :

$$A F = \sqrt{\frac{\eta k}{4\pi} \frac{1}{D} \frac{1}{Z_0} \frac{1}{|S_{21}|}} \quad (\text{D.18})$$

Annexe E

Résumé des travaux

Contents

E.1	Introduction	200
E.2	La sécurité électromagnétique (SECEM)	201
E.2.1	Menaces liées à l'émissivité des équipements électroniques	201
E.2.2	Menaces liées à la susceptibilité des équipements électroniques	202
E.2.3	Identification d'une menace peu prise en compte	202
E.3	Méthodes d'étude des couplages dans les cavités	203
E.3.1	Critères de sélection	203
E.3.2	Revue de la littérature	203
E.3.3	Choix des méthodes	205
E.4	Établissement et évaluation de deux modèles de châssis d'ordinateur	205
E.4.1	Définition des deux modèles	205
E.4.2	Comparaisons entre les deux modèles	206
E.5	Le modèle de couplages aléatoires	207
E.5.1	Présentation du modèle de couplages aléatoires	207
E.5.2	Mise en œuvre	209
E.5.3	Les deux configurations d'intérêts	209
E.5.4	Application aux couplages dans les châssis d'équipements informatiques	211
E.6	Conclusion	214
E.7	Travaux futurs	215

E.1 Introduction

La sécurité électromagnétique (SE) peut être considérée comme la réunion de la compatibilité électromagnétique (CEM) et de la sécurité des systèmes d'information (SSI). Pour rappel, l'immunité d'un équipement est son aptitude à fonctionner dans un environnement électromagnétique bruité, alors que le « mutisme » (émissivité de faible intensité) est sa capacité à ne pas perturber son environnement. L'étude de la SE d'équipements peut amener à considérer les couplages entre systèmes. En effet, si un signal traité par un équipement sensible se couple sur un autre équipement non maîtrisé, ou appartenant à un autre système d'information (SI), il est alors possible de perdre la confidentialité de l'information. Il s'agit de la menace TEMPEST. Il existe aussi le risque qu'un équipement perturbe volontairement un autre équipement et l'empêche de fonctionner correctement (perte de la

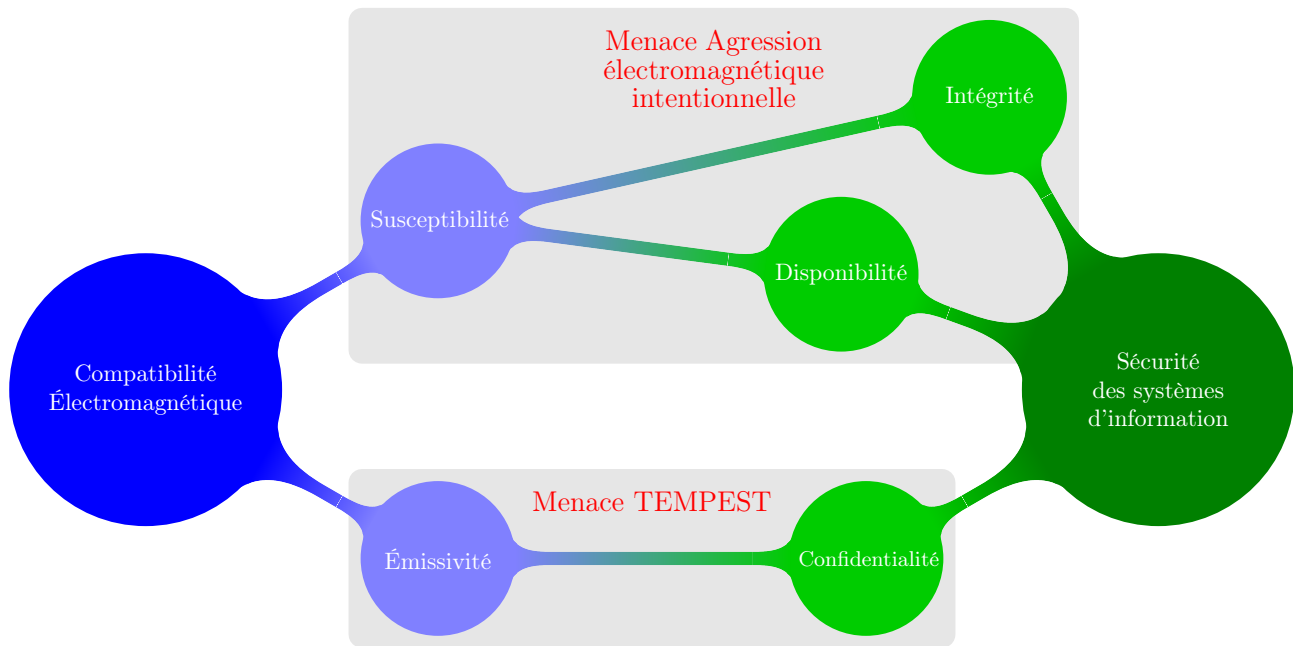


FIGURE E.1 – Liens entre la compatibilité électromagnétique (CEM) et la sécurité des systèmes d'information (SSI).

disponibilité ou de l'intégrité de l'information). Il s'agit de la menace agression électromagnétique intentionnelle (AGREMI). La figure E.1 présente les liens entre la CEM et la SSI.

Afin de faire évoluer ses connaissances sur ces sujets (couplages inter-équipements et intra-équipement), l'Agence nationale de la sécurité des systèmes d'information (ANSSI) a proposé le sujet de thèse suivant : "Sécurité de fonctionnement électromagnétique des systèmes d'information". Une collaboration avec le Laboratoire d'Électronique et Électromagnétisme (L2E) de Sorbonne Université (qui a fusionné ensuite avec le Laboratoire de génie électrique de Paris - GeePs) a été initiée pour travailler sur ce sujet. Ce qui suit est un résumé de ces travaux.

E.2 La sécurité électromagnétique (SECEM)

E.2.1 Menaces liées à l'émissivité des équipements électroniques

Considérons dans un premier temps les menaces liées à l'émissivité des équipements électroniques. Tout dispositif électronique, lorsqu'il est en fonctionnement, génère des émissions électromagnétiques parasites autour de lui. Lorsque ces dispositifs sont en fonctionnement, ils vont générer des interférences électromagnétiques. Ceci constitue la menace TEMPEST qui est étudiée depuis les années 1950. Si ces interférences sont corrélées à l'information traitée, et si elles peuvent être détectées par un système d'acquisition, alors la confidentialité de l'information ne peut plus être garantie. Certaines sources d'interférences électromagnétiques sont connues pour porter atteinte à la confidentialité de l'information. Parmi ces sources, on trouve les signaux des flux vidéo (signaux *Video Graphics Array* (VGA) par exemple). Il est possible, après une étape d'acquisition de ces interférences et de traitement du signal, de retrouver l'information. Dans le cas des signaux vidéo, il s'agit de l'image affichée à l'écran. On peut citer les travaux de [Van Eck, 1985] ou plus récemment de [Kuhn, 2005] sur ce sujet. De la même manière, et à partir des interférences générées par les claviers d'ordinateurs, il est possible de retrouver la frappe clavier [Vuagnoux and Pasini, 2009]. D'autres techniques permettent d'influer sur les interférences générées par un équipement électronique, et ce à partir d'un logiciel s'exécutant sur

cet équipement. On parle alors de soft-TEMPEST. En effet, l'exécution de la suite d'instructions que représente un programme informatique va générer des signaux électriques dans l'équipement. En écrivant un programme *ad hoc*, il est possible d'avoir une influence sur les signaux électriques parcourant l'équipement. Ces signaux électriques vont à leur tour générer des interférences qui seront corrélées à l'information qui aura été codée depuis le programme. Il s'agit d'une méthode permettant d'exfiltrer de l'information. On trouve dans la littérature des illustrations de cette méthode, comme par exemple dans [Kuhn and Anderson, 1998] ou [Guri et al., 2015].

E.2.2 Menaces liées à la susceptibilité des équipements électroniques

Considérons maintenant les menaces liées à la susceptibilité des équipements électroniques. L'objectif d'une AGREMI est de générer des perturbations des fonctions électroniques d'un équipement ou d'un système. Ces perturbations peuvent être temporaires ou aller jusqu'à la destruction physique des composants électroniques. Une perte de la disponibilité du système d'information que supporte cet équipement est alors à craindre. Dans [Hoad and Sutherland, 2007], une étude des effets de ces agressions est proposée pour des équipements électroniques sur étagère. Une classification des effets possibles d'une AGREMI est donnée dans [Sabath, 2010]. Les systèmes frontaux fonctionnant dans le domaine des radio-fréquences constituent un point d'entrée évident pour une AGREMI. Dans [Dubois et al., 2014] et [van de Beek et al., 2015], l'impact d'une AGREMI sur des éléments, tels que des boucles à verrouillage de phase ou des amplificateurs, est évalué vis-à-vis de la disponibilité du système de communication sous-jacent.

Parfois, l'AGREMI peut servir à créer un canal de communication caché, en utilisant la susceptibilité d'un système ou d'un composant. Ces canaux peuvent par exemple permettre de rompre l'isolation physique d'une machine déconnectée. Dans [Houchouas et al., 2016], la susceptibilité d'un capteur de température permet de créer un canal de communication. En effet, on peut montrer que la valeur de la température retournée par le système d'acquisition est linéairement liée à la densité surfacique de puissance électromagnétique à proximité du capteur. En modulant une AGREMI avec de l'information, un programme s'exécutant sur l'équipement cible peut, en surveillant la valeur de température, retrouver l'information.

E.2.3 Identification d'une menace peu prise en compte

Il est commun de trouver des équipements électroniques placés dans des châssis métalliques. Ils assurent un blindage électromagnétique qui permet de maintenir un bon niveau de compatibilité électromagnétique en limitant la susceptibilité des équipements qu'ils enferment à leur environnement, et réciproquement leur émissivité vers leur environnement. Si des couplages interviennent à l'intérieur de la cavité, et du point de vue de la sécurité électromagnétique, il existe le risque que :

- un système frontal radio-fréquence devienne indisponible ;
- un canal caché de communication soit établi ;
- un couplage mette à mal la confidentialité de l'information ;
- un composant cesse de fonctionner correctement ;
- etc.

Ces châssis peuvent se comporter comme des cavités réverbérantes, ce qui rend difficile l'estimation des couplages à l'intérieur de ceux-ci. Pour certains couples (fréquence, conditions aux limites), les résonances qui apparaissent à l'intérieur de ceux-ci favorisent les couplages. Or, ce sont ces couplages qui augmentent les risques vis-à-vis de la sécurité de l'information. De plus, il est très probable que les

conditions aux limites imposées au champ électromagnétique ne soient pas invariantes dans le temps. En effet, si un utilisateur décide d'ajouter un élément à l'intérieur de l'équipement, ces conditions aux limites vont alors changer et, par conséquent, les couplages. On peut aussi penser au cas où une paroi d'un châssis est déformée, par le poids d'un objet par exemple. De même, il est difficilement envisageable que la position des câbles dans un boîtier (s'ils ne sont pas contraints) soit invariante dans le temps. Enfin, il est également envisageable que la géométrie du châssis, à l'intérieur duquel un sous-système sera installé, ne soit pas connue précisément au moment de la conception de ce sous-système. Dès lors, une approche déterministe de ce problème ne semble donc pas être la plus adaptée. Il est plus pertinent de considérer les conditions aux limites du châssis étudié comme étant aléatoires.

Il devient alors nécessaire de définir des méthodes permettant d'obtenir des statistiques (sur des courants ou des tensions) pour un grand nombre de conditions aux limites différentes, chacune d'elles correspondant à une géométrie particulière de la cavité. Ces méthodes doivent permettre de prendre en compte à la fois les couplages entre éléments à l'intérieur d'un châssis (configuration 1), mais également le couplage d'une onde plane sur un élément placé dans le châssis au travers d'une ouverture (configuration 2).

E.3 Méthodes d'étude des couplages dans les cavités

E.3.1 Critères de sélection

Les méthodes qui ont été sélectionnées pour être évaluées devaient permettre de :

- déterminer des couplages au sein de la cavité pour une large bande de fréquences ;
- prendre en compte des couplages avec une ouverture dans la cavité ;
- changer les conditions aux limites à l'intérieur de la cavité.

De plus, les fréquences que ces méthodes devaient permettre de prendre en compte correspondent aux fréquences d'horloges présentes dans les châssis des équipements électroniques. Celles-ci s'étendent jusqu'à plusieurs dizaines de gigahertz.

L'état de l'art a été dressé à partir de ces trois critères.

E.3.2 Revue de la littérature

Les méthodes identifiées sont listées dans le tableau E.1. Certaines sont limitées à des cavités vides comme [Robinson et al., 1996], [Rabat et al., 2018] ou encore [Boutar et al., 2015]. Ces méthodes sont souvent basées sur des modèles de circuits, et nécessitent parfois le calcul des fonctions de GREEN de la cavité étudiée. Dans [Park et al., 2009], une méthode topologique est utilisée. Le champ électromagnétique y est également obtenu avec les fonctions de GREEN de la cavité. D'autres encore sont statistiques comme [Junqua, 2010], [Kovalevsky et al., 2014] ou encore [Flintoft et al., 2016], et nécessitent une densité de modes importante dans la cavité afin d'être appliquées (approche Power Balance). Quelle que soit l'approche envisagée, la caractérisation et le calcul des couplages ne sont pas aisés. Dans [Caudron et al., 2010] et [Antonsen et al., 2011], des modèles de « circuits » statistiques permettent de déterminer des couplages. Ils nécessitent également une densité de modes suffisante dans la cavité pour pouvoir être appliqués. Enfin, les méthodes basées sur la résolution numérique des équations de MAXWELL peuvent également être envisagées. On parle de simulateur *full-wave*. Ces approches permettent de simuler n'importe quelle géométrie de cavité, pourvu qu'elle puisse être décrite par un modèle 3D. Dans [Siah et al., 2003] ou [Vogt, 2016] une méthode de résolution fréquentielle est utilisée. Mais, les méthodes fréquentielles ne sont pas adaptées à des études sur un large spectre de fréquences. On trouve aussi des méthodes hybrides, telles que [Lange and Leone, 2017] et [Xiao et al., 2016], qui utilisent également des simulateurs *full-wave*.

Literature	Modèle Power balance	Modèle topologique	Modèle circuit	Modèle statistique	Modèle nécessitant des simulations full-wave	Modèle expérimental	Sans dépendance géométrique	Prise en compte des ouvertures	Densité de modes	Temps de calcul
Robinson et al. [1996]		●					●	U		⊕
Siah et al. [2003]				●		●		U		⊕⊕
Park et al. [2009]		●				◐	◐	U		⊕⊕
Junqua [2010]	●	●		●		●	●	O		⊕
Caudron et al. [2010]			●	●		●	◐	O		⊕
Antonsen et al. [2011]			●	●		●	◐	O		⊕
Kovalevsky et al. [2014]	●			●		●	●	O		⊕
Boutar et al. [2015]			●				●	O		⊕
Vogt [2016]			●	◐	●	●		O&U		⊕⊕⊕
Xiao et al. [2016]		●		●		◐	●	U		⊕⊕⊕
Flintoft et al. [2016]	●			●		●		O		⊕
Lange and Leone [2017]			●	●				U		⊕⊕
Rabat et al. [2018]		●					◐	U		⊕
Types de modèle					Capacités			Coûts		

TABLE E.1 – Comparaison de méthodes permettant de résoudre des problèmes de couplages électromagnétiques au sein de châssis d'équipements électroniques. Les demi-cercles ◐ indiquent des limitations. O indique que le modèle nécessite une densité de modes importante pour être appliqué, au contraire de U (peu de modes dans la cavité).

E.3.3 Choix des méthodes

Avant de réaliser une sélection parmi les méthodes identifiées, il est nécessaire d'exposer les propriétés découlant d'une densité de modes importante dans une cavité. Nous nous intéressons ici au cas où la densité de modes permet de décrire le champ électromagnétique comme une somme infinie d'ondes planes progressives. Cette description a d'abord été formulée dans [Berry, 1977], puis plus tard dans [Hill, 1998].

Cette description théorique peut être obtenue dans la pratique en réalisant une moyenne d'ensemble du champ électromagnétique présent dans une cavité et ce, pour un grand nombre de conditions aux limites différentes. Pour ce faire, il est commun de placer un élément métallique mobile, appelé brasseur de modes, dans une cavité pour en changer les conditions aux limites. L'ensemble des modes propres de la cavité sera donc différent pour chaque position de ce brasseur. Le calcul d'une moyenne d'ensemble du champ sur toutes ces conditions aux limites permet d'obtenir (sous certaines hypothèses) la description du champ telle que proposée par HILL.

Cette description du champ électromagnétique peut être utilisée à notre avantage. En effet, nous souhaitons ici considérer des cavités ayant des géométries et donc des conditions aux limites aléatoires. Si nous considérons un grand nombre de ces conditions aux limites, alors la description du champ électromagnétique à l'intérieur de la cavité proposée par HILL peut s'appliquer.

Parmi les modèles répondant à ces critères se trouvent les simulateurs *full-wave*. En effet, il est envisageable d'effectuer plusieurs simulations pour déterminer le couplage entre deux cartes, avec des conditions aux limites différentes. Par ailleurs, il existe peu, s'il en existe, d'études sur les couplages dans des cavités utilisant des simulations électromagnétiques dans le domaine temporel. Celles-ci ont l'avantage de fournir des informations sur les couplages pour une large bande de fréquences, ce qui était un des critères de sélection, établis précédemment.

Enfin, le modèle de couplages utilisé dans [Caudron et al., 2010] et [Antonsen et al., 2011] semble également très pertinent. Il permet de déterminer des couplages dans des cavités considérées comme chaotiques, et donc de prendre en compte un grand nombre de conditions aux limites différentes. Ce modèle sera donc également étudié.

E.4 Établissement et évaluation de deux modèles de châssis d'ordinateur

Nous avons décidé de nous intéresser aux couplages dans un milieu réverbérant très commun : les boîtiers d'ordinateur de bureau. Dans un premier temps, deux modèles de ce boîtier d'ordinateur ont été définis. Le premier prend la forme d'une maquette physique, et le second d'un modèle de simulation électromagnétique. Ce dernier comprend une description 3D de la structure à simuler, ainsi qu'un ensemble de paramètres de simulation.

E.4.1 Définition des deux modèles

E.4.1.1 Le modèle de simulation

Le modèle de simulation électromagnétique est défini pour le logiciel commercial de simulation [CST Studio Suite \(CST-SS\)](#). Ce dernier a été choisi car il permet de réaliser des simulations dans le domaine temporel. Il est donc capable de fournir des courants et des tensions sur une large bande de fréquences. La figure [E.2](#) présente un rendu 3D de ce modèle. La méthode permettant de résoudre les équations de MAXWELL mise en œuvre dans [CST-SS](#) est la technique d'intégration finie [finite integration technique \(FIT\)](#).

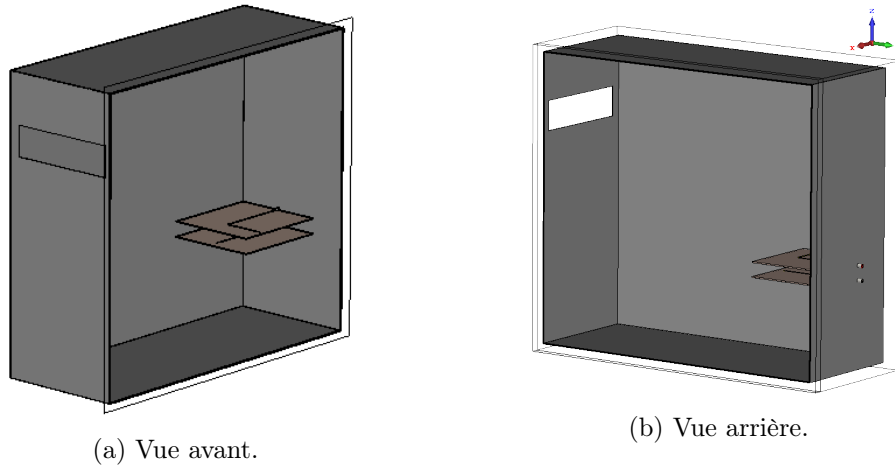


FIGURE E.2 – Modèle 3D du châssis d'ordinateur, avec une ouverture et deux circuits imprimés.

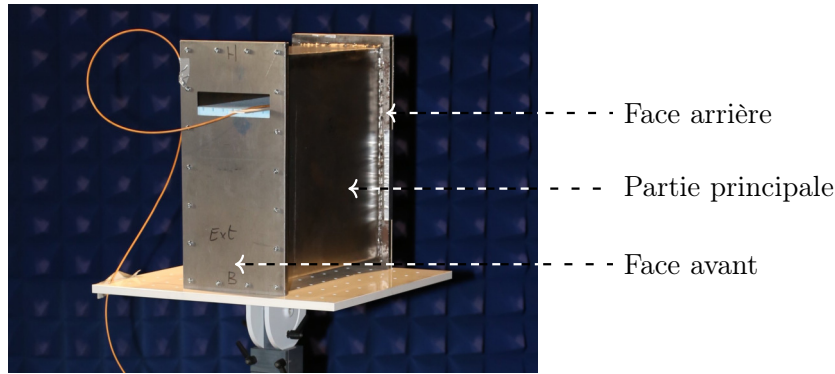


FIGURE E.3 – Photo de la maquette.

E.4.1.2 La maquette

Après avoir établi un cahier des charges qui visait à simplifier la simulation en termes de nombre de matériaux et de niveau de complexité géométrique, le boîtier a été réalisé au sein du L2E. La figure E.3 présente une photo de cette maquette. Lors de sa réalisation, des déformations sont apparues sur les quatre côtés du boîtier (sans doute dues à une élévation de température trop importante lors de l'étape de soudure qui avait été sous-traitée). Une étude a permis de montrer que ces déformations ont un impact significatif sur les résultats de simulations. Il est donc nécessaire de les intégrer au modèle numérique. Dans un second temps, sa conception a été validée expérimentalement en mesurant son efficacité de blindage qui est de 55 dB au minimum sur une bande de fréquence allant de 800 MHz à 3 GHz. La figure E.4 présente l'efficacité de blindage, également appelée atténuation, pour une incidence normale de l'onde plane sur la face avant de la maquette.

E.4.2 Comparaisons entre les deux modèles

Les deux modèles étant définis, ils peuvent être comparés. Deux configurations ont été testées. La première, la plus simple, correspond à un boîtier vide ayant une ouverture sur sa face avant. On cherchait alors à comparer des valeurs de champ électrique mesurées ou calculées par l'outil de simulation. Les deux techniques, mesure et simulation, ont donné des résultats similaires pour des évaluations de champ électrique à plusieurs positions dans le boîtier, et pour deux positions de l'ouverture sur la face

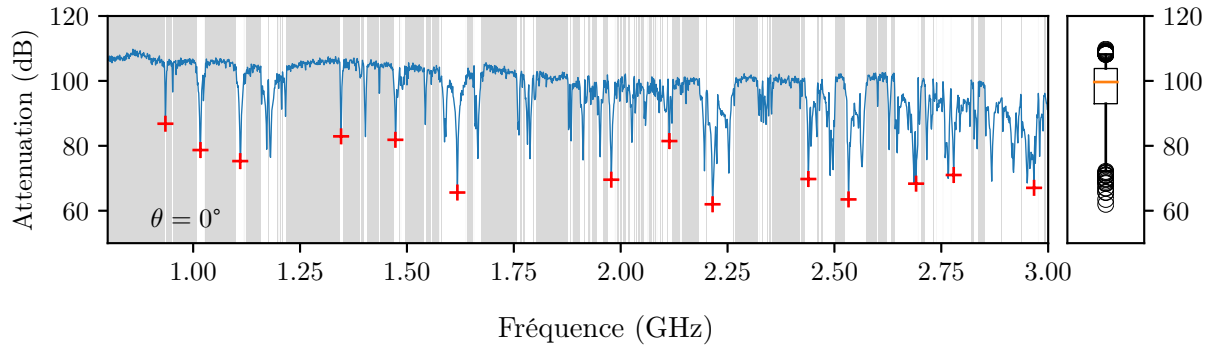


FIGURE E.4 – Efficacité de blindage pour une incidence normale d’une onde plane sur le boîtier.

avant de la maquette.

Pour la seconde configuration, des circuits imprimés comportant des lignes de transmission ont été ajoutés dans le boîtier. Il s’agissait dès lors de comparer les tensions mesurées ou simulées à l’extrémité de ces lignes de transmission. Un facteur d’antenne pour chaque modèle a été défini comme étant le module du champ électrique sur l’ouverture, divisé par la tension recueillie à l’extrémité de la ligne de transmission. Dans un premier temps, un empilement de deux cartes a été considéré. La figure E.5 présente la configuration mesurée. Les résultats ont montré une différence moyenne de ± 10 dB entre 1 GHz et 3 GHz. Une configuration à quatre cartes empilées a ensuite été testée, et une incertude plus importante a été obtenue qui est de ± 17 dB entre 1.25 GHz et 3 GHz. Ce dernier résultat est présenté sur la figure E.6.

L’objectif initial est d’obtenir des statistiques sur les courants et tensions couplés. Il est alors nécessaire d’effectuer un grand nombre de simulations avec des conditions aux limites aléatoires. Le temps de calcul est de 4 heures pour la configuration à quatre cartes. On peut raisonnablement penser que le nombre de simulations ne sera pas inférieur à quelques dizaines pour obtenir des statistiques pertinentes, ce qui donne plusieurs dizaines d’heures de simulations dans ce cas. Ce temps de calcul peut limiter l’intérêt de cette approche.

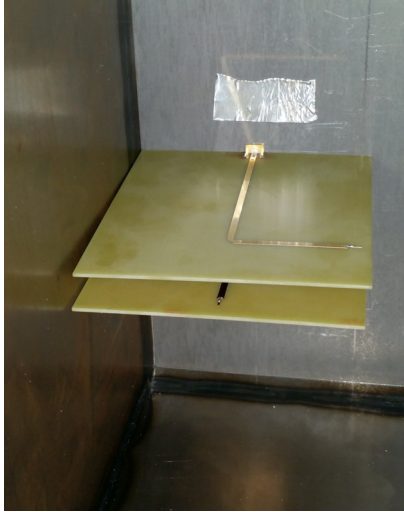
Il semble alors pertinent d’évaluer la seconde approche identifiée lors de l’état de l’art : le modèle de couplages aléatoires.

E.5 Le modèle de couplages aléatoires

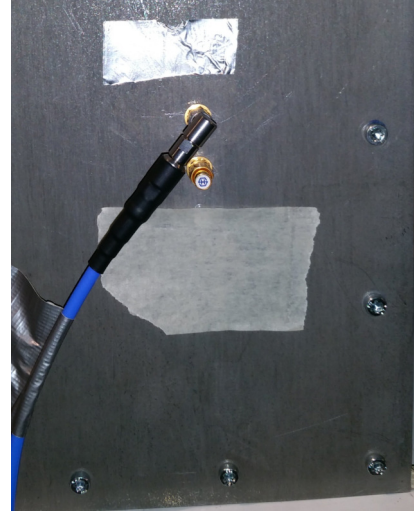
Depuis les années 1950, la théorie des matrices aléatoires se développe de plus en plus. Après avoir été utilisée pour résoudre des problèmes de physique quantique, elle s’applique à des problèmes de physique semi-classique, et particulièrement en électromagnétisme où elle est appelée Random Coupling Model (RCM), ou modèle de couplages aléatoires.

E.5.1 Présentation du modèle de couplages aléatoires

Le modèle de couplages aléatoires est un modèle statistique de circuit où les relations entre les accès d’un système réverbérant sont décrites par une matrice dite impédance de cavité $\underline{Z}^{\text{cav}}$. Pour utiliser ce modèle, il est nécessaire que la densité de modes dans la cavité soit suffisante pour qu’elle soit considérée comme chaotique. Il permet d’associer deux modes de couplages entre les accès. Le premier, déterministe, prend en compte le couplage en espace libre entre plusieurs accès dans un système (entre une carte et un câble, par exemple). Il peut être facilement obtenu, soit par la mesure, soit par la simulation, ou encore par un modèle *ad hoc*. Ce couplage est pris en compte dans la matrice de



(a) Configuration avec les cartes.



(b) Connecteur SMA (vu de l'extérieur).

FIGURE E.5 – Photo du dispositif.

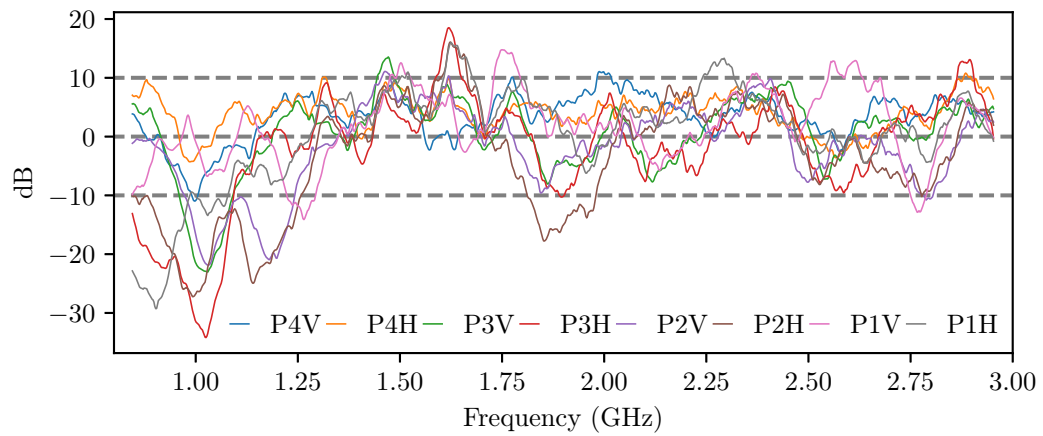


FIGURE E.6 – Moyenne glissante (sur 40 MHz) de la différence des facteurs d'antenne mesurés et calculés, pour 8 configurations (deux polarisations (V et H) et quatre cartes (1 à 4)).

rayonnement $\underline{\underline{Z}}^{\text{rad}}$. Le second mode considère les couplages des différentes résonances dans la cavité sur les accès, et est représenté par la matrice $\underline{\underline{\xi}}$. L'impédance de la cavité $\underline{\underline{Z}}^{\text{cav}}$ s'obtient alors grâce à l'équation :

$$\underline{\underline{Z}}^{\text{cav}} = \text{j}\Im \left\{ \underline{\underline{Z}}^{\text{rad}} \right\} + \left[\Re \left\{ \underline{\underline{Z}}^{\text{rad}} \right\} \right]^{1/2} \underline{\underline{\xi}} \left[\Re \left\{ \underline{\underline{Z}}^{\text{rad}} \right\} \right]^{1/2} \quad (\text{E.1})$$

Dans le cas déterministe, la matrice $\underline{\underline{\xi}}$ s'écrit comme une somme de contributions de M modes de cavité [Zheng et al., 2006a] :

$$\underline{\underline{\xi}}(k) = -\frac{\text{j}}{\pi} \sum_{n=1}^M \frac{\vec{\Phi}_n \otimes \vec{\Phi}_n^T}{\frac{k^2}{\Delta k^2} - \frac{k_n^2}{\Delta k^2} - \text{j}\alpha} \quad (\text{E.2})$$

où le vecteur $\vec{\Phi}_n$ caractérise les couplages entre les accès du système pour un mode n , k_n est le nombre d'onde du mode n , Δk est l'espacement moyen entre deux nombres d'ondes de modes propres consécutifs, enfin α permet de prendre en compte les pertes dans la cavité. Dans le cas statistique, on ne s'intéresse pas à une cavité déterminée mais à un échantillon de cavités. Les modes d'une cavité sont alors obtenus par un tirage aléatoire d'une matrice conformément à la théorie des matrices aléatoires [Hemmady, 2006]. On obtient alors la formulation matricielle suivante pour $\underline{\underline{\xi}}$:

$$\underline{\underline{\xi}} = -\frac{\text{j}}{\pi} \underline{\underline{W}} \left[\underline{\underline{\lambda}} - \text{j}\alpha \underline{\underline{1}} \right]^{-1} \underline{\underline{W}}^T \quad (\text{E.3})$$

où la matrice $\underline{\underline{W}}$ est une matrice aléatoire dont les éléments W_{ij} sont distribués selon une loi normale centrée réduite et la matrice diagonale $\underline{\underline{\lambda}}$ est issue de la théorie des matrices aléatoires [Hemmady, 2006]. Pour rendre le modèle statistique, on réalise un grand nombre de tirages de Monte-Carlo de matrices $\underline{\underline{\xi}}$ ($\underline{\underline{Z}}^{\text{rad}}$ étant déterministe). À partir de tirages de géométries de boîtiers, on obtient des probabilités d'occurrence de l'amplitude des courants induits.

E.5.2 Mise en œuvre

Pour faire converger ces probabilités, il est nécessaire d'effectuer de nombreux tirages. Avec une application naïve de l'équation E.3, on calcule des milliers de tirages en quelques heures. Pour réduire ce temps de calcul, des optimisations de plusieurs natures peuvent être réalisées. La matrice $\left[\underline{\underline{\lambda}} - \text{j}\alpha \underline{\underline{1}} \right]^{-1}$ est diagonale, ce qui permet de passer d'une complexité en $O(M^2N)$ à $O(MN)$ pour le calcul de la matrice $\left[\underline{\underline{\lambda}} - \text{j}\alpha \underline{\underline{1}} \right]^{-1} \underline{\underline{W}}^T$. De plus, il est possible de faire appel à des bibliothèques permettant d'utiliser des optimisations présentes sur certains processeurs. La bibliothèque *Math Kernel Library* d'INTEL en fait partie. Elle fournit des fonctions permettant d'utiliser des optimisations matérielles, et repose sur des algorithmes spécifiques aux types de matrices mises en jeu dans les calculs (hermitiennes, symétriques, etc.). Enfin, les tirages de Monte-Carlo étant indépendants, il est possible d'effectuer des tirages en parallèle en utilisant les différents cœurs des processeurs. Un programme développé en langage compilé utilisant ces optimisations permet d'obtenir des courants induits ou des tensions couplées en quelques minutes pour des milliers de tirages de la matrice $\underline{\underline{Z}}^{\text{cav}}$.

E.5.3 Les deux configurations d'intérêts

Revenons maintenant aux deux configurations d'études présentées précédemment. La première (configuration 1) était relative aux couplages entre une onde plane et un élément de la cavité. La seconde (configuration 2) se rapportait à l'étude des couplages entre éléments dans une cavité.

La figure E.7 présente la configuration 1. On peut montrer que le problème peut être divisé en deux sous-problèmes [Harrington and Mautz, 1976] : le problème intérieur (en bleu) et le problème extérieur (en rouge). Chacun de ces problèmes peut être décrit par deux admittances. L'onde plane

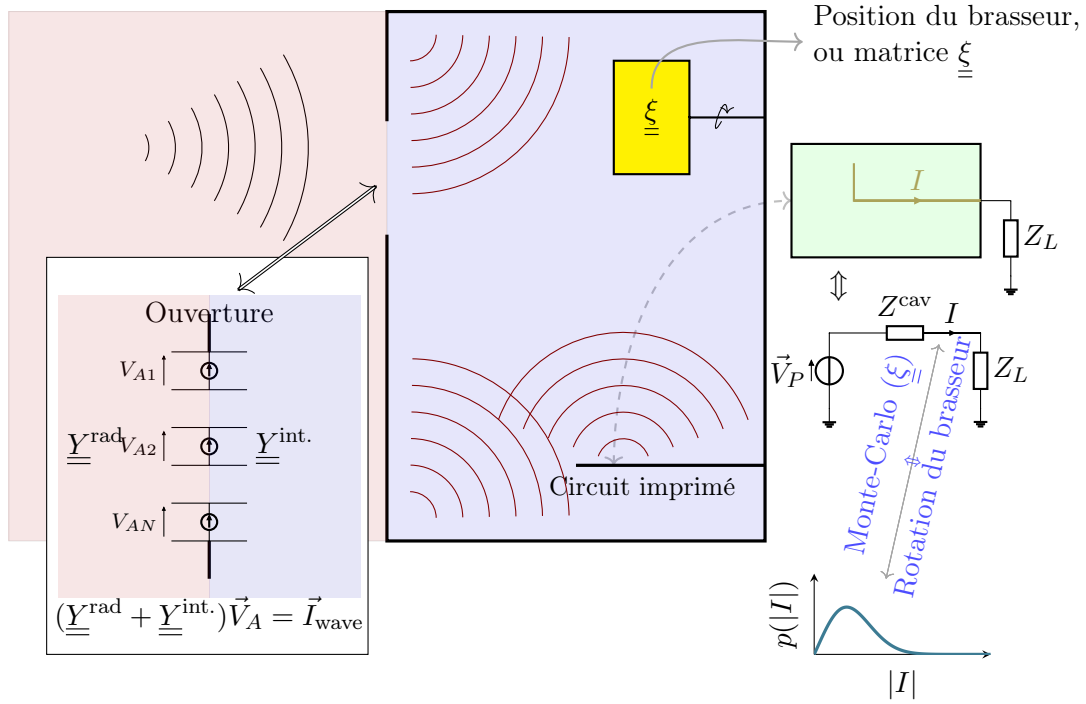


FIGURE E.7 – Configuration 1 - Couplage entre une ouverture et un élément placé à l'intérieur d'une cavité.

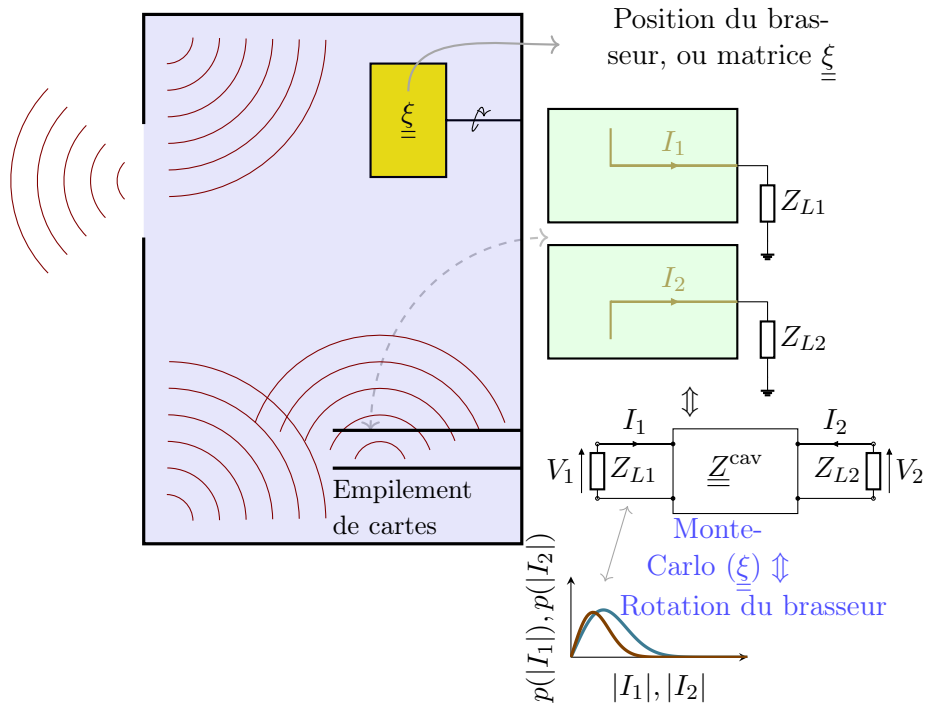


FIGURE E.8 – Configuration 2 - Couplages entre éléments d'un boîtier.

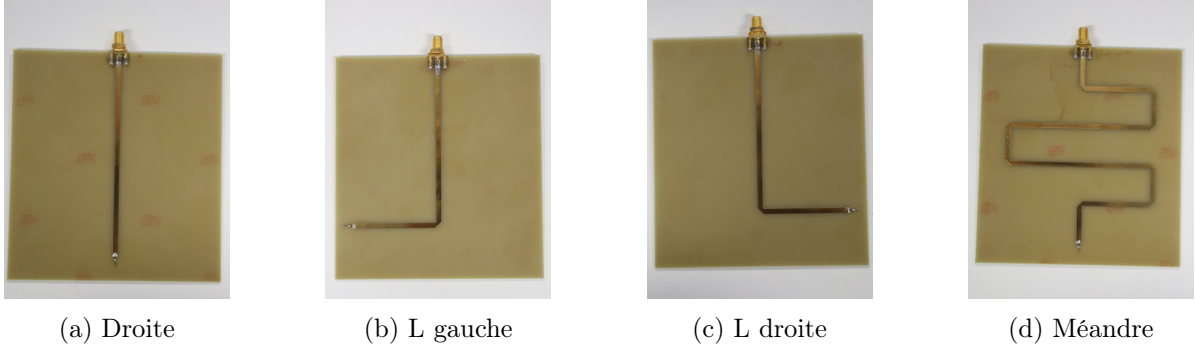


FIGURE E.9 – Les quatre cartes utilisées dans les empilements.

incidente est caractérisée par un vecteur courant \vec{I}^{inc} appliqué au niveau de l'ouverture. L'impédance d'une ouverture rectangulaire est de la forme [Antonsen et al., 2011] :

$$Y_{nm}^{\text{rad}}(k_0) = \sqrt{\frac{\epsilon_0}{\mu_0}} \int_{\mathbb{R}^3} \frac{1}{(2\pi)^3} \frac{2j}{k_0(k_0^2 - k^2)} \vec{e}_n \Delta \vec{e}_m^* d^3k \quad (\text{E.4})$$

où \vec{e}_n sont la transformée de FOURIER du mode dans l'ouverture et Δ une matrice. L'impédance Z^{cav} (un scalaire ici, car il n'y a qu'un seul port dans la cavité) est obtenue par le modèle de couplages aléatoires. Afin d'obtenir des statistiques, il est nécessaire de réaliser un grand nombre de tirages de la matrice $\underline{\xi}$. Cela revient à changer les conditions aux limites dans la cavité (grâce à un brasseur de modes par exemple). Avec $\underline{\xi}$ on calcule Z^{cav} et $\underline{Y}^{\text{int.}}$ puis l'amplitude du courant couplé $|I|$.

L'application du RCM $\underline{\xi}$ pour la seconde configuration est beaucoup plus directe et est représentée sur la figure E.8. Elle consiste à utiliser directement les équations (E.1) et (E.2).

E.5.4 Application aux couplages dans les châssis d'équipements informatiques

On va rechercher ici à estimer les probabilités d'occurrence d'amplitude de courants induits sur des pistes de circuits imprimés (cartes) empilés et placés dans un système aux conditions limites statistiques (changeantes). Des fonctions de répartition $F_{|I|}(i)$, donnant la probabilité d'occurrence d'un courant d'amplitude i , issues du modèle de couplages aléatoires, seront comparées aux valeurs obtenues par la mesure.

E.5.4.1 Configurations testées

Plusieurs configurations d'empilement (Tableau E.2) de cartes (Fig. E.9) ont été considérées. La position 1 correspond à l'emplacement le plus bas et la position 4 à l'emplacement le plus haut de l'empilement. Les emplacements sont distants de 2 cm. Ces configurations ont été choisies pour permettre de comparer les résultats du modèle de couplages aléatoires pour plusieurs configurations. Celles-ci présentent différents espacements entre les cartes afin d'obtenir des configurations modales différentes dans l'empilement.

E.5.4.2 Mesures

Pour valider les résultats issus de l'application du modèle de couplages aléatoires, une série de mesures a été réalisée. Afin d'obtenir des statistiques sur les amplitudes de courants induits et les tensions mesurées, un brasseur de modes a été monté dans cette maquette (Fig. E.10). À chacune de ses positions, il impose des conditions aux limites différentes, ce qui permet de simuler une géométrie de boîtier différente. Les mesures ont été réalisées avec un analyseur de réseau vectoriel relié aux

Conf.	Pos. 1	Pos. 2	Pos. 3	Pos. 4
1	Méandre	Droite	L droite	L gauche
2	L droite	Méandre	L gauche	Droite
3	L droite	-	-	L gauche
4	L droite	-	L gauche	-
5	Méandre	Droite	-	L gauche

TABLE E.2 – Configurations mesurées et simulées



FIGURE E.10 – Maquette et brasseur.

connecteurs (FIGURE E.5b) des cartes électroniques disposées en fonction de la configuration choisie (Table. E.2).

E.5.4.3 Détermination des paramètres du modèle de couplages aléatoires

Trois grandeurs sont nécessaires pour appliquer le modèle de couplages aléatoires : $\underline{\underline{Z}}^{\text{rad}}$, M et α . Les matrices impédances $\underline{\underline{Z}}^{\text{rad}}$ des cinq configurations ont été obtenues, par la mesure, à partir des matrices de répartition $\underline{\underline{S}}^{\text{rad}}$ acquises en espace libre. La position relative entre les cartes a été assurée grâce à des supports en mousse, électromagnétiquement transparente. Le paramètre M , qui représente le nombre de modes pris en compte dans la cavité, est issu de la littérature. On trouve par exemple dans [Gradoni et al., 2012] la valeur de $M = 600$. Plusieurs essais ont permis de mettre en évidence que le fait d'augmenter la valeur de M ne permet pas d'améliorer les résultats. Enfin, le paramètre le plus compliqué à estimer est α , qui caractérise les pertes dans le système étudié et qui dépend de la fréquence. Plusieurs techniques peuvent être mises en œuvre pour l'estimer [Hemmady, 2006] et [Gil et al., 2016]. Dans cette étude, α a été déterminé à partir des mesures de $\underline{\underline{S}}^{\text{cav}}$ qui permet de calculer $\underline{\underline{\xi}}^{\text{cav}}$ en inversant l'équation E.1. Dans [Gil et al., 2016], les auteurs montrent que les éléments de $\underline{\underline{\xi}}^{\text{cav}}$ suivent des lois normales et que :

$$\text{Var} [\Re [\xi_{ii}^{\text{cav}}]] = \text{Var} [\Im [\xi_{ii}^{\text{cav}}]] = \frac{1}{\pi\alpha_{ii}} \quad (\text{E.5})$$

$$\text{Var} [\Re [\xi_{ij}^{\text{cav}}]] = \text{Var} [\Im [\xi_{ij}^{\text{cav}}]] = \frac{1}{2\pi\alpha_{ij}} \quad (\text{E.6})$$

En calculant les variances des éléments de $\underline{\underline{\xi}}^{\text{cav}}$, on détermine les valeurs des α_{ij} en fonction de la fréquence. Enfin, on calcule leur moyenne qu'on égale à α ($\alpha = \langle \alpha_{ij} \rangle$).

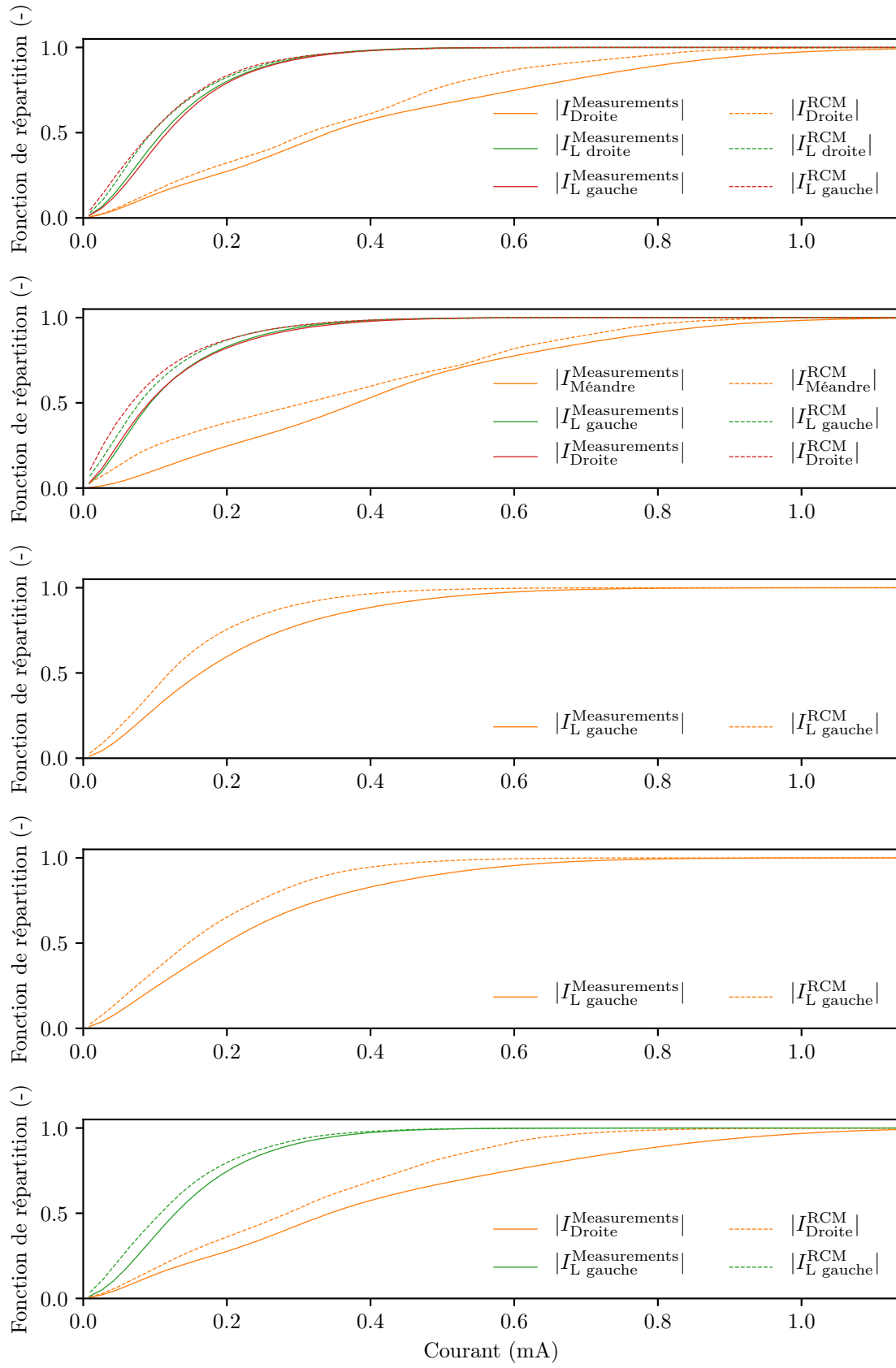


FIGURE E.11 – Comparaison des fonctions de répartition des amplitudes des courants induits obtenues avec des mesures et avec le modèle de couplages aléatoires, pour les cinq configurations.

E.5.4.4 Résultats

Les résultats (Fig. E.11) correspondent aux fonctions de répartition des amplitudes des courants induits sur les cartes présentes dans le boîtier. On s'intéresse ici aux couplages entre la carte source au bas de l'empilement, située à la position 1 (Table E.2), et les autres cartes de l'empilement. Une puissance de $P_0 = 10$ dBm est appliquée sur l'accès de la carte source. Les courants traversant les accès du système sont donnés par la formule suivante :

$$\bar{I}^{\text{Mesures/RCM}} = (\underline{\underline{Z}}^{\text{Mesures/cav}} + \underline{\underline{Z}}_l \underline{\underline{1}})^{-1} \begin{bmatrix} \sqrt{2Z_l P_0} \\ \vdots \end{bmatrix} \quad (\text{E.7})$$

où $Z_l = 50 \Omega$. Ces fonctions de répartition ont été obtenues en agrégeant pour chacun des 360 tirages de Monte-Carlo (pour le modèle de couplages aléatoires) ou chacune des 360 positions de brasseurs (pour les mesures), 16501 points de fréquences entre 10 et 26.5 GHz. Au total ce sont $16501 \times 360 = 5940360$ courants induits qui sont agrégés par courbe. La comparaison montre que les densités de probabilité obtenues avec le modèle de couplages aléatoires sont relativement proches de celles obtenues expérimentalement. Les résultats sont moins bons lorsqu'il y a des couplages directs entre les cartes, c'est-à-dire quand elles sont en regard l'une de l'autre comme observé sur $|I_{\text{Droite}}^{\text{Mesures/RCM}}|$ pour la configuration 1 ou encore sur $|I_{\text{L gauche}}^{\text{Mesures/RCM}}|$ pour les configurations 3 et 4. Le temps de calcul permettant de réaliser le tirage de ces courants afin d'estimer les fonctions de répartition pour un cas à quatre cartes est de 3 minutes, et de 2 minutes pour deux cartes. Ces courbes montrent également que la disposition des cartes électroniques a un impact sur les fonctions de répartition des amplitudes de courants induits, et donc sur les probabilités de couplages des informations traitées d'une carte vers une autre.

E.6 Conclusion

Dans le cadre d'une analyse de risque portant sur la sécurité de l'information traitée par un système d'information sensible, il est pertinent de vouloir estimer les probabilités d'occurrence des amplitudes des courants induits (ou des tensions couplées) dans des équipements réverbérants tels que des châssis d'équipements électroniques. Nous avons décidé de nous intéresser aux couplages dans des cavités très communes : les châssis d'ordinateur de bureau. Trois modèles ont été identifiés pour traiter ce problème. Le premier, qui prend la forme d'une maquette, sert à valider les deux autres qui sont décrits ci-après.

Le modèle de simulation Tout d'abord un modèle de simulation déterministe a été envisagé. Le choix s'est porté sur une technique permettant d'obtenir les couplages sur une large bande de fréquences. Le couplage entre des cartes placées dans une cavité et une onde plane qui se couple sur l'ouverture du boîtier est déterminé. On a alors estimé l'incertitude sur les résultats obtenus. Dans le cas à deux cartes, elle est de ± 10 dB, et dans le cas à quatre cartes, elle est de ± 17 dB entre 800 MHz et 3 GHz. Cette incertitude est importante. Seule sa connaissance permet de définir des marges à appliquer pour garantir un niveau de couplage acceptable du point de vue de la SECeM. Ces marges ont été définies grâce à une analyse de risque. De même, le temps de calcul nécessaire pour obtenir des statistiques sur les couplages peut être prohibitif.

Le modèle de couplages aléatoires Le modèle de couplages aléatoires peut fournir une estimation rapide des probabilités d'occurrence des courants induits, et donc de leurs percentiles. La procédure permettant d'appliquer le modèle de couplages aléatoires a été présentée, et des optimisations permettant d'accélérer les calculs ont été proposées. De plus, la méthode permettant d'acquérir des données expérimentales avec un petit brasseur a été décrite. Enfin, une comparaison entre des données expérimentales et des tirages de Monte-Carlo issus du modèle de couplages aléatoires a été effectuée. Elle

montre que l'usage du modèle de couplages aléatoires est pertinent pour évaluer rapidement des fonctions de répartition des amplitudes des courants couplés dans une cavité, quand les cartes ne sont pas en regard les unes des autres et que le système est chaotique. Cependant, l'application de ce modèle nécessite de pouvoir estimer les pertes dans la cavité, ainsi que l'impédance en espace libre entre les accès pour lesquels on souhaite déterminer les couplages. La détermination de ces deux quantités peut se révéler complexe.

E.7 Travaux futurs

Il pourra être intéressant d'appliquer le modèle de couplages aléatoires afin d'estimer l'impact en termes d'amplitude des courants induits lors d'une agression électromagnétique intentionnelle, provenant de l'extérieur de la cavité ou du boîtier. Ce type d'agression peut avoir un impact à la fois sur la disponibilité d'un système d'information, mais aussi sur l'intégrité des données manipulées. L'analyse théorique permettant d'intégrer les ouvertures dans le RCM étant réalisée, il reste encore à mener une comparaison des simulations du modèle de couplages aléatoires avec des données expérimentales.

Les pertes associées aux châssis ont un impact significatif sur les couplages à l'intérieur de ceux-ci. Une étude concernant l'effet de l'ajout de matériaux absorbants sur les tensions ou courants couplés pourra être entreprise. Avec cette analyse, il sera possible de déterminer la surface d'absorbant à ajouter dans une cavité pour réduire l'amplitude des courants et tensions couplés, afin de satisfaire les exigences de SECCEM.

Dans le cas où les pertes ne peuvent pas être modifiées dans la cavité, il pourra être intéressant de déterminer les agencements (c'est-à-dire les positions relatives entre elles) de cartes qui permettent de minimiser les couplages. Cela pourra être accompli en déterminant des impédances en espace libre pour plusieurs agencements de cartes (avec des simulations full-wave par exemple). Enfin, le modèle de couplages aléatoires pourra être appliqué afin de sélectionner l'agencement qui minimise les couplages.

Finalement, des tailles de cavités différentes de celle qui a été étudiée dans cette thèse, pourront être considérées. Les baies d'équipements informatiques seraient alors un cas d'étude pertinent pour la SECCEM car, à proximité d'un équipement sensible, peuvent cohabiter des équipements non maîtrisés.

Abstract :

The electromagnetic security (EMSEC) can be defined as the merging of the electromagnetic compatibility (EMC) and the information security. To guarantee the EMSEC of electronic devices, electromagnetic couplings must be taken into account. Yet, these couplings can be maximized (under certain conditions) within reverberant environments, such as casings. Thus, it is relevant to study and to characterize these couplings inside such environments. However, sometimes, the boundary conditions of the studied system can be unknown, or can vary over time. Therefore, statistical approaches, where the boundary conditions are randomized, are better suited than deterministic ones. Coupled currents and voltages are thus statistically determined. In this PhD thesis, three different models were set to assess the couplings within a desktop computer chassis. The first one is a mock-up and is used to compare the other two models. The second one is a full-wave simulation model of a computer casing. From its implementation, it was possible to determine the coupling between an aperture and transmission lines, with its associated uncertainty. This uncertainty is significant, however it is known. From the EMSEC perspective, its knowledge can be an input for a risk assessment process. It can be used to determine a safety margin in order to mitigate the coupling risks. Finally, the third one is a circuit model where the eigenmodes are randomized by means of the random matrix theory. From it, couplings between several transmission lines printed on circuit boards were determined. Nevertheless, to be applied, it requires several parameters whose determination can be quite difficult.

Keywords : *electromagnetic security (EMSEC), electromagnetic compatibility (EMC), coupling, reverberant environments, full-wave simulations, random matrix theory.*

Sécurité de fonctionnement électromagnétique des systèmes d'information
Estimation statistique de couplages en milieu réverbérant

Résumé :

La sécurité électromagnétique (SECEM) peut être considérée comme la réunion de la compatibilité électromagnétique et de la sécurité des systèmes d'information. L'étude de la SECEM des équipements électroniques amène à considérer les couplages électromagnétiques entre ceux-ci. Or, ces couplages peuvent être maximisés dans les environnements électromagnétiques réverbérants, tels que les châssis d'équipements électroniques. Dès lors, il est pertinent de vouloir caractériser les couplages au sein de ces châssis. Celle-ci n'est pas aisée car les conditions aux limites à l'intérieur de ces équipements peuvent ne pas être connues ou varier dans le temps. Il paraît alors pertinent de vouloir considérer les conditions aux limites du système à étudier comme étant aléatoires. Des statistiques sur les tensions ou les courants couplés seront alors obtenues. Dans ce travail, trois modèles ont été définis pour analyser statistiquement les couplages dans un châssis d'ordinateur. Le premier, une maquette physique, sert de référence pour les deux autres, à des fins de comparaisons. Le second est un modèle numérique. Il a permis de déterminer le couplage entre une ouverture et des lignes de transmission avec une incertitude non négligeable mais connue. Cette connaissance permet de définir des marges de sécurité afin de garantir la sécurité de l'information. Enfin, le troisième est un modèle de circuit qui suppose que les modes sont aléatoires. Fondé sur la théorie des matrices aléatoires, il a permis de déterminer rapidement des couplages entre des cartes électroniques. Toutefois, son application requiert la détermination de plusieurs grandeurs, dont l'estimation peut ne pas être triviale.

Mots clés : *sécurité électromagnétique (SECEM), compatibilité électromagnétique (CEM), couplage, environnement réverbérant, simulations électromagnétiques, théorie des matrices aléatoires.*